

UNIVERSIDAD DE VALENCIA-CSIC
DEPARTAMENTO DE FÍSICA ATÓMICA, MOLECULAR Y NUCLEAR
INSTITUTO DE FÍSICA CORPUSCULAR



**Study of beta-delayed neutron emitters in the
region of ^{78}Ni and its impact on r-process
nucleosynthesis**

Alvaro Tolosa Delgado

DOCTORADO EN FÍSICA
Julio 2020

Supervisor:
Jose Luis Tain Enriquez

A mi familia y amigos

José Luis Taín Enríquez, Investigador Científico del Consejo Superior de Investigaciones Científicas (CSIC)

CERTIFICA:

Que la presente memoria con título **Study of beta-delayed neutron emitters in the region of ^{78}Ni and its impact on r-process nucleosynthesis** ha sido realizada bajo su dirección en el Instituto de Física Corpuscular (Centro Mixto Universitat de València - CSIC) por **Alvaro Tolosa Delgado** para su presentación como Tesis Doctoral dentro del programa de doctorado en Física del Departamento de Física Atómica, Molecular y Nuclear de la Universidad de Valencia.

Y para que así conste, en cumplimiento con la legislación vigente, presenta ante el Departamento de Física Atómica, Molecular y Nuclear la referida memoria, firmando el presente certificado en Paterna (Valencia) a fecha de

Fdo. José Luis Taín Enríquez

This Thesis work has been supported by the Spanish Ministerio de Economía y Competitividad under grants FPA2014-52823-C2-1-P,
FPA2017-83946-C2-1-P.



Table of Contents

List of Figures	xiii
List of Tables	xxiii
List of common acronyms	xxv
Abstract	xxvii
1 Motivation and basic physics	1
1.1 β -delayed neutron emission	2
1.2 Nuclear structure of neutron rich nuclei	3
1.3 Astrophysical side. R-process	13
1.3.1 R-process sites	17
1.3.2 Numerical simulations	19
2 Experiment	21
2.1 Production of isotopes	21
2.2 Radioactive ion separation and identification. BigRIPS	22
2.3 Implanted ion and decay detector. AIDA	23
2.4 Beta delayed neutron setup. BRIKEN	25
2.4.1 Neutron counter	25
2.4.2 Gamma ray detectors	28
2.4.3 Ancillary detectors	29
2.4.4 BRIKEN Data Acquisition System (DAQ)	30
2.5 Summary of the experimental setup	32
2.6 Summary of run conditions	34
3 Analysis methodology	35
3.1 BigRIPS. Isotope identification	35
3.2 AIDA. Implant and beta event reconstruction	36
3.3 BRIKEN neutron counter	38
3.3.1 Energy calibration	38

Table of Contents

3.3.2	Detection efficiency	39
3.3.3	DAQ Live time determination	41
3.4	Merging the data from AIDA, BigRIPS and BRIKEN	43
3.5	Sort conditions	45
3.5.1	Implanted isotope identification	45
3.5.2	Beta-implant correlation	45
3.5.3	Beta-neutron correlation	47
3.5.4	Vetos	48
3.6	Isotope dependency of neutron efficiency	51
3.7	Fitting procedure	55
3.7.1	Beta activity functions	55
3.7.2	Correlated and uncorrelated background	57
3.7.3	Definition of fitting functions	58
3.7.4	Uncertainty estimation	61
3.8	Summary	62
4	Experimental results	63
4.1	^{86}Ge . High statistics case.	64
4.2	^{79}Zn . Sensitivity limit to small P_{1n}	66
4.3	^{93}Se . Sensitivity limit to small P_{2n}	69
4.4	^{92}As . Sensitivity limit to small number of implants	71
4.5	Summary and selected results	73
5	Discussion of results	81
5.1	Comparison with theoretical estimates	81
5.1.1	One neutron emission probabilities estimates	82
5.1.2	Two neutron emission probabilities estimates	89
5.1.3	Half-life estimates	94
5.1.4	$P_n/T_{1/2}$ versus $Q_{\beta 1n}$ systematics	100
5.2	Astrophysical impact	100
5.2.1	Core-collapse supernova	103
5.2.2	Neutron star mergers	106
5.2.3	Summary	111
6	Conclusions	113
Appendices		115
A	General results	117
B	Neutron detection efficiency for each isotope	121

C Fits of beta decay and neutron-beta decay curves	125
C.1 Fit of ^{75}Co decay curves	125
C.2 Fit of ^{75}Ni decay curves	126
C.3 Fit of ^{76}Ni decay curves	126
C.4 Fit of ^{77}Ni decay curves	127
C.5 Fit of ^{78}Ni decay curves	127
C.6 Fit of ^{76}Cu decay curves	128
C.7 Fit of ^{77}Cu decay curves	128
C.8 Fit of ^{78}Cu decay curves	129
C.9 Fit of ^{79}Cu decay curves	129
C.10 Fit of ^{80}Cu decay curves	130
C.11 Fit of ^{81}Cu decay curves	130
C.12 Fit of ^{79}Zn decay curves	131
C.13 Fit of ^{80}Zn decay curves	131
C.14 Fit of ^{81}Zn decay curves	132
C.15 Fit of ^{82}Zn decay curves	132
C.16 Fit of ^{83}Zn decay curves	133
C.17 Fit of ^{84}Zn decay curves	133
C.18 Fit of ^{82}Ga decay curves	134
C.19 Fit of ^{83}Ga decay curves	134
C.20 Fit of ^{84}Ga decay curves	135
C.21 Fit of ^{85}Ga decay curves	135
C.22 Fit of ^{86}Ga decay curves	136
C.23 Fit of ^{87}Ga decay curves	136
C.24 Fit of ^{85}Ge decay curves	137
C.25 Fit of ^{86}Ge decay curves	137
C.26 Fit of ^{87}Ge decay curves	138
C.27 Fit of ^{88}Ge decay curves	138
C.28 Fit of ^{89}Ge decay curves	139
C.29 Fit of ^{88}As decay curves	139
C.30 Fit of ^{89}As decay curves	140
C.31 Fit of ^{90}As decay curves	140
C.32 Fit of ^{91}As decay curves	141
C.33 Fit of ^{92}As decay curves	141
C.34 Fit of ^{91}Se decay curves	142
C.35 Fit of ^{92}Se decay curves	142
C.36 Fit of ^{93}Se decay curves	143
C.37 Fit of ^{94}Br decay curves	143
D Post neutron star merger nucleosynthesis. Disk ejecta	145

Table of Contents

E Resumen en castellano	153
E.1 Motivación	153
E.1.1 Estructura nuclear de la desintegración beta	154
E.1.2 Astrofísica del proceso de captura rápida de neutrones	156
E.2 Experimento	157
E.2.1 Identificación de los iones radioactivos. BigRIPS	157
E.2.2 Dector de implantaciones y desintegraciones. AIDA	158
E.2.3 Detector de neutrones beta retardados. BRIKEN	159
E.2.4 Condiciones del experimento	160
E.3 Método de análisis	161
E.3.1 Procesado de datos	161
E.3.2 Construcción de las curvas de desintegración	163
E.3.3 Dependencia isotópica de la eficiencia de detección de neutrón	164
E.3.4 Ajuste de las curvas de desintegración	168
E.4 Resultados	169
E.5 Discusión de los resultados	171
E.5.1 Comparación con predicciones teóricas	172
E.5.2 Impacto astrofísico	175

List of Figures

1.1	Schematic representation of multistep beta-delayed neutron emission.	2
1.2	Ratio of half-lives (left) and one neutron emission probabilities (right) predicted by Möller et al. [Möl03] and recommended experimental values taken from the last evaluation [BdN-IAEA].	5
1.3	Ratio of half-lives (left) and one neutron emission probabilities (right) predicted by Möller et al. [Möl19] and recommended experimental values taken from the last evaluation [BdN-IAEA].	7
1.4	Ratio of half-lives (left) and one neutron emission probabilities (right) predicted by Koura et al. [KTUY05] and experimental values [BdN-IAEA].	9
1.5	Ratio of half-lives (left) and one neutron emission probabilities (right) predicted by Marketin et al. [Mar16] and experimental values [BdN-IAEA].	10
1.6	Ratio of experimental values of P_n and $T_{1/2}$ plotted as a function of $Q_{\beta 1n}$ for nuclei with $28 \leq Z \leq 43$. From [McC12]	12
1.7	Ratio of one neutron emission probabilities predicted by Miernik [Mie14] and experimental values [BdN-IAEA].	13
1.8	Schematic representation of abundance evolution of r-process (blue line) and s-process (red line). [Hor19]	14
1.9	Estimated contributions from s-process and r-process to the observed Solar System (SS) abundances. Plotted values are $12 + \log_{10}$ of abundance relative to hydrogen. The peaks which are caused by r-process appear at lower masses than s-process peaks. In case of stars enriched with r-process and s-process, a double peak is observed. [Cow04].	15
1.10	Abundance pattern in HD 108317, a metal-poor star [Roe14]. Red and blue curves correspond to Solar System patterns, normalized to Eu or Ba abundance of HD 108317.	16
1.11	Schematic evolution of a neutron star merger. From [Mar].	19

List of Figures

2.1	Layout of the BigRIPS separator. The ion optics foci and the dipole magnets are labeled with the letters F and D, respectively. The particle identification is performed in the second part.	22
2.2	Layout of the BigRIPS plus ZeroDegree separators [Kub12]. The BRIKEN neutron counter and the ion/beta detector AIDA are placed at the last focal plane F11.	23
2.3	AIDA DSSD stack	24
2.4	AIDA electronic chain. Each channel has two preamplifiers.	24
2.5	Schematic of BRIKEN electronics (top panel) and a more detailed schematic of the test pulse generation (lower panel).	26
2.6	There are four different tube types: from RIKEN, UPC, ORNL 1 inch, ORNL 2 inch. Each group has different characteristics, and consequently their energy spectra have different shapes.	27
2.7	BRIKEN tubes distribution. The tubes are grouped by distance to the center into 7 rings (solid lines). The colors indicate the tube type: RIKEN (green), UPC (red), ORNL 1" (blue), ORNL 2"(pink).	28
2.8	HDPE matrix layout and tube distribution. From [Tar17].	28
2.9	Ancillary detectors in the experimental area	30
2.10	Sketch of clock signal distribution.	32
2.11	BRIKEN experimental setup layout.	33
3.1	particle identification (PID) plot corresponding to the experiment RIBF127.	36
3.2	Energy spectrum of a pulser measurement in a regular (top) and noisy strip (bottom). The X-axis corresponds to energy in ADC channels.	37
3.3	The energy deposited by implants in the last layer has a quasi-linear dependency with the velocity β (measured by BigRIPS) if the implantation layer is correctly identified. Two representative cases are shown: ^{80}Zn (left) and ^{89}As (right).	38
3.4	BRIKEN neutron spectrum of a ^{252}Cf source. Tubes are grouped in rings, almost by its distance to the center. The black line corresponds to the sum over all the rings, and the other lines corresponds to the individual rings.	39
3.5	GEANT4 simulated detector neutron efficiency as function of the neutron energy. The total efficiency, as well as the efficiency of each ring, are shown.	40
3.6	Rossi plot for a neutron ^{252}Cf source.	41
3.7	Neutron energy spectrum of a ^{252}Cf source [NDS-IAEA]. Its neutron mean energy is $\langle E_n \rangle = 2.28$ MeV.	42
3.8	Live time of individual DAQ channels, each one corresponding to a proportional tube, calculated as in Eq. (3.3). This plot corresponds to a measurement with the intense ^{252}Cf neutron source.	42

3.9	Live time of each proportional tube during RIBF127 experiment.	43
3.10	Merger FlowChart [Tol19]	44
3.11	Time difference between particle identification events (BigRIPS) and implant events (AIDA).	45
3.12	Different scenarios of implant-decay spatial correlation.	46
3.13	Size of X-clusters (continuous line) and Y-clusters (dashed line) of ^{80}Zn implants (left panel) and decays (right panel).	46
3.14	Beta-neutron time correlation curve for decays of ^{83}Ga . The neutron moderation extends up to 200 μs after the beta decay (central filled area). It is also shown a -500 μs to -300 μs widow used to determine accidental correlations.	47
3.15	Number of neutrons (multiplicity) in a 200 μs long window, after a decay of ^{92}Se (solid line) or before (dashed line). Decays are temporally and spatially correlated with implants identified as ^{92}Se	48
3.16	Beam correlated events: neutrons(left), betas (right).	49
3.17	F11 instant rate during the RIBF127 experiment.	49
3.18	XY distribution of decays of two arsenic isotopes (left), and its projection on the X axis (right).	50
3.19	Effect of few noisy strips on the uncorrelated background of ^{92}As beta decay curve.	50
3.20	On the left, beta Y-cluster energy vs beta X-cluster energy. The energy cut was applied on the average cluster energy E_β at 240 keV (dashed line). On the right, the beta decay curve of ^{80}Zn obtained using different energy cuts. The implant-induced noise is contained in the first 50 ms after the implantation.	51
3.21	Comparison of detection efficiency as function of the neutron energy (solid blue), and the averaged efficiency as function of the averaged neutron energy of some measured neutron spectrum (red dots).	52
3.22	Neutron efficiency assuming Eq. (3.6), and normalized to the nominal value 66.8%. Values of average energy $\langle E_n \rangle$ are taken from [Möl19]. Neutron spectra of $^{83,84}\text{Ga}$ were measured by Madurga et al. [Mad16], and the corresponding neutron efficiency is marked with orange dots, presenting a large discrepancy with the theoretical value.	53
3.23	Experimental values [Bra89, Mad16] of averaged energy of beta-delayed neutrons versus the $Q_{\beta 1n}$ window. They show deviations up to a factor 2 with the model which assumes constant $S_\beta(E)$ in Eq. (3.7).	54

List of Figures

3.24	Calculated neutron detection efficiency as function of $Q_{\beta 1n}$. Each marker represents one isotope appearing in one or more decay chains. The efficiency error band (gray filled area) derives from the uncertainty range of the model which relates averaged neutron energy and $Q_{\beta 1n}$, shown in Fig. 3.23. Two green markers corresponds to the neutron detection efficiency of $^{83,84}\text{Ga}$ calculated using measured neutron energy spectra [Mad16] and MC simulated efficiency as a function of E_n .	54
3.25	Calculated neutron detection efficiency as function of $Q_{\beta 2n}$. Each marker represents one isotope appearing in one or more decay chains. The efficiency error band (gray filled area) derives from the uncertainty range of the model which relates averaged neutron energy and $Q_{\beta 2n}$, shown in Fig. 3.23.	55
3.26	Decay-implant curves, without gating and 1n and 2n gated of ^{86}Ga .	56
3.27	Uncorrelated background can be built as time differences of implants and decays spatially separated by more than ten strips. A linear fit is performed in the region $t_{\beta i} < 0$, and then mirrored for $t_{\beta i} > 0$.	58
3.28	Fraction of ^{92}Se decay events that are correlated accidentally with a given number n of random neutrons. The fraction of betas that is correlated with zero random neutrons is $r_0 = 0.9825$. This plot corresponds to the neutron multiplicity of backwards beta-neutron time-correlations presented in Fig. 3.15, normalized to the number of correlations.	59
4.1	^{79}Zn decay chain.	65
4.2	Result of the simultaneous fit of the beta decay and beta-one-neutron decay curves.	65
4.3	Result of the simultaneous fit of the beta decay, beta-one-neutron decay and beta-two-neutron decay curves.	66
4.4	^{79}Zn decay chain.	67
4.5	Result of the simultaneous fit of the beta decay and beta-one-neutron decay curves.	67
4.6	Result of the simultaneous fit of the beta decay and beta-one-neutron decay curves, disregarding the correlated background.	69
4.7	^{92}As decay chain.	70
4.8	Result of the simultaneous fit of ^{93}Se beta decay, beta-one-neutron decay and beta-two-neutron decay curves.	70
4.9	^{92}As decay chain.	72
4.10	Result of the simultaneous fit of ^{92}As beta decay, beta-one-neutron decay and beta-two-neutron decay curves.	73
4.11	^{78}Ni decay chain.	75

5.1	Ratio of one neutron emission probabilities from theoretical estimates and experimental values obtained in this Thesis. The top-left panel corresponds to predictions by Möller et al. [Möl03], top-right to Möller et al. [Möl19], bottom-left to Marketin et al. [Mar16], and bottom-right to Koura et al. [KTUY05].	82
5.2	Cobalt P_{1n} experimental value compared to theoretical estimates.	83
5.3	Nickel P_{1n} experimental values compared to theoretical estimates.	84
5.4	Copper P_{1n} experimental values compared to theoretical estimates.	85
5.5	Zinc P_{1n} experimental values compared to theoretical estimates.	86
5.6	Gallium P_{1n} experimental values compared to theoretical estimates.	86
5.7	Germanium P_{1n} experimental values compared to theoretical estimates.	87
5.8	Arsenic P_{1n} experimental values compared to theoretical estimates.	88
5.9	Selenium P_{1n} experimental values compared to theoretical estimates.	88
5.10	Bromine P_{1n} experimental values compared to theoretical estimates.	89
5.11	Ratio of two neutron emission probabilities from theoretical estimates and experimental values obtained in this Thesis. The top-left panel corresponds to predictions by Möller et al. [Möl03], top-right to Möller et al. [Möl19], bottom-left to Marketin et al. [Mar16], and bottom-right to Miernik [Mie14].	90
5.12	Zinc P_{2n} experimental values compared to theoretical estimates.	91
5.13	Zinc P_{2n} experimental values compared to theoretical estimates.	91
5.14	Gallium P_{2n} experimental values compared to theoretical estimates.	92
5.15	Germanium P_{2n} experimental values compared to theoretical estimates.	92
5.16	Arsenic P_{2n} experimental values compared to theoretical estimates.	93
5.17	Selenium P_{2n} experimental values compared to theoretical estimates.	93
5.18	Ratio of half-lives from theoretical estimates and experimental values obtained in this Thesis. The top-left panel corresponds to predictions by Möller et al. [Möl03], top-right to Möller et al. [Möl19], bottom-left to Marketin et al. [Mar16], and bottom-right to Koura et al. [KTUY05].	94
5.19	Cobalt P_{1n} experimental value compared to theoretical estimates.	95
5.20	Nickel $T_{1/2}$ experimental values compared to theoretical estimates.	95
5.21	Copper $T_{1/2}$ experimental values compared to theoretical estimates.	96
5.22	Zinc $T_{1/2}$ experimental values compared to theoretical estimates.	97
5.23	Gallium $T_{1/2}$ experimental values compared to theoretical estimates.	97
5.24	Germanium $T_{1/2}$ experimental values compared to theoretical estimates.	98
5.25	Arsenic $T_{1/2}$ experimental values compared to theoretical estimates.	98
5.26	Selenium $T_{1/2}$ experimental values compared to theoretical estimates.	99
5.27	Bromine $T_{1/2}$ experimental values compared to theoretical estimates.	99

5.28	Experimental values of $P_n/T_{1/2}$ as a function of $Q_{\beta 1n}$, each marker corresponds to a single nuclide studied in this Thesis work. The red line corresponds to the formula $P_n/T_{1/2} = cQ_{\beta 1n}^d$, with parameters $c = 0.0097(9)$ and $d = 4.87(7)$ [McC12].	100
5.29	Ratio of $\langle n \rangle$ (i.e., $P_{1n} + 2P_{2n}$) values obtained in this Thesis work, and the ones included in JINA REACLIB database [REACLIB]. REACLIB database includes experimental values from [WC17], corresponding to black-filled bars, or theoretical estimates from [Mö103, Mum16a], represented by red-filled bars.	101
5.30	ratio of $T_{1/2}(\text{Exp})$ and $T_{1/2}(\text{[REACLIB]})$	102
5.31	Ratio of half-lives values obtained in this Thesis work, and the ones included in JINA REACLIB database [REACLIB]. REACLIB database includes experimental values from [WC17], corresponding to black-filled bars, or theoretical estimates from [Mö103], represented by red-filled bars.	102
5.32	Abundance pattern corresponding to the representative trajectory studied in [Win12], and calculated using the default REACLIB (<i>REACLIB</i>) and the REACLIB database updated with the results presented in this Thesis (<i>REACLIB & BRIKEN</i>).	104
5.33	R-process abundance pattern calculated in the astrophysical scenario named <i>350C-RS</i> , from [Obe17]. The pattern labeled as <i>REACLIB</i> is calculated using the default REACLIB, and the one tagged with <i>REACLIB & BRIKEN</i> corresponds to REACLIB database updated with the results presented in this Thesis.	105
5.34	Weak r-process abundance pattern produced by the astrophysical scenario named <i>350C-RS</i> , from [Obe17].	105
5.35	Abundance pattern produced by dynamic ejecta, trajectory number #517 from [Bov17].	107
5.36	Abundance pattern produced by dynamic ejecta, trajectory number #651 from [Bov17].	107
5.37	Density profile in $x-z$ plane at the beginning of the simulation. One representative thermodynamic trajectory is chosen for each angular bin (Fig. 2 from [Mar15]).	108
5.38	Abundance pattern produced by neutrino-wind ejecta in the aftermath of a two neutron star merger [Mar15], trajectory corresponding to fourth angular bin in Fig. 5.37.	109
5.39	Abundance pattern produced by neutrino-wind ejecta in the aftermath of a two neutron star merger [Mar15], trajectory corresponding to third angular bin in Fig. 5.37.	109
5.40	Abundance pattern produced by neutrino-wind ejecta in the aftermath of a two neutron star merger [Mar15], trajectory corresponding to second angular bin in Fig. 5.37.	110

5.41 Abundance pattern produced by disk ejecta in the aftermath of a two neutron star merger, trajectory from [Lip17].	111
C.1 Result of the simultaneous fit of β -decay and $\beta1n$ -decay curves of ^{75}Co	125
C.2 Result of the simultaneous fit of β -decay and $\beta1n$ -decay curves of ^{75}Ni	126
C.3 Result of the simultaneous fit of β -decay and $\beta1n$ -decay curves of ^{76}Ni	126
C.4 Result of the simultaneous fit of β -decay and $\beta1n$ -decay curves of ^{77}Ni	127
C.5 Result of the simultaneous fit of β -decay and $\beta1n$ -decay curves of ^{78}Ni	127
C.6 Result of the simultaneous fit of β -decay and $\beta1n$ -decay curves of ^{76}Cu	128
C.7 Result of the simultaneous fit of β -decay and $\beta1n$ -decay curves of ^{77}Cu	128
C.8 Result of the simultaneous fit of β -decay and $\beta1n$ -decay curves of ^{78}Cu	129
C.9 Result of the simultaneous fit of β -decay and $\beta1n$ -decay curves of ^{79}Cu	129
C.10 Result of simultaneous fit of β , $\beta1n$ and $\beta2n$ -decay curves of ^{80}Cu	130
C.11 Result of simultaneous fit of β , $\beta1n$ and $\beta2n$ -decay curves of ^{81}Cu	130
C.12 Result of the simultaneous fit of β and $\beta1n$ -decay curves of ^{79}Zn	131
C.13 Result of the simultaneous fit of β and $\beta1n$ -decay curves of ^{80}Zn	131
C.14 Result of the simultaneous fit of β and $\beta1n$ -decay curves of ^{81}Zn	132
C.15 Result of the simultaneous fit of β and $\beta1n$ -decay curves of ^{82}Zn	132
C.16 Result of the simultaneous fit of β , $\beta1n$ and $\beta2n$ -decay curves of ^{83}Zn	133
C.17 Result of the simultaneous fit of β , $\beta1n$ and $\beta2n$ -decay curves of ^{84}Zn	133
C.18 Result of the simultaneous fit of β and $\beta1n$ -decay curves of ^{82}Ga	134
C.19 Result of the simultaneous fit of β and $\beta1n$ -decay curves of ^{83}Ga	134
C.20 Result of simultaneous fit of β , $\beta1n$ and $\beta2n$ -decay curves of ^{84}Ga	135
C.21 Result of simultaneous fit of β , $\beta1n$ and $\beta2n$ -decay curves of ^{85}Ga	135
C.22 Result of simultaneous fit of β , $\beta1n$ and $\beta2n$ -decay curves of ^{86}Ga	136
C.23 Result of simultaneous fit of β , $\beta1n$ and $\beta2n$ -decay curves of ^{87}Ga	136
C.24 Result of the simultaneous fit of β and $\beta1n$ -decay curves of ^{85}Ge	137
C.25 Result of the simultaneous fit of β and $\beta1n$ -decay curves of ^{86}Ge	137
C.26 Result of simultaneous fit of β , $\beta1n$ and $\beta2n$ -decay curves of ^{87}Ge	138
C.27 Result of simultaneous fit of β , $\beta1n$ and $\beta2n$ -decay curves of ^{88}Ge	138
C.28 Result of simultaneous fit of β , $\beta1n$ and $\beta2n$ -decay curves of ^{89}Ge	139
C.29 Result of simultaneous fit of β , $\beta1n$ and $\beta2n$ -decay curves of ^{88}As	139

C.30 Result of simultaneous fit of β , $\beta1n$ and $\beta2n$ -decay curves of ^{89}As .	140
C.31 Result of simultaneous fit of β , $\beta1n$ and $\beta2n$ -decay curves of ^{90}As .	140
C.32 Result of simultaneous fit of β , $\beta1n$ and $\beta2n$ -decay curves of ^{91}As .	141
C.33 Result of simultaneous fit of β , $\beta1n$ and $\beta2n$ -decay curves of ^{92}As .	141
C.34 Result of the simultaneous fit of β and $\beta1n$ -decay curves of ^{91}Se .	142
C.35 Result of the simultaneous fit of β and $\beta1n$ -decay curves of ^{92}Se .	142
C.36 Result of simultaneous fit of β , $\beta1n$ and $\beta2n$ -decay curves of ^{93}Se .	143
C.37 Result of the simultaneous fit of β and $\beta1n$ -decay curves of ^{94}Br .	143
D.1 Time evolution of the temperature and the neutron-to-seed ratio during the trajectory number #991 of [Lip17].	146
D.2 Abundances (top) and relative abundance difference (bottom) at the beginning of the r-process, $t=0.52$ s.	147
D.3 Abundances (top) and relative abundance difference (bottom) at $t=0.67$ s.	148
D.4 Abundances (top) and relative abundance difference (bottom) at $t=0.80$ s.	149
D.5 Abundances (top) and relative abundance difference (bottom) at $t=0.93$ s.	150
D.6 Abundances (top) and relative abundance difference (bottom) at the r-process freeze-out, $t=0.998$ s.	151
E.1 Representación esquemática de la emisión retardada de neutrones.	153
E.2 Cociente de los valores experimentales de la probabilidad total de emisión de neutrón P_n y vida media $T_{1/2}$ en función de $Q_{\beta1n}$ para núcleos con $28 \leq Z \leq 43$ [McC12]	156
E.3 Esquema del separador BigRIPS y ZeroDegree [Kub12]. El contador de neutrones de BRIKEN y el detector de implantes y desintegraciones AIDA se encuentran en el plano focal F11, al final de la línea del separador ZeroDegree.	158
E.4 A la izquierda, esquema de la distribución de los tubos proporcionales en la matriz. Los tubos se agrupan por distancia al centro en siete anillos (líneas continuas). A la derecha, una foto del montaje.	159
E.5 Esquema del montaje experimental (vista lateral).	160
E.6 Vista lateral (arriba) y frontal (abajo) del montaje experimental.	161
E.7 Diagrama de flujo que resume el procesado de los datos.	162
E.8 Indetificación de los isótopos implantados durante el experimento RIBF127.	163
E.9 Curvas de desintegración beta, beta-1-neutrón y beta-2-neutrones correspondientes al isótopo ^{86}Ga .	164

E.10 Eficiencia de detección en función de la energía de neutrón, simulada mediante GEANT4. Se muestra tanto la eficiencia total (en negro), como la eficiencia de cada anillo.	165
E.11 Comparación de la eficiencia de detección en función de la energía de neutrón (línea azul), y la eficiencia calculada para algunos núcleos cuyo espectro de neutrones ha sido medido en función de la energía promedio de neutrón (puntos rojos).	166
E.12 Valores experimentales de las energías promedio de neutrón [Bra89, Mad16] en función del $Q_{\beta 1n}$. Los valores reales muestran una desviación con respecto del modelo dado en la Eq. E.8 contenida en un factor 2.	167
E.13 Eficiencia de detección de neutrón en función del $Q_{\beta 1n}$, calculada según las aproximaciones expuestas en esta sección. Cada punto corresponde a un isótopo que aparece en una o varias cadenas de desintegración de los isótopos implantados. La banda de error, sombreada en gris, se deriva de la incertidumbre del modelo que relaciona la energía promedio de neutrón y el $Q_{\beta 1n}$, mostrado en Fig. E.12. Los dos puntos verdes se corresponden con la eficiencia de detección para los núcleos $^{83,84}\text{Ga}$	167
E.14 Valores experimentales de los P_{1n} (en %) obtenidos en esta Tesis. Los puntos marcan los núcleos cuyo P_{1n} ha sido medido por primera vez en este trabajo de Tesis.	170
E.15 Valores experimentales de los P_{2n} (en %) obtenidos en esta Tesis.	171
E.16 Valores experimentales de las vidas medias $T_{1/2}$ (en milisegundos) obtenidos en este trabajo de Tesis. Un marcador identifica los núcleos cuya vida media ha sido medida por primera vez en este trabajo de tesis.	171
E.17 Cociente de los valores P_{1n} calculados por diferentes modelos teóricos, y los valores experimentales obtenidos en este trabajo de Tesis. En el panel superior izquierdo se corresponde a la comparación de las predicciones de Möller y col. [Möll03], la superior derecha a Möller y col. [Möll19], la inferior izquierda a Marketin y col. [Mar16], y la inferior derecha a Koura y col. [KTUY05].	172
E.18 Cociente de los valores experimentales P_{1n} obtenidos en esta Tesis y las predicciones teóricas del modelo empírico de Miernik [Mie14].	173
E.19 Cociente de los valores P_{2n} calculados por diferentes modelos teóricos, y los valores experimentales obtenidos en este trabajo de Tesis. En el panel superior izquierdo se corresponde a la comparación de las predicciones de Möller y col. [Möll03], la superior derecha a Möller y col. [Möll19], la inferior izquierda a Marketin y col. [Mar16], y la inferior derecha a Miernik [Mie14].	174

E.20 Cociente de las vidas medias $T_{1/2}$ calculadas por diferentes modelos teóricos, y los valores experimentales obtenidos en este trabajo de Tesis. En el panel superior izquierdo se corresponde a la comparación de las predicciones de Möller y col. [Mölo3], la superior derecha a Möller y col. [Mölo19], la inferior izquierda a Marketin y col. [Mar16], y la inferior derecha a Koura y col. [KTUY05].	175
E.21 Cociente de los valores experimentales $P_n/T_{1/2}$ en función de $Q_{\beta^{1n}}$. Cada punto se corresponde con un núcleo estudiado en este trabajo de Tesis. Los valores $Q_{\beta^{1n}}$ están tomados de la última evaluación [BdN-IAEA]. La línea roja se corresponde con la fórmula $P_n/T_{1/2} = cQ_{\beta^{1n}}^d$, con parámetros $c = 0,0097(9)$ y $d = 4,87(7)$ [McC12].	176
E.22 Patrón de abundancias calculado, siguiendo la trayectoria termodinámica representativa mostrada en [Win12], usando la base de datos REACLIB (<i>REACLIB</i>) y esta base de datos actualizada por los resultados experimentales presentados en este trabajo de Tesis (<i>REACLIB & BRIKEN</i>).	177
E.23 Patrón de abundancias calculado, siguiendo la trayectoria termodinámica llamada <i>350C-RS</i> , presentada en [Obe17]. Las abundancias etiquetadas como <i>REACLIB</i> están calculadas usando la base de datos REACLIB, y las abundancias marcadas como <i>REACLIB & BRIKEN</i> resultan de usar la base de datos REACLIB actualizada con nuestras medidas experimentales.	178
E.24 Patrón de abundancias de un eyecta dinámico caliente, calculado siguiendo la trayectoria número #651 de [Bov17].	179
E.25 Perfil de densidad en el plano $x - z$ al comienzo de la simulación. Se eligió una trayectoria representativa para cada región angular (Fig. 2 de [Mar15]).	180
E.26 El patrón de abundancias causado por los eyectas del viento de neutrinos tras una colisión de dos estrellas de neutrones [Mar15], calculado según la trayectoria correspondiente al tercer rango de latitudes en Fig. E.25.	180
E.27 Patrón de abundancias producido en un eyecta de disco de acreción resultante de la colisión de dos estrellas de neutrones, siguiendo la trayectoria dada en [Lip17].	181

List of Tables

2.1 Main characteristics of the ${}^3\text{He}$ proportional tubes used in BRIKEN.	27
2.2 Summary of run conditions and some representative integral quantities.	34
4.1 Half-life and P_{1n} of ${}^{86}\text{Ge}$.	66
4.2 Half-life and P_{1n} of ${}^{79}\text{Zn}$.	68
4.3 Half-life and P_{1n} of ${}^{93}\text{Se}$.	71
4.4 Half-life and P_{xn} of ${}^{92}\text{As}$.	72
4.5 P_{1n} of all isotopes, obtained from the simultaneous fit of beta and beta-neutron decay curves. Reference values [BdN-IAEA] are shown if available.	76
4.6 P_{2n} of all isotopes, obtained from the simultaneous fit of beta and beta-neutron decay curves. Reference values [BdN-IAEA] are shown if available.	77
4.7 Half-lives of all isotopes, obtained from the corresponding fit, if the reference value in [BdN-IAEA] does not exist or it can be improved.	78
A.1 Number of implants of each isotope N_i , and its number of beta decays N_0 obtained from the simultaneous fit of beta and neutron-beta decay curves. ε_β is the ratio of number of decays and the number of implants.	117
A.2 Number of beta, $\beta 1n$ and $2n$ -beta decays of all isotopes (background subtracted), and its ratio to background. The total background is formed by an uncorrelated background, that is originated by accidental time-correlations of an implant with non-physically correlated decay events, plus a correlated background in case of beta-one-neutron or beta-two-neutron decay curves, which is caused by correlation of a beta decay with one or more neutrons that do not come from the decay (see Sec. 3.7.2 for further details).	118
B.1 Neutron efficiency estimated from $Q_{\beta 1n}$.	121
B.2 Neutron efficiency estimated from $Q_{\beta 2n}$.	123

List of common acronyms

ΔE energy loss. 22, 29, 30, 35

P_{xn} x-neutron emission probabilities. 21, 35, 45

$T_{1/2}$ half-lives. 21, 35

A/Q mass-to-charge ratio. 22, 35, 36

AIDA Advanced Implantation Detector Array. xv, 1, 21, 23–26, 29–32, 34, 35, 38, 43, 45, 46, 48, 49, 62, 63, 66, 73, 75, 77, 162

AME Atomic Mass Evaluation. 4, 6

$B\rho$ magnetic rigidity. 22, 23, 35

BigRIPS Superconducting Radioactive Isotope Beam Separator. 22, 23, 29–32, 35, 38, 43, 45, 62, 66, 73, 77

BRIKEN Beta-delayed neutrons at RIKEN. xv, 1, 2, 21, 23, 25–31, 35, 38, 41, 43, 46, 48, 51, 62, 65, 66, 69, 73, 75, 76, 106, 117, 162

CCSN core-collapse supernova. 16–19

DAQ Data Acquisition System. 21, 23–26, 29–32, 35, 37, 38, 41–44, 46, 51

DSSD Double-sided Silicon Strip Detector. 23–25, 29, 30, 32, 34, 36, 38, 45, 46, 58, 65, 66

FRDM Finite Range Droplet Model. 4, 6, 83, 94, 158, 159

GT Gross Theory. 4, 83, 84

HDPE high-density polyethylene. 25, 27, 28, 32, 38

Lupo Logic Unit for Programmable Operation. 30, 31

MUSIC multi-sampling ionization chamber. 22, 29, 30, 32

NSM neutron star merger. 16, 17, 149

ORNL Oak Ridge National Laboratory. 29

PID particle identification. 22, 23, 35, 36, 43

PMT photomultiplier tube. 29, 30

pn-RQRPA proton-neutron relativistic Quasiparticle Random Phase Approximation. 8, 83, 159

PPAC position sensitive gas detector. 22, 32, 35

QRPA Quasiparticle Random Phase Approximation. 4, 6, 10, 83, 84, 94, 158, 159

r-process rapid neutron capture. xv, xvi, 1, 2, 13–20, 103, 105–110, 112, 114, 115, 117, 149–151, 154–156

RHB relativistic Hartree Bogoliubov. 8, 83, 159

RI Rare Isotope. 22, 23, 25, 29, 32

RIBF Rare Isotope Beam Factory. xv, 1, 21

s-process slow neutron capture. 13–15

SCMF self consistent mean field. 8, 83

SM Shell Model. 8, 83, 85

SS Solar System. 14, 15, 105, 108, 110

SSSD Single-sided Silicon Strip Detector. 30, 32

TOF Time-Of-Flight. 22, 35

WAS3ABi Wide-range Active Silicon-Strip Stopper Array for Beta and ion detection. 66

Z atomic number. 22, 36

Abstract

In the present work we have studied beta-delayed neutron emission of nuclei around the doubly magic nuclei ^{78}Ni ($Z=28$ and $N=50$). Theoretical models lack often the necessary accuracy to predict nuclear properties, in particular one and more neutron emission. New experimental values of half-lives and neutron emission probabilities are required to improve and expand our current knowledge of such form of decay. Moreover, since this kind of beta decay is characteristic of very neutron-rich nuclei, it has an key role in rapid neutron capture (r -process) abundance calculations. Given the lack of experimental data, these calculations rely on theoretical predictions and the uncertainties of the resulting abundances are not small enough to constraint the astrophysical site of such process, or to utilize them in galactic chemical evolution studies.

The Beta-delayed neutrons at RIKEN (BRIKEN) collaboration was founded with the aim of measuring with high-precision a large number of half-lives and neutron emission probabilities of neutron rich nuclides. The commissioning was carried out in 2016, and the first experimental campaign in 2017. The setup is formed by an implant and decay detector Advanced Implantation Detector Array (AIDA), surrounded by a neutron counter. It receives the radioactive ion beam produced by the Rare Isotope Beam Factory (RIBF) of the RIKEN Nishina Center (Japan), which produced the highest intensities of the most neutron-rich nuclei at that moment.

The data analyzed and the results quoted in this Thesis correspond to the BRIKEN experiment RIBF127, complemented with data from the commissioning experiment. We have studied 37 beta-delayed neutron emitters in the mass range $A=75\text{-}94$. We have measured 39 P_{1n} , of which 12 are determined for the first time including the P_{1n} of the doubly-magic ^{78}Ni , and we have improved importantly the uncertainty of the rest. Some of the nuclei are also multi-neutron emitters, and 17 P_{2n} were measured, of which 15 are new values and we improve greatly the other two previously measured ones. This work confirm the half-lives from the last evaluation of 25 isotopes, and report 14 half-lives of which 7 are completely new, improving significantly the uncertainty for the rest.

A comparison of the experimental values obtained in this Thesis and theoretical predictions is presented, as well as an evaluation of the impact of such values in

r-process calculations corresponding to several astrophysical sites. When looking to individual nuclei the different theoretical models can show from agreement to severe disagreement but none of them is able to give a consistent description for all the set of nuclei. With respect to the astrophysical impact we found negligible to significant impact of our data depending on the thermodynamic trajectory of the r-process. Specially interesting is the case of ejecta from the accretion disk formed after a two neutron star merger, where the final abundances of lanthanides is increased by a factor two.

Chapter 1

Motivation and basic physics

Our knowledge about the atomic nucleus has been greatly expanded since Becquerel discovered natural radioactivity in 1896 [Bec96]. This knowledge is reflected not only in technical developments, but also at a scientific level. Nowadays, state-of-the-art nuclear detection systems located in the most advanced facilities provide an exceptional opportunity to study exotic nuclei that only live briefly and that exist in nature during some cataclysmic astrophysical events. Although the current theoretical frameworks are capable of predicting many nuclear properties, based on macroscopic-microscopic descriptions or even on first principles, new experimental data are required in order to improve such models and increase their predictive power over the entire nuclear chart.

Among the many nuclear properties that can be measured, this Thesis work is devoted to the study of beta-delayed neutron emission decay. This kind of decay is characteristic of very neutron rich nuclei, far from the valley of beta stability. On Earth the less exotic species are produced during the operation of nuclear reactors but the most exotic species only exist briefly during some astrophysical events, where nucleosynthesis of heavy elements through rapid neutron capture (*r*-process) takes place. Such events are reproduced by computer simulations, which partially rely on theoretical predictions of nuclear properties. However, better nuclear physics data is mandatory for any meaningful comparison of *r*-process model calculations with observations [Hor19].

All of the above reasons motivated the creation of Beta-delayed neutrons at RIKEN (BRIKEN) collaboration [BRIKEN], which aims to improve and increase the data of very neutron rich nuclei decay, particularly half-lives and neutron emission probabilities. To do so, a high efficiency neutron detector together with a state-of-the-art implant and decay detector, so called Advanced Implantation Detector Array (AIDA), exploit the very intense beams of exotic neutron rich nuclei produced at the RIKEN Nishina Rare Isotope Beam Factory (RIBF). Although several experiments have already been carried out, from heavy nuclei around ^{156}Ce to the lighter region in the vicinity the double magic ^{78}Ni , this Thesis work focus in obtaining half-lives and neutron emission probabilities of nuclei in the latter region.

The structure of this document is the following. This first chapter introduces

the concept of beta-delayed neutron emission, its description by different theoretical nuclear models and its role during the r-process nucleosynthesis in different astrophysical scenario. The experimental setup and run conditions are outlined in the second chapter. An exhaustive revision of the analysis method is provided in the third chapter. The next one contains the results corresponding to nuclei close to ^{78}Ni , produced during the RIBF127 BRIKEN experiment. The fifth chapter includes two parts, where the results are compared to theoretical predictions, and another section where the impact of the new experimental data on different astrophysical environments is presented.

1.1 β -delayed neutron emission

Beta delayed neutron emission is a form of radioactive decay in which one or more neutrons are emitted in addition to an antineutrino and an electron. This decay mode was observed for the first time by Roberts et al. in 1939 [Rob39a, Rob39b] while studying fission products. This process is possible if the decay populates states of the daughter nucleus which are above the neutron separation energy. It can be considered as a multistep process [Bor05] consisting of the beta decay of the precursor (A, Z) which results in feeding the excited states of the emitter nucleus ($A, Z+1$) followed by either gamma deexcitation to the ground state, or neutron emission to an excited state or to the ground state of the final nucleus ($A-1, Z+1$), as it is shown in Fig. 1.1.

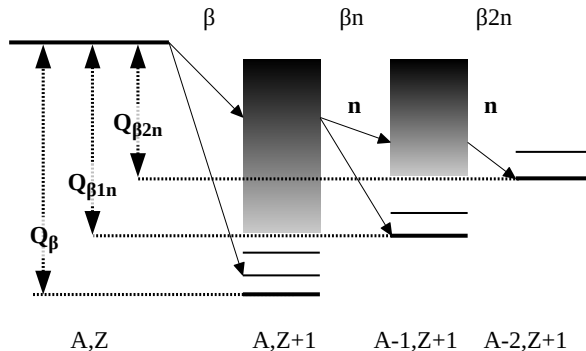


Figure 1.1: Schematic representation of multistep beta-delayed neutron emission.

The calculation of β -decay half-lives and emission probabilities requires the evaluation of the wave function of the nuclear ground state of the parent nucleus and final states of the daughter nucleus, together with the transitions between them. There are different prescriptions for calculating the ground state and excited states, as well as several models that calculate allowed and first forbidden beta

decay transition probabilities. Once transition probabilities are calculated, the half-life value can be obtained as in Eq. 1.1, where f is the Fermi statistical rate function, S_β the beta strength function, and $[0, Q_\beta]$ corresponds to the energy window for the decay. The function f accounts for the leptonic phase space, while S_β reflects the probability of the transition from an initial nuclear state in the mother nucleus to the final state at excitation energy E_x in the daughter nucleus. In the following section, different theoretical approaches of how to calculate this beta strength function are briefly reviewed.

$$1/T_{1/2} = \int_0^{Q_\beta} S_\beta(E_x) f(Z, A, Q_\beta - E_x) dE_x \quad (1.1)$$

In case that states above the x-neutron separation energy S_{xn} are populated, x-neutron emission becomes energetically possible, and the probability can be calculated as in Eq. 1.2. The probability of emitting x-neutrons is called the P_{xn} value.

$$P_{xn} = \frac{\int_{S_{xn}}^{Q_\beta} S_\beta(E_x) f(Z, R, Q_\beta - E_x) p_{xn}(E_x) dE_x}{\int_0^{Q_\beta} S_\beta(E_x) f(Z, R, Q_\beta - E_x) dE_x} \quad (1.2)$$

The particle emission probability from the initial level of the emitter to the final nucleus is given in Eq. 1.3,

$$p_{xn}(E_x) = \frac{\Gamma_{xn}(E_x)}{\Gamma_n(E_x) + \Gamma_\gamma(E_x)} \quad (1.3)$$

where $\Gamma_n = \sum_x \Gamma_{xn}$ is the neutron escape width and Γ_γ is the γ -ray width of the emitter. It is usually assumed that $\Gamma_n \gg \Gamma_\gamma$, and therefore $p_{xn} \approx 1$, so for example, the formula of P_{1n} results in Eq. 1.4. This approximation implies that neutron-gamma competition is disregarded and may cause overestimated predictions of P_{xn} values.

$$P_{1n} = \frac{\int_{S_{1n}}^{Q_\beta} S_\beta(E_x) f(Z, R, Q_\beta - E_x) dE_x}{\int_0^{Q_\beta} S_\beta(E_x) f(Z, R, Q_\beta - E_x) dE_x} \quad (1.4)$$

1.2 Nuclear structure of neutron rich nuclei

A great effort has been made developing new theoretical formalism that are capable of estimating half-lives and neutron emission probabilities P_{xn} far from stability. This section is focused on three models which are able to calculate these nuclear

properties for all the neutron rich nuclei up to the neutron drip line. Some other models which make local predictions around the nuclei studied in this Thesis work are also briefly described. Additionally, two empirical models based on systematics are presented at the end of this section.

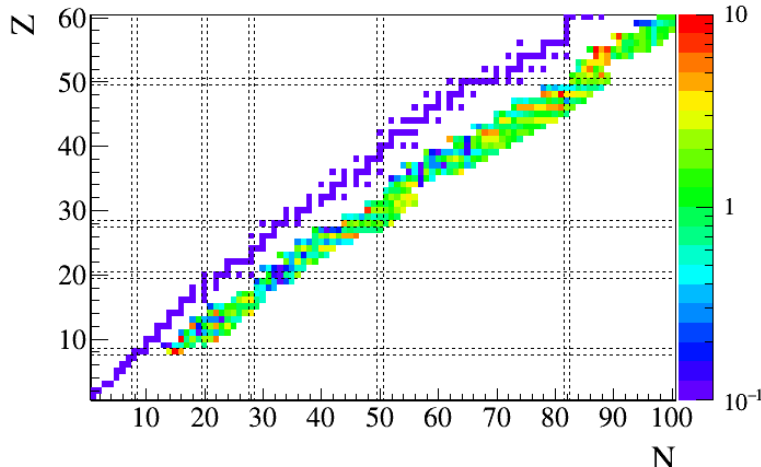
One of the first large-scale beta strength calculations was performed by Möller et al. Several improvements of the model have been done since the first publication in 1981. This section starts focusing in the calculations published in [MöL03]. These calculations are base on Quasiparticle Random Phase Approximation (QRPA) on top of a semiempirical global mass model. Specifically, the utilized mass model [MöL95] is based on a Finite Range Droplet Model (FRDM) for the macroscopic energy and a folded-Yukawa single particle potential for the microscopic corrections, in addition to pairing corrections provided by the Lipkin Nogami model, and includes deformation through eight order Strutinsky shell corrections. Since the parameters were fixed on 1992, this particular mass model is also called FRDM(1992). The experimental masses from Atomic Mass Evaluation (AME)(1989) were employed for optimizing the aforementioned parameters. Two magnitudes, which are obtained from the mass model, are required for calculating beta decay rates, namely beta energy window Q_β and neutron separation energy S_{xn} . Since single-particle energies and wave functions are calculated, this mass model provides other nuclear properties like ground state deformations. However, the mass model is forced to assume spherical shape for a certain set of isotopes, which includes all the nuclides studied in this Thesis work.

Beta decay allowed transition strength is calculated using QRPA. Although QRPA formalism was developed for spherical nuclei, it was extended to deformed ones, which is necessary in global calculations of beta-decay properties. An empirical spreading is used to convert each spike-like transition strength above 2 MeV into a Gaussian whose width is calculated as in Eq. 1.5. This procedure removes unphysical jumps in P_{xn} predictions and is necessary because the model lacks of sufficient configuration mixing to spread the beta-strength.

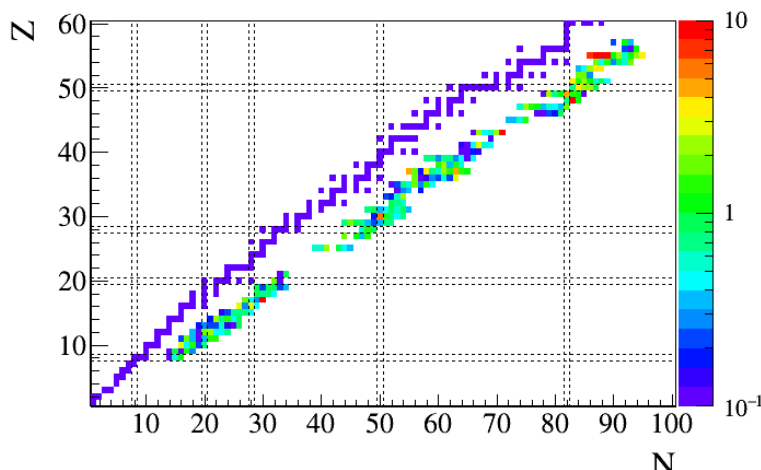
$$\Delta_{sw} = \frac{8.62}{A^{0.57}} \quad (1.5)$$

First forbidden transitions are calculated in the statistical Gross Theory (GT), separately from the allowed transitions. The strength of these transitions depends smoothly with energy, in contrast to the spike-like behavior of the allowed transitions. The final beta strength is the sum of both, allowed and first forbidden transitions. Half-lives and neutron emission probabilities are obtained integrating the beta strength as in Eq. 1.1 and a modification of Eq. 1.4 respectively. This modification restricts the integrals between S_{1n} and S_{2n} for P_{1n} , between S_{2n} and S_{3n} for P_{2n} and so on. This way of calculating the neutron emission probability not only disregards neutron- γ competition, but also competition between the different xn channels. This approximation is called the sharp-cutoff model. A comparison of the predicted half-lives and one neutron emission probabilities and the experimental

values is show in Fig. 1.2. As it can be seen in Fig. 1.2a, half-lives are overestimated by a factor 3 in the “north-east” of ^{78}Ni , which is the region studied in this Thesis work.



(a) $T_{1/2}([\text{M\"oller03}]) / T_{1/2}([\text{BdN-IAEA}])$



(b) $P_{1n}([\text{M\"oller03}]) / P_{1n}([\text{BdN-IAEA}])$

Figure 1.2: Ratio of half-lives (left) and one neutron emission probabilities (right) predicted by Möller et al. [Möller03] and recommended experimental values taken from the last evaluation [BdN-IAEA].

A newer version of this model is found in [Mö19]. The mass model is evolved from the aforementioned one, and it is often referred to as FRDM(2012) [Mö16]. It improves the determination of ground state shapes very significantly, including a description of compressibility effects, and a new model for the average neutron and proton pairing gaps. In addition, a zero-point energy is added to the calculated potential energy at the ground state shape, and a larger number of experimental masses available in AME(2003) were used for fitting the parameters of this mass model. The QRPA formalism which is used for calculating the beta decay allowed transitions is the same as the previous version.

A major change with respect to the earlier calculations is the inclusion of competition between all decay channels abandoning the sharp-cutoff model. This competition is included in the model by coupling the QRPA calculation with a statistical Hauser-Feshbach model (for further details refer to [Kaw08, Mum16a]). This new feature takes neutron competition with γ -emission into account assuming a sequential x-neutron decay and following the statistical decay of each subsequent daughter generation until the initial excitation energy is exhausted. The fundamental assumption of this new model is that the initial population of the daughter nucleus can be treated as the formation of a compound nucleus, which depends only on its overall properties rather than the details of the formation mechanism. The statistical Hauser-Feshbach stage of the calculation relies on several ingredients like the γ -strength function, nuclear level density and the nuclear optical model. The neutron- γ competition is progressively more important when the nuclei are closer to the drip line [Mum16a]. The ratio of the predicted half-lives and one neutron emission probabilities and the experimental values is show in Fig. 1.3. As it can be seen in Fig. 1.3a, half-lives of nuclei in the north-east form ^{78}Ni are now underestimated, while in the previous version were overestimated. Overall in this new calculation there is a somewhat better agreement with experimental half-lives and one neutron emission probabilities.

Another theoretical global model was developed by Koura et al. The mass model [KTUY05] is composed by a general part, which captures the trend of the masses as a function of proton and neutron numbers, and another part which accounts for the deviations from this general trend, caused by the shell structure. The procedure for obtaining such shell energy corrections is detailed in a previous publication [KTUY00]. This term can take into account energy corrections caused by deformation. An additional term was added in the last version of this mass model [KTUY05] for describing variations in odd-even and odd-odd nuclei. The parameters of the model were optimized to reproduce experimental masses available in Atomic Mass Evaluation (AME)(2003). Beta decay allowed and first forbidden transition probabilities were obtained by gross theory formalism [Tac90], which is a modern revision of the seminal gross theory given by Takahashi [Tak73]. This newer version amends the treatment of pairing energy and the beta strength due to single particle transitions. The keystone of gross theory consist in handling nuclear levels as a continuum, given by the Fermi gas model, with few discrete levels at the

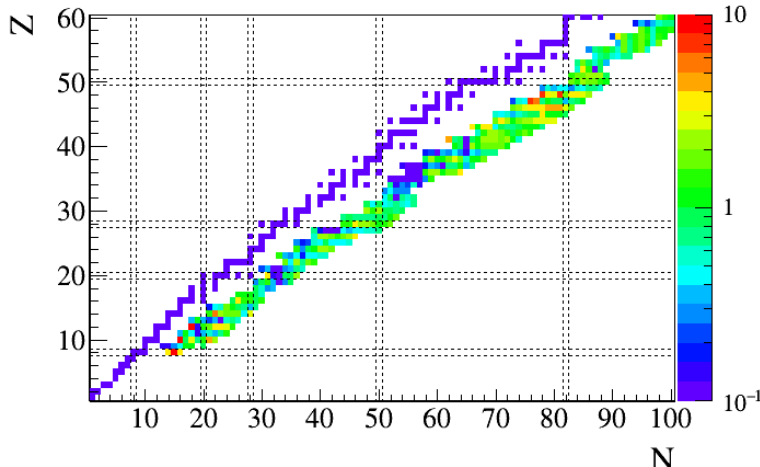
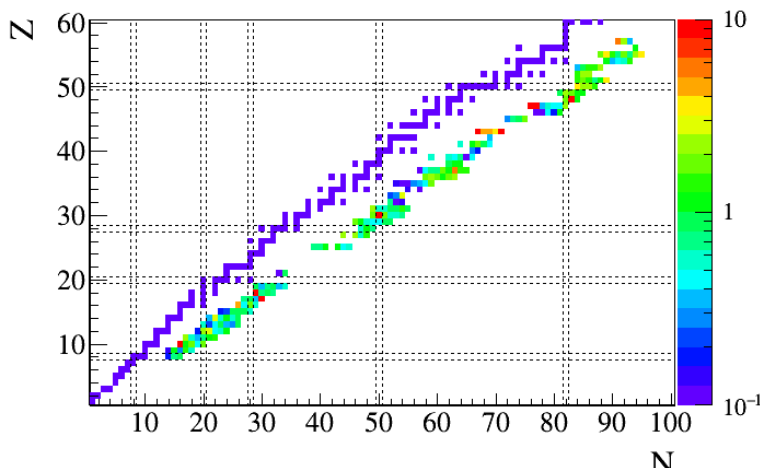

 (a) $T_{1/2}(\text{[Möll19]}) / T_{1/2}(\text{[BdN-IAEA]})$

 (b) $P_{1n}(\text{[Möll19]}) / P_{1n}(\text{[BdN-IAEA]})$

Figure 1.3: Ratio of half-lives (left) and one neutron emission probabilities (right) predicted by Möller et al. [Möll19] and recommended experimental values taken from the last evaluation [BdN-IAEA].

Fermi surface. In particular, single particle states are obtained calculating the wave functions by the cluster variation method [Tac90]. Beta strength function varies

smoothly and extends over a wide range of energy. As in the case of [Möл03], half-lives and neutron emission probabilities are obtained integrating this beta strength as in Eq. 1.1 and Eq. 1.4. A comparison of the predicted half-lives and one neutron emission probabilities and the experimental values is displayed in Fig. 1.4. As it can be seen in Fig. 1.4a, half-lives of nuclei to the north-east of ^{78}Ni with $N > 50$ are underestimated.

Both models, from Möller et al. [Möл03, Möл19] and Tachibana [Tac90], are categorized as macroscopic-microscopic models, because nuclear mass is parametrized in terms of macroscopic properties, such as volume energy, asymmetry energy, etc; plus a microscopic term due to shell corrections, which are calculated using a phenomenological potential [Ben03]. On the opposite side, ab initio methods provide a description of nuclear properties from very first principles, that is, an effective interaction which describes nucleon-nucleon interactions. In between these two extremes, there are two models that work at a microscopic level but employ effective interactions: Shell Model (SM) approaches, and self consistent mean field (SCMF) methods.

Theoretical predictions of half-life and P_{xn} calculated by Marketin et al. [Mar16] follow a self consistent mean field (SCMF) model. The ground state in the daughter nucleus is described using the relativistic Hartree Bogoliubov (RHB) framework [Vre05], which includes pairing effects, using the D3C* parametrization [Mar07]. Excited states are obtained using proton-neutron relativistic Quasiparticle Random Phase Approximation (pn-RQRPA). The same density functional is used for the description of the ground state and for the residual interaction, and therefore it keeps self-consistency in the calculation of Q_β and beta strength functions. RHB plus pn-RQRPA framework can handle both allowed and first forbidden transitions consistently. As other similar models, a quenching of these transitions by a global effective factor has to be included. Although the model is strictly reliable for even-even nuclei, it was extended to odd-A and odd-odd nuclei. Half-lives are calculated integrating the total beta strength function, as prescribed in Eq. 1.1. Beta delayed neutron emission is obtained as in Eq. 1.4, after applying an artificial Lorentzian smearing to the beta strength function to take into account additional spreading due to configuration mixing. Since mean fields models can not reproduce odd-even effects of the neutron separation energy S_{1n} , this quantity is obtained from a different mass model [Liu11]. The ratio of the predicted half-lives and one neutron emission probabilities and the experimental values is show in Fig. 1.5. As it can be seen in Fig. 1.5a, half-lives of nuclei with $Z \gtrsim 28$ are overestimated for $N < 50$ but underestimated for nuclei with $N > 50$. This tendency is also present in the previous models [Möл19, KTUY05]. Additionally, from Fig. 1.5b it can be concluded that estimated P_{1n} values are lower than most of the experimental ones.

Another calculation which also employs SCMF was performed by Borzov [Bor05]. The ingredients of the approach are a SCMF potential described by the Fayans phenomenological density functional DF3 [Fay00], for the ground state properties; and universal effective nucleon-nucleon interaction for description of

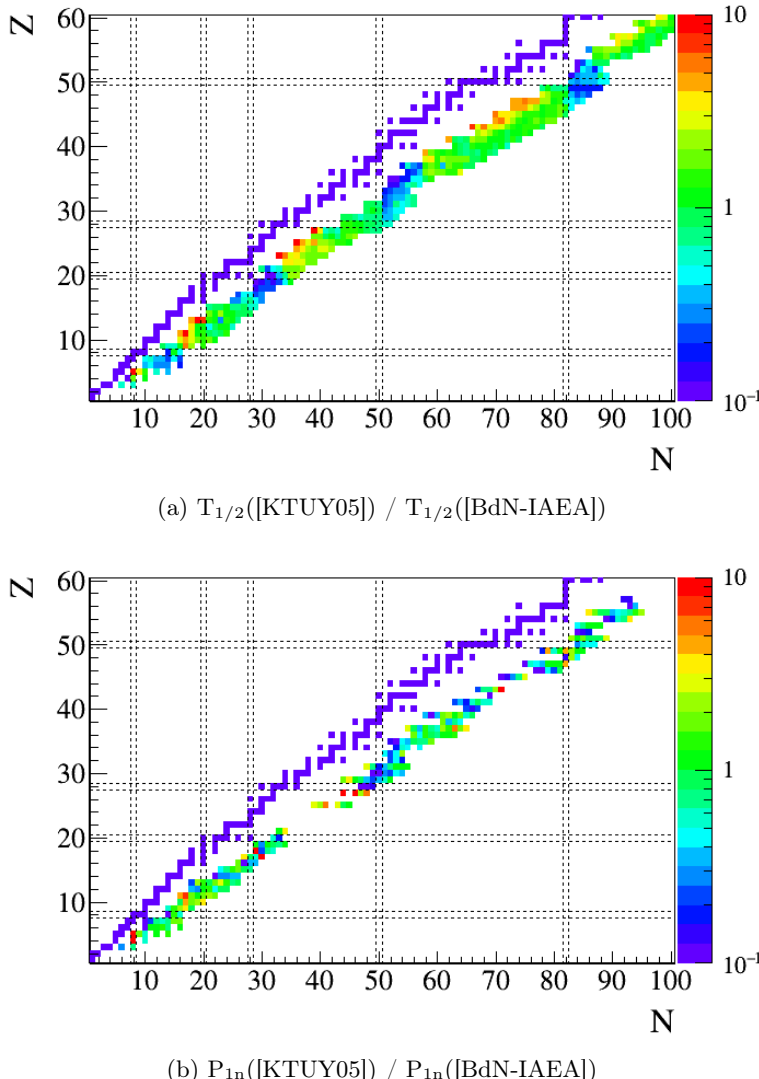


Figure 1.4: Ratio of half-lives (left) and one neutron emission probabilities (right) predicted by Koura et al. [KTUY05] and experimental values [BdN-IAEA].

the excited states. Although ideally both originate from the unique nuclear energy-density functional, some restrictions exist in applications of the fully self-consistent approach to nuclear spin excitations. Beta strength functions

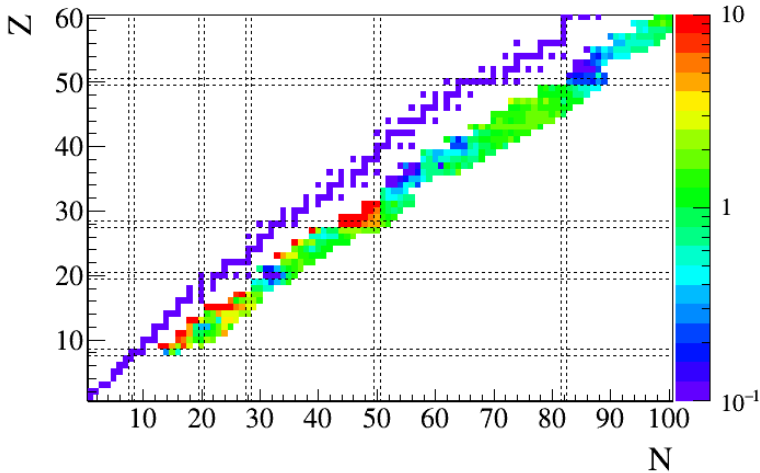
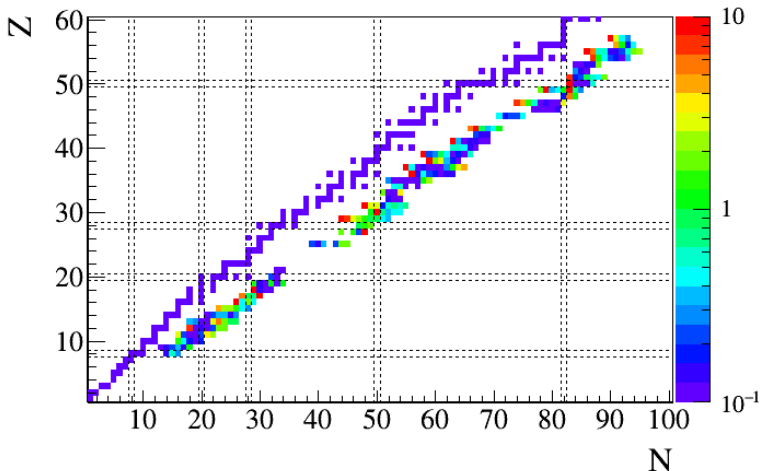

 (a) $T_{1/2}(\text{[Mar16]}) / T_{1/2}(\text{[BdN-IAEA]})$

 (b) $P_{1n}(\text{[Mar16]}) / P_{1n}(\text{[BdN-IAEA]})$

Figure 1.5: Ratio of half-lives (left) and one neutron emission probabilities (right) predicted by Marketin et al. [Mar16] and experimental values [BdN-IAEA].

are obtained from continuous-QRPA equations. As in previous cases, half-lives and neutron emission probabilities are obtained by integrating the beta strength function in the corresponding energy windows. Implicitly, neutron-gamma

competition is disregarded and it is assumed that all the beta strength above the neutron separation energy undergoes neutron emission.

The other approach between ab initio methods and phenomenological models that has been applied corresponds to shell model calculations. In particular, predictions computed by Zhi et al. [Zhi13] are based on the interacting shell model, which improves the treatment of nucleon-nucleon correlations, and therefore the beta strength function of allowed and first forbidden transitions in beta decay. Although the shell model usually gives a good account of the relative strength distributions, it overestimates the total strength and a global quenching factor has to be used. In addition, first forbidden calculations are computationally inaccessible, so the corresponding beta strength function is derived within the Lanczos scheme. Therefore, the lowest energy states correspond to physical states, while the Lanczos states at higher excitation energies are unphysical and represent strength per energy interval. Results provided in [Zhi13] are limited to nuclei with a magic neutron number.

Apart from these sophisticated microscopic theoretical models, which predict half-lives and neutron emission probabilities from a microscopic approach, there are some phenomenological models which calculate these beta decay parameters from gross quantities, like energy window of the beta decay Q_β , the neutron separation energy S_{1n} and few empirically adjusted parameters. One of the more recent works was performed by McCutchan et al. [McC12], where they showed that the ratio of the total neutron emission probability P_n , which corresponds to $\sum_{x>0} P_{xn}$, and $T_{1/2}$ is systematically correlated with $Q_{\beta 1n}$. It can be shown that one of the integrals in the definition of the neutron emission probability can be absorbed into the half-life, by multiplying Eq. 1.4 by Eq. 1.1, resulting in Eq. 1.6.

$$\frac{P_n}{T_{1/2}} = \int_{S_{1n}}^{Q_\beta} S_\beta(E_x) f(Z, R, Q_\beta - E_x) dE_x \quad (1.6)$$

Assuming that the beta strength function $S_\beta(E_x)$ is constant, and that the phase-space factor can be approximated as in Eq. 1.7,

$$f(Z, R, Q_\beta - E_x) \approx (Q_\beta - E_x)^n \quad (1.7)$$

the integral is simplified to Eq. 1.8.

$$\frac{P_n}{T_{1/2}} \approx c Q_{\beta 1n}^d \quad (1.8)$$

Fig. 1.6 displays the data utilized for fitting the parameters c and d in the region of the nuclear chart which includes nuclei with $28 \leq Z \leq 43$. This Thesis work study nuclei with $28 \leq Z \leq 43$, and the corresponding parameters are $c = 0.0097(9)$ and $d = 4.87(7)$ [McC12]. This kind of simple calculation provides a powerful method for predicting the systematic behavior of P_n , and it can be used to point

out new manifestation of nuclear structure. However it requires a knowledge of the half-lives.

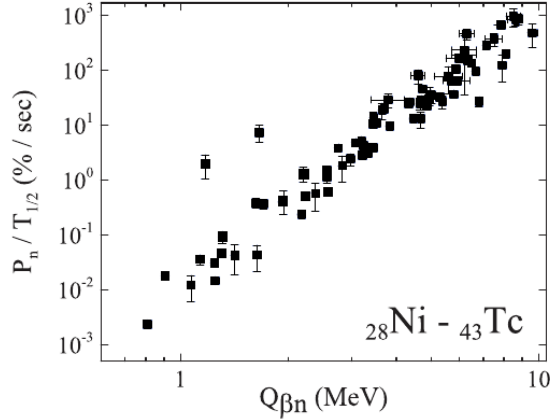


Figure 1.6: Ratio of experimental values of P_n and $T_{1/2}$ plotted as a function of $Q_{\beta n}$ for nuclei with $28 \leq Z \leq 43$. From [McC12]

Another phenomenological systematic study was carried out by Miernik [Mie14]. Similarly to previous works, the beta strength function is assumed to be proportional to an effective level density as in Eq. 1.9.

$$S_\beta(E_x) \sim \rho(E_x) = \frac{\exp(a_d \sqrt{E_x})}{E_x^{3/2}} \quad (1.9)$$

If this beta strength is substituted in Eq. 1.4, the total beta-delayed neutron emission is calculated from Eq. 1.10.

$$P_{1n} = \frac{\int_{S_{1n}}^{Q_\beta} \exp(a_d \sqrt{E_x}) E_x^{-3/2} f(Z+1, Q_\beta - E_x) dE_x}{\int_0^{Q_\beta} \exp(a_d \sqrt{E_x}) E_x^{-3/2} f(Z+1, Q_\beta - E_x) dE_x} \quad (1.10)$$

The mass model beneath these predictions corresponds to Hartree Fock Bogoliubov, HFB-21 calculated by Goriely et al. [Gor10]. Gamma-neutron competition is included using the approximation of the threshold method. Four parameters are used to describe the behavior of a_d with the number of protons Z and neutrons N . Fig. 1.7 shows a comparison of the predicted one neutron emission probabilities and the experimental values from [BdN-IAEA].

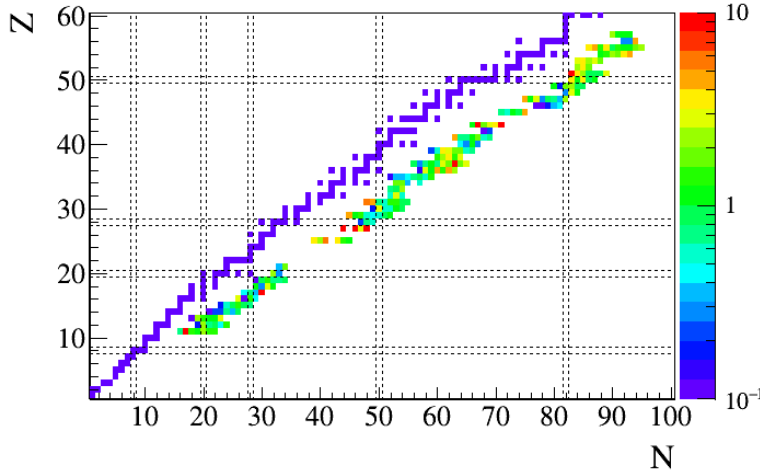


Figure 1.7: Ratio of one neutron emission probabilities predicted by Miernik [Mie14] and experimental values [BdN-IAEA].

1.3 Astrophysical side. R-process

The immense part of the baryonic matter in the Universe is made of hydrogen. Elements from helium to iron are produced by the nuclear reactions that power the stars. How chemical elements heavier than iron are produced is one of the most important scientific questions that remains open nowadays. Burbidge et al. [B²HF], and independently Cameron [Cam57], proposed neutron capture by seed nuclei as the main source of such heavy elements. Depending on the timescale of neutron capture and the beta decay rate of the resulting nucleus, two processes are identified. In case of slow neutron capture (s-process), the neutron capture time scale is generally longer than the decay time scale, while rapid neutron capture (r-process) happens if the neutron capture is much faster than beta decay back to stability. Therefore, r-process runs far away from stability, while s-process involves nuclei at or close to stability. This is illustrated in Fig. 1.8, where an example of each process path is detailed in a small region of the nuclear chart.

Although s-process is narrowed down to occur in late stages of the stellar evolution of massive stars, the astrophysical scenario of the r-process is still under discussion. The most likely sites are explosive events, where the required high neutron densities can be achieved, namely, supernova explosions, and collisions of a neutron star with another compact object.

The best characterizing r-process signature is the elemental abundance pattern. Several peaks appear in this pattern, caused by accumulation of matter around

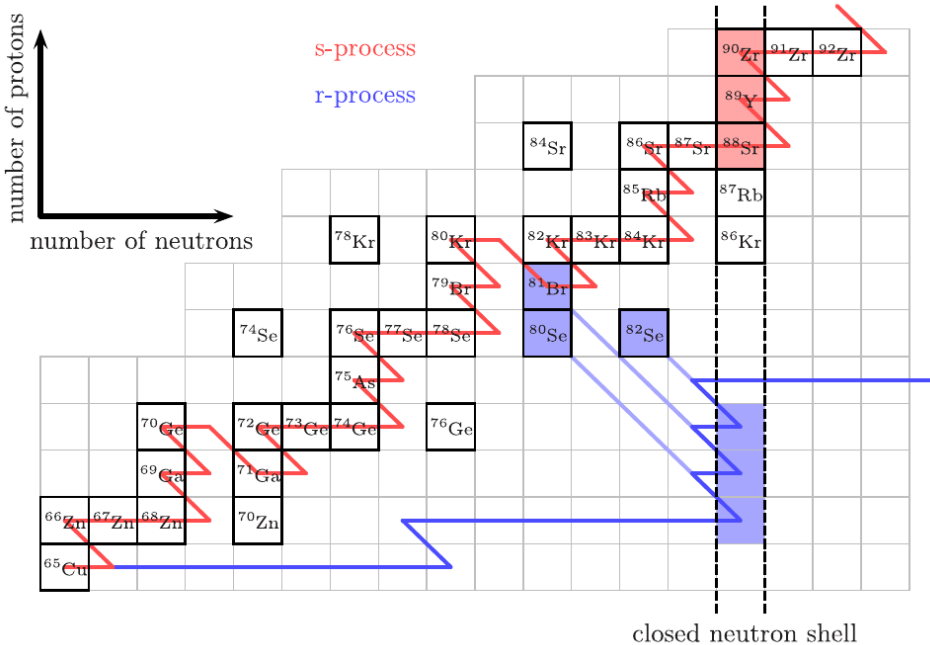


Figure 1.8: Schematic representation of abundance evolution of r-process (blue line) and s-process (red line). [Hor19]

nuclei with neutron magic number during the neutron capture process. In the case of the s-process, peaks correspond to stable closed neutron shell nuclei. On the contrary, r-process runs far from stability and the nuclei that are built up around isotones with a magic neutron number are neutron rich. Then, they decay beta to stability, and the corresponding peaks appear at lower masses than s-process peaks. This feature is illustrated in Fig. 1.9, where contributions from both processes are displayed separately.

Heavy elements in our Solar System (SS) were created by different processes before its formation 5 Ga¹ ago. The contribution from s-process can be computed with certain confidence and subtracted from the observed abundances in our SS, resulting in the so-called Solar System r-process residual pattern. In the following, r-process residuals calculated by Sneden et al. [Sne08] are used as reference.

This r-process abundance pattern is found in a variety of astrophysical environments, and matches the r-process residual abundances found in our SS for elements between $A \approx 140$ and $A \approx 200$. However, lighter r-process elements show

¹gigaannum, 10^9 years

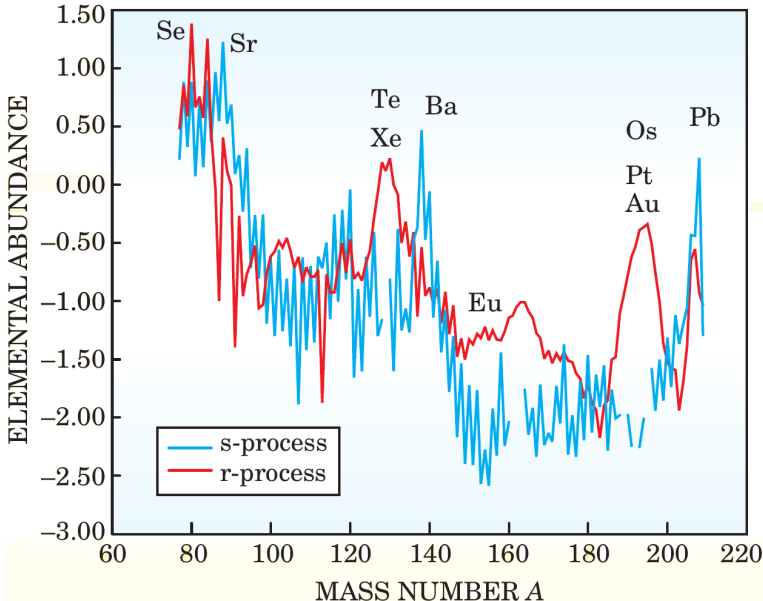


Figure 1.9: Estimated contributions from s-process and r-process to the observed Solar System (SS) abundances. Plotted values are $12 + \log_{10}$ of abundance relative to hydrogen. The peaks which are caused by r-process appear at lower masses than s-process peaks. In case of stars enriched with r-process and s-process, a double peak is observed. [Cow04].

certain variation between stars, and differences with respect to SS pattern.

One of the astrophysical objects where the r-process fingerprint can be found are metal-poor stars in the galactic halo. Star formation stopped long time ago in this region of the galaxy, and the stars which are observed nowadays are older than 12 Ga [Kal12]. Few of them were formed by r-process polluted mass of gas, and present a larger proportion of heavy chemical elements. This observations point to short-lived astrophysical events as source of r-process at early times in the galaxy formation. However, abundance variations are found in these r-process-enhanced metal-poor stars. This suggest that different kind of events enriched the interstellar medium before these stars were born [Hor19]. Further intriguing is the abundance of elements strontium, yttrium and zirconium ($A \sim 90$), which present a larger star-to-star variation [Sne08]. The abundance pattern of a metal-poor star is shown in Fig. 1.10, compared to the scaled SS pattern. Although both patterns agree for elements heavier than tin ($Z=50$), there are large variations for elements between germanium ($Z=32$) and indium ($Z=49$).

State-of-the-art instrumentation opens new possibilities to observe events where

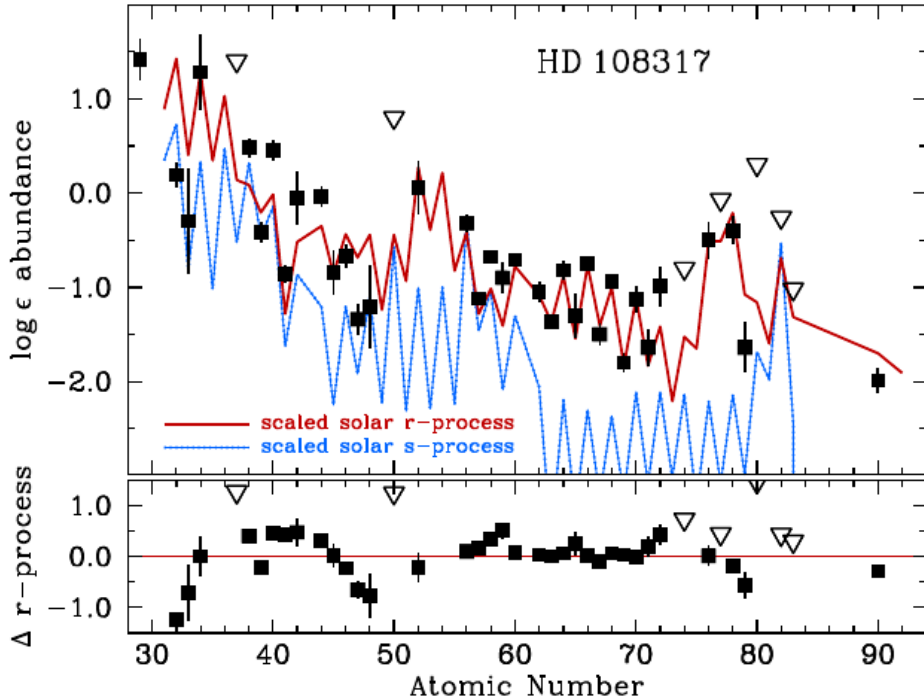


Figure 1.10: Abundance pattern in HD 108317, a metal-poor star [Roe14]. Red and blue curves corresponds to Solar System patterns, normalized to Eu or Ba abundance of HD 108317.

r-process take place. Neutrino detectors, even the ones dedicated to other kind of measurements like double-beta decay, can observe neutrinos coming from a core-collapse supernova (CCSN). Gravitational Wave Astronomy became ready in 2015, when the Advanced LIGO Observatory ended its last upgrade; few months later a two black-hole merger was announced [Abb16]. Since then, many other mergers have been reported, including a neutron star merger (NSM) called GW170817 [Abb17a]. The importance of this event lies on the simultaneous measurement [Abb17b] of the gravitational waves and different parts of the electromagnetic spectrum. Particularly important is the UV/visible/infrared electromagnetic transient, also called kilonova [Met10], and the identification of r-process elements as strontium [Wat19].

Simulations of nucleosynthesis processes in the different astrophysical scenarios are used to constraint astrophysical models, and understand the origin of elements heavier than iron. These models link the nuclear physics, both theoretical estimates and measurements, with astrophysical observable quantities

like elemental abundance in different objects or electromagnetic transients in the aftermath of neutron star mergers. Moreover, theoretical yield estimates are also used in galactic chemical evolution models, which explain how heavy elements are spread throughout the interstellar medium and integrated into new stars. Thus, reduced uncertainties in the nuclear physics side are required in order to refine astrophysical models and improve their predictions.

1.3.1 R-process sites

There are two main requirements to produce elements by means of r-process, in particular, a large ratio of neutron to seed nuclei and a large neutron density. If the ratio is large enough, a complete r-process abundance pattern up to the heaviest elements is achieved. A high neutron density is needed to keep the neutron capture process path far from stability. Several astrophysical sites are proposed as sources of r-process nuclei, namely CCSN and NSM.

Both sites are the result of the evolution of massive stars, which can be summarized as follows. A new star is born when the interstellar gas is gathered and compressed by its own weight. If the density and temperature in its inner part is high enough, nuclear fusion reactions, mainly fusion of hydrogen into helium, become possible. When hydrogen is consumed in the star core, nuclear fusion stops and the core is compressed by the outer part of the star. This compression increases the temperature, and heavier elements can be fused. There are several stages, where products of the previous stage are nuclear fuel of the next one. If the mass of the star is not enough to compress the core and subsequently increase the temperature, its evolution ends. If the stellar mass is larger than $8 M_{\odot}$ (solar masses), a silicon burning stage may be reached. At this point, core temperature is high enough to destroy all the previously synthesized elements and favor the formation of stronger bound nuclei, around atomic mass 60 corresponding to iron group elements. When the most bounded nuclei are formed in the core, nuclear energy production ends and there is nothing to balance its own weight. As a consequence, star's core is compressed and becomes several times more dense than an atomic nucleus, until the repulsive component of the nuclear force stops its collapse. The outer layers of the star that are falling towards the core are rebounded off, setting up a shock wave that reverse the flow of matter, and consequently setting up a CCSN explosion. This shock wave compresses and heats the outer layers, that can undergo r-process nucleosynthesis.

Different processes during the collapse and the subsequent explosion can change the composition of ejected material and thus alter the r-process yields. The core of the star is cooled down by neutrino emission. This neutrino-wind is able to expel out the outer layers, and can launch a r-process, by heating and compressing these ejected material. However, the neutron richness may not be enough to achieve a complete r-process. In addition, neutrinos can decrease the initial neutron-to-seed ratio if the flux is large. In spite of the high temperature and moderate neutron

richness that characterize this type of event, synthesis of heavy elements with mass below 140 can be achieved following the so-called weak r-process.

There is another proposed mechanism to explain even more energetic CCSN explosions. During the collapse, different effects can amplify the existing magnetic field, so it can be stronger than 10^{12} G. Magnetorrotationally driven CCSN are a reasonable r-process site, since its ejecta is much less exposed to neutrinos than in the previous scenario, so neutron richness is preserved. Supernovae may have been more important at the beginning of the Universe, and therefore variations in abundance pattern for lighter r-process elements among metal-poor stars can be explained by nucleosynthesis in CCSN explosions.

If the progenitor star had enough mass, after experiencing a CCSN, the remaining core forms a neutron star (or a black hole). This compact object is characterized by a mass around $1.4 M_{\odot}$ and a radius around 10 km, so its density is comparable to atomic nuclei. Another unique property is their strong magnetic field, around $10^{11} - 10^{15}$ G. Sometimes these compact objects appear in binary systems, which eventually collide. Although there is not any neutron star and a black hole coalescence observed yet [Abb19], existence of two neutron star mergers were confirmed by gravitational wave measurements [Abb17a].

In case of neutron star mergers, once neutron rich matter is ejected, the neutron capture process must happen much faster than the conversion of neutrons into protons by beta decay. Fig. 1.11 sketches several mechanisms that can unbind matter at different moments of the coalescence. Before the collision, tidal forces can tear apart the neutron stars. Additional material is expelled when both neutron stars come into contact. Matter ejected by these mechanisms, so-called dynamical ejecta, is very neutron rich and therefore a complete r-process nucleosynthesis up to the heaviest elements can be reached.

On a longer timescale, debris are grouped forming a disk around the resulting central object, which can be a massive neutron star or black-hole. Viscous turbulence, produced by the strong magnetic fields, can unbind a large amount of material. In case the central object is a black hole, the amount of disk ejected material is smaller than in case of a neutron star, but its neutron richness is not altered by neutrinos [Shi19]. If the final central object is a neutron star, its neutrino flux can be as high as in CCSN and produce neutrino-driven wind ejecta. Neutrinos are blocked by the aforementioned disk, so matter ejected by neutrino wind have an angular dependency, being more important in polar direction. As in CCSN site, such high neutrino flux can decrease the neutron richness of ejected material [Hor19]. Combination of these ejecta produce all elements, mainly around and below mass 140.

Numerical simulations are used to estimate the total amount of ejected material by each process, and its r-process yields. However, more experimental data and more advanced nuclear models are required in order to improve astrophysical simulations and determine the contribution of CCSN and neutron star mergers to the synthesis of heavy nuclei.

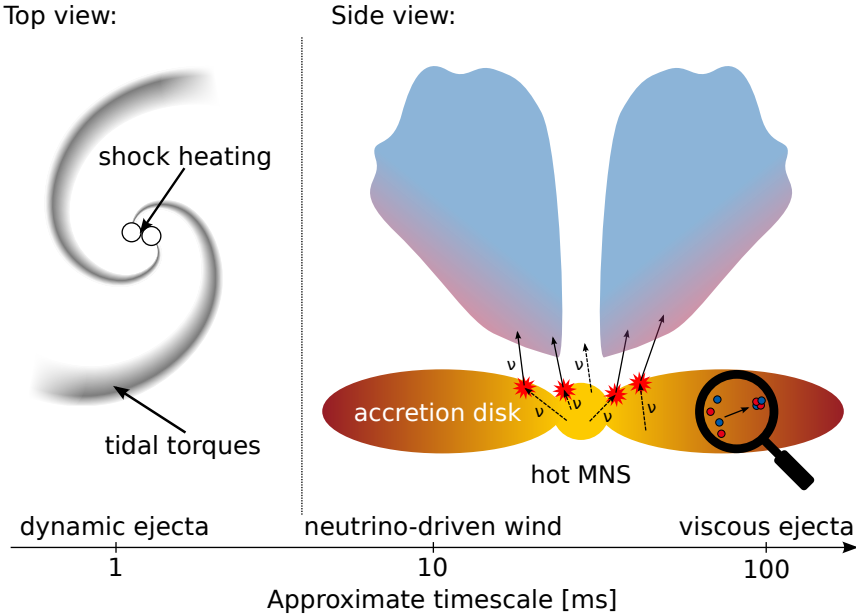


Figure 1.11: Schematic evolution of a neutron star merger. From [Mar].

1.3.2 Numerical simulations

Neutron star mergers or CCSN enrich the interstellar medium in different amounts and material composition, depending on certain astrophysical properties like progenitor mass or magnetic fields. Numerical calculations try to reproduce and explain these events. In addition, they are used to quantify their contribution to the observed abundances, and therefore constraint the astrophysical scenarios where r-process may happen. The usual approach decouples the hydro-dynamical evolution of the event and the nucleosynthesis process. The approach followed by the group of A. Arcones in the T.U. Darmstadt which was used to make the abundance calculations presented in Sec. 5.2, is summarized as follows.

Firstly, a hydro-dynamic simulation calculates the thermodynamical evolution of the ejected material. This kind of simulations are quite computer demanding, and it is challenging to include a complete treatment of some characteristics of the astrophysical events like a full implementation of general relativity, strong magnetic fields or multi-flavor neutrino transport. Since simulations run over a finite time, a criteria has to be established to select jets that are gravitationally unbound and contribute to the observed abundances.

Different jets may have slightly different thermodynamic trajectories, so abundance evolution is calculated for a representative selection of them. A huge

nuclear reaction network [Win13, Win12], derived from BasNet [Thi11] take into account all the possible reactions among more than 5000 nuclides. The nuclear reaction and decay information is compiled in the JINA REACLIB database [Cyb10, REACLIB]. The version which was updated in October 2017 is the one used for the present Thesis work. This version included experimental values from Nuclear Wallet Card 2017 [WC17]. Theoretical mass model correspond to [Mö195], half-lives to [Mö103] and neutron branching ratios to [Mum16a]. Additionally, neutron induced fission rates and beta-delayed fission probabilities are taken from [Pan10] and [Pan05] respectively. Nuclear reaction rates are from [Rau00], and weak interaction rates are the same as in [Arc11].

Among the input nuclear properties, half-lives and neutron emission probabilities play a key role in r-process calculations. On the one hand, half-lives determine the pace of the r-process, and also its path in cold environments like dynamical ejecta from a neutron star merger. In general, beta half-lives can modify the final abundance pattern at different stages of the process [Mum16b]. On the other hand, beta-delayed neutron emission provide neutrons for late captures after r-process freeze-out, and also redistribute matter while nuclei decay back to stability, softening abundance pattern peaks and moving them to lower masses.

Final elemental abundances depend on the thermodynamical evolution of the ejected material, but also on the nuclear physics input which is used by the reaction network. The resulting abundance pattern, and other calculated magnitudes, are affected by nuclear physics uncertainties, which limit the predictive power of these kind of simulations. In order to increase the reliability of the r-process calculations, new experiments are required to provide new data and in parallel improve the nuclear models utilized by the calculations. Smaller uncertainties are required in order to use these calculations to quantify the contributions of each r-process site to the observed abundances and get a better understanding about the galactic chemical evolution. In particular, this Thesis work is devoted to the measurement of half-lives and neutron emission probabilities of nuclei close to ^{78}Ni , and thus contributes to reduce the uncertainty around the so-called first r-process abundance peak from the nuclear physics side.

Chapter 2

Experiment

The purpose of the Beta-delayed neutrons at RIKEN (BRIKEN) experiment is to measure x -neutron emission probabilities (P_{xn}) and half-lives ($T_{1/2}$) of very neutron rich nuclei with high precision. In order to accomplish that, state-of-the-art neutron and ion/beta detectors are used at RIKEN Rare Isotope Beam Factory (RIBF), which currently provides the most intense beams of such exotic isotopes.

The BRIKEN neutron counter is a result of a international collaboration and several years of preparation. It consists of 140 ^3He proportional tubes distributed in a polyethylene moderator, and so far it is the most efficient neutron detector dedicated to beta-delayed neutron emission measurements. Given the very large number of tubes and their different characteristics (length, pressure, diameter) a parameterized Monte Carlo optimization algorithm was developed [Tar17] in order to fully optimize their positions inside the moderator, and reach a high and flat neutron efficiency. On the other hand, Advanced Implantation Detector Array (AIDA) represents the last generation of pixelated silicon detectors for beta decay studies with high energy radioactive beams. Its high granularity and event-less Data Acquisition System (DAQ) grant a high efficiency and low accidental correlation background.

The results presented in this work correspond to the BRIKEN experiment RIBF127, scheduled in June-2017 [Sch17], that was taking data for 4.7 days which resulted on 84.4 hours of effective measuring time.

This chapter is dedicated to details of the facility and the experimental setup.

2.1 Production of isotopes

The very exotic neutron-rich nuclei to be studied can be produced by different techniques. The method exploited by RIKEN-CNS¹ RIBF is the separation in-flight of products from fragmentation and fission of medium energy heavy-ion beams [Kub12]. In particular, for the production of nuclei around ^{78}Ni , a very intense (20-50 pnA) primary ^{238}U beam at 345 aMeV ($\sim 70\%$ of the speed of

¹Center of Nuclear Study (CNS), University of Tokyo

light) was used. After its collision with a 4 mm thick beryllium target, the fragmentation products travel through the spectrometers BigRIPS and ZeroDegree in few hundreds of nanoseconds.

2.2 Radioactive ion separation and identification. BigRIPS

As explained in [Fuk13], the Superconducting Radioactive Isotope Beam Separator (BigRIPS) is a two-stage tandem separator, composed by fourteen quadrupole and six dipole magnets which define seven ion optics foci, marked in Fig. 2.1 as F1 to F7.

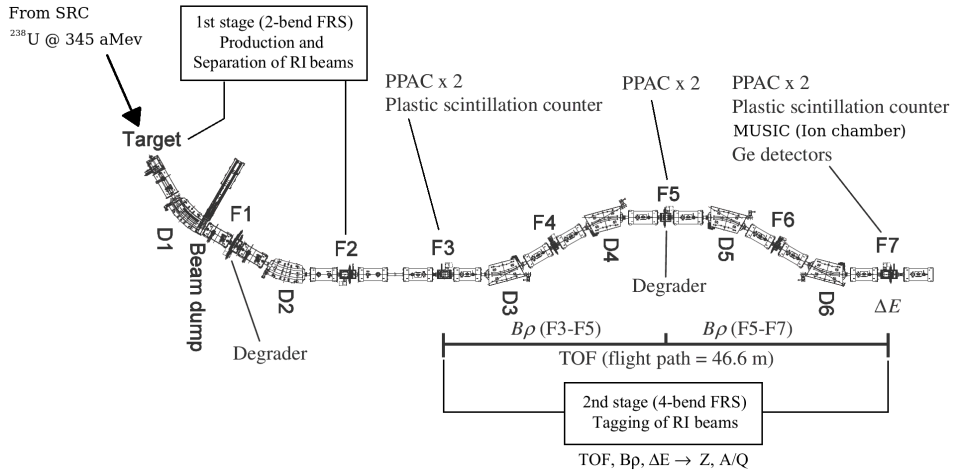


Figure 2.1: Layout of the BigRIPS separator. The ion optics foci and the dipole magnets are labeled with the letters F and D, respectively. The particle identification is performed in the second part.

The first part, from F1 to F3, separates the Rare Isotope (RI) by its energy; the RI are identified in the later part, from F3 to F7. The mass-to-charge ratio (A/Q) and atomic number (Z) of each fragment are derived from the measurement of its Time-Of-Flight (TOF), magnetic rigidity ($B\rho$) and energy loss (ΔE), and used for particle identification (PID). Different detectors along the beam line are used to measure these quantities. As displayed in Fig. 2.1, there are two plastic scintillation detectors at F3 and F7 focal planes, used to measure TOF, and a multi-sampling ionization chamber (MUSIC) [Car15] detector at F7 used for determining ΔE . The central $B\rho$ value is obtained by measuring the dipoles' magnetic field. The position sensitive gas detector (PPAC) [Kum13] placed at F3, F5 and F7 are

2.3. Implanted ion and decay detector. AIDA

used to reconstruct the path and improve the precision of the $B\rho$ value. The information from the different detectors placed along the spectrometer, magnetic field and degrader settings are acquired and stored by the BigRIPS independent DAQ. PID is endorsed by the isomer tagging technique [Kub12, Fuk13] at the F7 focal plane, which consist in measuring the isomer delayed gamma rays from an identified fragment. The PID plot corresponding to RIBF127 BRIKEN experiment is shown in Fig. 3.1. Further technical information can be found in [BigRIPS].

After the BigRIPS separator, the RI beam travels through Zero Degree spectrometer and is delivered to the experimental area, located after the latest focal plane F11. Fig. 2.2 shows a complete layout of the last stages of the accelerator complex, the BigRIPS and ZeroDegree separators.

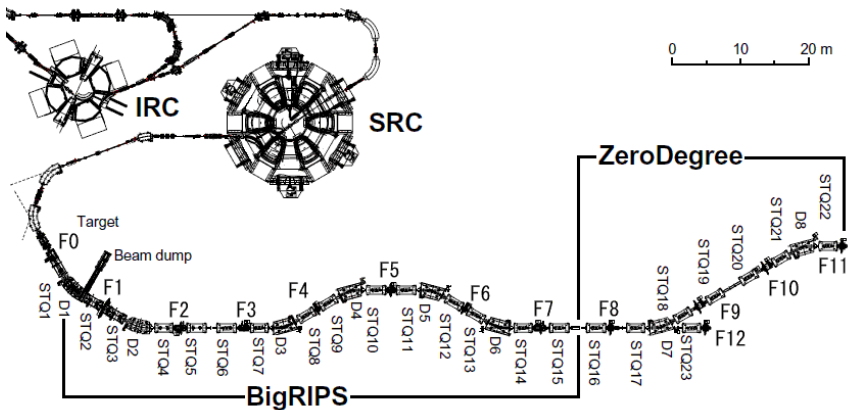


Figure 2.2: Layout of the BigRIPS plus ZeroDegree separators [Kub12]. The BRIKEN neutron counter and the ion/beta detector AIDA are placed at the last focal plane F11.

2.3 Implanted ion and decay detector. AIDA

The RI beam produced and identified by the BigRIPS separator is stopped in the Advanced Implantation Detector Array (AIDA), which is placed after the last focal plane F11. AIDA consists in a stack of six Double-sided Silicon Strip Detectors (DSSD), see Fig. 2.3, and is dedicated to detect every implant and its subsequent beta decays. The area of the silicon detectors is $71.68 \text{ mm} \times 71.68 \text{ mm}$ and is 1 mm thick. Each side of the DSSD has 128 strips, 0.51 mm wide [Bra11, Gri19, Hal20]. The strips on one side are perpendicular to the strips on the other side, resulting in 16384 pixels per silicon detector, allowing the offline position reconstruction of decay and implant events. The DSSD stack is suspended on four

titanium rods and is mounted inside an aluminum nose with side wall 1 mm tick and a square cross-section of 100 mm × 100 mm. The nose end is covered by a piece of aluminized Mylar foil. The read-out electronics is 70 cm behind the silicon detectors, connected by special 64-channel flat cables.

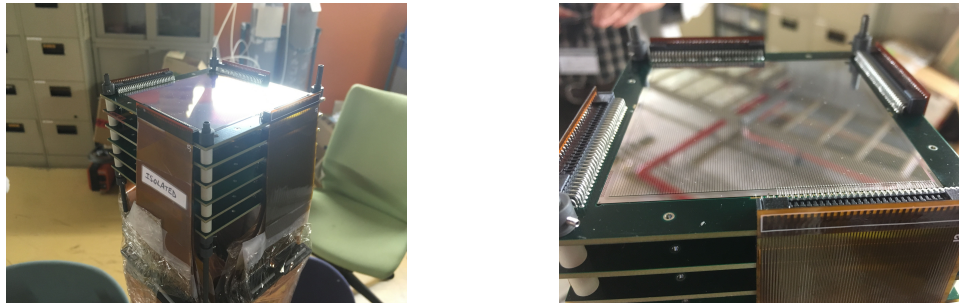


Figure 2.3: AIDA DSSD stack

Two different electronic chains are used to acquire the signal of every strip. On the one hand, the low-gain branch, with a range of 20 GeV, is used for implant events. On the other hand, the high-gain branch, with a range of 20 MeV is dedicated to select beta decay events. By default, signals are amplified by the high-gain preamplifier, but if its amplitude exceeds a certain threshold (≈ 200 MeV) the signal is diverted to the low-gain preamplifier [Bra11]. The basic schematic of the electronics is presented in Fig. 2.4. A digital event-less DAQ register individual strip events, granting a negligible dead time. AIDA DAQ software is based on MIDAS suite of programs [MIDAS].

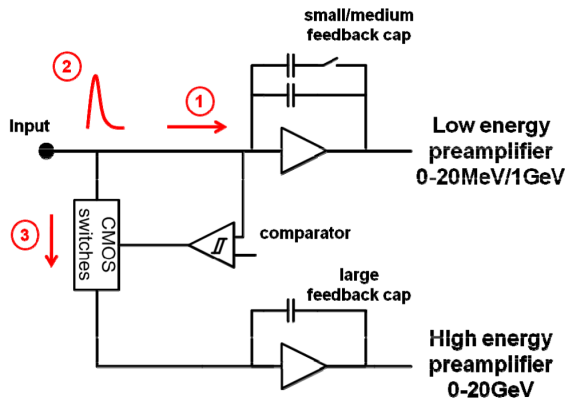


Figure 2.4: AIDA electronic chain. Each channel has two preamplifiers.

2.4 Beta delayed neutron setup. BRIKEN

This section is dedicated to the neutron detector and its DAQ system. A brief description of gamma and ancillary detectors, which are also read out by BRIKEN DAQ, is included.

2.4.1 Neutron counter

The Beta-delayed neutrons at RIKEN (BRIKEN) neutron counter surrounds AIDA, so the stack of DSSD is at its center. The counter is formed by 140 ^3He filled proportional tubes inserted in a high-density polyethylene (HDPE) matrix. The matrix side facing the beam is square, 90 cm wide, and the matrix depth is 75 cm. The beam goes into the neutron counter through a central square hole 11.6 cm wide. The AIDA stack is introduced into the matrix from the opposite side of the beam entrance. A more detailed scheme is shown in Fig. 2.8.

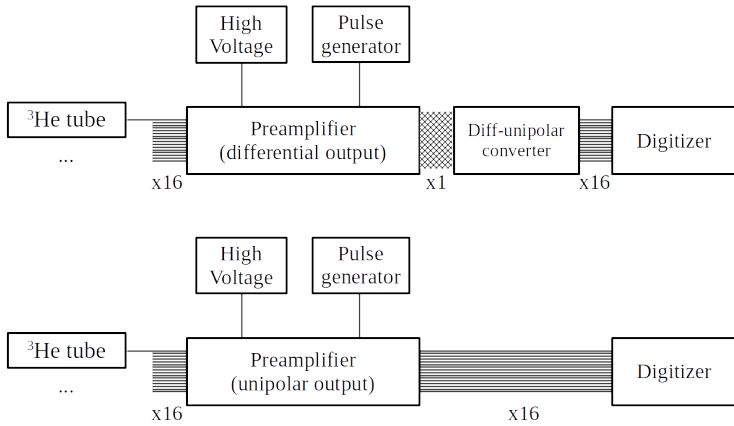
The neutrons emitted by the RI implanted in the DSSD are thermalized by the HDPE, via elastic scattering with hydrogen nuclei [Leo87, Chapter 2.8]. If a thermal neutron enters a tube, there is a chance to be absorbed by the ^3He inside, inducing the following nuclear reaction



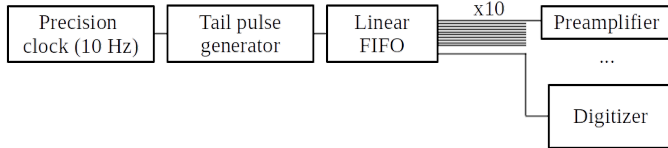
The probability of this reaction depends strongly on the neutron energy, the lower its energy the higher probability to be absorbed by a ^3He nucleus. This nuclear reaction is exothermic, and the energy released at the Center of Mass is 764 keV. This energy is divided among the proton and the triton ^3H , 573 and 191 keV respectively. This energy is deposited inside the tube in form of ionizations. In some cases, either the proton or the triton may hit the tube wall (and will be stopped) before depositing all its energy. This effect appears in the energy distribution of the signals as a tail below 764 keV.

If there is no voltage difference between anode and cathode, most of the ions inside the tube would recombine without producing any output signal. If a certain voltage difference is applied to the tube, electrons and ions can not instantly recombine and a current signal is produced, whose amplitude depends on the voltage, geometry and the gas mixture inside the tube. In the case of proportional counters, the voltage must be appropriate for working in the so-called proportional regime of a gas detector [Leo87, Chapter 6.5].

Mesytec MPR-16-HV modules [Mesytec] are used in order to amplify the current signals from the proportional tube. This module also distributes high voltage bias to the tubes, and introduces a tail-pulse signal in every preamplifier output channel, which is used to measure DAQ dead time. This pulser signal is triggered by a 10 Hz external clock, which is also registered by a dedicated DAQ channel, so the



(a) Schematic of BRIKEN electronics. Preamplifiers distribute the high voltage to the tubes, amplify the neutron signals from the tubes and add a test pulse to the output. Four preamplifiers have differential output, which has to be converted to a unipolar signal in order to feed it to the digitizers.



(b) The test pulse signal is generated by a tail pulse generator, which is triggered by an external precision clock at 10 Hz, and distributed by a Linear FIFO to all the preamplifiers and to one dedicated channel in BRIKEN DAQ.

Figure 2.5: Schematic of BRIKEN electronics (top panel) and a more detailed schematic of the test pulse generation (lower panel).

DAQ live time is obtained by comparison with this pulser reference channel. The schematic of the pulser distributions is shown in Fig. 2.5.

As detailed in [Tar17, Tol19], four different types of ^3He tubes are used in BRIKEN, with different specifications of size and bias (see Tab. 2.1). These differences appear in the neutron spectra as small shape changes, as it can be seen in 2.6. The 140 tubes are grouped by its distance to AIDA into 7 rings, as shown Fig. 2.7.

A common high voltage (HV) is applied to all the tubes connected to a preamplifier module, thus the 140 tubes are distributed according to tube type into 10 Mesytec preamplifier modules. The high voltage is provided by a remotely

2.4. Beta delayed neutron setup. BRIKEN

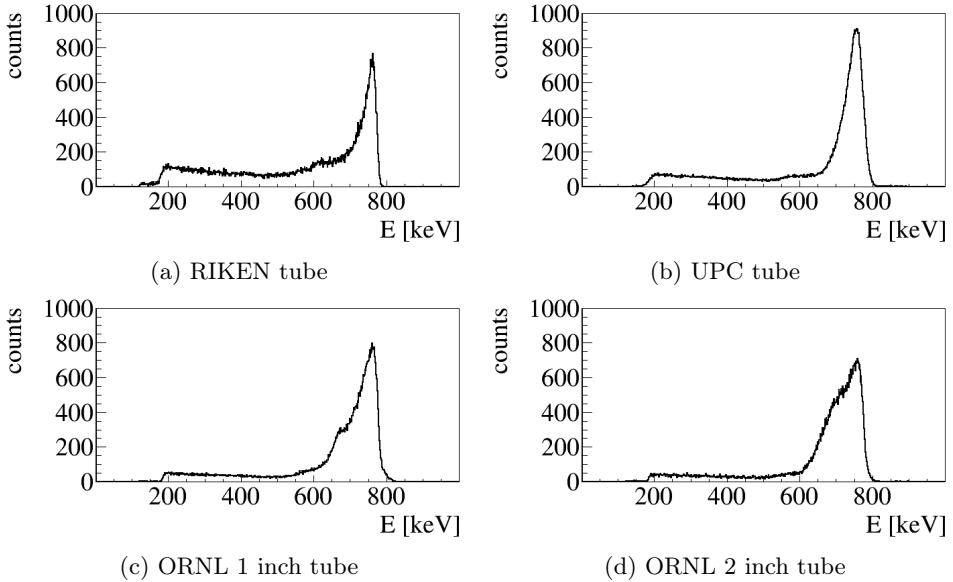


Figure 2.6: There are four different tube types: from RIKEN, UPC, ORNL 1 inch, ORNL 2 inch. Each group has different characteristics, and consequently their energy spectra have different shapes.

Type	RIKEN	UPC	ORNL-1	ORNL-2
Length (mm)	300	600	609.6	609.6
Diameter (mm)	25.4	25.4	25.4	50.8
Pressure (atm)	5	8	10	10
Voltage (V)	1450	1450	1350	1750
Number of tubes	24	40	16	60

Table 2.1: Main characteristics of the ${}^3\text{He}$ proportional tubes used in BRIKEN.

controllable MPOD system from Wiener with ISEG HV cards [MPOD].

The neutron background is reduced adding some pieces that act as shielding. A large HDPE piece, which is 20 cm thick and has the same cross-section as the matrix, is placed 50 cm upstream with respect the neutron counter. Its mission is to reduce the background coming from beam interactions with materials before the neutron counter. Top and lateral sides of the matrix are covered with a 1 mm

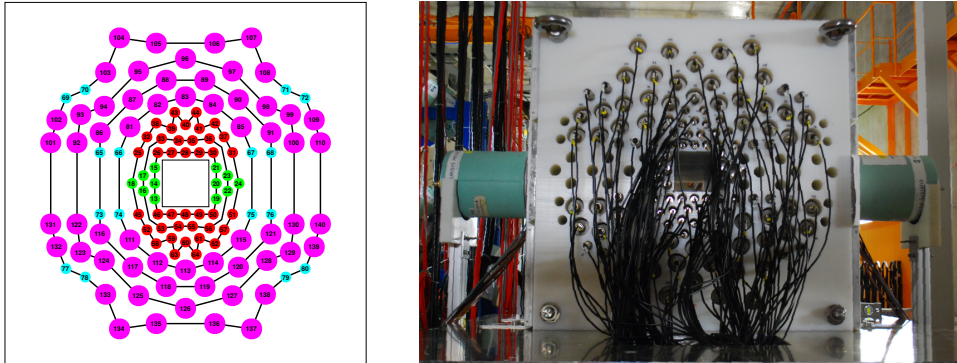


Figure 2.7: BRIKEN tubes distribution. The tubes are grouped by distance to the center into 7 rings (solid lines). The colors indicate the tube type: RIKEN (green), UPC (red), ORNL 1" (blue), ORNL 2"(pink).

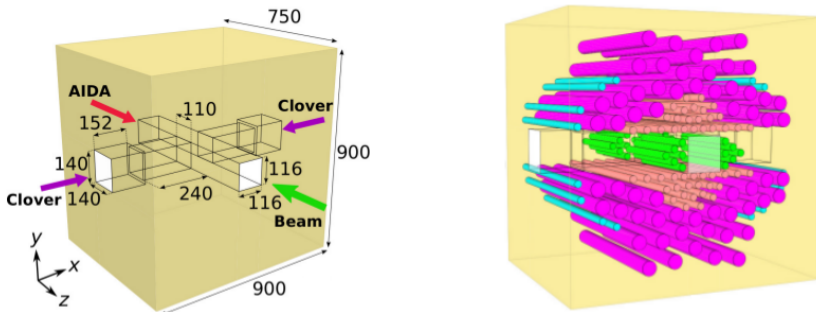


Figure 2.8: HDPE matrix layout and tube distribution. From [Tar17].

cadmium film and blocks of HDPE, 2.5 cm thick. In addition, boron enriched rubber sheet was placed over the matrix and kept in position using a HDPE slab. In Fig. 2.11 top and front shieldings are labeled as *PE Shielding*. All of these external HDPE pieces, as well as the outer part of the matrix, act as neutron reflectors, and moderate the background neutrons so they can be easily absorbed by the boron and cadmium sheets.

2.4.2 Gamma ray detectors

In the measurements the so-called hybrid BRIKEN setup was used. It enhances the original setup adding gamma-ray detection capability. The hybrid BRIKEN setup includes two HPGe CLOVER-type detectors, belonging to CLARION array from

Oak Ridge National Laboratory (ORNL) [Gro00]. They are placed perpendicular to the beam, surrounding AIDA as close as it is possible in order to maximize their geometrical efficiency. A photograph showing the placement of the CLOVER detectors is shown in Fig. 2.7 and a schematic drawing is shown in Fig. 2.8.

Each CLOVER has four crystals with a diameter of 50 mm and a length around 80 mm, assembled at 10 mm from the front face. The aluminum housing has a section of 10.1 cm × 10.1 cm. Each crystal is longitudinally two-fold segmented, and both the segment signals and the central contact are connected to independent preamplifiers. We only use the central contact signal and the preamplifier output is directly acquired by the BRIKEN DAQ.

The Wiener MPOD system [MPOD] provides the high voltage, while the CLOVER temperature is continuously monitored by a LabJack unit [LabJack]. If the temperature is not below a certain threshold, the LabJack order the MPOD system to ramp down the high voltage. The CLOVER dewars with liquid nitrogen are automatically refilled twice a day. The electronics of liquid nitrogen refilling system were surrounded by a metallic shielding in order to avoid noise in the DAQs.

2.4.3 Ancillary detectors

In addition to CLOVER detectors, other ancillary detectors play a significant role in our measurements. They are placed between the end of the spectrometer and our setup. A schematic distribution of the detectors in the experimental area is presented at the end of this chapter, in Fig. 2.11.

After the last MUSIC chamber, there is a very thin plastic scintillator, being both part of BigRIPS (see Fig. 2.9a). Since they are located close to the last focal plane F11, they are referred as F11 MUSIC and F11 plastic. The RI beam flies on air from the F11 MUSIC to AIDA DSSD , passing through the F11 plastic, a metallic degrader, and a ΔE silicon detector.

The F11 plastic is a 1 mm thick plastic scintillator connected to two PMTs. This detector is used as part of the BigRIPS triggering system. In addition, the anode signal from both PMTs passes through an Ortec 474 TFA [TFA474] and is fed into BRIKEN DAQ. Its energy calibration is based on the estimation of the energy lost by ions, around 65 MeV, given by the LISE++ [Tar08] simulation. Just after the F11 plastic, a variable degrader is used to optimize the implantation depth in AIDA (see Fig. 2.9b).

Two large plastic detectors, with dimensions 45 cm × 20 cm × 1 cm, are attached to the upstream side of the neutron shielding, above and below the beam axis. The mission of this detectors is to tag any scattered neutron coming from beam interactions. However it was found later during the analysis that it was not providing any useful information. The PMT dynode signal is amplified by an ORTEC 474 TFA [TFA474] and acquired by the BRIKEN DAQ.

A Single-sided Silicon Strip Detector (SSSD) is used as energy loss (ΔE) for identification of light particles and possible nuclear reactions in the degrader. This

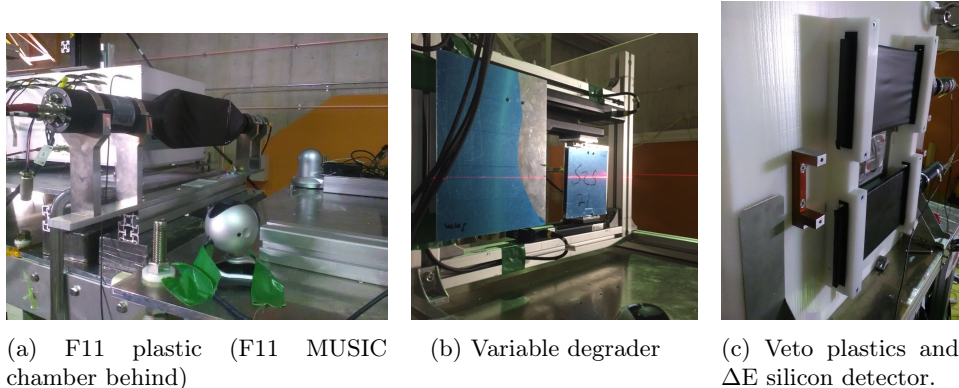


Figure 2.9: Ancillary detectors in the experimental area

detector has a thickness of 320(15) μm and an effective area of 134 mm \times 123 mm, bigger than the beam profile. There are 26 vertical strips which are added to form two readout channels, *top* and *bottom* with respect to the orientation of the BRIKEN counter). This detector was placed in the front neutron shielding hole. The F11 veto plastics and ΔE silicon detector are shown in Fig. 2.9c. A general schematic of the setup is given in Fig. 2.11.

Further to this, a thick plastic scintillation detector was placed on the beam axis, 70 cm after the AIDA stack of DSSD. This detector is used to distinguish light beam particles traversing the setup and nuclear reactions in AIDA itself. The signal from the PMT is amplified and acquired by the BRIKEN DAQ.

2.4.4 BRIKEN Data Acquisition System (DAQ)

The BRIKEN DAQ is based on the Struck modules SIS3316 and SIS3302 [SYS]. The modules SIS3316 are 16-channels VME digitizers, 14-bit resolution and 5 V dynamic input range; whereas the modules SIS3302 are 8-channels VME digitizers, 16-bit resolution and 5 V dynamic input range. The gamma ray detectors and a small number of the proportional tubes are read by digitizers of 3302-type, with the rest of the proportional tubes and ancillary signals being read by 3316-type modules. A total of seven 3316 units and seven 3302 units were employed during RIBF127 experiment.

A common 25 MHz periodic signal is shared by BigRIPS, AIDA and BRIKEN systems in order to keep them synchronized (see Sec. 2.4.4 for further details). In case of BRIKEN, the frequency of this signal is upgraded to 50 MHz by a Logic Unit for Programmable Operation [Bab09] module, and split up among all the digitizers using the SIS3820 Logic Module. This external 50 MHz clock signal is the reference of the digitizers for sampling the input signals and time-stamp the acquired data at

50 MHz (see Sec. 2.4.4 for further details). Detector signal is sampled by an ADC and filtered by the FPGA using a trapezoidal Finite Impulse Response (FIR) filter to determine signal energy. Parameters of the filter and ADC are optimized for each detector. Since each channel is self-triggered and digitizer’s readout is performed simultaneously to acquisition, DAQ dead time is channel dependent and very low.

The digitizer modules are controlled by GASIFIC 7.0, a dedicated software developed at IFIC (Valencia) [Agr16, Agr18]. It is a modular software, with a rich Graphical User Interface (GUI) based on Qt and ROOT [Bru97] interactive display tools.

This GUI is used for the DAQ slow control, like start and stop the acquisition, write data onto disk, open a socket for sending synchronization signal data, or send NIM analog signals from the VME controller module. This is used in the BRIKEN setup to reset the time-stamp scalers of all the systems. In addition, the GUI can be used for setting the digitizer configuration in a very simple and robust way, and real time analysis can be performed, like time and energy correlations between different channels or event-building. Given the large number of parameters, the configuration file was formatted as a spreadsheet, simplifying the modification and expansion of the configuration.

Synchronization of the different data acquisition systems The final stage of data analysis requires merging the data from BigRIPS, AIDA and BRIKEN independent DAQs in order to build the necessary correlations between particle identification signals, implantation and beta events, and neutron, gamma and ancillary signals, on the basis of a common absolute time. To achieve this, a single 25 MHz reference signal is distributed among the three DAQs. Each system treats this signal in a different manner. For instance, BRIKEN DAQ directly takes the shared clock signal as the digitizer sampling frequency and the time-stamp reference (after upgrading its frequency to 50 MHz). On the other side, BigRIPS DAQ uses a LUPO [Bab09] module to time-stamp its data. AIDA uses a MACB system to distribute the time-stamp information to each FEE unit (see [Gri19] and [Hal20] for further details). Fig. 2.10 shows a sketch of the clock distribution, and the time-stamp reset. This reset is controlled manually, setting a common origin of absolute time for the three autonomous DAQs.

Synchronization check Keeping the synchronization between the three DAQs is a critical issue for the success of the experiment. In order to be able to monitor the synchronization between the systems, a synchro-check signal is acquired by all the DAQs. At the same time, a process running in each DAQ spies the raw data flow and sends the absolute time of this synchro-check signal to a central server, where a data sink routine [Agr18] receives time-stamps from the three systems and allow a real time monitoring of the synchronization.

During the first experimental campaign, a 10 Hz clock signal was used as

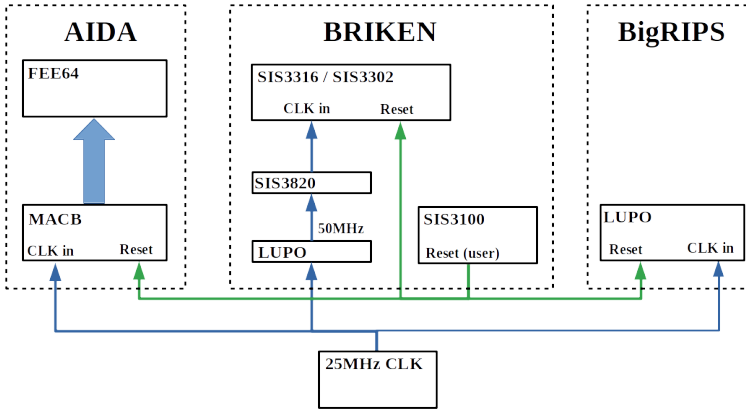


Figure 2.10: Sketch of clock signal distribution.

synchro-check signal for monitoring the synchronization. However, in the following campaigns BigRIPS trigger signal was used as the synchro-check. This latter method has two advantages: on one side, remove the possible dead time in BigRIPS DAQ induced by the additional trigger of the synchro-check signal; and on the other side, a non-periodic synchro-check signal would allow to realign offline the time of the data in case of (very improbable) loss of synchronization.

2.5 Summary of the experimental setup

The experimental setup is placed at the F11 focal plane of the mass-separator BigRIPS. After the last PPAC detector, the RI beam travels in air, passing through the last elements of the separator: a MUSIC and a thin plastic scintillator detector, which is also known as F11 plastic. Then, a combination of a fixed and a variable degrader slows down the beam, so implantation depth in AIDA can be optimized, and a thin SSSD detector (Si ΔE detector) is used to measure energy loss before implantation in AIDA. AIDA DSSDs are centered inside the HDPE matrix, where the ${}^3\text{He}$ proportional tubes are inserted. One ancillary plastic scintillator detector is placed on the beam axis, 70 cm downstream, surrounded by AIDA read-out electronics. In addition, two thick plastic scintillator detectors are placed on the upstream side of the neutron HDPE shielding. A schematic layout of the experimental area at F11 is shown in Fig. 2.11.

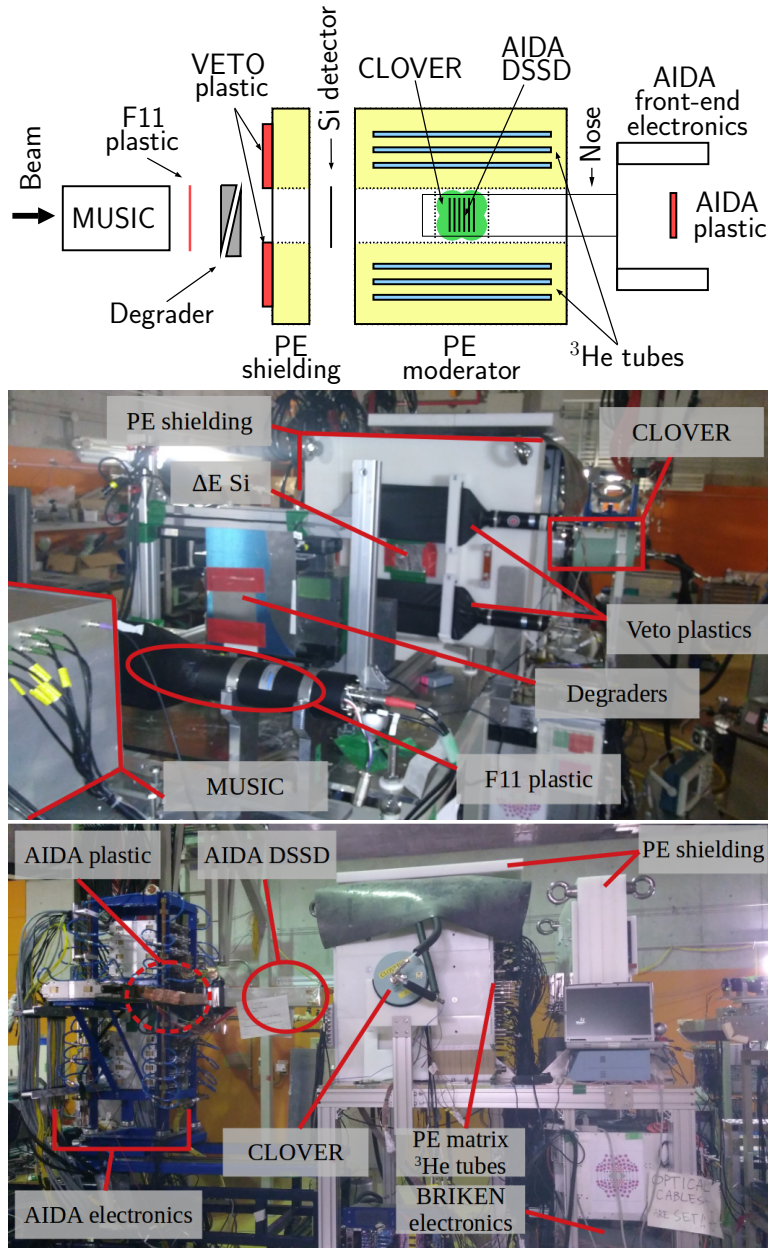


Figure 2.11: BRIKEN experimental setup layout.

2.6 Summary of run conditions

The experimental run was organized in three parts, corresponding to three different configurations of degraders that were used. The first part (Configuration A) used a total of 15 mm of aluminum degrader, all of it placed at F11. This amount of degrader centered the implantation depth of ^{78}Ni in the last two DSSD of AIDA.

The isotopes of selenium and bromine were stopped in the degrader and not implanted in AIDA, therefore 1 mm of aluminum degrader was removed during the next part (Configuration B). A thinner degrader moved the implantation depth of ^{78}Ni to the last layer, and part of the production of this isotope passed through AIDA without being implanted.

A total of 15 mm of aluminum degrader was chosen for the last part (Configuration C), in order to ^{78}Ni be fully implanted in AIDA. Since the degrader can be a source of neutron background, 5 mm of aluminum were placed in F7 focal plane and the other 10 mm remained at F11, close to the experimental setup. The idea of moving away part of the degrader was to investigate if the beam induced neutron background that affect this measurement could be reduced.

The key parameter defining the background rate is r , the probability that indeed a neutron accidentally correlates with a beta particle (see Sec. 3.7.2 for a more detailed explanation). From Tab. 2.2, it can be concluded that a reduced amount of degrader in front of the experimental setup decreased neutron background, but this reduction was not proportional to the material removed.

Configuration	A	B	C
Degrader at F7 (mm of Al)	0	0	5
Degrader at F11 (mm of Al)	15	14	10
Net meas. time (h)	8.7	16.5	57.9
Implants (total)	$2.5 \cdot 10^6$	$7.5 \cdot 10^6$	$2.0 \cdot 10^7$
Implants (^{78}Ni)	$7.8 \cdot 10^2$	$2.0 \cdot 10^3$	$4.3 \cdot 10^3$
Implants (^{93}Se)	$5.8 \cdot 10^2$	$1.3 \cdot 10^4$	$5.4 \cdot 10^2$
r (^{78}Ni)	0.014	0.018	0.012
r (^{93}Se)	0.017	0.018	0.010

Table 2.2: Summary of run conditions and some representative integral quantities.

Chapter 3

Analysis methodology

As it was explained in the previous chapter, three independent DAQs (BigRIPS, AIDA and BRIKEN) work independently and simultaneously, each one reading a certain set of detectors. Some details about each system can be found in Chap. 2. A more detailed account about the work flow between the three systems is described in the present chapter. The first part of this chapter is dedicated to how each individual DAQ acquire the data and process it. The second part explains how the data is merged into a single data flow that can be used to reconstruct the correlations needed to extract the half-lives ($T_{1/2}$) and x-neutron emission probabilities (P_{xn}) values, and how it is done. The third part is dedicate to explain how data analysis is effectively performed.

3.1 BigRIPS. Isotope identification

The particle identification (PID) is obtained from the measurement of three quantities: Time-Of-Flight (TOF) from F3 to F7 foci, energy loss (ΔE) at F7 focal plane, and dipoles' magnetic rigidity ($B\rho$); in addition, horizontal position, measured by position sensitive gas detector (PPAC), is used for correcting the magnetic rigidity ($B\rho$) value. The whole procedure is explained in [Fuk13].

The BigRIPS Data Acquisition System (DAQ) [Bab10] registers the data from all the detectors along the beam line each time it is triggered by a combination of selected detectors (plastic scintillators, including the one at the last focal plane F11). This fact makes the data stream event-wise by construction. Dedicated software was used to unpack and build the PID events, based on the ANAROOT library [Iso13]. Each event has the necessary information, absolute time-stamp and the particle identification (PID), plus some additional information about different detectors like position in the position sensitive gas detector (PPAC), energy loss (ΔE) deposited in the F7 MUSIC, and velocity measured between F3 and F7. This additional information can be used in the following analysis steps to improve the PID, by removing some dependencies (for example, mass-to-charge ratio (A/Q) vs velocity), rejecting pile-up events, or even used by the implant detector (cf. Sec. 3.2). The output data format is a ROOT TTree [Bru97]. The particle

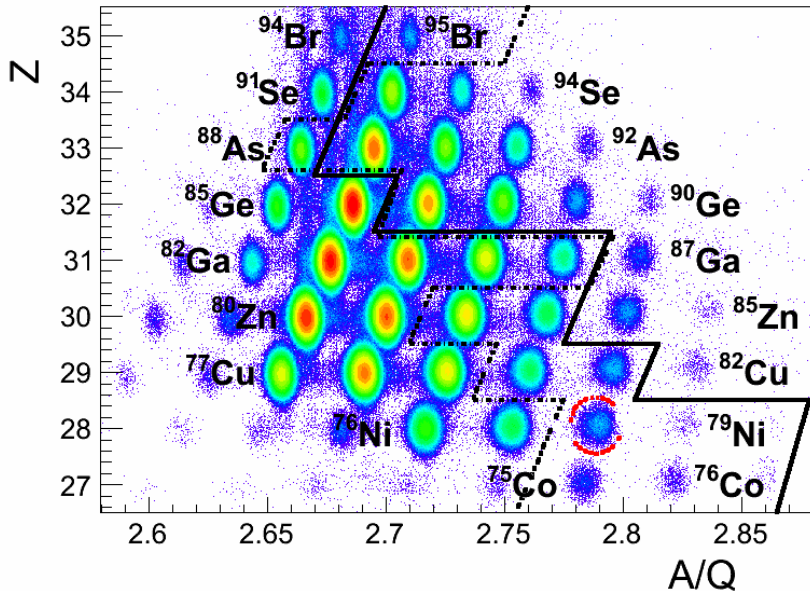


Figure 3.1: particle identification (PID) plot corresponding to the experiment RIBF127.

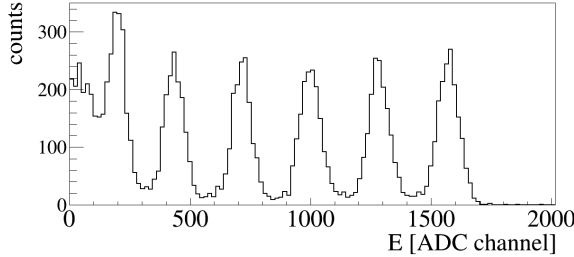
identification (PID) identification plot, i.e. atomic number (Z) versus A/Q for the full statistics accumulated in the experiment is shown in Fig. 3.1.

3.2 AIDA. Implant and beta event reconstruction

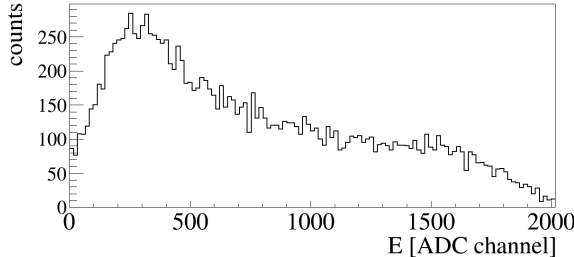
The software used initially was the LuckyDoll suite [Pho17], but AIDASort program [Hal18] was used for the results presented here.

As explained in [Gri19, Hal20], the reconstruction of every event happens in two stages, for each Double-sided Silicon Strip Detector (DSSD) and for each electronic branch. First of all, spatially consecutive strips in each DSSD side which have been triggered in a narrow time-window ($\pm 4 \mu\text{s}$, this is related to the read-out time of strips) are grouped together in a so-called cluster. Several clusters in the same DSSD side may happen simultaneously if not all the triggered strips are contiguous. Each cluster has an energy given by the sum of the individual strip energies. After clustering in both sides of the DSSD, clusters from both detector sides are paired. An event is accepted if the energy of one cluster is similar to the energy of a cluster from the other side. A fix energy tolerance of 150 keV is used for beta events (i.e., $|E_x - E_y| < 150 \text{ keV}$), and 1000 keV for implant events (i.e., $|E_x - E_y| < 1000 \text{ keV}$).

LuckyDoll suite¹ and AIDASort program implement this method, but the first one applied an event rejection based on the cluster size and a dedicated algorithm for cluster pairing.



(a) The bump at the lowest energy correspond to the regular noise, and the other 6 peaks at higher energy correspond to the pulser signals with amplitudes $A, 2A...6A$.



(b) The noise hides the pulser peaks, and no offset calibration can be obtained. In this case, zero offset is assumed.

Figure 3.2: Energy spectrum of a pulser measurement in a regular (top) and noisy (bottom). The X-axis corresponds to energy in ADC channels.

Before summing individual strip energies, an energy calibration must be applied. Given the technical specifications, the electronic gain is assumed to be the same for all the strips. However, each strip may have different offset that is determined by means of a pulser signal. This procedure consists in feeding a 10Hz signal into all the DAQ channels, and take short measurements with different pulser amplitudes ($A, 2A... 6A$), as presented in Fig. 3.2a. Afterwards, the offset can be obtained by extrapolating the peak position down to zero pulser amplitude. If the strip is too noisy to recognize the pulser peaks, as in Fig. 3.2b, null offset is set. Background measurements are used to validate the calibration procedure. They use the alpha particles from radon decays that are detected in a single pixel triggering the high gain DAQ branch.

¹July, 2017 version.

Every AIDA event, beta or implant, corresponds to a pair of clusters, one cluster from each side of one DSSD. A given event has the minimal information: an absolute time-stamp, energy of the clusters, averaged X and Y coordinates in the DSSD, the DSSD position inside the stack, and the clusters' size (i.e., the number of strips that form each cluster).

The AIDASort program [Hal18] determines the stopping DSSD as the last layer of the detector stack that has triggered the implant DAQ branch. The implant branch of AIDA DAQ has an energy threshold of 200 MeV. It may happen that an implant pass through a DSSD and deposits less than 200 MeV in the next one; in this case, the software misidentifies the stopping layer as the previous one. This artifact can be recognized in a velocity-energy plot: the isotope velocity (measured by BigRIPS along the separator) has a quasi-linear dependency with the energy deposited in the last layer in AIDA, the more velocity, the more energy it has to deposit. But, if the isotope punched through the identified stopping layer, then a lower energy than expected will be observed. No punch through effect was identified in the present work, as it can be seen in Fig. 3.3.

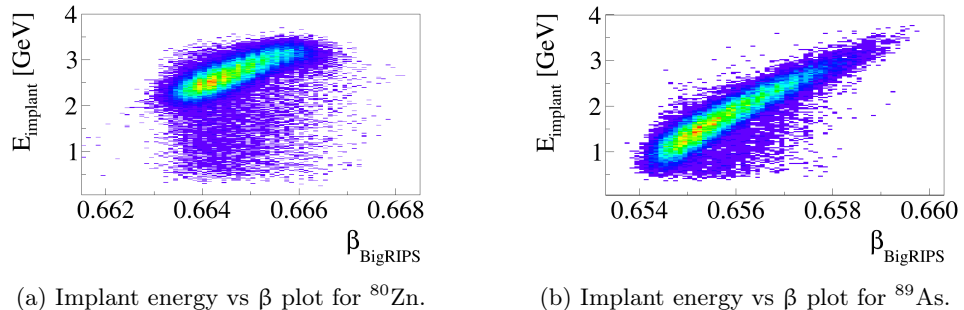


Figure 3.3: The energy deposited by implants in the last layer has a quasi-linear dependency with the velocity β (measured by BigRIPS) if the implantation layer is correctly identified. Two representative cases are shown: ^{80}Zn (left) and ^{89}As (right).

3.3 BRIKEN neutron counter

This section is dedicated to energy and efficiency calibration of the BRIKEN neutron counter, and the calculation of BRIKEN DAQ live-time factor.

3.3.1 Energy calibration

Neutrons are moderated by high-density polyethylene (HDPE) in order to largely increase the probability of neutron detection by a ^3He proportional tube. This

has two main consequences: first, moderation takes time (from tens to hundreds of micro-seconds), and secondly, a single proportional tube is not sensitive to the neutron original energy.

As explained in Sec. 2.4, every time a neutron is captured by a ^3He nucleus inside the tube, it is released 764 keV shared among a proton and a triton. The energy spectrum of a ^3He proportional detector has a particular shape: a total energy deposition peak at 764 keV, and two overlapping tails starting at 191 and 573 corresponding to partial energy deposition. A linear calibration was applied to each tube, using a ^{252}Cf source and taking the position of the peak as reference. The offset is zero as it corresponds to a digital trapezoidal filter. Fig. 3.4 displays the aggregated tube spectra grouped by ring and the total, showing the quality of calibration. We found the calibration of the detectors to be very stable over time.

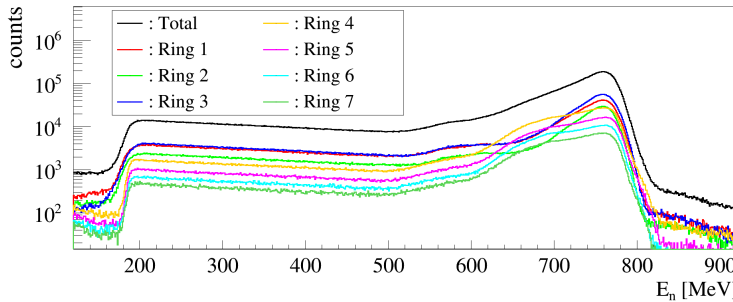


Figure 3.4: BRIKEN neutron spectrum of a ^{252}Cf source. Tubes are grouped in rings, almost by its distance to the center. The black line corresponds to the sum over all the rings, and the other lines corresponds to the individual rings.

3.3.2 Detection efficiency

According to GEANT4 simulations [Tar17], detector efficiency is very flat for neutron energies below 1 MeV, and drops moderately up to 5 MeV, as shown in Fig. 3.5. The value of absolute neutron detection efficiency for energies below 1 MeV is on average 66.8(20)% [Tol19].

The absolute value of the simulated efficiency curve was validated by several measurements with an un-calibrated intense ^{252}Cf neutron source, which had a nominal activity of 100 μCi and a neutron output of $4.037 \cdot 10^5$ n/s on May 12th, 2006.

The source activity and the detector efficiency are derived from the counting of neutron pairs and the total neutrons detected in a given time [Cro12]. The method relies on the well known values of the first $\langle \nu \rangle = 3.757(10)$ and second $\langle \nu(\nu - 1) \rangle = 11.95(2)$ factorial moments of the neutron multiplicity distribution of

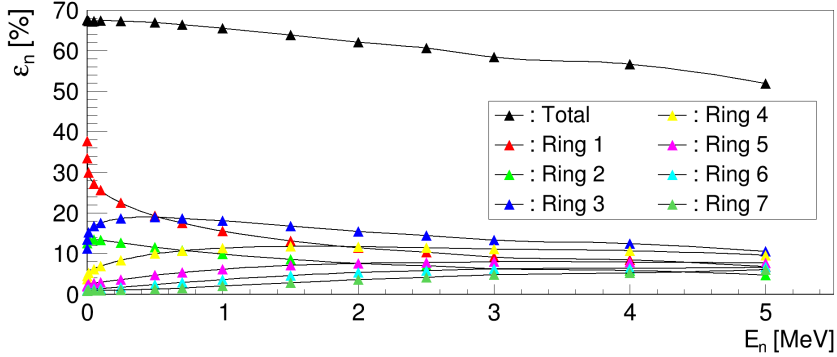


Figure 3.5: GEANT4 simulated detector neutron efficiency as function of the neutron energy. The total efficiency, as well as the efficiency of each ring, are shown.

a ^{252}Cf source [San08]. The number of single neutrons N_s and neutron pairs N_d is related to the number of fissions N_f and the detection efficiency ε_n as in Eq. (3.1).

$$N_s = \varepsilon_n \langle \nu \rangle N_f \quad (3.1a)$$

$$N_d = \varepsilon_n^2 \frac{\langle \nu(\nu - 1) \rangle}{2} N_f \quad (3.1b)$$

The detection efficiency ε_n can be obtained by dividing expressions given in Eq. (3.1b) and (3.1a), arriving to Eq. (3.2).

$$\varepsilon_n = \frac{2 \langle \nu \rangle}{\langle \nu(\nu - 1) \rangle} \frac{N_d}{N_s} \quad (3.2)$$

The amount of singles N_s corresponds to the number of detected neutrons. Neutron doublets N_d can be experimentally determined as follows. The time difference between a detected neutron and all consecutively detected neutrons, also called Rossi plot, is presented in Fig. 3.6. Time difference of neutrons coming from the same fission event produce a time distribution given by the moderation time, while random coincidences produce a flat distribution. The number of neutron doublets N_d is given by the integral of the curve over a flat background, shadowed in Fig. 3.6.

Fig. 3.6 corresponds to a short measurement, 259.909 s long, carried out on May 25th, 2017. Using Eq. (3.2), the calculated detection efficiency is 61.72(20)%.

The simple formula given in Eq. (3.2) disregards a number of corrections: neutron multiplication (in the source or setup), (α, n) reactions in the setup, neutron induced fission (in the source) and dead-time corrections. The first three can

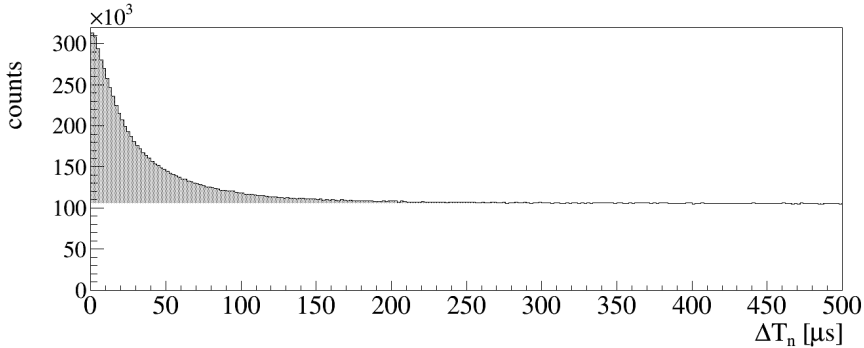


Figure 3.6: Rossi plot for a neutron ^{252}Cf source.

be safely neglected. A Monte Carlo simulation was used to estimate dead-time corrections for the counting of single neutrons N_s and neutron doublets N_d .

The simulation first creates a time sequence of neutrons, according to the multiplicity of ^{252}Cf and the rate of the source which was used, and assigns each neutron to a certain tube following the experimental counting rate of the individual tubes. Secondly, a check is performed: if a second neutron arrives to the tube within the trigger gate length of a previous neutron, it is marked. At this point, there are two time sequences: the original time sequence, and the dead-time affected sequence. Next, Rossi plots of both, original and dead-time affected sequence, are built. Each Rossi plot provides a value of doublets N_d , a dead-time affected N_d and an original N_d . The ratio of these values is the dead-time correction factor for the experimental N_d . Similarly, the amount of single neutrons corresponds to the number of neutrons in each sequence, and their ratio is the dead-time correction factor for singles. The live-time correction factor $f_{lt}^{\varepsilon_n}$ obtained by this mean is 98.44(3)% , and the dead-time corrected value for the neutron detection efficiency is then 62.70(20)% .

Using the well known shape of the neutron energy distribution of a ^{252}Cf source shown in Fig. 3.7, a GEANT4 simulation obtains a detection efficiency of 62.0(18)%, which agrees within the uncertainty with the experimental value of 61.72(20)% calculated using Eq. 3.2, thus validating the Monte Carlo simulation.

3.3.3 DAQ Live time determination

BRIKEN DAQ is a digital system, where each channel is self-triggered, which results in a very low acquisition dead time in our measurements as will be shown. In order to determine live time, a 10 Hz tail-shaped signal is fed into every DAQ channel. Live time of an individual channel is calculated as the ratio of the number of recorded pulser signals C_i and the number of pulser signals recorded

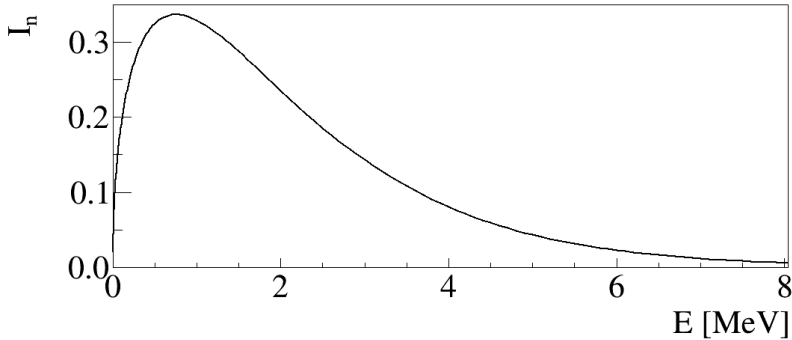


Figure 3.7: Neutron energy spectrum of a ^{252}Cf source [NDS-IAEA]. Its neutron mean energy is $\langle E_n \rangle = 2.28$ MeV.

by a dedicated DAQ channel C_{mp} (master pulser), as in Eq. (3.3).

$$f_{lt}(i) = \frac{C_i}{C_{mp}} \quad (3.3)$$

Live time of a measurement with the intense ^{252}Cf neutron source, which was used for energy and efficiency calibration as explained in the previous sections, is shown in Fig. 3.8 as function of the tube number.

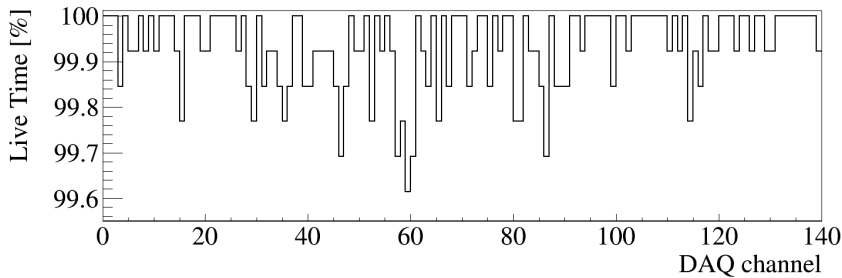


Figure 3.8: Live time of individual DAQ channels, each one corresponding to a proportional tube, calculated as in Eq. (3.3). This plot corresponds to a measurement with the intense ^{252}Cf neutron source.

The global live-time correction factor f_{lt} is obtained averaging the live-time factor of each tube channel $f_{lt}(i)$, weighted by the contribution of that tube to the total neutron count rate, n_i/n_{tot} , as in Eq. (3.4).

$$f_{lt} = \sum_i \frac{n_i}{n_{tot}} f_{lt}(i) \quad (3.4)$$

The individual channel live-time factor $f_{lt}(i)$ for the intense ^{252}Cf neutron source measurement is between 99.62% and 100%. The average correction factor, weighted by the neutron count rate, during the measurement is 99.91%, indicating a nearly negligible effect. A similar situation is found for RIBF127 experiment: individual live-time factor $f_{lt}(i)$ is between 99.66% and 100% (see Fig. 3.9), and the weighted average is 99.90%.

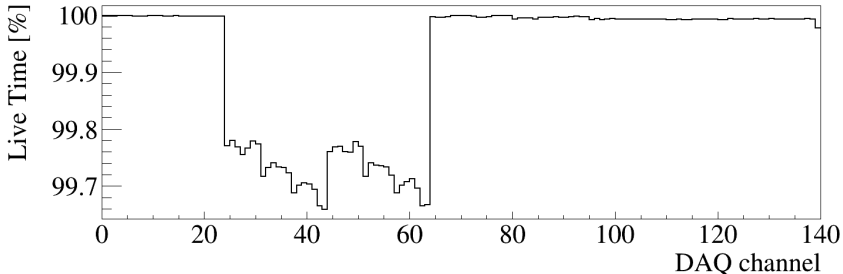


Figure 3.9: Live time of each proportional tube during RIBF127 experiment.

3.4 Merging the data from AIDA, BigRIPS and BRIKEN

The data recorded by BigRIPS, AIDA and BRIKEN DAQs is unpacked and converted into TTrees independently by 3 dedicated sorting programs. In the case of BigRIPS and AIDA, also a certain preprocessing (event building) is needed (described in sections 3.1 and 3.2 respectively). At this point, the TTree corresponding to each system contains meaningful physical events, grouped in the following types: PID events from BigRIPS; implant and decay events from AIDA; neutron, gamma and ancillary detector events from BRIKEN.

Once the data from all the systems has been processed and converted into TTree format, it can be merged into a single data stream using a dedicated software developed at IFIC (Valencia) [Merger, Agr18]. As explained in Sec. 2.4.4, the three systems mark the data with a time-stamp using the same absolute time scale, allowing to order the data from the three systems by time (merging). As it will be discussed later, time correlations over long time periods between different detectors must be done in the analysis stage. The dedicated BRIKEN Merger software performs at once the merging itself and the grouping of events from a given data type in time slices associated to another detector, saving computing time and data storage, and at the same time offers a flexible and simple way of correlating any of the 6-types of data aforementioned. The work flow is summarized in Fig. 3.10.

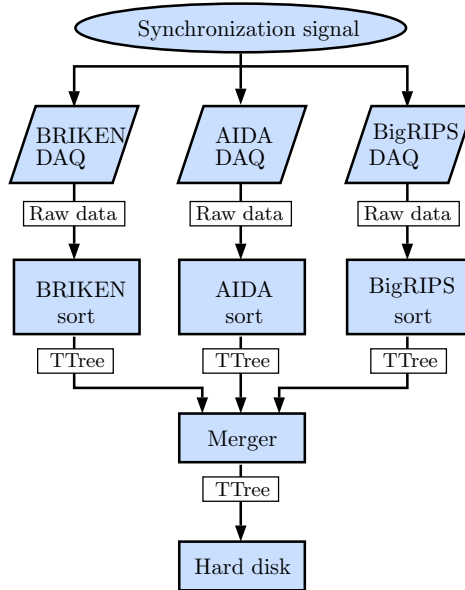


Figure 3.10: Merger FlowChart [Tol19]

During the experiments, the raw data from the three DAQs is periodically copied to a central server, where it can also be processed. To follow the entire Merger workflow takes as long as the data acquisition itself. This allows to process the data with a delay of one run (typically one or two hours), so it can be used as diagnostic tool during the measurements.

The keystone of the BRIKEN Merger software is the use of `maps`, a type of key-value associative data structure from C++ STL, as temporal key-ordered buffer for the data. Each file is read by an independent `thread`, from C++11 STL, and the data merging is carried out by a dedicated thread, which builds the time correlations and writes the output data stream in `TTree` format. Each output event corresponds to an input event plus up to six vectors, and each vector contains time-correlated events of certain type. Each time correlation window is set independently in the input configuration file for the BRIKEN Merger software². The main advantage of this output format is that each entry contains all the correlations that may be needed for the final analysis step, allowing an optimized and easy parallelizable processing. Merger program requires intensive CPU power, so GNU Parallel [Tan11] was used for automatic and controlled job scheduling.

The Merger performs also the association of an implant in AIDA with its particle

²For example, beta events entries can have a filled vector of correlated implant events; but the implant events may have empty vectors of correlated beta events

identification in BigRIPS, based on a specified time window coincidence. Given the huge number of pixels in AIDA, the time correlation of beta events with implants is spatially constrained. In order to speed up the merging process and reduce the size of output files, beta entries which are not correlated with any implant are not written in the output file.

3.5 Sort conditions

The Merger configuration file defines which vectors of time correlated data of a given event type will be filled for each entry. Since the time window needed for correlating betas and implants is up to tens of seconds, but the window needed to correlate beta with neutrons or ancillary is below a millisecond, beta entries are chosen to have all the correlated data needed to build decay curves required for the determination of half-lives and P_{xn} .

3.5.1 Implanted isotope identification

The radioactive isotopes are identified as they travel through the BigRIPS spectrometer, and finally are implanted in a DSSD of AIDA. Isotope identification of each implant is obtained from the closest time-correlated BigRIPS identification event. This assignation is done by the Merger program at run time, if BigRIPS data is available and if the time window for correlating implants and identification is properly set. Considering the time-correlation curve presented in Fig. 3.11, the time window used for the present work was from $-20 \mu\text{s}$ to $-5 \mu\text{s}$.

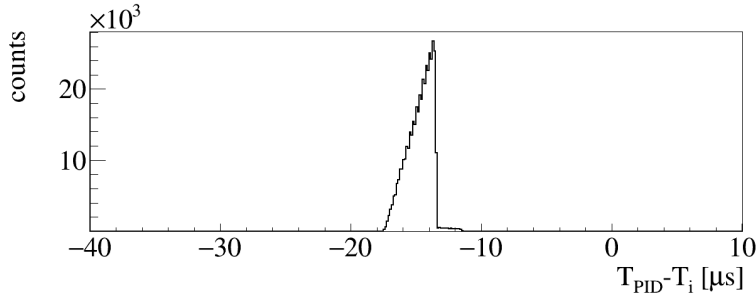


Figure 3.11: Time difference between particle identification events (BigRIPS) and implant events (AIDA).

3.5.2 Beta-implant correlation

Decay curves are built as time differences between the implant event and the subsequent decay events. The time correlation window used was $\pm 10 \text{ s}$, which

is wide enough to include more than ten half-lives of the parent nucleus of each decay chain. However, a previous spatial condition between implants and decays is used to reduce the accidental correlations. This position correlation is performed by the Merger program at run time.

As explained in Sec. 3.2, each AIDA event is characterized by a XY averaged centroid and a certain area, given by the strips which were triggered. The simplest approach is based on the distance between decay and implant XY centroids: the spatial correlation is accepted if the centroids are closer than a given distance and in the same DSSD. This procedure was used as a first approximation, but it was improved later on. Currently, the method implemented by the Merger software is based on the overlap of implant and decay areas: the correlation is accepted if the areas overlap or are contiguous, as shown in Fig. 3.12. As it is shown in Fig. 3.13, the typical area of beta and implant events is few strips wide, thus this spatial correlation is very stringent.

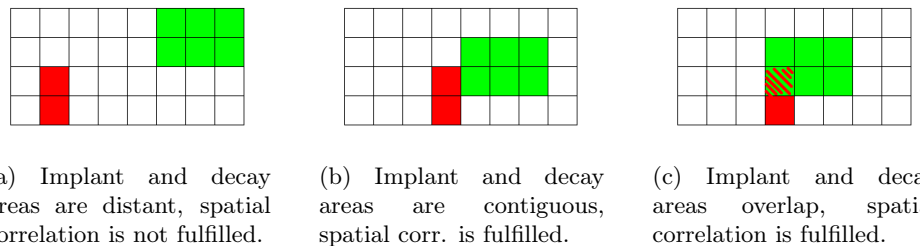


Figure 3.12: Different scenarios of implant-decay spatial correlation.

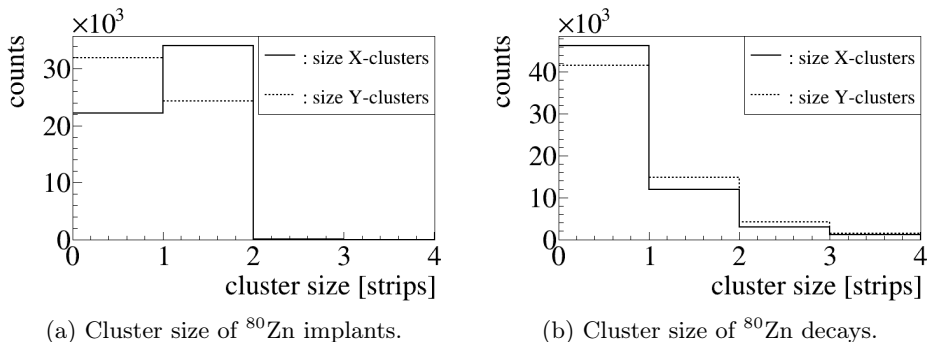


Figure 3.13: Size of X-clusters (continuous line) and Y-clusters (dashed line) of ^{80}Zn implants (left panel) and decays (right panel).

3.5.3 Beta-neutron correlation

Time differences among implants of certain isotope and spatially correlated decay events form the decay curve of that isotope. If beta decays are correlated with neutron events, neutron-gated implant-decay curves can be built. Given the long time needed by neutrons to be detected after their emission, a beta-neutron correlation window of 200 μs is used. Different neutron-gated decay curves are built according to the number of neutrons in this window: 1-neutron-gated decay curves and 2-neutrons-gated decay curves.

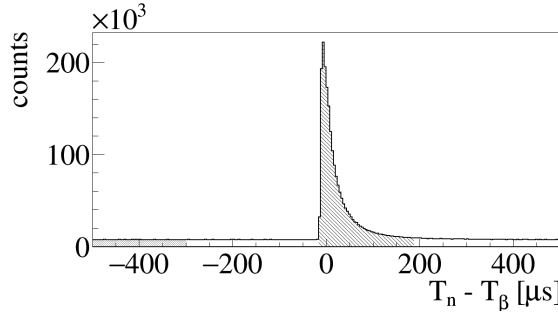


Figure 3.14: Beta-neutron time correlation curve for decays of ^{83}Ga . The neutron moderation extends up to 200 μs after the beta decay (central filled area). It is also shown a -500 μs to -300 μs widow used to determine accidental correlations.

The beta-neutron time correlation curve is shown in Fig. 3.14. A time-offset between AIDA and BRIKEN DAQs causes the moderation curve to start at -14 μs . A correlation window 200 μs long contains 98% of neutrons coming from the decay. This fraction has a small ($\approx 1\%$) isotopic dependency, which is included as part of the total uncertainty of the effective neutron efficiency. Both numbers come from a dedicated analysis. The idea of restricting the beta-neutron time correlation window is to reduce the amount of accidentally correlated neutron background.

The moderation curve is on top of a flat background, formed by random coincidences with background neutrons coming mainly from beam interactions and by beta-delayed neutrons that do not come from the same decay. These neutrons that do not come from the decay can gate a beta-implant correlation, creating an accidental background [Tol19]. The number of neutrons which do not come from the decay is obtained counting beta-neutron correlations backwards in time. A window from -500 μs to -300 μs was used for counting the number of these random neutrons for the results presented in this work.

Neutron multiplicity inside the beta-neutron correlation window, forward and backward with respect the decay event, for the ^{92}Se case is shown in Fig. 3.15. The backward window includes only accidental beta-neutron correlations, but forward window includes accidental correlations and beta-delayed neutrons.

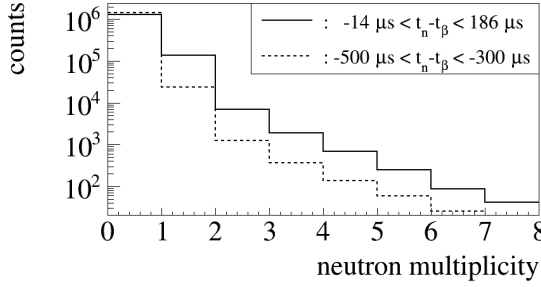


Figure 3.15: Number of neutrons (multiplicity) in a 200 μs long window, after a decay of ^{92}Se (solid line) or before (dashed line). Decays are temporally and spatially correlated with implants identified as ^{92}Se .

3.5.4 Vетос

The experimental setup includes several ancillary detectors, which register signals from the beam itself (the F11 plastic, the Si ΔE detector and the AIDA plastic) or generated by its interaction with materials (the VETO plastic detector); see Sec. 2.4.3 for further details. It was observed that certain BRIKEN neutron events and also some AIDA beta events are in time coincidence with the passage of the beam, and thus are not coming from a real radioactive decay. This represents a source of accidental time correlations contributing to the background. In order to improve the signal-to-noise ratio of decay curves, events correlated with the beam are vetoed.

Many neutron events are clearly correlated with the beam induced signals in the F11 plastic, as it can be seen in Fig. 3.16a. Beam-induced neutron background was reduced using a veto 200 μs long after every F11 plastic signal (gray filled area). The same F11 signal was also used to discard some beta events correlated with the beam, by applying 100 μs veto after an F11 signal. Fig. 3.16b represents the time correlation of beta events (that are also correlated with at least 1 implant) and F11 signals.

Application of this F11 signal as veto induce a certain dead time, which is paralyzable by construction. The live time factor of this veto f_{veto} is given by Eq. (3.5), that depends on F11 rate R and the length of the veto time window w .

$$f_{veto} = e^{-wR} \quad (3.5)$$

Fig. 3.17 shows the variation of the instant rate of the F11 plastic veto detector recorded along the RIBF127 experiment. The average rate is 252 Hz, leading to a veto live-time factor of 95.1% for neutrons and 97.5% for betas.

Accidental time correlations contributing to the background have other sources in addition to the beam. A small number of AIDA strips are quite noisy and may

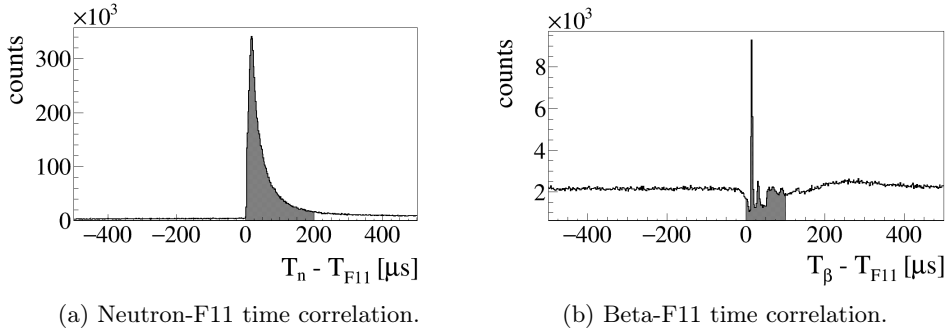


Figure 3.16: Beam correlated events: neutrons(left), betas (right).

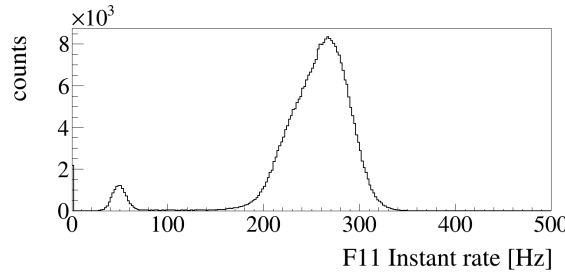
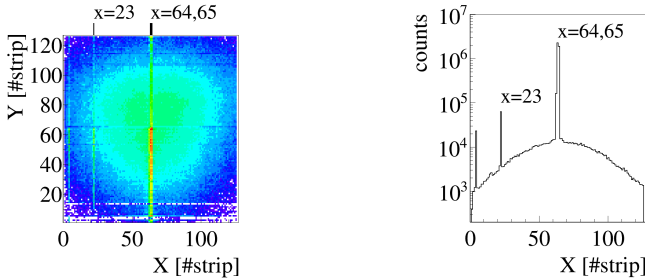


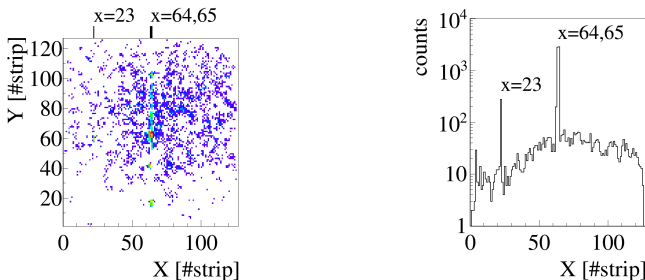
Figure 3.17: F11 instant rate during the RIBF127 experiment.

contribute up to 70% of the uncorrelated background of every decay curve, as can be seen for two arsenic isotopes in Fig. 3.18. This source is specially important in case of the less implanted species, whose decay curves may be buried below the background. Signal-to-noise ratio in all decay curves improve if these few noisy strips are removed at the final stage of the analysis. In Fig. 3.19 is presented the case of ^{92}As , where the uncorrelated background is reduced a factor ≈ 4 rejecting the beta events whose centroid is on the central strips or strip number 5 or 23.

A beam induced noise extending for an unexpected long time period was observed in the high gain AIDA branch during the RIBF127 experiment. It happens after every implantation and extends for up to 20 ms. This noise affects the implant-beta time correlation distribution at short times becoming a limiting factor for half-lives comparable to the extension of the noise. As it can be seen in Fig. 3.20, the mean energy of these noise events is ≈ 120 keV, so a beta energy threshold of 240 keV suppresses most of it. Although this high threshold reduces the beta efficiency by almost a factor 2, it cleans the decay curves off this implant-induced noise, necessary for obtaining new half-lives and reliable P_{xn} values. Later it was found that this noise originated in the design of the coupling cards of detector cables



(a) XY distribution of ^{88}As decays (left), and its projection on the X axis (right).



(b) XY distribution of ^{92}As decays (left), and its projection on the X axis (right).

Figure 3.18: XY distribution of decays of two arsenic isotopes (left), and its projection on the X axis (right).

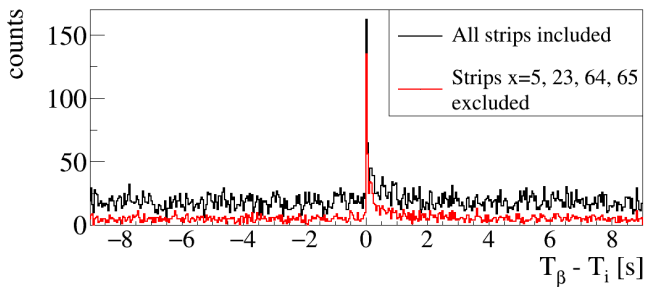


Figure 3.19: Effect of few noisy strips on the uncorrelated background of ^{92}As beta decay curve.

to the electronics. These cards have been changed for newer ones with improved design since then.

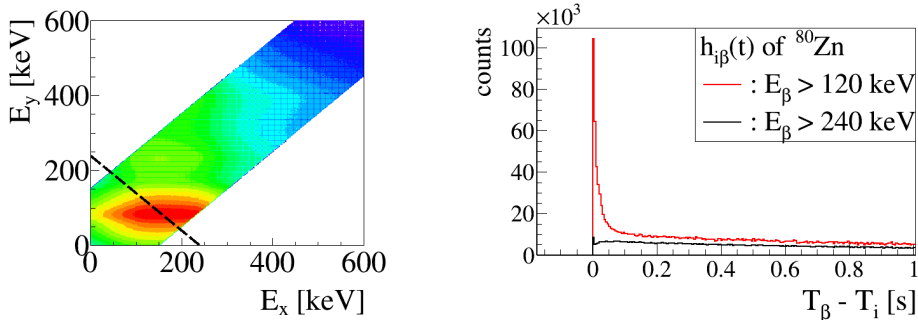


Figure 3.20: On the left, beta Y-cluster energy vs beta X-cluster energy. The energy cut was applied on the average cluster energy E_β at 240 keV (dashed line). On the right, the beta decay curve of ^{80}Zn obtained using different energy cuts. The implant-induced noise is contained in the first 50 ms after the implantation.

3.6 Isotope dependency of neutron efficiency

In Sec. 3.3.2, neutron detection efficiency curve of the BRIKEN detector obtained by Monte Carlo simulations was shown, and how the absolute detection efficiency value was experimentally validated using an intense uncalibrated ^{252}Cf neutron source.

The neutron efficiency used finally in the fits corresponds to the detection efficiency scaled by three factors, which have been discussed in previous sections. One factor is the BRIKEN DAQ live-time that was shown in Sec. 3.3.3 to be 99.90%. The other two scaling factors are caused by the offline analysis. On the one hand, the beta-neutron time correlation window of 200 μs which registers only 98(1)% of the total of truly correlated neutrons. On the other hand, the offline F11 plastic veto, which is used to reject beam induced background neutrons, affects also neutrons coming from the decay, resulting in a scaling factor of 95.1(3)% as determined in Sec. 3.5.4. Using the average value of the of the neutron efficiency up to 1 MeV and these correction factors, it is obtained an effective neutron efficiency $\bar{\varepsilon}_n$ of 62.3(21)% for decays with small and moderate $Q_{\beta n}$ windows where most of the neutrons are emitted with energies less than 1 MeV. However, this effective neutron detection efficiency cannot be applied for nuclei far away from the stability, in particular for the most exotic nuclei with the largest $Q_{\beta n}$ windows.

This can be seen in Fig. 3.21 which shows the calculated neutron detection efficiency ε_n as a function of average neutron energy $\langle E \rangle$ for a number of β -delayed neutron emitters for which the neutron spectrum has been measured. It is to be noticed that they represent the full set of nuclei with mass $A > 60$ for which this information is available. Thirty-four of these are fission products coming from the evaluation of M.C. Brady [Bra89] that includes ^{91}Br as the most exotic nuclei

$(Q_{\beta 1n} = 5.78 \text{ MeV})$. We have added $^{83,84}\text{Ga}$ ($Q_{\beta 1n} = 8.1 \text{ MeV}$ and 8.8 MeV) measured by Madurga et al [Mad16] and ^{252}Cf for comparison. As we observe in Fig. 3.21 the efficiency drops by 10% for ^{84}Ga . Since we have measured isotopes with $Q_{\beta 1n}$ reaching 12 MeV, all of them with unmeasured spectrum, it is clear that a way to extrapolate the neutron efficiency is needed. In Fig. 3.21 it is also shown the absolute neutron efficiency as function of neutron energy (blue line) which runs very close (maximum deviation of 0.5%) demonstrating that the approximation expressed in Eq. 3.6 can be safely used.

$$\langle \varepsilon_n(E) \rangle \approx \varepsilon_n(\langle E \rangle) \quad (3.6)$$

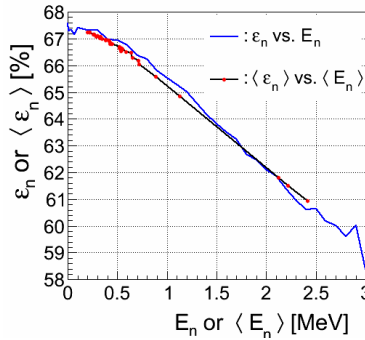


Figure 3.21: Comparison of detection efficiency as function of the neutron energy (solid blue), and the averaged efficiency as function of the averaged neutron energy of some measured neutron spectrum (red dots).

Nuclear theory calculations of beta strength distributions can provide apart from half-lives and P_{xn} values, the average energy of emitted beta-delayed neutrons if they are coupled with a Hauser-Feshbach statistical model of neutron emission [Möl19]. This average energy can be used in Eq. 3.6 to estimate the average neutron detection efficiency. In Fig. 3.22 the neutron efficiency under this approximation is shown as ratio to the nominal efficiency, taking the average neutron energies from Möller et al. [Möl19] for the nuclei investigated in this Thesis. Although the $Q_{\beta 1n}$ windows can be up to 12 MeV, the theoretical average neutron energy in [Möl19] is quite small and thus the derived neutron efficiency is close to the nominal value. In particular for $^{83,84}\text{Ga}$ where the neutron spectrum has been measured there is a large underestimation of the correction. It can be concluded that the calculations of [Möl19] are not useful in this respect.

A possible origin of the failure to predict the correct neutron spectrum is that the calculations tend to concentrate the strength in few theoretical levels. An alternative is to take a very simple model of the beta strength function often used in the past [Pap72], namely that the beta strength function $S_\beta(E_x)$ is constant

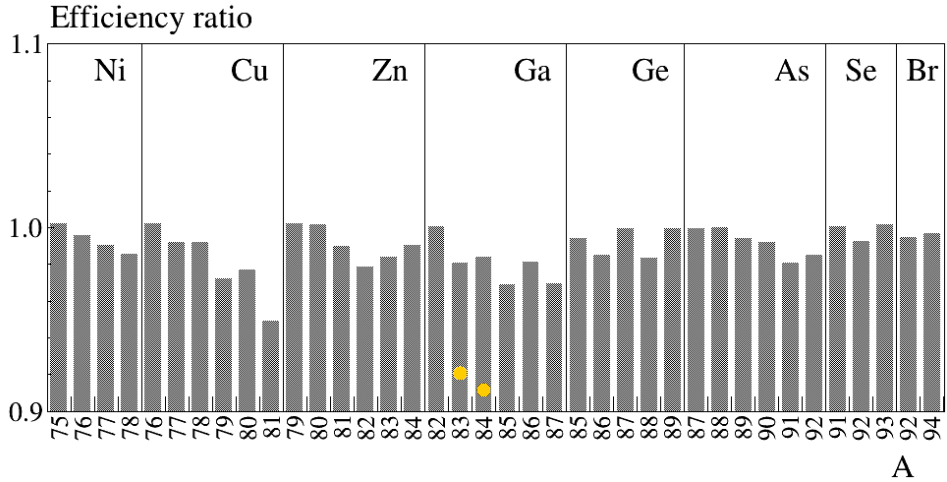


Figure 3.22: Neutron efficiency assuming Eq. (3.6), and normalized to the nominal value 66.8%. Values of average energy $\langle E_n \rangle$ are taken from [Möl19]. Neutron spectra of $^{83,84}\text{Ga}$ were measured by Madurga et al. [Mad16], and the corresponding neutron efficiency is marked with orange dots, presenting a large discrepancy with the theoretical value.

above S_{1n} . The average of neutron energy $\langle E_n \rangle$ is calculated as in Eq. (3.7), where $f(Z, Q_\beta - E)$ corresponds to the Fermi function. In this equation we further assume that all the excited levels above S_{1n} decay by neutron emission only to the ground state of the final nucleus with energy $E_n = E_x - S_{1n}$.

$$\langle E_n \rangle \approx \frac{\int_{S_{1n}}^{Q_\beta} (E_x - S_{1n}) f(Z, Q_\beta - E_x) dE_x}{\int_{S_{1n}}^{Q_\beta} f(Z, Q_\beta - E_x) dE_x} = \langle E_n \rangle (Q_{\beta 1n}) \quad (3.7)$$

Fig. 3.23 represents the average neutron energy calculated with this formula (blue points) showing that the dependency with $Q_{\beta 1n}$ is very well approximated by a linear relation (green line). Fig. 3.23 also compares them with the true value (red points) calculated with the measured neutron energy spectrum for the 36 β -delayed neutron emitters mentioned above [Bra89, Mad16]. We observe that the values scatter around this line but that they are basically all contained within the green dotted lines which represent a factor of 2 higher and lower with respect to the model calculation. This observation is the basis of our prescription to evaluate the neutron efficiency for the nuclei without measured spectrum and the associated systematic error based only on its $Q_{\beta xn}$ value. We use the Monte Carlo simulated

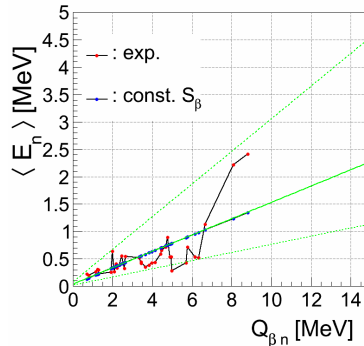


Figure 3.23: Experimental values [Bra89, Mad16] of averaged energy of beta-delayed neutrons versus the $Q_{\beta 1n}$ window. They show deviations up to a factor 2 with the model which assumes constant $S_\beta(E)$ in Eq. (3.7).

efficiency as a function of E_n (see Fig. 3.21) and the approximation represented by Eq. 3.7 to calculate the central value of the average efficiency (using the continuous green line in Fig. 3.23) and the maximum deviations (using the dotted green lines in Fig. 3.23). The result is represented in Fig. 3.24.

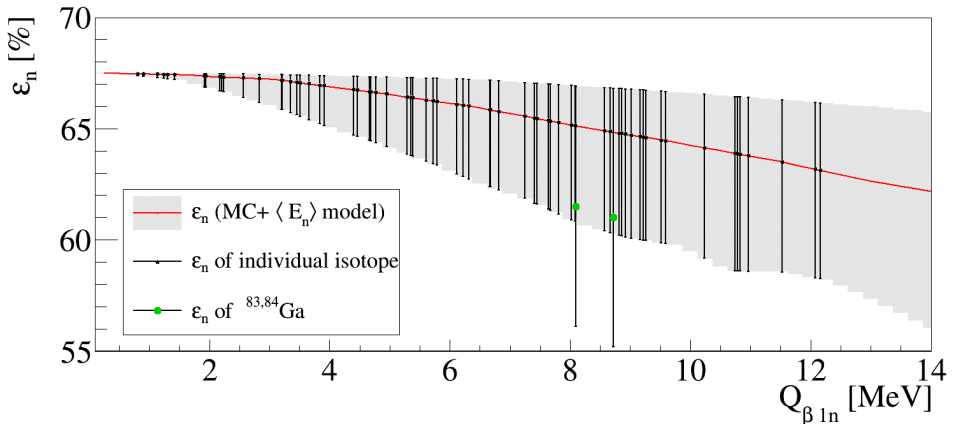


Figure 3.24: Calculated neutron detection efficiency as function of $Q_{\beta 1n}$. Each marker represents one isotope appearing in one or more decay chains. The efficiency error band (gray filled area) derives from the uncertainty range of the model which relates averaged neutron energy and $Q_{\beta 1n}$, shown in Fig. 3.23. Two green markers corresponds to the neutron detection efficiency of $^{83,84}\text{Ga}$ calculated using measured neutron energy spectra [Mad16] and MC simulated efficiency as a function of E_n .

Neutron detection efficiency of two-neutron beta decay mode is calculated using $Q_{\beta 2n}$ instead $Q_{\beta 1n}$. The result is plotted in Fig. 3.25. Neutron detection efficiency central values and uncertainties are given in App. B.

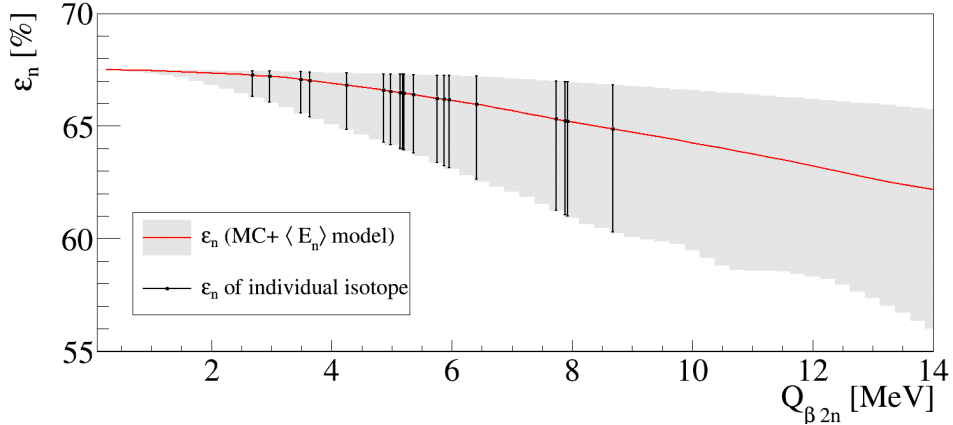


Figure 3.25: Calculated neutron detection efficiency as function of $Q_{\beta 2n}$. Each marker represents one isotope appearing in one or more decay chains. The efficiency error band (gray filled area) derives from the uncertainty range of the model which relates averaged neutron energy and $Q_{\beta 2n}$, shown in Fig. 3.23.

This isotope dependent neutron detection efficiency was used for the results presented in this work. Although the central value of the efficiency as function of $Q_{\beta 1n}$ does not deviates severely from the nominal value 66.8% even for the largest $Q_{\beta 1n}$, the ample error bars should ensure that any isotope dependency is within the error band.

3.7 Fitting procedure

This section is split into three parts. The first one is dedicated to the general fit function describing the activity of a decay chain. The second one explains two different ways of modeling the backgrounds, and therefore, two sets of fitting functions are presented in the last part of this section.

3.7.1 Beta activity functions

Half-lives and neutron emission probabilities are determined fitting the decay curves corresponding to implant-beta, implant-beta-1n and implant-beta-2n time-correlations, after correction for backgrounds. The case of ^{86}Ga is presented in Fig. 3.26.

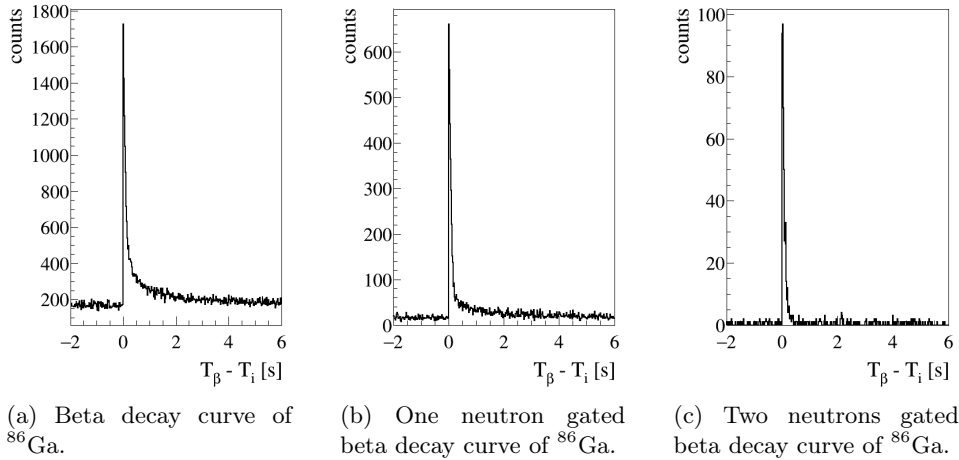


Figure 3.26: Decay-implant curves, without gating and 1n and 2n gated of ^{86}Ga .

Bateman equations [Bat10] describe the time evolution of individual abundances in a decay chain. The general solution, which include prompt production or divergences in the decay chain, is given in [Skr74]. However, it can be simplified if initially only the parent isotope of the decay chain is present and there is just decay (without production over time of any element in the chain). This is the situation that describes our data, so that the solution is represented by Eq. 3.8.

$$N_n(t) = N_1(0) \prod_{j=1}^{n-1} (\lambda_j b_{j,j+1}) \sum_{i=1}^n \sum_{j=i}^n \left(\frac{e^{-\lambda_j t}}{\prod_{p=i, p \neq j}^n (\lambda_p - \lambda_j)} \right) \quad (3.8)$$

The parameter N_n represents the number of isotopes of the n-th nucleus, and λ_n its decay constant. The branching ratio $b_{j,j+1}$ represents the fraction of decays that undergo a particular decay-mode with respect to the total of decays for a given isotope. In the present case, this number corresponds to the one neutron emission probability, P_j^{1n} , two neutron emission probability, P_j^{2n} , or zero neutron emission probability P_j^{0n} . Since the sum of all probabilities P_j^{xn} must be normalized, this last value is computed from the other neutron emission probabilities $P_j^{0n} = 1 - P_j^{1n} - P_j^{2n}$.

Depending on the extension of the decay network, the number of parameters in this function can be quite large. However in the fit only few parameters are varied. This includes the number of parent nuclei initially present $N_1(0)$, their neutron emission probabilities P_j^{xn} , and in case it is not well known the half-life. With a few exceptions the remaining parameters are fixed to the previously measured half-lives and neutron emission probabilities of all nuclei in the decay chain. These values are compiled by the *Reference Database for Beta-Delayed Neutron Emission Data* [BdN-IAEA].

The beta decay curve of a given parent isotope, built as implant-decay time correlations, is formed by the sum of the beta decay activity of each isotope in the decay chain plus a certain background. Since the activity is related to the number of isotopes by $A_i(t) = \lambda N_i(t)$, and taking into account the detector efficiencies, the total activity of the beta decay curve is given in Eq. (3.9a). $\overline{\varepsilon}_i^\beta$ corresponds to averaged efficiency weighted by β -intensity distribution, which was assumed to be the same for all the isotopes and decay channels as will be commented later. Similar activity functions are deduced for the 1 or 2 neutron-gated implant-decay curves, Eq. (3.9b) and (3.9c) respectively. In these cases, neutron averaged efficiency $\overline{\varepsilon}_i^{xn}$ must be also included using the isotope dependent parametrization described in Sec. 3.6. In Eqs. 3.9b-(3.9c) the index i represents all isotopes contributing to the respective beta-x-neutron branch.

$$A_\beta(t) = \sum_{i \in \beta} \overline{\varepsilon}_i^\beta \lambda_i N_i(t) \quad (3.9a)$$

$$A_{\beta 1n}(t) = \sum_{i \in \beta 1n} \overline{\varepsilon}_i^\beta \overline{\varepsilon}_i^{1n} P_i^{1n} \lambda_i N_i(t) \quad (3.9b)$$

$$A_{\beta 2n}(t) = \sum_{i \in \beta 2n} \overline{\varepsilon}_i^\beta \overline{\varepsilon}_i^{2n} P_i^{2n} \lambda_i N_i(t) \quad (3.9c)$$

3.7.2 Correlated and uncorrelated background

Decay curves are built as time difference of implants and spatially-correlated beta decays. In order to build the activity curve of a parent isotope in particular, implants identified as such are selected. So, time differences of an implant and its own decays form the activity curve, and the accidental time-correlations of an implant with non-physically correlated decay events constitute the uncorrelated background. Non-flatness of this background is caused by beam interruptions (in general, changes in beam intensity) which can also cause a forward-backward asymmetry in the background.

For this work, this type of background is modeled as linear in the region $t_{\beta i} < 0$, and mirrored in the region $t_{\beta i} > 0$. The linear-mirror approximation was validated building the time correlations between implants and non-spatially correlated (more than 10 strips away) decays in the same DSSD. Relative fit deviations Δ_{rel} are smaller than 0.5%, as can be seen for the case of ^{88}As which is shown in Fig. 3.27.

In addition to this uncorrelated background, neutron-gated decay curves present another kind of background [Tol19]. This one is originated by the correlation of a beta decay with one or more neutrons that do not come from the decay. In Sec. 3.5.3 it is explained how to obtain neutron multiplicity plots, counting the number of neutrons within the beta-neutron time-correlation window. Backward in time correlation (in this case, $t_n - t_\beta$ from -500 μs to -300 μs) include only neutrons

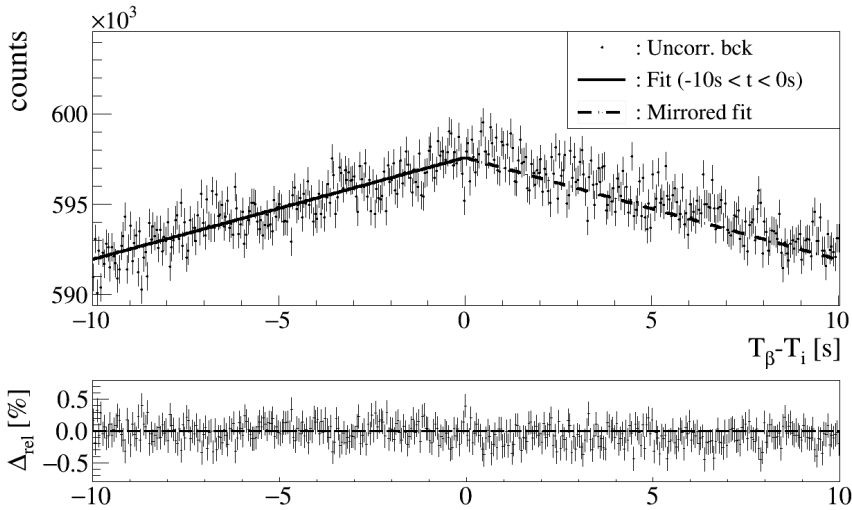


Figure 3.27: Uncorrelated background can be built as time differences of implants and decays spatially separated by more than ten strips. A linear fit is performed in the region $t_{\beta i} < 0$, and then mirrored for $t_{\beta i} > 0$.

not coming from the decay. The fraction of betas that are accidentally correlated with a certain number of neutrons is obtained from this backward multiplicity plot, normalized to the total number of beta-neutron correlations. The fraction of betas correlated accidentally with n random neutrons is represented by r_n . This quantity depends on the isotope, and can be used as a figure of merit to quantify the neutron background. Fig. 3.28 represents r_n values corresponding to the isotope ^{92}Se .

Beta-neutron forward in time correlations (in this case, $t_n - t_\beta$ from $-14 \mu\text{s}$ to $186 \mu\text{s}$) include not only neutrons coming from the decay, but also accidentally correlated background neutrons. Therefore, the 1n-gated and 2n-gated beta activity curves include this correlated background. There are two possibilities to obtain this type of background: from the experimental decays curves, or from analytic formulas for the activity given in Eqs. (3.9).

3.7.3 Definition of fitting functions

Let us consider the case of a decay chain with beta-delayed neutron emission up to one neutron. The accidentally correlated neutrons have two effects in the 1n-beta-implant curve $h_{i\beta 1n}(t)$, as it is shown in Eq. (3.10). On the one hand, term (a) represents the decays that are correlated with a neutron from decay plus an accidental background neutron, so the beta-1n activity $A_{\beta 1n}(t)$ given in Eq.

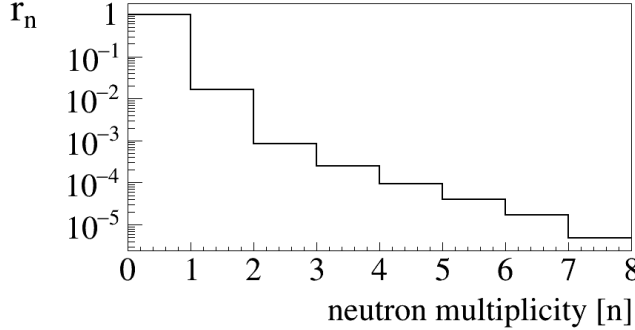


Figure 3.28: Fraction of ^{92}Se decay events that are correlated accidentally with a given number n of random neutrons. The fraction of betas that is correlated with zero random neutrons is $r_0 = 0.9825$. This plot corresponds to the neutron multiplicity of backwards beta-neutron time-correlations presented in Fig. 3.15, normalized to the number of correlations.

(3.9b) has to be scaled down by r_0 . This factor corresponds to the fraction of betas which is not correlated with any background neutrons, and in general is quite close to 1 (see Fig. 3.28). On the other hand, term (b) corresponds to decays without neutron emission that are accidentally correlated with one background neutron. The activity of this zero-neutron beta decay is the difference of beta decay activity and beta-1n decay activity, $A_\beta(t) - A_{\beta 1n}(t)$; the fraction of beta decays that are correlated with just one background neutron is given by the factor r_1 . The last term bck^u corresponds to the uncorrelated background described in Sec. 3.7.2.

$$h_{i\beta 1n}(t) = \underbrace{r_0 A_{\beta 1n}(t)}_{(a)} + \underbrace{r_1 [A_\beta(t) - A_{\beta 1n}(t)]}_{(b)} + bck_{\beta 1n}^u(t) \quad (3.10)$$

After grouping terms in Eq. (3.10), the fitting functions $f(t)$ including correlated background are presented in Eqs. (3.11). The model fit functions of the beta decay, beta-1n decay and beta-2n decay curves are $f_\beta(t)$, $f_{\beta 1n}(t)$ and $f_{\beta 2n}(t)$ respectively.

$$f_\beta(t) = A_\beta(t) + bck_\beta^u(t) \quad (3.11a)$$

$$f_{\beta 1n}(t) = (r_0 - r_1) A_{\beta 1n}(t) + r_1 A_\beta(t) + bck_{\beta 1n}^u(t) \quad (3.11b)$$

The fit function of the beta-1n activity $f_{\beta 1n}$ in Eq. 3.11b depends on the beta activity $A_\beta(t)$. The analytical function can be replaced by the experimental data, $A_\beta(t) = h_{i\beta}(t) - bck_\beta^u(t)$, in order to make the fit function of the 1n-beta decay curve depend only on the beta-1n activity $A_{\beta 1n}$, Eqs. (3.12).

$$f_\beta(t) = A_\beta(t) + bck_\beta^u(t) \quad (3.12a)$$

$$f_{\beta 1n}(t) = (r_0 - r_1)A_{\beta 1n}(t) + r_1 h_{i\beta}(t) + \widetilde{bck}_{\beta 1n}^u(t) \quad (3.12b)$$

The case of a decay chain with beta-delayed neutron emission up to two neutrons is detailed in [Tol19]. The corresponding fit functions are given in Eqs.(3.13).

$$f_\beta(t) = A_\beta(t) + bck_\beta^u(t) \quad (3.13a)$$

$$f_{\beta 1n}(t) = a_0 A_\beta(t) + a_1 A_{\beta 1n}(t) + a_2 A_{\beta 2n}(t) + bck_{\beta 1n}^u(t) \quad (3.13b)$$

$$f_{\beta 2n}(t) = b_0 A_\beta(t) + b_1 A_{\beta 1n}(t) + b_2 A_{\beta 2n}(t) + bck_{\beta 2n}^u(t) \quad (3.13c)$$

As we see both $f_{\beta 1n}(t)$ and $f_{\beta 1n}(t)$ depend on all beta activities $A_\beta(t)$, $A_{\beta 1n}(t)$ and $A_{\beta 2n}(t)$. As before we can make the fit function of the β -x-neutron channel dependent only on the β -x-neutron activity making use of the measured data as presented in Eqs. (3.14).

$$f_\beta(t) = A_\beta(t) + bck_\beta^u(t) \quad (3.14a)$$

$$f_{\beta 1n}(t) = p_0 h_{i\beta} + p_1 A_{\beta 1n}(t) + p_2 h_{i\beta 2n}(t) + \widetilde{bck}_{\beta 1n}^u(t) \quad (3.14b)$$

$$f_{\beta 2n}(t) = q_0 h_{i\beta} + q_1 h_{i\beta 1n}(t) + q_2 A_{\beta 2n}(t) + \widetilde{bck}_{\beta 2n}^u(t) \quad (3.14c)$$

Summarizing, the correlated background can be built in two different ways: as linear combination of the experimental decays curves, or as a linear combination of the analytic formulas for the activity. The first approach set a fixed background during the fitting procedure. The later method implies that the correlated background has to be calculated for each step during the minimization, but in return is more reliable for the less implanted cases, since the analytical correlated background does not introduce additional statistical fluctuations. The results presented here use both methods: analytical correlated background was used to obtain the central values, and the experimental correlated background was used for the Monte Carlo error propagation stage in order to reduce the computation time to reasonable levels.

As said before, parameters in model functions are known (and therefore constant during the fitting procedure) except the number of parent isotope decays $N_1(t=0)$ and its P_{xn} values. In some cases, also parent half-life is unknown or the literature value can be improved. These parameters are obtained from simultaneous fit of the beta decay, 1-neutron gated beta decay, and in some cases 2-neutron gated beta decay, using **ROOT::Fit** classes [Mon08]. A negative log-likelihood estimator **PoissonLLFunction** is created for each decay curve that has to be fitted, from the decay curve itself and the corresponding model function. A global

negative log-likelihood estimator, built as sum of the individual estimators, is minimized in order to obtain the unknown parameters using the built-in function **Fitter::FitFCN**. The chosen minimizer was **MIGRAD**, from **MINUIT2** library.

The parameters of the model functions can be classified into two groups. The chain parameters correspond to half-lives and branching ratios of every isotope in the decay chain, which have been previously measured [BdN-IAEA], and the corresponding beta and neutron efficiencies. Beta efficiency is assumed to be the same for all the isotopes and decay modes. The neutron efficiency that appears in Eqs. (3.9a) – (3.9c) corresponds to the neutron detection efficiency obtained in Sec. 3.6 scaled down by live-time factors. The uncorrelated background parameters, which are determined before the fitting procedure, and the correlated background, which are calculated from the neutron multiplicities (cf. Sec. 3.7.2), are fixed during the fitting process.

3.7.4 Uncertainty estimation

During the fitting procedure most of the parameters are fixed: the term of the uncorrelated background, the random neutron correlation factors r_n required for computing the correlated background, neutron efficiencies and most of neutron branching ratios and half-lives of the decay chain. The fitter uses **MINOS** [MINOS] to calculate an uncertainty which reflects the statistics (statistical uncertainty), based on the model functions and the experimental data. Although **MINOS** gives asymmetric uncertainties, σ_- and σ_+ , their relative difference Δ_S (calculated as in Eq. (3.15)) is smaller than 1% for most of the cases.

$$\Delta_S = \frac{|\sigma_+| - |\sigma_-|}{|\sigma_+| + |\sigma_-|} \quad (3.15)$$

The exception are the less implanted isotopes (^{75}Co , ^{78}Ni , ^{81}Cu , ^{84}Zn , ^{87}Ga , ^{89}Ge , ^{92}As and ^{94}Br), which have a relative asymmetry Δ_S between 1% and 10%. Since asymmetry is small, the statistical uncertainty quoted in Chap. 4 corresponds to the average of asymmetric uncertainties provided by **MINOS**.

The uncertainty of all the fixed parameters is propagated using Monte Carlo method, resulting in systematic uncertainty. This method consist in repeating the fitting procedure many times, varying all these fixed parameters within their uncertainty in each iteration. Half-lives, neutron emission probabilities and correlated background factors r_i are sampled as independent Gaussian distributions. The uncorrelated background is modeled as linear, so each pair of slope and intercept is sampled as a bi-variate Gaussian distribution, taking into account their correlation. Individual neutron efficiencies obtained as in Sec. 3.6 are sampled following a square distribution. The fitted parameters follow a bell-like distribution, which is mostly centered at the value obtained using the central values of all the fixed parameters. Uncertainty of global factors which scale the neutron efficiency is sampled as an independent Gaussian distribution.

Systematic uncertainty of a given parameter is obtained from the dispersion of the values obtained from the fit. In general, the mean value of the distribution is close to the central value, and therefore this distribution is fitted by a Gaussian function, and its width σ corresponds to the systematic uncertainty. The total uncertainty is the squared sum of the systematic uncertainty, which is calculated using the Monte Carlo method just explained, and the statistical uncertainty given by the fitter.

3.8 Summary

The analysis method can be summarized as follows. Firstly, BigRIPS, AIDA and BRIKEN data is merged. Then, decay curves for each nuclide are built as time difference between spatially-correlated decays and implants identified as such nuclide. Neutron-beta decay curves are built if one (or two) neutron are time correlated with the beta decay. An ancillary signal is used to reduce the neutron and beta beam-induced background. Correlated background is experimentally determined from backward neutron-beta decay time-correlations.

Neutron branching ratios P_{xn} of a given nuclide are obtained from a simultaneous fit of its beta decay and beta-neutron decay curves. In some cases, its half-life is also obtained. Systematic errors originated by fixed parameters of the fit function are calculated using a Monte Carlo method. All the decay curves are built in a range from $t_\beta - t_i$ from -10 s to 10 s. The bin size of the decay curves was optimized in order to fulfill two requirements: it has to be sufficiently smaller than the parent half-life, and at the same time, wide enough to prevent statistical fluctuations from hiding a defect of the fit.

The uncorrelated background is modeled as linear, or flat in cases of low statistics, in the range $t_\beta - t_i$ from -10 s to 0 s and then mirrored in the fit range. The fit range corresponds to $t_\beta - t_i$ from 0 s to 10 s. In few cases, the fit range starts few tens of milliseconds after 0 s in order to avoid a bump that appears in the beta-implant decay curves around 20 ms, which is caused by an implantation noise in AIDA and mostly removed by using a high energy threshold on beta-decay events. The correlated background that appears in 1n-decay and 2n-decay curves is calculated experimentally from the number of neutrons correlated backwards in time with betas.

Chapter 4

Experimental results

This chapter introduces the results corresponding to the nuclei produced during the RIBF127 experiment (May 2017), plus re-analysis of four isotopes implanted during the commissioning of Beta-delayed neutrons at RIKEN (BRIKEN) (November 2016), obtained following the analysis method described in Chap. 3. The first part of this chapter presents detailed results of four isotopes that serve to exemplify the variety of cases encountered. Tables with P_{xn} and $T_{1/2}$ obtained for all the nuclei analyzed in this Thesis work are presented at the end of this chapter. These results are obtained applying a threshold of 240 keV on energy of decay events. This high threshold grants a better signal-to-background ratio and mostly eliminates the implant induced noise, which causes a bump at the beginning of decay curve around $T_\beta - T_i \approx 20$ ms. Even so, results presented here are consistent with an analysis using 120 keV threshold on energy of decay. In case of lower threshold, half-life extraction from the fit is affected by the implant-induced noise, which forces to exclude the first 20-100 ms at the beginning of all the decay curves.

The trade-off of using a 240 keV threshold is a reduction of the effective beta efficiency by almost a factor two when compared to using 120 keV instead. An experimental average beta efficiency can be calculated from the number of decays given by the fit. For each decay chain, it is assumed a constant effective beta efficiency in the beta decay and beta-neutron activities for all the isotopes and decay modes, so the number of parent decays obtained from the fit N_1 corresponds to the amount of implants N_{imp} scaled down by an effective beta efficiency $\overline{\varepsilon_\beta}$. This relationship is used to compute an effective beta efficiency as in Eq. (4.1). Experimental values for the average beta efficiency are provided in Appendix A.

$$\overline{\varepsilon_\beta} = \frac{N_1}{N_{imp}} \quad (4.1)$$

A side effect of the energy threshold on the beta events is to introduce a dependency of the beta efficiency with the isotope and decay mode [Agr16]. Since decays are detected by the same Double-sided Silicon Strip Detector (DSSD) where the radioactive isotope is implanted, the beta efficiency also depends on the implantation depth. This systematic effect causes the fit functions to overestimate

the experimental decay curves at their beginning $T_{\beta i} < 1\text{s}$ as was explained in [Tol19]. Some preliminary results were presented in that work, but using a different method than the one used in this Thesis work. In that previous work, since the effect seems to be related to the beta efficiency of the parent isotope, the beta efficiency was fitted together with neutron emission probability and the number of parent decays. However, further analysis show that fitting the beta efficiency introduces a systematic effect. Thus we decided to use the same beta efficiency for all isotopes. The fact that the results with 120 keV beta threshold and 240 keV beta threshold are consistent within uncertainties, as mentioned earlier, supports this approach.

A second experiment in the region of ^{78}Ni was performed later in November 2017. The BigRIPS spectrometer setting was different from the one used during RIBF127, however more than twenty isotopes appeared in both experiments with good statistics. In this experiment the Wide-range Active Silicon-Strip Stopper Array for Beta and ion detection (WAS3ABi) [Nis13] was used as implant and decay detector, instead of Advanced Implantation Detector Array (AIDA) detector, which was used during the RIBF127 experiment. The WAS3ABi detector is somewhat simpler, with a reduced number of strips (16 instead of 128 per DSSD side) that makes easier to set a reduced beta threshold. As a consequence the efficiency effect is smaller than with AIDA. Results from both experiments, obtained keeping a fixed beta efficiency, agree within the uncertainties. This further supports our new approach and therefore it is concluded that this issue do not affect the results presented in this Thesis work.

4.1 ^{86}Ge . High statistics case.

The most implanted isotope in AIDA during the RIBF127 BRIKEN experiment is ^{86}Ge , with a total of six million identified implants. Its decay chain, presented in Fig. 4.1, has three beta-delayed neutron emitters: the parent nucleus and its descendants $^{85,86}\text{As}$.

Half-lives and P_{xn} values of all isotopes in the decay chain have been previously measured [BdN-IAEA]. The previous half-life measurements of ^{86}Ge are 221.6(11) ms [Xu14a] and 226(21) ms [Maz13]. Although the evaluation [BdN-IAEA] accepts only the second value, the first one, with a much smaller uncertainty, was used for the fit. The previous measurement of the parent P_{1n} is 45(15)% [Mie13b]. This value was obtained from ^{86}Ga gamma decay, together with P_{xn} values of ^{86}Ga .

A simultaneous fit of beta decay and one-neutron-beta decay curve, shown in Fig. 4.2, gives P_{1n} and number of ^{86}Ge decays. The other parameters of the decay chain are fixed during the fit. As can be observed in the lower part of the figures there is a relative deviation of up to 5% between data and fit function that we interpret as the result of the beta efficiency dependency with isotope that is not

4.1. ^{86}Ge . High statistics case.

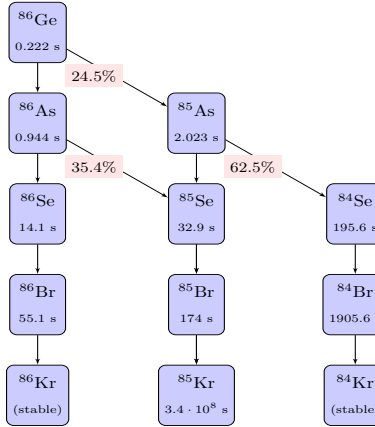


Figure 4.1: ^{79}Zn decay chain.

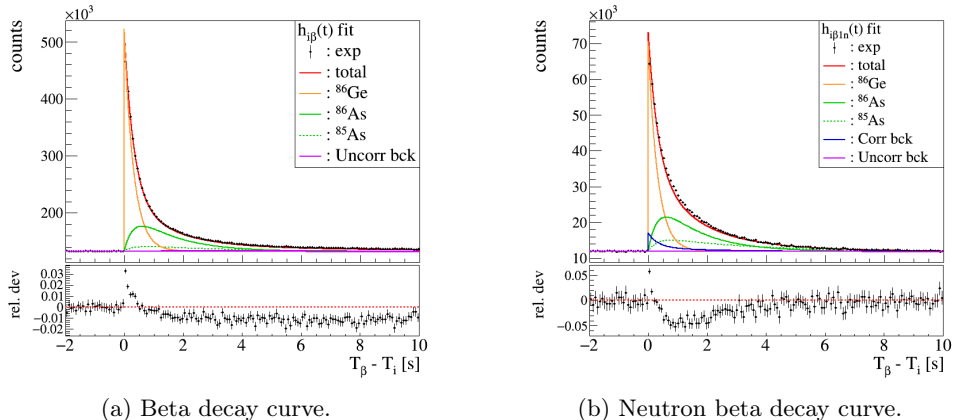


Figure 4.2: Result of the simultaneous fit of the beta decay and beta-one-neutron decay curves.

taken into account for the reasons explained in the previous chapter. This effect is clearly visible in this case because of the very high statistics. Parent half-life and one-neutron emission probability are presented in Tab. 4.1.

The energy window for two neutron emission $Q_{\beta 2n}$ of ^{86}Ge is 0.3 MeV, hence no two-neutron emission is expected with such small window. If the fit function includes parent two-neutron beta-delayed emission, it results in a slightly increase of P_{1n} to 25.0(12)% and P_{2n} value of 0.0(1)%. In Fig. 4.3 the simultaneous fit to the three decay curves is presented. The small difference in P_{1n} values, between

^{86}Ge	Value	σ^{total}	σ^{stat}	σ^{syst}	[BdN-IAEA]
$P_{1n} [\%]$	24.52	1.19	0.11	1.19	45(15)% [Mie13b]
$T_{1/2} [\text{ms}]$	—	—	—	—	221.6(11) ms [Xu14a]

 Table 4.1: Half-life and P_{1n} of ^{86}Ge .

including or not the beta-2n decay curve in the fitter, is caused by the method, which computes the correlated background of beta-2n decay curve from beta and beta-1n activities and thus the fitter optimizes the P_{1n} value in order to fit also the correlated background of this extra curve. The method which builds the correlated background from the experimental decay curves gives the same P_{1n} value either two-neutron emission is included or not, because it decouples the P_{1n} from the fitting function of the beta-2n decay curve. A null P_{2n} is obtained using both methods. Notice that beta-2n decay curve is only formed by correlated background.

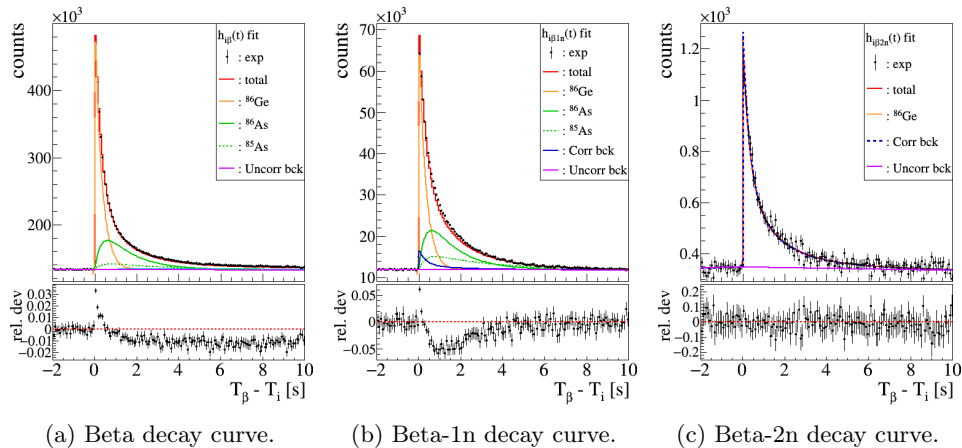


Figure 4.3: Result of the simultaneous fit of the beta decay, beta-one-neutron decay and beta-two-neutron decay curves.

4.2 ^{79}Zn . Sensitivity limit to small P_{1n}

In beta-neutron decay curves, correlated background can be a contribution larger than the number of beta-delayed neutrons, if neutron emission probabilities P_{1n} in the decay chain are small. In order to show the relevance of corrections for correlated background, ^{79}Zn decay is chosen, since it is a weak neutron emitter. Its daughter ^{79}Ga , which is even a weaker neutron emitter with $P_{1n} = 0.084\%$, is the

4.2. ^{79}Zn . Sensitivity limit to small P_{1n}

other neutron emitter in the decay chain, so the number of beta-delayed neutrons mainly come from ^{79}Zn decays.

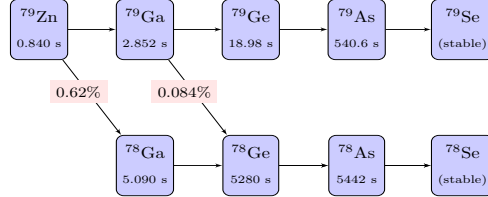


Figure 4.4: ^{79}Zn decay chain.

Half-life of ^{79}Zn has been measured several times in the last 50 years, reporting progressively lower values: 3.00(9) s [Gra74], 2.63(9) s [Rud76], 1.0(1) s [Eks86], 0.995(19) s [Kra91], 0.746(42) s [Hos10]; this last value is adopted by the current data evaluation [BdN-IAEA]. There are two previous measurements of its P_{1n} : 1.3(4)% [Kra91], and 2.2(14)% [Hos10]. The recommended value by the new evaluation is the unweighted average of these two measurements, 1.75(45)% [BdN-IAEA].

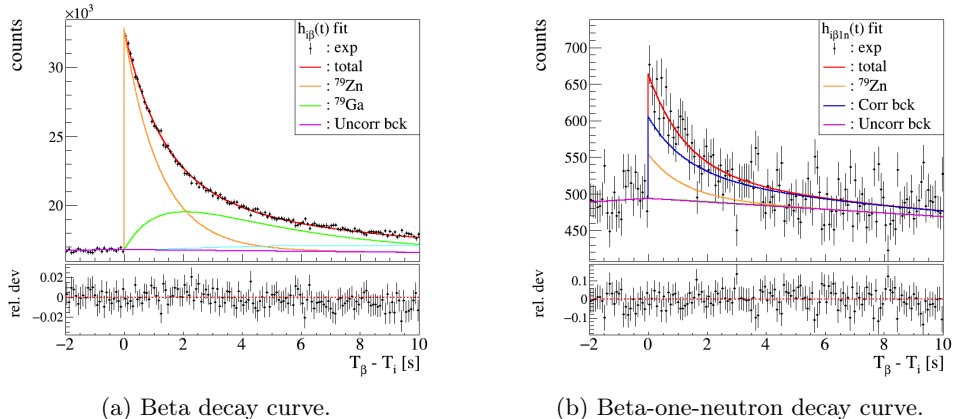


Figure 4.5: Result of the simultaneous fit of the beta decay and beta-one-neutron decay curves.

A total of 807 thousand ^{79}Zn nuclei were implanted during the BRIKEN commissioning. As it can be seen in Fig. 4.4, most of beta-delayed neutrons come from parent decays. Half-lives of the descendants are well known [BdN-IAEA], and therefore are fixed during the fit. No isomers are reported for any of the nuclides in the decay chain.

Fig. 4.5 shows ^{79}Zn decay curves, and the corresponding fit. In this case we included the parent half-life as a parameter in the fit. The main contributions in the beta decay curve come from the parent decays and its daughter ^{79}Ga . The beta-one-neutron decay curve is formed by several components. Uncorrelated background was modeled as linear for both decay curves. The fraction of betas that is correlated accidentally with one background neutron is $r_1 = 0.00704(4)$. According to the fit, the number of beta-delayed neutrons coming from ^{79}Zn is 907, and its daughter ^{79}Ga contributed with another 107, whereas the total counts of correlated background is 3432. Each component is mounted on the uncorrelated background, which is subtracted before integrating the aforesaid quantities. Values obtained from the fit are presented in Tab. 4.2, and compared with the current data evaluation. Systematic uncertainty is obtained from a Monte Carlo propagation of uncertainties of half-lives and P_{1n} of every element in the decay chain, neutron efficiencies and backgrounds. As can be observed our P_{1n} value is about one-third of the value in the evaluation and our half-life is 12% higher than in the evaluation.

^{79}Zn	Value	σ^{total}	σ^{stat}	σ^{syst}	[BdN-IAEA]
$P_{1n}[\%]$	0.62	0.17	0.13	0.10	1.75(45)
$T_{1/2}[\text{ms}]$	839.13	7.50	7.12	2.37	746(42)

Table 4.2: Half-life and P_{1n} of ^{79}Zn .

Fig. 4.6 shows ^{79}Zn decay curves, and the corresponding fit without correction for this correlated background. The fit for the beta decay curve does not change significantly, but the fit of the beta-one-neutron activity is slightly worse, increasing its χ^2/ν from 1.36 to 1.56. Without a correction for this correlated background, the value P_{1n} obtained is 2.06%. It is almost 4 times larger than if the correlated background is included, whereas the half-life is 843 ms, quite close to the value obtained including the correction for the correlated background. In this particular case, disregarding the correlated background changes dramatically the P_{1n} value, although it has a small effect in the goodness of the fit (value of χ^2/ν) and the half-life. The correlated background has the same shape as the beta decay curve, whose main contributor is the parent isotope ^{79}Zn and its daughter ^{79}Ga . The beta-one-neutron decay curve is determined by the same isotopes (in a different proportion), so the main effect of not taking into account the correlated background is mainly reflected in a much larger P_{1n} .

It can be concluded that a fit without taking into account such correlated background would result in hugely overestimated P_{xn} values. In addition, this type of background can be a limiting factor for determining small P_{xn} values.

4.3. ^{93}Se . Sensitivity limit to small P_{2n}

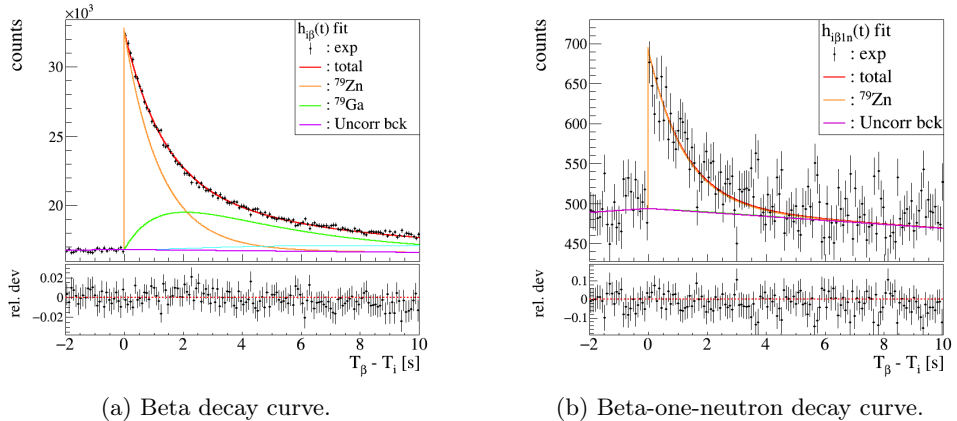


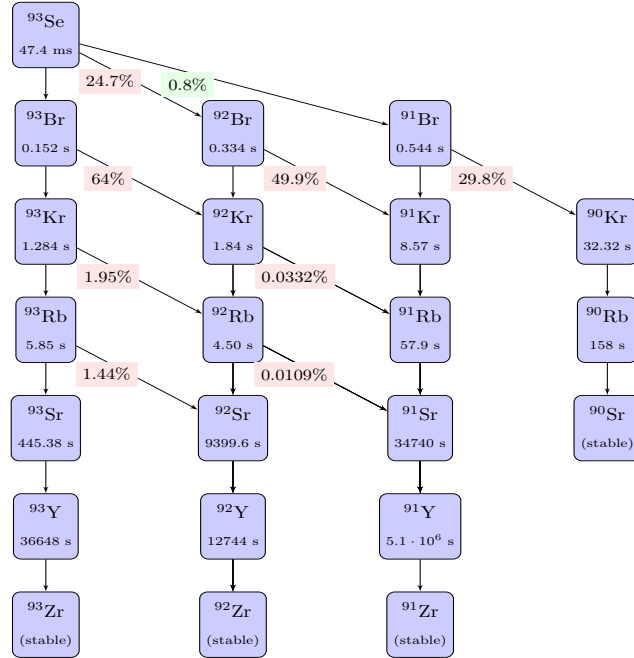
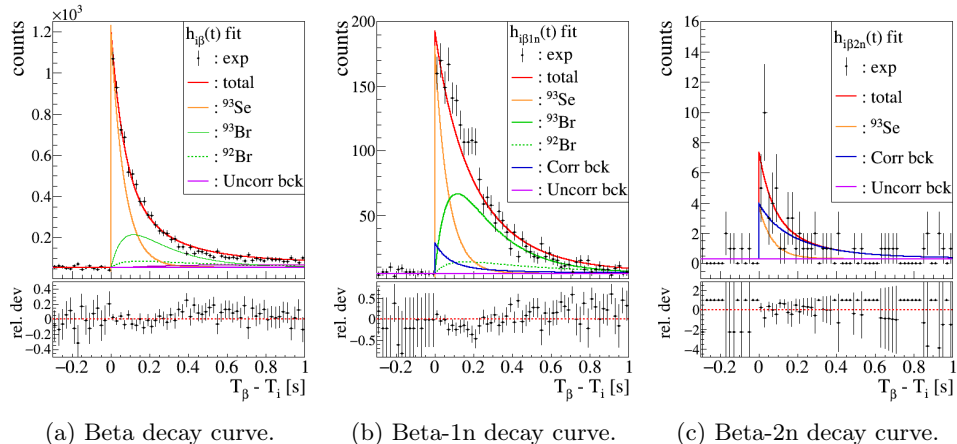
Figure 4.6: Result of the simultaneous fit of the beta decay and beta-one-neutron decay curves, disregarding the correlated background.

4.3 ^{93}Se . Sensitivity limit to small P_{2n}

A table with all the half-lives and P_{xn} of the nuclei studied in this Thesis work can be found at the end of this chapter. As it can be seen in Tab. 4.6, which presents all the P_{2n} obtained in this Thesis work, most of them are around 1%. Therefore, corrections for correlated background are critical for a proper determination of P_{2n} values. The case of ^{93}Se is one of many examples with a small P_{2n} , and a complex decay chain where the parent nucleus is the only two-neutron beta-delayed emitter. Fig. 4.7 shows the decay chain of ^{93}Se . Although there are eight beta-delayed neutron emitters, the major contributions come from the parent and its daughters $^{92,93}\text{Br}$.

As it can be seen in the fit of the decay curves presented in Fig. 4.8, correction for correlated background is the major contribution to the beta-2n decay curve, while in the beta-1n decay curve the correction is a proportionally smaller contribution. The fraction of betas that are accidentally correlated with one background neutron is $r_1 = 0.0167(5)$, and the fraction of betas correlated accidentally with two neutrons is $r_2 = 0.00077(10)$.

Fit results are shown in Tab. 4.3. Half-life, P_{1n} and P_{2n} of ^{93}Se are reported here for the first time. Similarly to the case of ^{79}Zn , if the corrections for correlated background are not taken into account, the fitter compensates the lack of this component with an increase of the beta-delayed neutron emission probabilities. The values of P_{1n} and P_{2n} obtained disregarding the correlated background are 10% and 180% larger. Even the determination of the half-life is affected, obtaining a 2% bigger value, since the main components of the beta-1n and beta-2n decay


 Figure 4.7: ^{92}As decay chain.

 Figure 4.8: Result of the simultaneous fit of ^{93}Se beta decay, beta-one-neutron decay and beta-two-neutron decay curves.

curves come from parent decays. The value χ^2/ν of beta-1n decay curve increases from 1.59 to 1.67, although the χ^2/ν value corresponding to beta and beta-2n decay curves does not change significantly.

^{93}Se	Value	σ^{total}	σ^{stat}	σ^{syst}	[BdN-IAEA]
P _{1n} [%]	24.67	3.71	2.55	2.69	–
P _{2n} [%]	0.79	0.63	0.62	0.07	–
T _{1/2} [ms]	47.40	1.96	1.63	1.10	–

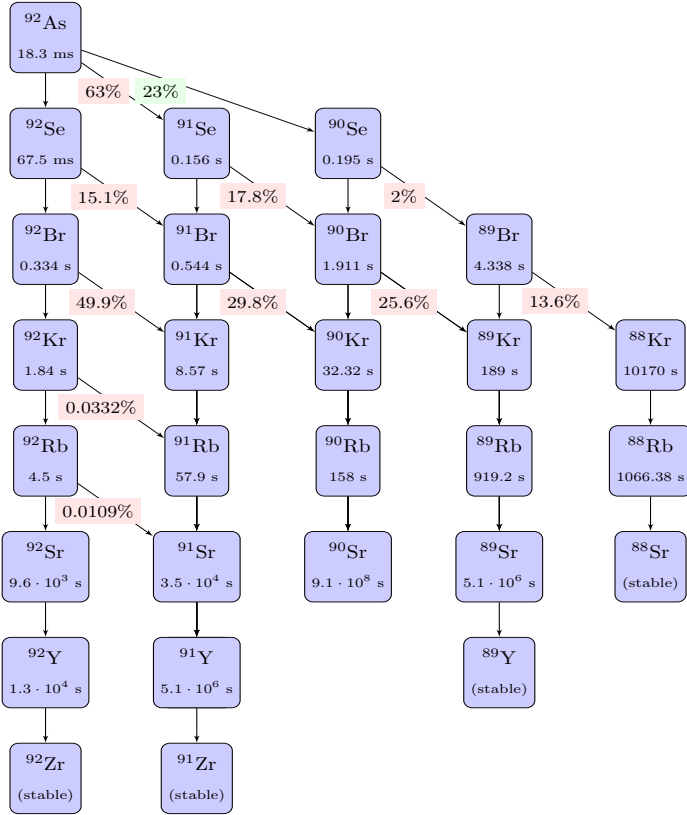
Table 4.3: Half-life and P_{1n} of ^{93}Se .

4.4 ^{92}As . Sensitivity limit to small number of implants

A total of 658 nuclei were identified as ^{92}As by BigRIPS and afterwards implanted in AIDA during the BRIKEN experiment RIBF127. The decay chain of ^{92}As , shown in Fig. 4.9, has ten beta-delayed neutron emitters. Only the parent nucleus, which has a Q _{β 2n} of 8.7 MeV, is expected to have significant two-neutron beta-delayed emission. Its daughters, ^{92}Se and ^{91}Se have Q _{β 2n} values of 1.5 MeV and 1.1 MeV respectively. These nuclei were also implanted, and therefore studied in this Thesis work, finding null P_{2n} values. There is only one previous ^{90}Se half-life measurement, $195^{(+95)}_{(-65)}$ ms [Qui12]. There is no previous measurement of its P_{1n}, although the energy window Q _{β 1n} is 4.4(3) MeV, large enough to expect beta-delayed neutron emission. Theoretical calculations by Möller et al. [Möll19] predict a value of 2%. This value was used in the fit function as a fixed parameter. For the evaluation of the systematic uncertainties, this parameter was sampled uniformly between 0% and 4%, instead of a Gaussian function like the rest of fixed parameters. Although uncertainties of ^{90}Se half-life and P_{1n} are large, they have little impact on the results.

The main contributions to the beta-one-neutron decay curve are from the parent nucleus ^{92}As and one of its grand-daughters, ^{91}Br , which is originated by either beta-1n decay of ^{92}Se or beta decay of ^{91}Se . The only contributor to the beta-2n decay curve is the parent nucleus.

The beta decay, beta-one-neutron and beta-two-neutron decay curves of ^{92}As are show in Fig. C.33. Correlated background is smaller than the number of beta-delayed neutrons in both beta-neutron decay curves. The number of beta-one-neutron is 105 counts, of which 61 are from ^{92}As and 16 from ^{91}Br . These total numbers are obtained integrating the beta-one-neutron activity over the fitting range, for $t_\beta - t_i$ from 0 s to 10 s.


 Figure 4.9: ^{92}As decay chain.

The simultaneous fit of the decay curves in Fig. C.33 provides for the first time $T_{1/2}$, P_{1n} and P_{2n} of ^{92}As . The results are presented in Tab. 4.4. This case probes that with less than one thousand implants it is possible to measure P_{xn} values of the order of 10-60% and $T_{1/2}$ of the order of tens of milliseconds.

^{92}As	Value	σ^{total}	σ^{stat}	σ^{syst}	[BdN-IAEA]
$P_{1n}[\%]$	62.94	16.25	15.97	2.98	-
$P_{2n}[\%]$	23.02	9.75	9.61	1.63	-
$T_{1/2}[\text{ms}]$	18.30	2.93	2.92	0.30	-

 Table 4.4: Half-life and P_{xn} of ^{92}As .

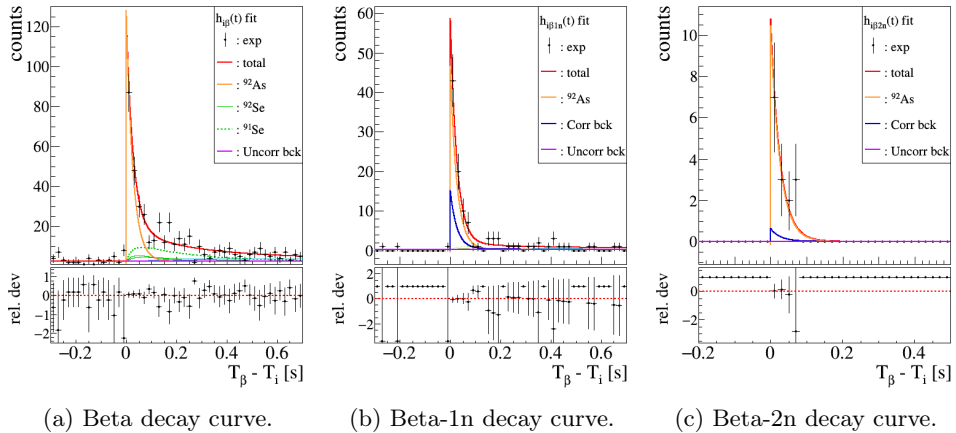


Figure 4.10: Result of the simultaneous fit of ^{92}As beta decay, beta-one-neutron decay and beta-two-neutron decay curves.

4.5 Summary and selected results

One-neutron branching ratios P_{1n} of every nuclide studied in this Thesis are gathered in Tab. 4.5. These are a total of 39 P_{1n} values, of which 12 have been determined for the first time and 27 have greatly improved values. All of them but four were produced during the BRIKEN experiment RIBF127. Two nuclides, ^{87}As and ^{92}Br , have a previously measured P_{1n} which is not compatible with our data, as they result in very poor fits of the respective decay curves. These nuclei are daughters of two implanted nuclides, ^{87}Ge and ^{92}Se respectively, but were not themselves implanted during the BRIKEN RIBF127 experiment. Our conclusion is that the previous P_{1n} values are incorrect. In these cases, P_{xn} of the parent nuclei, as well as P_{1n} of its daughter, are fitted simultaneously. Four nuclides, ^{75}Ni , ^{76}Cu , ^{79}Zn and ^{82}Ga , were produced during the BRIKEN commissioning. The result of ^{82}Ga neutron emission probability quoted in the present work 25.2(11)% is significantly larger (3 sigma) than the value given in my previous work [Tol19] $P_{1n} = 21.6(3)\%$. The main difference between both results is the software used for sorting and preprocessing AIDA data. However we find compatible results from both analysis for other nuclei.

The neutron branching ratio of descendants nuclei in each decay chain has been previously measured [BdN-IAEA], with the exception of ^{90}Se . Since there is no previous measurement, the theoretical prediction of 2% given by Möller et al. [Mö19] is used, which has anyway little effect on the analysis. Uncomfortable as this situation is, we accept the new value as our final result.

Most of the nuclides have an energy window $Q_{\beta 2n}$ larger than 1 MeV, and

therefore two-neutron emission is energetically allowed. However, only 17 cases show two-neutron emission. P_{2n} values of those nuclides are presented in Tab. 4.6. All of them except two have been obtained in this work for the first time. The corresponding value to ^{80}Cu and ^{84}Zn are quoted as upper limits, calculated as the sum of the central value and the total uncertainty (0.24(31)% and 0.8(12)% respectively).

Half-lives of the studied nuclei were previously measured, except for arsenic and selenium isotopes, and we give in this work experimental values for the first time. For the remaining cases we provide a half-life if a smaller uncertainty than previous measurements is obtained. Tab. 4.7 contains the half-life values of all the parent nuclei studied in this work. If no experimental value is provided in the table, half-life from evaluation [BdN-IAEA] is used. The values of ^{84}Ga and ^{86}Ge measured by Xu [Xu14a] are employed for this Thesis work, instead the evaluation's ones. Both measurements appear in the compilation, but the first one is mistaken and the second one is disregarded in the evaluation.

In general the half-life is obtained, together with P_{1n} and P_{2n} , from the simultaneous fit of beta decay, beta-one-neutron decay and beta-two-neutron decay curves. Special case are isotopes ^{83}Ga and ^{78}Cu . These nuclides are the only neutron emitters in their respective decay chains, hence the only contribution to their beta-one-neutron decay curves, which provides the opportunity of determining the half-life in a cleaner way (smaller systematic error). So, the fit procedure had two stages, firstly a fit to the beta-1n decay curve gives their half-life. The model function used to fit the data is the corresponding to the beta-1n activity plus the correlated background. The experimental correlated background is used for obtaining the half-life value, as well as for estimating its systematic uncertainties. It is not possible to use the calculated correlated background, since it needs the P_{1n} value, which is obtained afterwards. Next, P_{1n} is determined by a simultaneous fit to the beta decay and beta-one-neutron decay curves, keeping fix the half-life obtained previously.

Three nuclides with long-lived isomeric states appear in some decay chains of the implanted nuclides, namely ^{80}Ga , ^{76}Cu and ^{77}Zn . Two ^{80}Ga isomers are known [Lic14], with $T_{1/2}=1.9(1)$ s ($J_\pi = 6^-$) and $T_{1/2}=1.3(2)$ s ($J_\pi = 3^-$), although the high spin isomer is only weakly populated and therefore it was disregarded. Another case is the isotope ^{76}Cu , which has two isomeric states with half-lives 641(6) ms and 1.27(30) s [Win90]. Beta delayed neutron emission is associated with the first one [Sin95], and our fit of the beta-1n decay curve support that conclusion. No further information about spin, parity or isomeric branching ratios is available. This nucleus was implanted during the BRIKEN commissioning, and appears in the decay path of two isotopes $^{76,77}\text{Ni}$ studied in this Thesis work. The shorter ^{76}Cu half-life was used for these three cases.

In a previous measurement of ^{77}Cu decay [Ily09], two ^{77}Zn isomeric states were identified, with $T_{1/2}=2.08(5)$ s ($J_\pi = 7/2^+$), which corresponds to the ground state, and $T_{1/2}=1.05(10)$ s ($J_\pi = 1/2^-$). According to this measurement, the

shorter-lived isomer is populated by 31.4(33) % of ^{77}Cu decays, and it has an internal transition branching ratio of 34.4(9) % relative to ^{77}Zn low-spin isomer decays (or 10.8(3) % relative to ^{77}Cu decays). This isotope appears as descendant of ^{77}Cu , and if the low-spin ^{77}Zn isomer is not included in the decay chain, a neutron emission probability of $P_{1n} = 29.0(11)\%$ is obtained for ^{77}Cu . However, if isomeric branching ratios of ^{77}Zn from [Ily09] are assumed (that is, 31.4(33) % of ^{77}Cu decays populates the low-spin isomer and an isomeric transition of 34.4(9) %), results in a larger value $P_{1n} = 30.8(11)\%$ for ^{77}Cu . Although the χ^2/ν value of the beta decay fit increases from 1.74 to 2.11, the P_{1n} value obtained including both ^{77}Zn isomers is the result included in the Tab. 4.5. This zinc isotope appears also in ^{78}Cu decay chain, but according to previous measurements [Van05, Kor12a] it seems ^{78}Cu does not populates the short lived ^{77}Zn isomer. In addition to $^{77,78}\text{Cu}$ decay chain, ^{77}Zn appears in $^{77-78}\text{Ni}$ decay chains as grand-daughter but its impact is negligible. Results presented in the following tables are obtained assuming that ^{77}Cu populates ^{77}Zn as detailed in [Ily09]. The decay chain of ^{78}Ni is shown in Fig. 4.11

Finally, it is worth to mention that the neutron emission probability of the doubly-magic ^{78}Ni has been measured by neutron counting for the first time in this Thesis work, finding a value of $P_{1n}=25.8(38)\%$. A total of 7170 isotopes were identified by BigRIPS and implanted in AIDA detector, and 1641 β -decays of ^{78}Ni were observed. The unpublished value $P_{1n}=33(14)\%$ [Xu14a] is obtained from 66(9) counts of 730 keV γ -ray from the grad-daughter ^{78}Zn , and the absolute γ -ray intensity of ^{78}Cu which populates the corresponding state, measured during the same experiment. The determination of this intensity requires some assumptions.

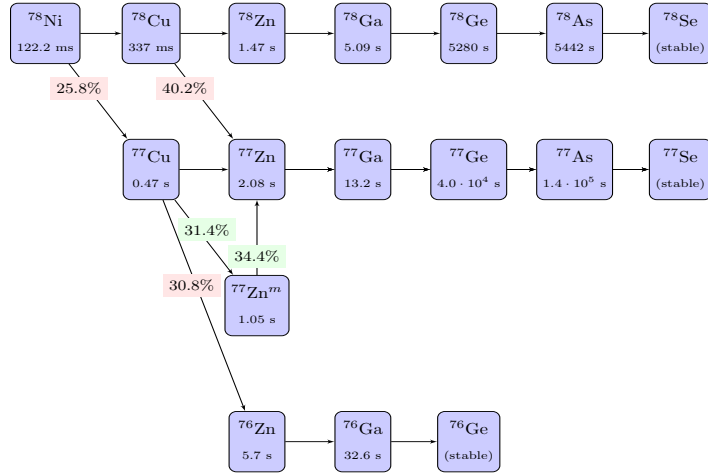


Figure 4.11: ^{78}Ni decay chain.

Table 4.5: P_{1n} of all isotopes, obtained from the simultaneous fit of beta and beta-neutron decay curves. Reference values [BdN-IAEA] are shown if available.

Nuc.	$P_{1n}[\%]$	$\sigma^{total}[\%]$	$\sigma^{stat}[\%]$	$\sigma^{syst}[\%]$	[BdN-IAEA]
^{75}Co	19.44	6.40	6.30	1.15	< 16
^{75}Ni	6.20	0.83	0.73	0.39	10.0(28)
^{76}Ni	8.78	0.82	0.71	0.42	14.0(36)
^{77}Ni	18.36	1.47	1.06	1.01	30(24)
^{78}Ni	25.79	3.80	3.45	1.58	—
^{76}Cu	6.65	0.55	0.48	0.27	7.2(5) <i>m</i>
^{77}Cu	30.76	1.26	0.53	1.14	30.5(20)
^{78}Cu	40.15	1.53	0.20	1.51	51(10)
^{79}Cu	59.85	2.40	0.39	2.36	66(12)
^{80}Cu	56.50	2.81	1.55	2.34	58(9)
^{81}Cu	71.14	5.67	4.65	3.24	81(20)
^{79}Zn	0.62	0.17	0.13	0.10	1.75(45)
^{80}Zn	1.10	0.12	0.09	0.09	1.0(5)
^{81}Zn	18.88	0.73	0.15	0.71	9.8(30)
^{82}Zn	61.39	2.46	0.43	2.42	69(7)
^{83}Zn	57.36	2.87	1.72	2.29	67(25)
^{84}Zn	64.00	5.93	4.64	3.69	73(26)
^{82}Ga	25.17	1.06	0.50	0.93	22.7(20)
^{83}Ga	84.66	4.38	0.20	4.38	66(6)
^{84}Ga	37.26	2.24	0.23	2.23	50.5(83)
^{85}Ga	71.20	2.45	0.56	2.39	70(5)
^{86}Ga	57.60	3.95	2.99	2.58	60(10)
^{87}Ga	80.85	10.82	10.52	2.51	—
^{85}Ge	21.40	1.43	1.16	0.84	16.2(18)
^{86}Ge	24.52	1.19	0.11	1.19	45(15)
^{87}Ge	33.50	1.54	0.27	1.52	—
^{88}Ge	37.80	2.72	0.66	2.64	—
^{89}Ge	43.88	6.17	5.64	2.50	—

Continued on next page

Table 4.5 – continued from previous page

Nuc.	$P_{1n}[\%]$	$\sigma^{total}[\%]$	$\sigma^{stat}[\%]$	$\sigma^{syst}[\%]$	[BdN-IAEA]
⁸⁷ As	77.88	3.91	0.57	3.87	15.4(22)
⁸⁸ As	53.06	2.09	0.80	1.93	–
⁸⁹ As	83.79	2.72	0.24	2.71	–
⁹⁰ As	75.97	3.65	0.81	3.55	–
⁹¹ As	84.08	4.9	2.20	4.34	–
⁹² As	62.94	15.91	15.63	2.98	–
⁹¹ Se	17.80	1.38	1.03	0.92	21(10)
⁹² Se	15.14	0.76	0.41	0.64	–
⁹³ Se	24.67	3.68	2.51	2.69	–
⁹² Br	49.90	1.79	0.63	1.68	33.1(25)
⁹⁴ Br	70.81	9.73	9.30	2.85	30(10)

Table 4.6: P_{2n} of all isotopes, obtained from the simultaneous fit of beta and beta-neutron decay curves. Reference values [BdN-IAEA] are shown if available.

Nuc.	$P_{2n}[\%]$	$\sigma^{total}[\%]$	$\sigma^{stat}[\%]$	$\sigma^{syst}[\%]$	[BdN-IAEA]
⁸⁰ Cu	< 0.55	–	–	–	–
⁸¹ Cu	2.19	1.32	1.30	0.21	–
⁸³ Zn	2.17	0.44	0.42	0.13	–
⁸⁴ Zn	< 2.00	–	–	–	–
⁸⁴ Ga	1.61	0.13	0.06	0.12	–
⁸⁵ Ga	1.90	0.16	0.14	0.09	< 0.1
⁸⁶ Ga	16.18	1.86	1.45	1.15	20(10)
⁸⁷ Ga	15.30	5.03	4.90	1.14	–
⁸⁷ Ge	0.26	0.06	0.05	0.03	–
⁸⁸ Ge	0.22	0.16	0.13	0.09	–
⁸⁹ Ge	2.08	1.3	1.29	0.17	–
⁸⁸ As	0.48	0.17	0.17	0.03	–
⁸⁹ As	0.25	0.05	0.05	0.02	–
⁹⁰ As	5.46	0.55	0.30	0.47	–

Continued on next page

Table 4.6 – continued from previous page

Nuc.	P _{2n} [%]	σ^{total} [%]	σ^{stat} [%]	σ^{syst} [%]	[BdN-IAEA]
⁹¹ As	2.13	0.61	0.59	0.16	–
⁹² As	23.02	8.88	8.68	1.89	–
⁹³ Se	0.79	0.57	0.57	0.07	–

Table 4.7: Half-lives of all isotopes, obtained from the corresponding fit, if the reference value in [BdN-IAEA] does not exist or it can be improved.

[†]The values corresponding to ⁸⁴Ga and ⁸⁶Ge are taken from [Xu14a] instead of the evaluation.

Nuc.	T _{1/2} [ms]	σ^{total} [ms]	σ^{stat} [ms]	σ^{syst} [ms]	[BdN-IAEA]
⁷⁵ Co	–	–	–	–	26.5(12)
⁷⁵ Ni	–	–	–	–	331.8(32)
⁷⁶ Ni	–	–	–	–	234.7(27)
⁷⁷ Ni	–	–	–	–	158.4(⁺⁴⁴ ₋₃₉)
⁷⁸ Ni	–	–	–	–	122.2(51)
⁷⁶ Cu	–	–	–	–	637(8)
⁷⁷ Cu	–	–	–	–	469.8(20)
⁷⁸ Cu	–	–	–	–	331.7(20)
⁷⁹ Cu	–	–	–	–	241.3(21)
⁸⁰ Cu	114.03	2.41	2.35	0.52	113.3(64)
⁸¹ Cu	75.75	3.83	3.76	0.73	73.2(68)
⁷⁹ Zn	839.13	7.47	7.08	2.37	746(42)
⁸⁰ Zn	–	–	–	–	561.9(30)
⁸¹ Zn	–	–	–	–	303.5(31)
⁸² Zn	–	–	–	–	177.9(25)
⁸³ Zn	–	–	–	–	99.7(30)
⁸⁴ Zn	–	–	–	–	53.6(81)
⁸² Ga	–	–	–	–	601(2)
⁸³ Ga	–	–	–	–	310(1)
⁸⁴ Ga	–	–	–	–	92.7(7) [†]
⁸⁵ Ga	–	–	–	–	91.9(12)

Continued on next page

Table 4.7 – continued from previous page

Nuc.	$T_{1/2}$ [ms]	σ^{total} [ms]	σ^{stat} [ms]	σ^{syst} [ms]	[BdN-IAEA][ms]
^{86}Ga	–	–	–	–	50.3(68)
^{87}Ga	31.33	3.09	3.06	0.40	$26(^{+17}_{-11})$
^{85}Ge	–	–	–	–	497(6)
^{86}Ge	–	–	–	–	$221.6(11)s^\dagger$
^{87}Ge	–	–	–	–	103.2(35)
^{88}Ge	–	–	–	–	60.8(61)
^{89}Ge	43.08	2.38	2.33	0.50	–
^{88}As	189.05	2.52	2.19	1.24	$200(^{+200}_{-90})$
^{89}As	81.05	0.71	0.19	0.68	–
^{90}As	54.44	1.23	0.43	1.16	–
^{91}As	38.31	1.62	0.82	1.39	–
^{92}As	18.30	2.66	2.65	0.25	–
^{91}Se	155.57	3.68	3.47	1.23	270(50)
^{92}Se	67.54	0.72	0.55	0.46	–
^{93}Se	47.40	1.95	1.60	1.10	–
^{94}Br	244.01	31.12	30.29	7.16	70(20)

Chapter 5

Discussion of results

The analysis procedure is covered in Chap. 3, from raw data conversion and generation of physical events to the extraction of half-lives and neutron branching ratios by simultaneous fit of beta and beta-neutron activities. Results obtained using such analysis method are presented in the preceding chapter.

A comparison of these results with several theoretical calculations is presented in the first part of this chapter. The second part is devoted to evaluate the impact of our measurements in different astrophysical sites, exposing the important role of new nuclear data in the abundance calculations.

5.1 Comparison with theoretical estimates

Several theoretical models are described in Sec. 1.2. A macroscopic-microscopic approach based on the mass model Finite Range Droplet Model (FRDM)(1992) and Quasiparticle Random Phase Approximation (QRPA) by Möller et al. [Möll03] will be labeled as *Möller (2003)* in the following. A more recent and improved version of the same model [Möll19] will be referred to as *Möller (2019)*. Another set of theoretical estimates of half-lives and neutron emission probabilities is given by Koura et al. [KTUY05] using Gross Theory (GT), and it will be tagged as *Koura*. Marketin et al. [Mar16] utilizes relativistic Hartree Bogoliubov (RHB) plus proton-neutron relativistic Quasiparticle Random Phase Approximation (pn-RQRPA) to calculate ground state and excited states with the same density functional, and will be quoted as *Marketin* in the following. Another self consistent mean field (SCMF) model is provided by Borzov, who calculates the ground state and excited states from the same energy functional and beta decay transitions using continuous-QRPA, and it will be referred to as *Borzov, Borzov (2012)* or *Borzov (2016)* for estimates which are published in [Bor05], [Bor12] or [Bor16] respectively. Additionally, Zhi et al. [Zhi13] Shell Model (SM) estimate for P_{1n} of ^{78}Ni will be labeled as *Zhi+*. Estimates obtained from the phenomenological model of Miernik [Mie14] will be tagged as *Miernik*. Lastly, recommended experimental values from the last evaluation auspiced by the IAEA [BdN-IAEA] that will be published in Nuclear Data Sheets will be named as *NDS*, and the experimental results of this

Thesis work are labeled as *BRIKEN*.

5.1.1 One neutron emission probabilities estimates

A comparison of P_{1n} from some of the models and experimental values obtained in this Thesis work is shown in Fig. 5.1. In general a different behaviour is observed for *Möller (2003)*, *Möller (2019)* and *Marketin* which tend to under-predict P_{1n} in the upper-right corner ($N > 50$, $Z > 28$) in comparison to *Koura* that under-predicts P_{1n} for $N \approx 50$, $Z \approx 28$. In addition it is noticeable the case of ^{80}Zn showing a clear difference between QRPA and GT but here P_{1n} is very small and it is not really significant. A more detailed comparison is presented in the following pages.

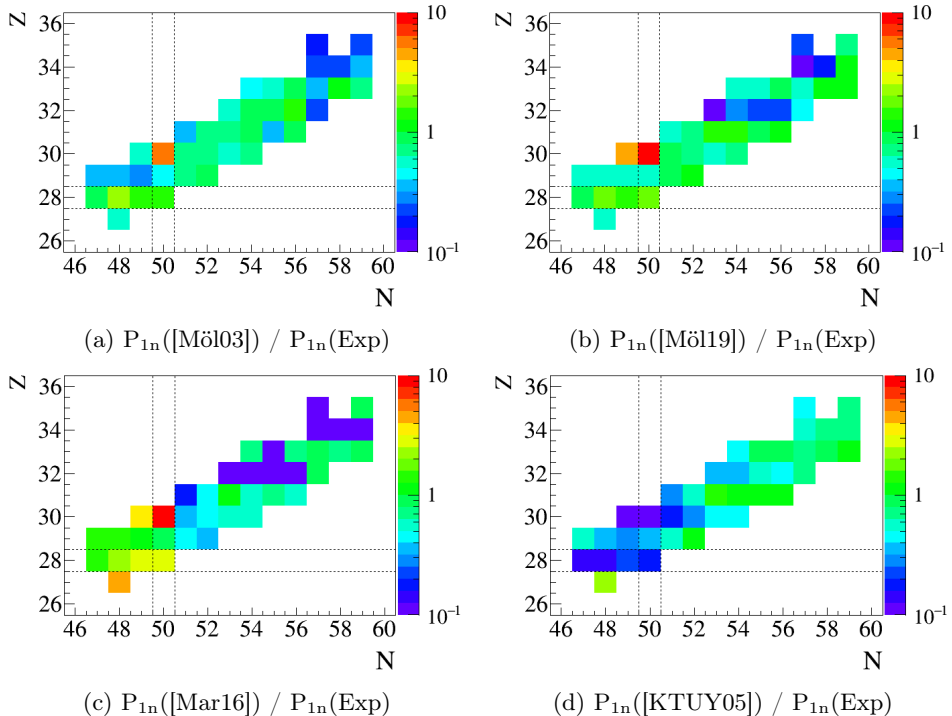


Figure 5.1: Ratio of one neutron emission probabilities from theoretical estimates and experimental values obtained in this Thesis. The top-left panel corresponds to predictions by Möller et al. [Möl03], top-right to Möller et al. [Möl19], bottom-left to Marketin et al. [Mar16], and bottom-right to Koura et al. [KTUY05].

Cobalt ($Z = 27$) isotope ^{75}Co P_{1n} value is shown in Fig. 5.2. The only previous measurement by Hosmer et al. [Hos10] was an upper limit of 16%. Regarding the

5.1. Comparison with theoretical estimates

theoretical predictions, *Moller (2019)* value is low just outside the uncertainty, and the rest of predictions are too high.

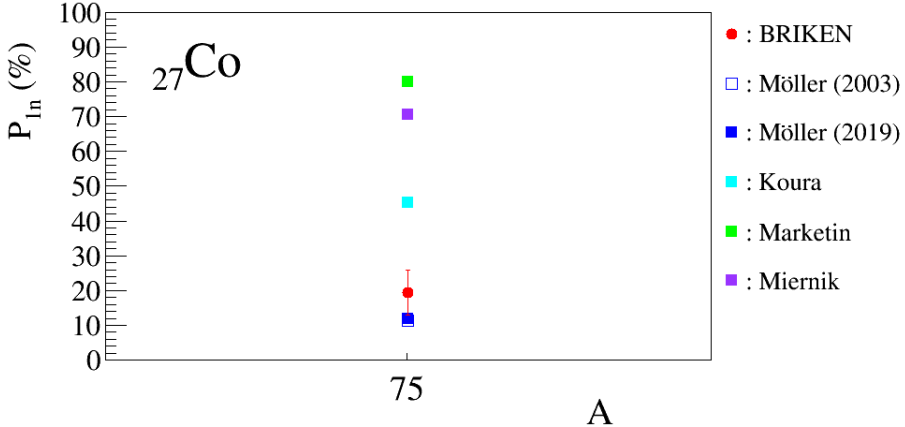


Figure 5.2: Cobalt P_{1n} experimental value compared to theoretical estimates.

One neutron emission probabilities P_{1n} of nickel ($Z = 28$) isotopes are presented in Fig. 5.3. Our experimental values are in between the theoretical estimates, and are systematically lower than the data from a previous measurement by Hosmer et al. [Hos10], which had in any case much larger uncertainties.

We obtain for the first time the P_{1n} value of the doubly magic ⁷⁸Ni based on neutron detection. The unpublished experimental result for ⁷⁸Ni [Xu14a] from the EURICA collaboration was determined by gamma and beta spectroscopy under a number of assumptions and it is affected by a large uncertainty. The spread between theoretical calculations increase with N and is maximal for ⁷⁸Ni (the largest deviation is that of the SM calculation). The best overall agreement is that of *Moller (2003)/Moller (2019)*. *Marketin* and *Borzov* predicts too large values and *Koura* estimates are too small in general. The empirical formula of *Miernik* reproduces well the values except for ⁷⁸Ni .

Copper ($Z = 29$) P_{1n} values are displayed in Fig. 5.4. Our experimental results improve significantly the uncertainties with respect to the current evaluation [BdN-IAEA] and tend to be lower. ⁷⁶Cu has been measured several times previously, obtaining 3(2)% [Rud93], 2.2(5)% [Kos00] and 7.2(5)% from [Win09], being this latest recommended by the current evaluation. Two isomers have been reported [Win90] with half-lives 0.641(6) s and 1.27(30) s, but the neutron emission is associated to the faster decaying isomer [Sin95]. Our fit results supports this conclusion, and the latest measurement [Win09] is in agreement within the uncertainties with our P_{1n} value, which reduces the uncertainty by one order of magnitude. Our P_{1n} of ⁷⁸Cu is smaller than the evaluated one, which is calculated

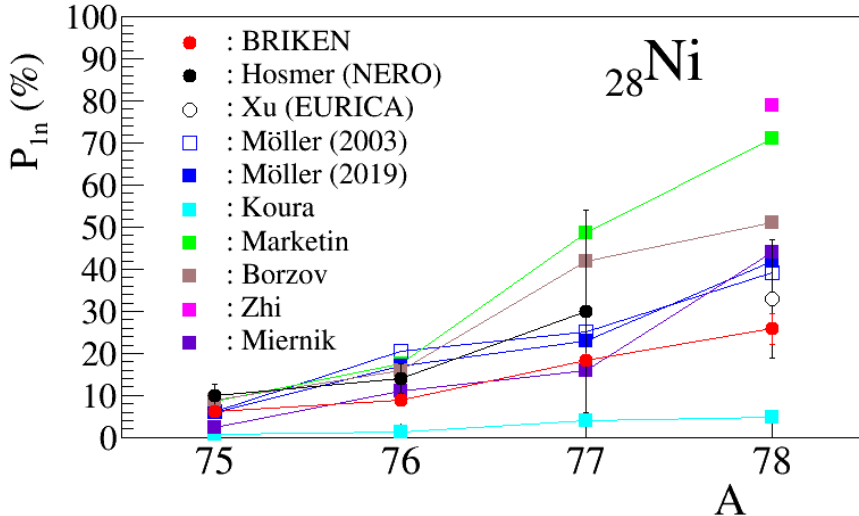


Figure 5.3: Nickel P_{1n} experimental values compared to theoretical estimates.

as the weighted average of two measurements, 65(8)% [Win09] and 44.0(54)% [Hos10], although our measurement agrees within the uncertainty with the later one. The evaluated P_{1n} ^{79}Cu is also the weighted average of two measurements, 55(17)% [Kra91] and 72(12)% [Hos10]. Our measurement, which has 10 times smaller uncertainties, is in between those previous values. Unpublished P_{1n} result from [Xu14a], with large uncertainties, agree with our values for $^{80-81}\text{Cu}$, which have a significantly smaller uncertainty. The trend of experimental results with N is best reproduced by *Borzov (2016)*. *Marketin* reproduces also the trend up to $N = 50$ but significantly underpredicts the results above. *Moller (2003)*, *Moller (2019)* and *Koura* are too low up to $N = 50$ but are in better agreement for $N > 50$ ($A > 79$). *Miernik* model follows a trend similar to the latter.

Fig. 5.5 displays the experimental P_{1n} values of zinc ($Z = 30$) isotopes obtained in this Thesis, as well as theoretical estimates from several models. Our experimental results improve importantly the uncertainties of the values from the recent evaluation [BdN-IAEA]. The P_{1n} of ^{79}Zn from the evaluation is 1.75(45)% [BdN-IAEA], coming from the unweighted average of two measurements, 1.3(4)% [Kra91] and 2.2(14)% [Hos10]. These values are much larger than our result 0.62(17)% (see Sec. 4.2 for a further discussion). In case of P_{1n} of ^{80}Zn there is one previous measurement 1.0(5)% [Kra91], and an upper limit <1.8% [Hos10], which agrees with our more precise value. Above $N = 51$ ($A = 81$) our results are somewhat smaller than the evaluation. We found a large discrepancy for ^{81}Zn . The evaluated P_{1n} of ^{81}Zn corresponds to the weighted average of three

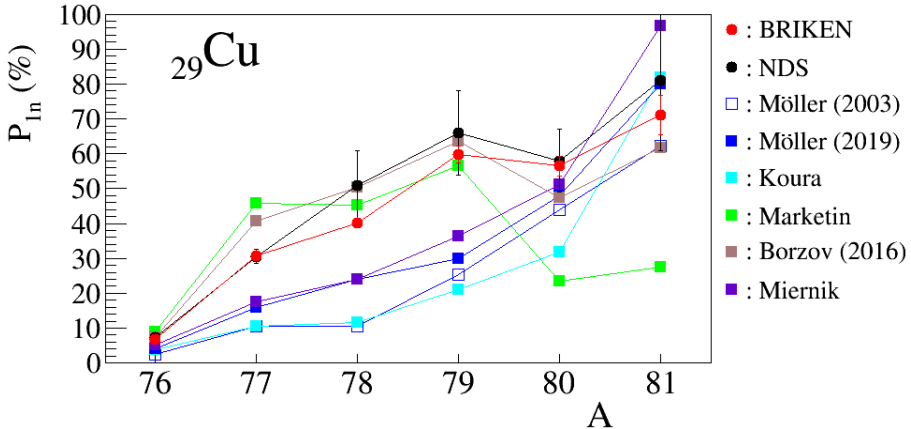
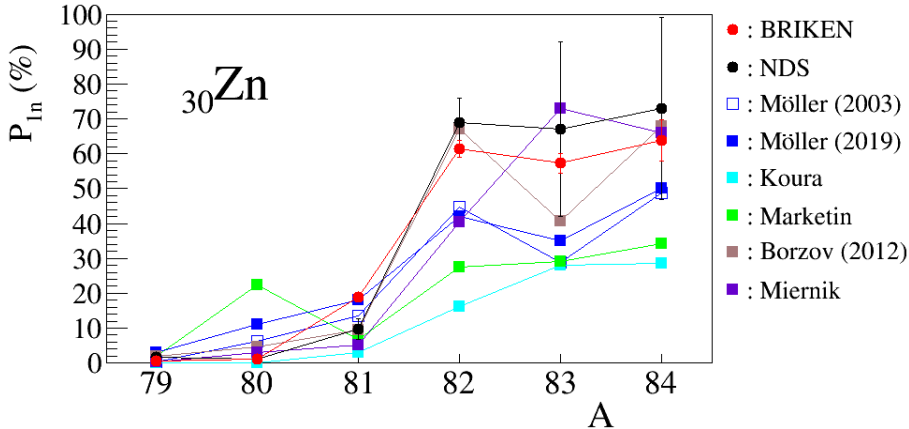


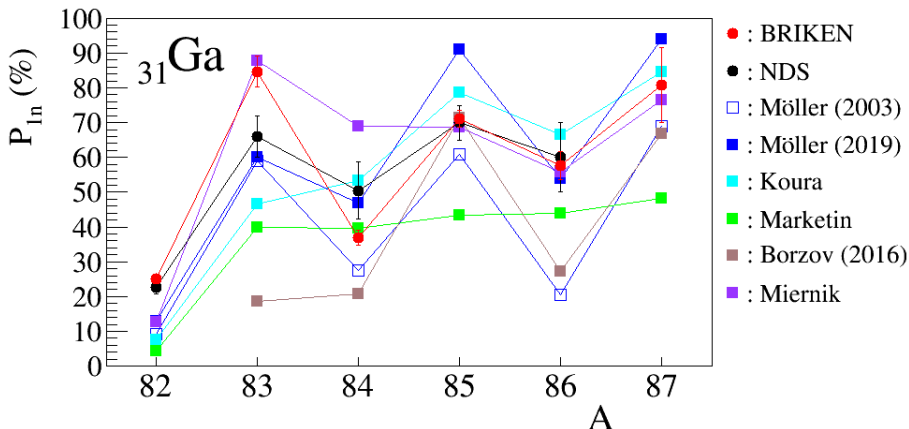
Figure 5.4: Copper P_{1n} experimental values compared to theoretical estimates.

previous measurements, 7.5(30)% [Kra91], 12(4)% [Pad10] and 30(13)% [Hos10]. The last one is in agreement with our more precise value, although the evaluated value is 50% smaller than ours. For ^{82–84}Zn isotopes, there is one previous measurement of each one only. In case of P_{1n} of ⁸²Zn there is only one previous measurement [Als16], which agrees with our value with smaller uncertainty. For isotopes ^{83,84}Zn we improve importantly the unpublished results [Xu14a] from the EURICA collaboration, an upper limit >71(29)% for ⁸³Zn and a rather uncertain value 73(26)% for ⁸⁴Zn, and also we report for the first time very small two-neutron emission probabilities for these nuclei. The theoretical models reproduce more or less the experimental trend of an increased P_{1n} value for $N > 51$ ($A > 81$), although *Marketin* shows a somewhat erratic behavior and *Koura* is too low. The best overall agreement is that of *Borzov (2012)*. For $N = 50$ ($A = 80$) most predictions are too high while the opposite is true for $N = 51$ ($A = 81$). The estimate of the phenomenological model of *Miernik* is too low for $N = 51, 52$.

Gallium ($Z = 31$) isotopes P_{1n} values are shown in Fig. 5.6. Our measurements of ^{82,85,86}Ga isotopes confirm the recommended values from the evaluation [BdN-IAEA]. The P_{1n} value of ⁸³Ga has been measured previously seven times, obtaining a range of values between 14.9(18)% and 85(4)%. This particular isotope has very large decay energy window $Q_\beta = 11719.3(36)$ keV and $Q_{\beta 1n} = 8086.6(34)$ keV, which can explain enlarged systematic errors due to beta and neutron detection efficiencies. Our result is 28% higher than the recommended value. The next heavier isotope ⁸⁴Ga has been measured five times in the past, obtaining 70(15)% [Kra91], 74(14)% [Win10], 40(7)% [Mad16] and 53(20)% [Ver17], and the recommended value is their weighted average 50.5(83)%. An additional value of 51(28)% [Tes14] was disregarded in the evaluation. The value obtained in


 Figure 5.5: Zinc P_{1n} experimental values compared to theoretical estimates.

this Thesis work is 37.0(21)%⁸⁶, which is closer but smaller than the two most recent measurements. Regarding the theoretical estimates, the increase and odd-even N staggering of P_{1n} above $N = 51$ ($A > 82$) is reproduced by the models, except *Marketin* that shows no staggering, and *Koura* and *Borzov (2016)* that fail to reproduce the large jump at $N = 52$. There is no clear best model in this region. All the models produce too low values for $N = 51$.


 Figure 5.6: Gallium P_{1n} experimental values compared to theoretical estimates.

One neutron emission probabilities P_{1n} of germanium ($Z = 32$) isotopes are displayed in Fig. 5.7. Our measurements improve the evaluated P_{1n} of $^{85-86}\text{Ge}$

5.1. Comparison with theoretical estimates

[BdN-IAEA], and provide new values for $^{87-89}\text{Ge}$. Our experimental results show a smooth increasing trend with N . Similar trend is found in the theoretical calculations although most are either too low (*Marketin, Moller (2019), Koura*) or too high. The best reproduction of the data up to $N = 56$ is that of *Moller (2003)*. For $N = 57$ it predicts however a too low value, while *Marketin and Borzov (2012)* reproduce the experimental result. It is to be noticed that *Moller (2019)* is much lower than *Moller (2003)* (except for $N = 57$) the opposite of what happens for gallium isotopes. *Miernik* phenomenological model obtains the right value except for $N = 53$ and $N = 56$. We provide for the first time P_{1n} values for $^{87-89}\text{Ge}$. Compared to the evaluation [BdN-IAEA] based on previous data our result is 32% larger for ^{85}Ge and 54% lower for ^{86}Ge which corresponds to a single measurement with large uncertainty [Mie13c].

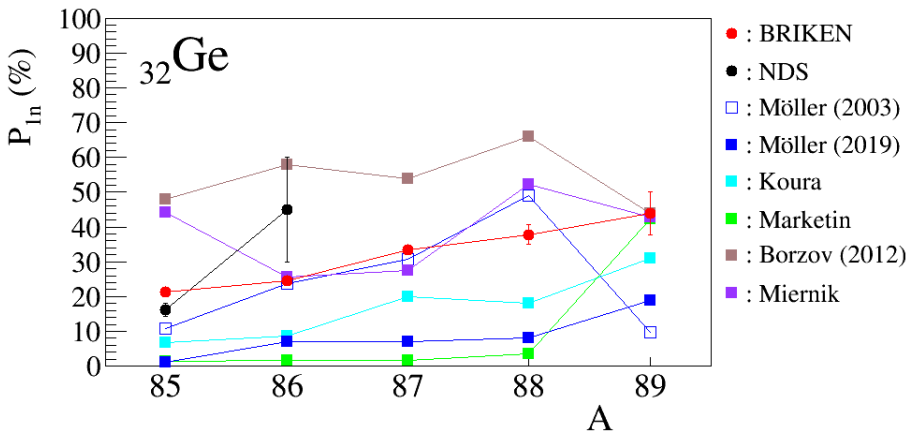


Figure 5.7: Germanium P_{1n} experimental values compared to theoretical estimates.

Arsenic ($Z = 33$) P_{1n} values are presented in Fig. 5.8. All the isotopes are measured for the first time, except ^{87}As . There are two previous measurements of ^{87}As P_{1n} value, 51(35)% [Cra78] and 15.4(22)% [Rud93]. The second one is the recommended value in [BdN-IAEA]. However, such small P_{1n} results in a very poor fit of ^{87}Ge decay curves, thus ^{87}As P_{1n} is also fitted together with P_{xn} of ^{87}Ge , obtaining 77.9(1.6)%. Regarding the theoretical estimates, *Koura* gives the closer values to our experimental data (except for $N=54$). Both *Moller (2003)* and *Moller (2019)* predict quite similar values except for $N=59$. All the models reproduce the staggering except *Marketin* for nuclei $A > 89$ ($N > 53$). The phenomenological model of *Miernik* produces values that are too small in all the cases.

Fig. 5.9 shows the experimental P_{1n} of selenium ($Z = 34$) isotopes obtained in this Thesis, as well as theoretical estimates from several models. Measurements of $^{92-93}\text{Se}$ P_{1n} are reported for the first time. In case of ^{91}Se there is a single

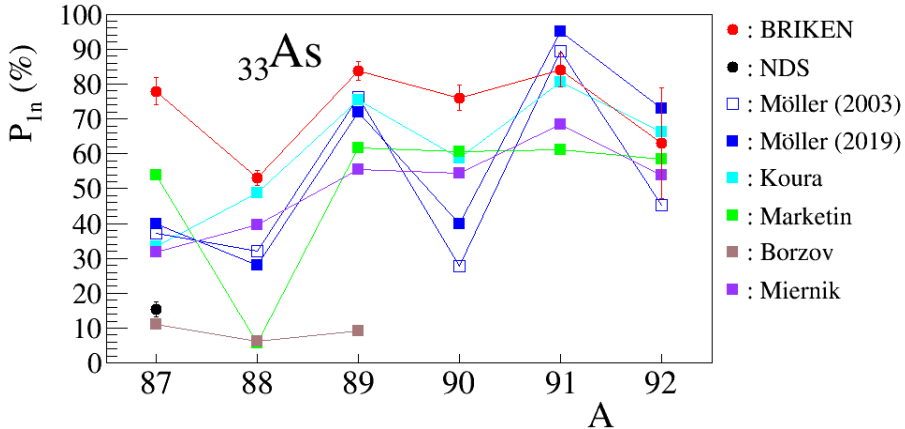


Figure 5.8: Arsenic P_{1n} experimental values compared to theoretical estimates.

measurement with large uncertainty [Asg75] which is superseded by our result. From the theoretical models the best overall agreement with our data is obtained by *Koura* although their values are 55%, 66% and 37% lower than our experimental values for ^{91}Se , ^{92}Se and ^{93}Se respectively. The rest, although reproduce somehow the staggering, give too low values, except *Möller (2019)* for ^{93}Se . *Miernik* phenomenological model produces a trend with N opposite to the one observed.

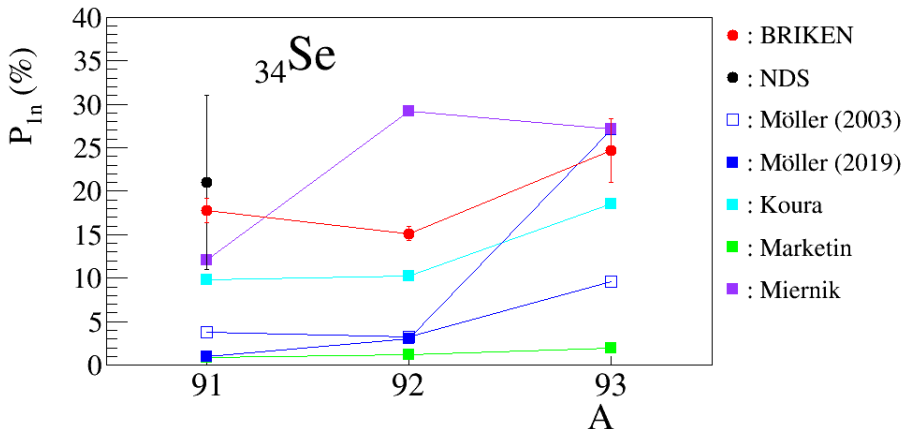


Figure 5.9: Selenium P_{1n} experimental values compared to theoretical estimates.

Bromine ($Z = 35$) isotopes P_{1n} values are shown in Fig. 5.10. The result of the recent evaluation [BdN-IAEA] for ^{92}Br , which is the weighted average of

several measurements, causes a poor fit of ^{92}Se decay curves. Therefore, ^{92}Br P_{1n} is obtained from ^{92}Se decay curves fit, together with P_{xn} and $T_{1/2}$ of ^{92}Se . Regarding the P_{1n} of ^{94}Br , the evaluation recommends 30(10)% from [Kra88], and dismiss the value 68(16)% from [Pfe02]. This last value is in agreement with our result 71(10)% within the uncertainty. Theoretical models underpredict P_{1n} of $^{92,94}\text{Br}$, except *Marketin* for ^{94}Br .

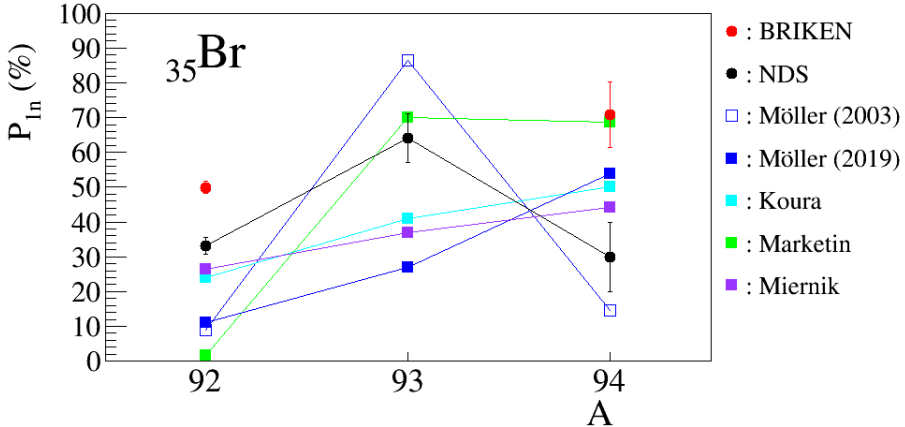


Figure 5.10: Bromine P_{1n} experimental values compared to theoretical estimates.

5.1.2 Two neutron emission probabilities estimates

A comparison of P_{2n} from global models and experimental values obtained in this Thesis work is shown in Fig. 5.11. Predictions from *Möller (2003)* tend to predict better the heaviest isotopes of each element but overestimate the small P_{2n} values corresponding to lighter nuclei. However, the newer predictions of *Möller (2019)* tend to underestimate P_{2n} for the heaviest isotopes, and predict zero probability of two-neutron emission for the lightest nuclei. *Marketin* is in fair agreement with data for the lightest isotopes but underestimates the heaviest ones, in particular with odd Z. The phenomenological model of *Miernik* shows agreement with odd N nuclei and underestimates the P_{2n} of ^{88}Ge and ^{89}As . A more detailed comparison of gallium and arsenic P_{2n} is given in the following.

Copper ($Z = 29$) P_{1n} values are displayed in Fig. 5.12. Although there is an unpublished measurement of the P_{1n} of $^{80-81}\text{Cu}$ [Xu14a], we report here P_{2n} values of these isotopes determined by neutron counting for the first time. All theoretical models calculate too high P_{2n} values. The empirical model of *Miernik* is close for the isotope ^{80}Cu , but overpredicts the value of ^{81}Cu .

Fig. 5.13 displays the experimental P_{2n} values of zinc ($Z = 30$) isotopes

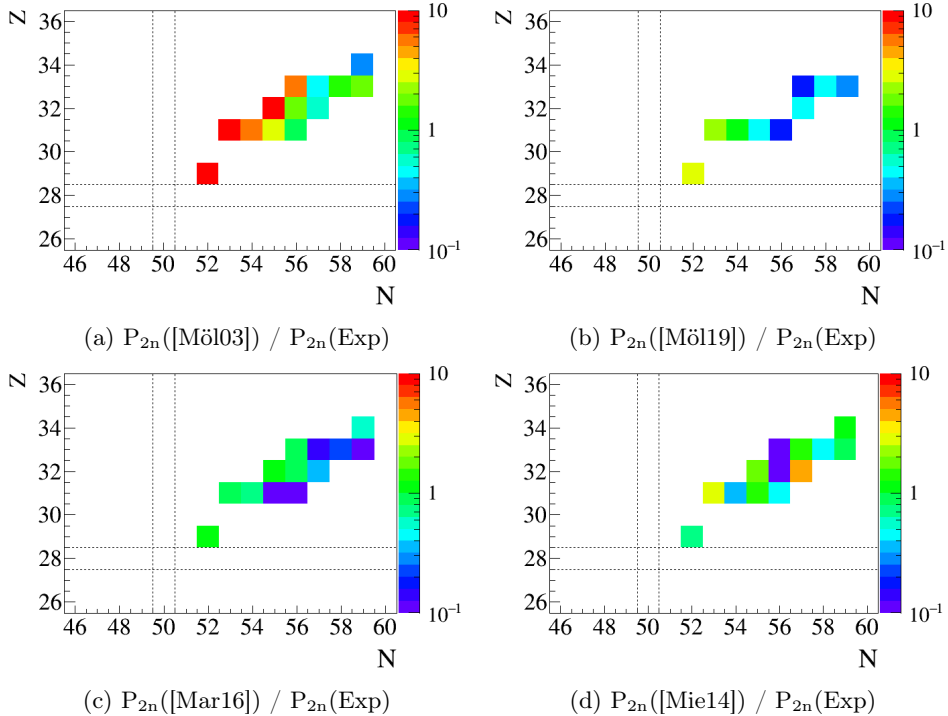
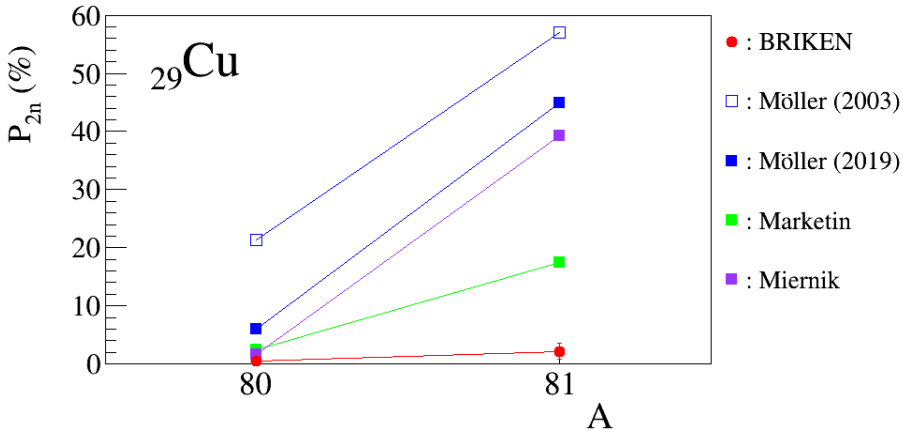
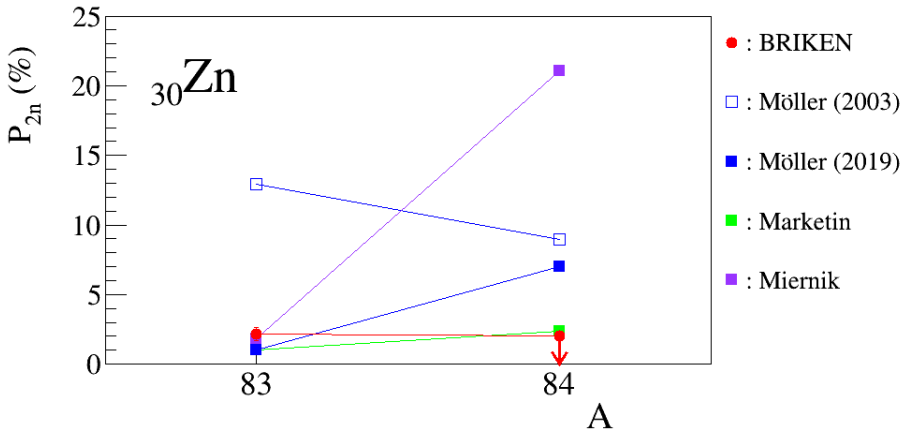


Figure 5.11: Ratio of two neutron emission probabilities from theoretical estimates and experimental values obtained in this Thesis. The top-left panel corresponds to predictions by Möller et al. [Möller03], top-right to Möller et al. [Möller19], bottom-left to Marketin et al. [Mar16], and bottom-right to Miernik [Mie14].

obtained in this Thesis, which have been measured for the first time. *Moller (2003)* overestimate P_{2n} , although the modern version *Moller (2019)* gives a closer value for ^{83}Zn . *Marketin* agrees well with the experimental values. The phenomenological model of *Miernik* [Mie14] give a close value for ^{83}Zn , but quite large in case of ^{84}Zn .

Two neutron emission probabilities P_{2n} of gallium ($Z = 31$) isotopes are presented in Fig. 5.14. There is one previous measurement of ^{86}Ga , obtaining $P_{2n} 20(10)\%$ [Mie13c]. In addition, a previous measurement of ^{85}Ga with P_{2n} as an upper limit $< 0.1\%$ [Mie18]. It is worth to notice that the staggering is found for one and two neutron emission probabilities, obtaining larger P_{1n} values of odd- A gallium isotopes and enhanced P_{2n} values for even- A ones. Theoretical estimates from *Borzov (2016)* are in fair agreement with experimental values except for ^{85}Ga . *Moller (2003)* overestimate all P_{2n} of gallium isotopes lighter than mass 87. *Marketin* and *Moller (2019)* agree somewhat with data for $^{84,85}\text{Ga}$


 Figure 5.12: Zinc P_{2n} experimental values compared to theoretical estimates.

 Figure 5.13: Zinc P_{2n} experimental values compared to theoretical estimates.

but underestimate the values for $^{86,87}\text{Ga}$. Notice the large difference between the newer *Möller (2019)* and the older *Möller (2003)* QRPA+FRDM models. The phenomenological model of *Miernik* reproduces the data trend except for ^{87}Ga .

Germanium ($Z = 32$) isotopes P_{2n} values are shown in Fig. 5.15. These experimental values are measured for the first time in this Thesis work. Predictions from *Möller (2019)* and *Marketin* are in fair agreement within the experimental uncertainty for $^{87,89}\text{Ge}$ isotopes, but overestimate the value of ^{88}Ge . *Miernik* gives a close value for ^{89}Ge , but too high for ^{87}Ge and too low for ^{87}Ge .

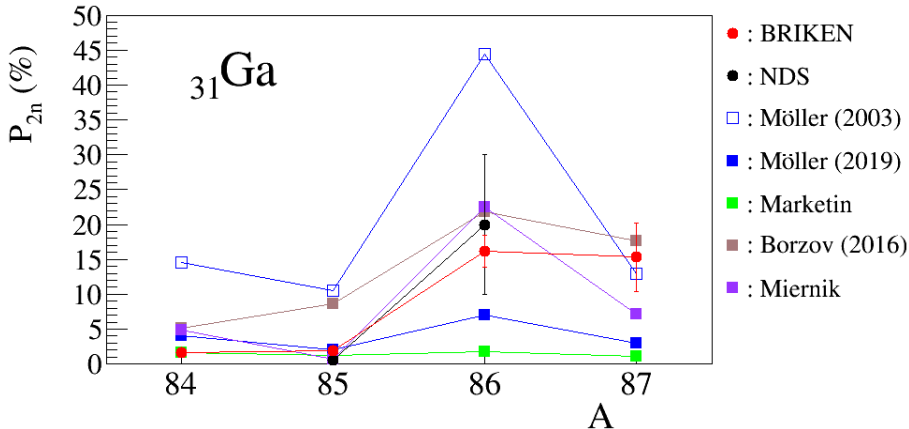
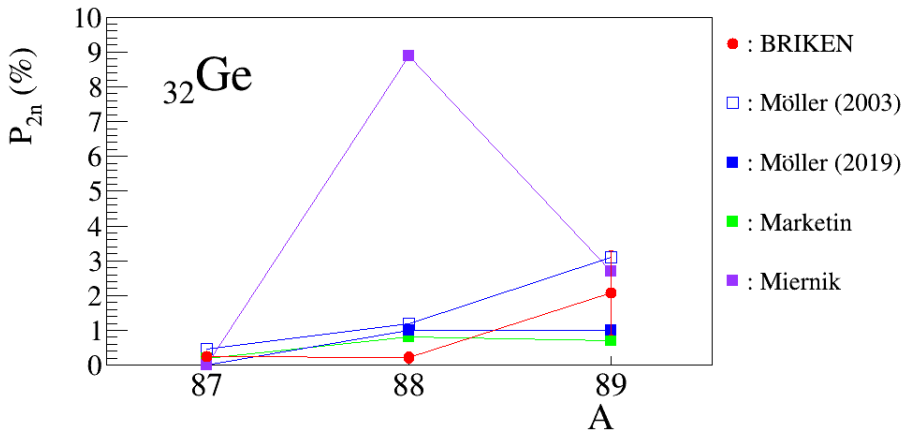

 Figure 5.14: Gallium P_{2n} experimental values compared to theoretical estimates.

 Figure 5.15: Germanium P_{2n} experimental values compared to theoretical estimates.

Fig. 5.16 displays P_{2n} values of arsenic ($Z = 33$) isotopes measured for the first time in this Thesis, as well as theoretical estimates from several models. As it happens in case of gallium isotopes, P_{2n} values of even- A arsenic isotopes are larger than odd- A ones, while P_{1n} of odd- A ones are greater than even- A ones. *Miernik* predictions are in quite good agreement with experimental data. *Möller (2003)*, *Möller (2019)* and *Markitin* reproduce the small values of $^{88-91}\text{As}$ but miss the increase at ^{92}As . *Markitin* fails to reproduce the P_{2n} value jump for ^{92}As , while

5.1. Comparison with theoretical estimates

Möller (2019) underestimates and *Möller (2003)* overestimates the value.

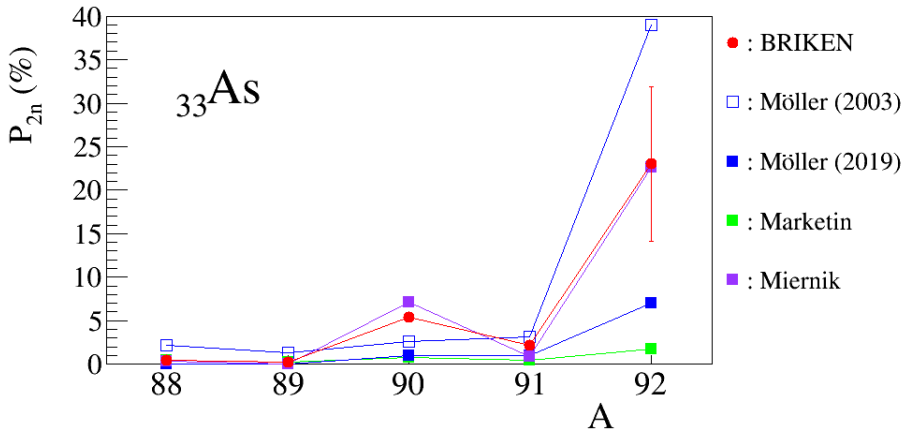


Figure 5.16: Arsenic P_{2n} experimental values compared to theoretical estimates.

Fig. 5.17 shows the experimental P_{2n} of selenium ($Z = 34$) obtained in this Thesis for the first time, as well as theoretical estimates from several models. All the theoretical models predict a much lower value than the experimental one.

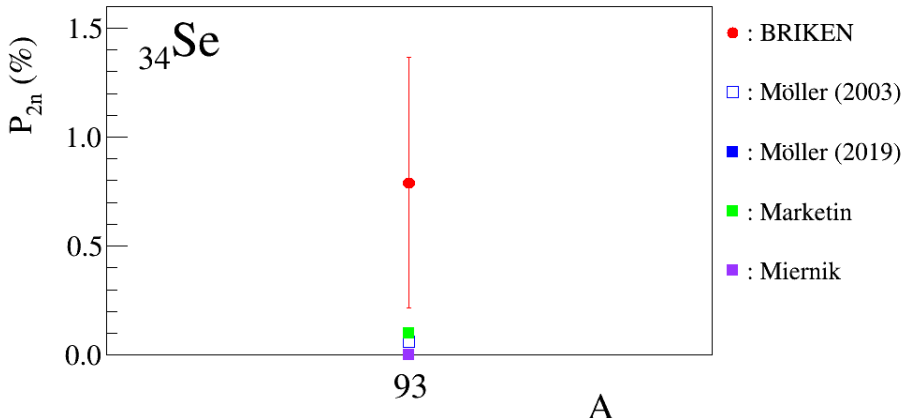


Figure 5.17: Selenium P_{2n} experimental values compared to theoretical estimates.

5.1.3 Half-life estimates

A comparison of $T_{1/2}$ from global models and experimental values obtained in this Thesis work is shown in Fig. 5.18. It is worth to remember that in this Thesis a half-life is reported only when the value of the analysis improves existing data. For the remaining cases our results confirm existing data. A more detailed comparison for each set of isotopes is given in the following pages.

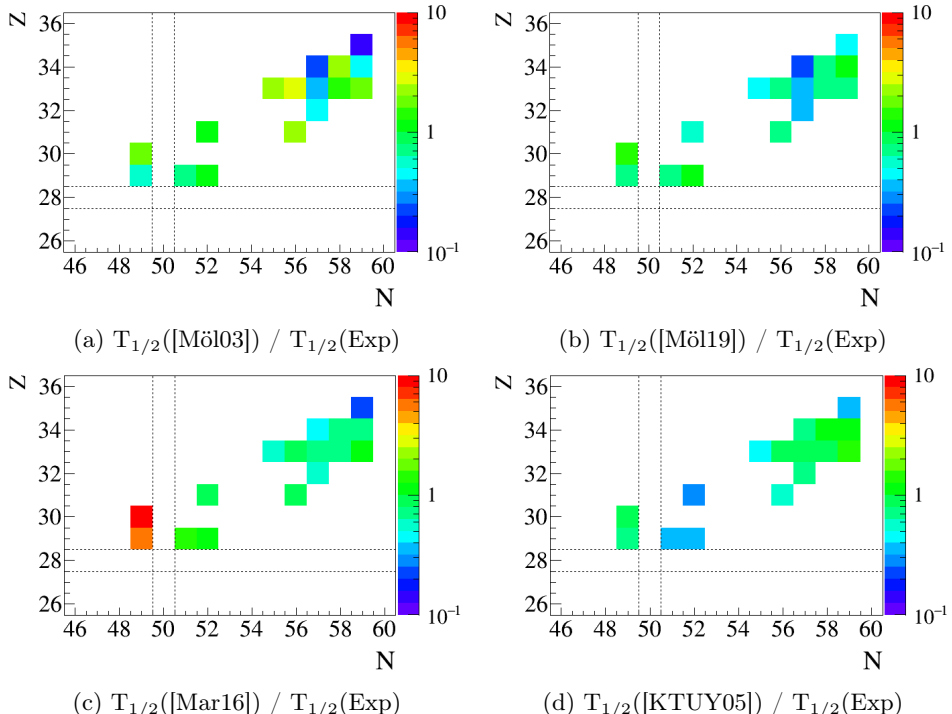


Figure 5.18: Ratio of half-lives from theoretical estimates and experimental values obtained in this Thesis. The top-left panel corresponds to predictions by Möller et al. [Möll03], top-right to Möller et al. [Möll19], bottom-left to Marketin et al. [Mar16], and bottom-right to Koura et al. [KTUY05].

Cobalt ($Z = 27$) isotope ^{75}Co half-life value is shown in Fig. 5.2. Our fits support the result from the latest evaluation [BdN-IAEA], which comes from a weighted average of two previous measurements, 30(11) ms by Hosmer et al. [Hos10] and 26.5(12) ms by [Xu14b]. *Koura* predicted half-life agrees within the uncertainty with the experimental value. *Marketin* gives a too long half-life, while *Möller (2003)/Möller (2019)* predictions are too low.

Nickel ($Z = 28$) isotopes $T_{1/2}$ values are shown in Fig. 5.20. We confirm

5.1. Comparison with theoretical estimates

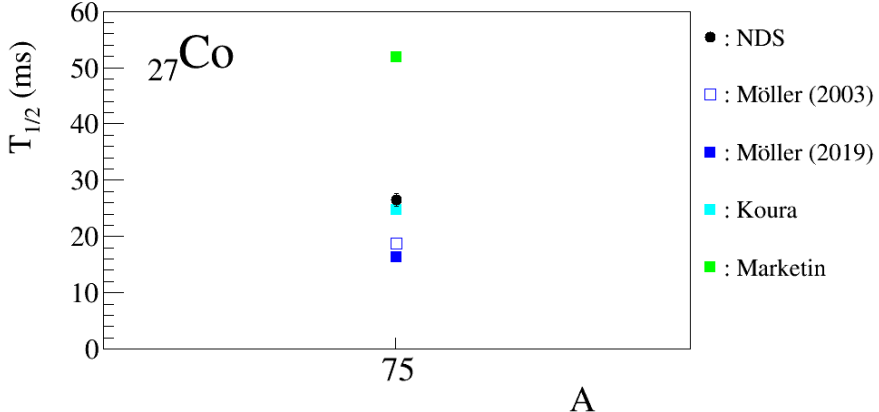


Figure 5.19: Cobalt P_{1n} experimental value compared to theoretical estimates.

half-lives for ^{75–78}Ni isotopes from the latest evaluation [BdN-IAEA], each result corresponds to a weighted average of two measurements, [Hos10] and [Xu14b]. Predictions from *Koura* are in very good agreement with the experimental values, and *Möller (2019)* for ⁷⁸Ni. The predictions from *Möller (2003)*, *Möller (2019)* for ^{75–77}Ni, and specially *Marketin* overestimate the experimental values.

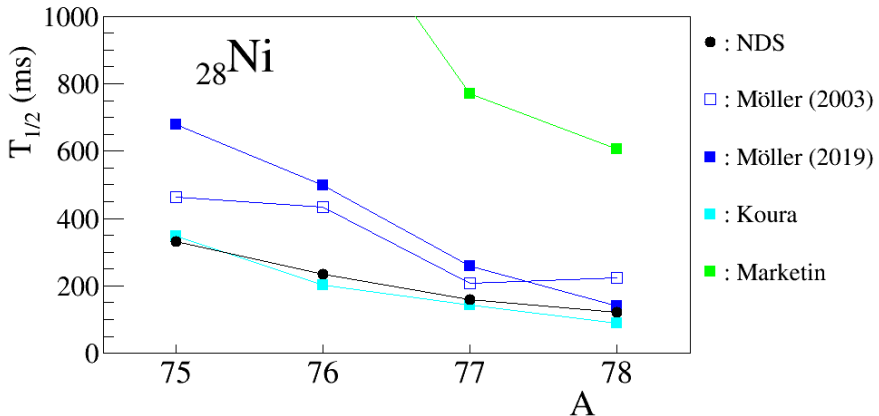


Figure 5.20: Nickel T_{1/2} experimental values compared to theoretical estimates.

Half-lives of copper ($Z = 29$) isotopes are presented in Fig. 5.21. We report T_{1/2} values for ^{78,80,81}Cu because we obtain reduced uncertainties compared to the best available data [Xu14b]. Our result agrees within uncertainties thus confirm the average values from the evaluation. All theoretical calculations, except *Marketin*,

underestimate the measured half-lives although the agreement is quite good for Moller et al. prediction for the heaviest isotopes. *Marketin* severely overpredicts $T_{1/2}$ below $N = 51$.

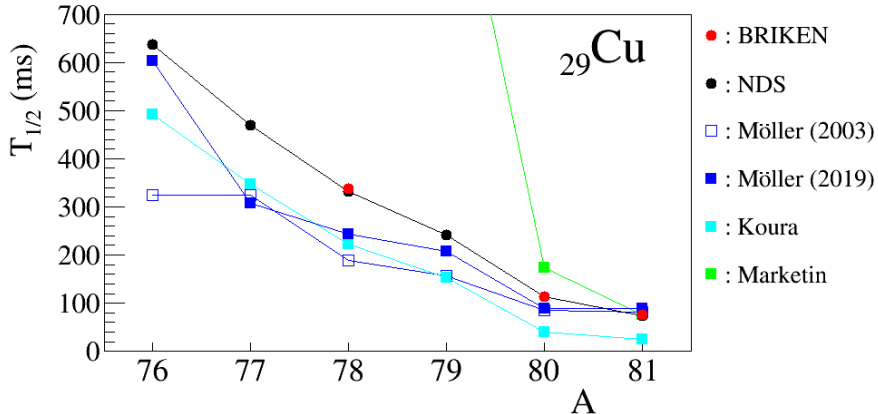
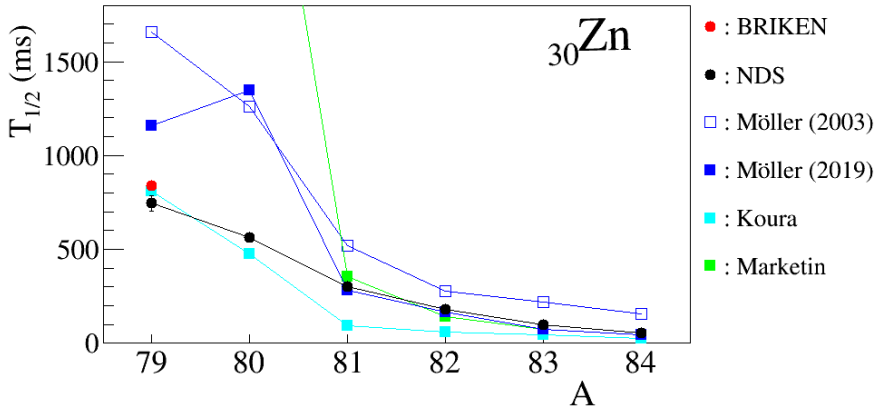
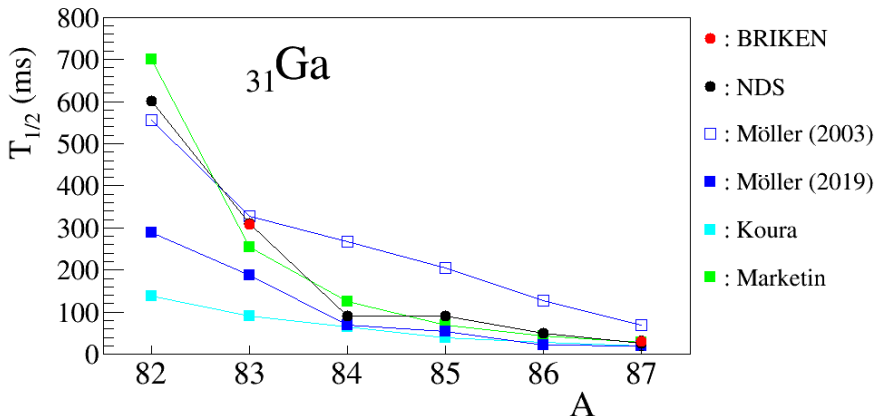


Figure 5.21: Copper $T_{1/2}$ experimental values compared to theoretical estimates.

Fig. 5.22 displays the experimental $T_{1/2}$ values of zinc ($Z = 30$) isotopes obtained in this Thesis, as well as theoretical estimates from several models. We only report a new value for ^{79}Zn which differs clearly from the evaluation, which takes the value reported in [Hos10] and disregards four previous measurements (see Sec. 4.2 for further details). Similarly to P_{1n} comparison, there is a transition when $N = 50$ ($A = 80$) is crossed. *Koura* predictions agree with data for the lightest and heaviest isotopes but underpredict the values for $N = 51, 52$. *Moller (2019)* and *Marketin* agree very well for $N > 50$, while *Moller (2003)* is somewhat high, but they overestimate the $T_{1/2}$ for $N < 51$, in the case of *Marketin* severely.

Gallium ($Z = 31$) isotopes $T_{1/2}$ values are shown in Fig. 5.23. We report new half-lives for ^{83}Ga , because our result is somewhat smaller than the average value recommended in the evaluation [BdN-IAEA], and for ^{87}Ga , because we reduce significantly the uncertainty of the only previous measurement [Xu14a]. A very good reproduction of the experimental trend is obtained by *Marketin*. *Moller (2019)* is in good agreement with data for $N < 83$ but overestimates it above. *Moller (2003)* predicted values are close to the experimental ones for isotopes $A < 84$, and overestimates the half-lives of heavier isotopes. The opposite situation happens for *Moller (2019)* and *Koura* estimates, which are in fair agreement with isotopes with $A \geq 84$ but underestimate half-lives of isotopes $A < 84$.

Half-lives of germanium ($Z = 32$) isotopes are displayed in Fig. 5.24. We only report a new value for ^{89}Ge which we have measured for the first time. Experimental data is between *Moller (2003)* estimates, which give larger values than the experimental ones, and the rest of model predictions, although all the


 Figure 5.22: Zinc $T_{1/2}$ experimental values compared to theoretical estimates.

 Figure 5.23: Gallium $T_{1/2}$ experimental values compared to theoretical estimates.

models tend to converge to ^{89}Ge half-life.

Arsenic ($Z = 33$) $T_{1/2}$ values are presented in Fig. 5.25. All the isotopes are measured for the first time, except ^{88}As . There is a close agreement with *Koura* and *Marketin* for isotopes heavier than mass 88.

Fig. 5.26 shows the experimental $T_{1/2}$ of selenium ($Z = 34$) isotopes obtained in this Thesis, as well as theoretical estimates from several models. Half-life measurements of $^{92-93}\text{Se}$ are reported for the first time. Our value for ^{91}Se is discrepant from a previous measurement [Asg75], that reported a 1.7 times longer half-life. *Koura* estimated half-lives are in fair agreement with the experimental

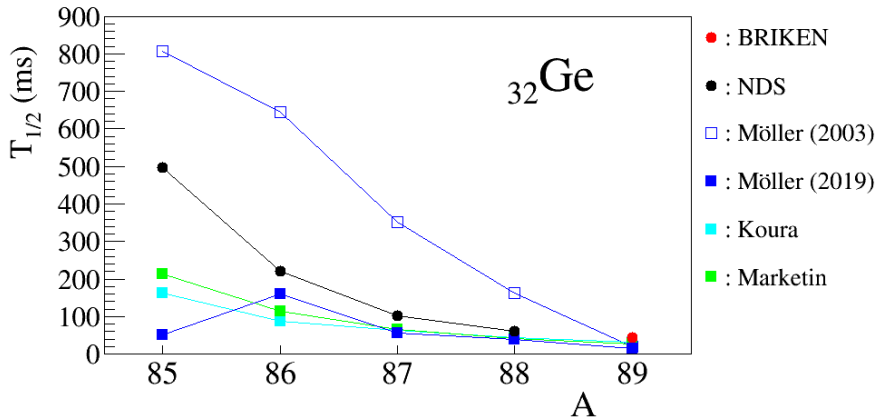


Figure 5.24: Germanium $T_{1/2}$ experimental values compared to theoretical estimates.

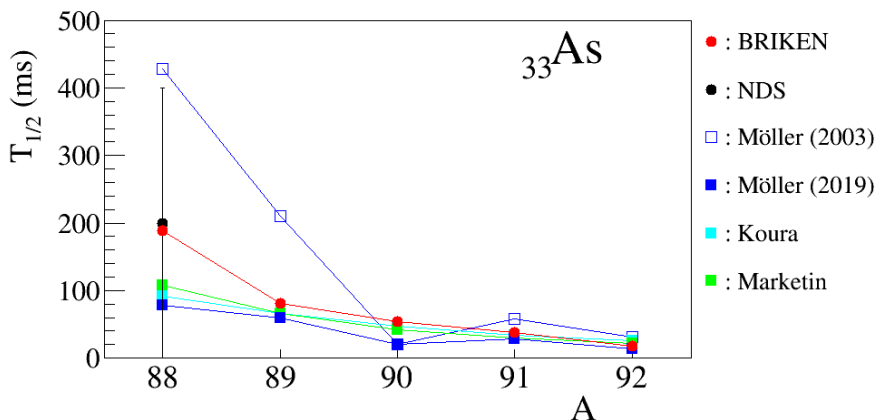


Figure 5.25: Arsenic $T_{1/2}$ experimental values compared to theoretical estimates.

data reported by this work. *Marketin* gives smaller values, while *Moller (2019)* is closer to the experimental half-lives than the previous version of the same model *Moller (2003)*.

Bromine ($Z = 35$) isotopes $T_{1/2}$ values are shown in Fig. 5.27. We confirm half-lives for $^{92,93}\text{Br}$ isotopes from the latest evaluation [BdN-IAEA]. Half-life of ^{92}Br results from an unweighted average of four measurements: 365(7) ms [Rud76], 350(40) ms [Cra78], 310(20) ms [Ewa84] and 310(10) ms [Kra88]. Three additional values, which are 80% lower than those, are disregarded by the evaluation. The

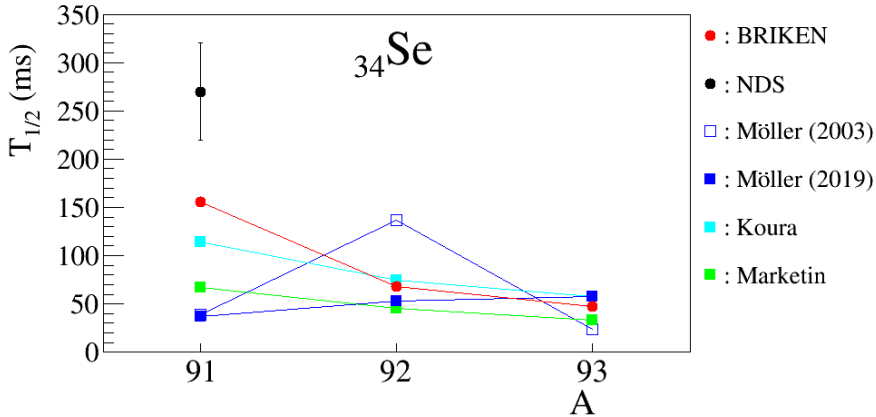


Figure 5.26: Selenium $T_{1/2}$ experimental values compared to theoretical estimates.

value which is taken by the latest evaluation for the half-life of ^{93}Br corresponds to 152(8) ms measured by [Mie13a], although two shorter values were previously reported. In addition, we provide a new value for ^{94}Br , which was measured previously by [Kra88] finding 70(20) ms. However, this value causes a poor fit of ^{94}Br decay curves, so its half-life and P_{1n} are fitted simultaneously resulting in a 3.5 times longer half-life. Regarding the theoretical estimates, all of them underpredict the half-lives of $^{92,93}\text{Br}$ from evaluation and our new value for ^{94}Br , except Moller (2003) for ^{93}Br .

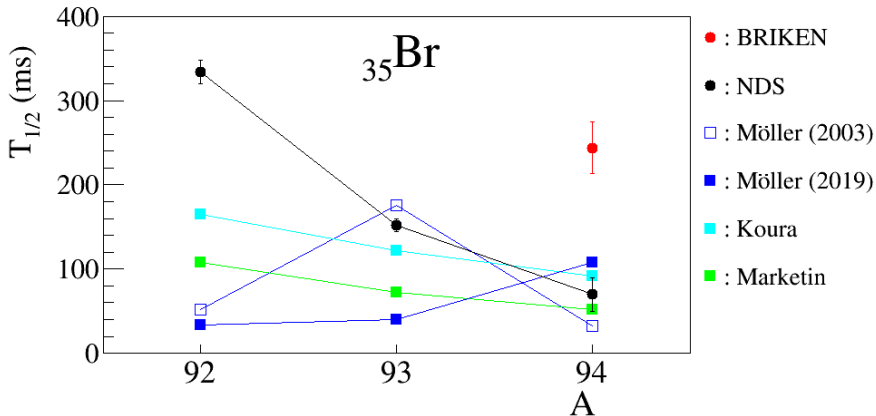


Figure 5.27: Bromine $T_{1/2}$ experimental values compared to theoretical estimates.

5.1.4 $P_n/T_{1/2}$ versus $Q_{\beta 1n}$ systematics

McCutchan et al. [McC12] studied the correlation between the ratio of total neutron emission probability and half-life $P_n/T_{1/2}$, and the beta-delayed neutron emission energy window $Q_{\beta 1n}$ (see Sec. 1.2). They found that the formula $P_n/T_{1/2} = cQ_{\beta 1n}^d$ adjust well the data available at the time in the low-mass fission group with parameters $c = 0.0097(9)$ and $d = 4.87(7)$ [McC12]. Fig. 5.28 shows the experimental values of nuclei investigated in this Thesis work as a function of $Q_{\beta 1n}$ values as individual markers, and the empirical model as a solid line. $Q_{\beta 1n}$ values are taken from [BdN-IAEA]. A linear correlation (in log-log scale) is clearly observed for experimental values of nuclides with the same atomic number.

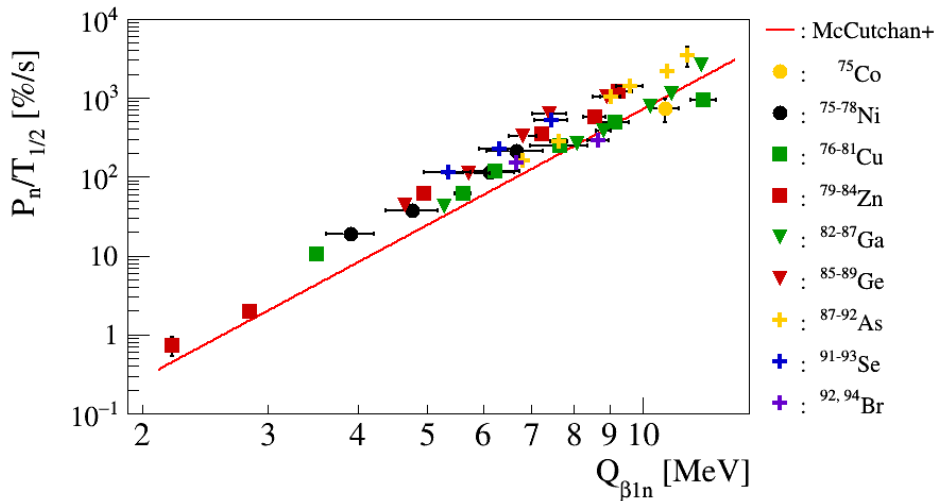


Figure 5.28: Experimental values of $P_n/T_{1/2}$ as a function of $Q_{\beta 1n}$, each marker corresponds to a single nuclide studied in this Thesis work. The red line corresponds to the formula $P_n/T_{1/2} = cQ_{\beta 1n}^d$, with parameters $c = 0.0097(9)$ and $d = 4.87(7)$ [McC12].

5.2 Astrophysical impact

As it is explained in Sec. 1.3, simulations of r-process require a vast amount of nuclear physics data as input, provided by experiments and theoretical models. More experimental data is required to improve these models, and increase the reliability of simulations, so their results can be used to narrow down the astrophysical site of r-process.

In this section we show the impact of our newly measured half-lives and P_{xn} in the nucleosynthesis at different astrophysical sites. To do so, two nuclear datasets have been prepared. One, with the nuclear physics input described in Sec. 1.3.2, and another one which is exactly the same except for the half-lives and P_{xn} values reported in Sec. 4.5 of this Thesis work. In the following, the first dataset is labeled as *REACLIB*, and the second one as *REACLIB & BRIKEN*.

A comparison of $\langle n \rangle$ (i.e., $P_{1n} + 2P_{2n}$) values of nuclei obtained in this Thesis work to the ones included in the latest REACLIB database [REACLIB] it is shown in Fig. 5.29. The REACLIB average neutron emission of nickel, copper, gallium, bromine and most of arsenic isotopes agrees or is larger than the corresponding experimental values obtained in this Thesis work. However, REACLIB neutron emission probabilities for zinc and germanium isotopes are importantly underestimated.

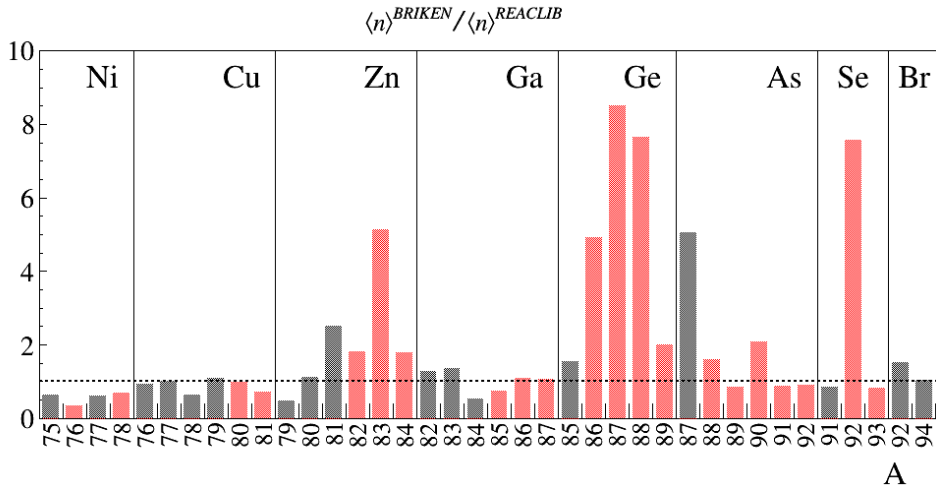


Figure 5.29: Ratio of $\langle n \rangle$ (i.e., $P_{1n} + 2P_{2n}$) values obtained in this Thesis work, and the ones included in JINA REACLIB database [REACLIB]. REACLIB database includes experimental values from [WC17], corresponding to black-filled bars, or theoretical estimates from [Möll03, Mum16a], represented by red-filled bars.

Fig. 5.30 shows a comparison of experimental half-lives and the ones included in JINA REACLIB database [REACLIB]. As previously explained in the analysis and result chapters in this work we only quote a half-live value if our result improves the result of previous measurements, otherwise our result confirms the recommended value of the evaluation [BdN-IAEA] which is the one taken. The half-life of isotopes ^{89}Ge , $^{88-92}\text{As}$, $^{91-93}\text{Se}$ is measured for the first time, and we improve the values for $^{80-81}\text{Cu}$, ^{87}Ga and ^{94}Br . JINA REACLIB database includes experimental values from [WC17] and theoretical ones from [Möll03]. Experimental values included

in REACLIB (black-filled bars in Fig. 5.30) agree with the results from the data evaluation [BdN-IAEA], except for isotopes ^{93}Se and ^{94}Br , which are 2 and 4 times larger respectively in REACLIB than our results. In general, REACLIB theoretical estimates of half-lives (red-filled bars in Fig. 5.30) are larger than the values obtained or confirmed in this Thesis work, except for isotopes ^{89}Ge and ^{90}As .

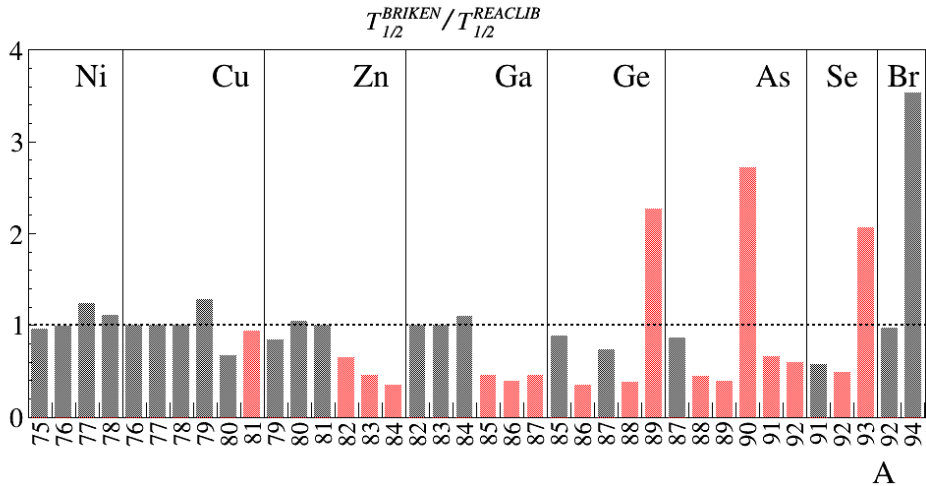


Figure 5.30: ratio of $T_{1/2}(\text{Exp})$ and $T_{1/2}(\text{[REACLIB]})$.

Figure 5.31: Ratio of half-lives values obtained in this Thesis work, and the ones included in JINA REACLIB database [REACLIB]. REACLIB database includes experimental values from [WC17], corresponding to black-filled bars, or theoretical estimates from [Möl03], represented by red-filled bars.

In the following, final abundances calculated using different trajectories are shown. The abundance of elements with atomic mass A , denoted by $Y(A)$, is calculated as in Eq. 5.1, where $\rho(A)$ corresponds to the mass density of all the elements with atomic mass A , and ρ_{tot} to the total mass density.

$$Y(A) = \frac{1}{A} \frac{\rho(A)}{\rho_{tot}} \quad (5.1)$$

The calculated abundance patterns are normalized as $\sum Y_i A_i = 1$ (mass conservation). Solar System (SS) r-process abundances from Sneden et al. [Sne08] are plotted as reference, being normalized to 100 at silicon. Because of the different normalization the comparison of both abundances is restricted to the shape.

5.2.1 Core-collapse supernova

Stellar evolution of massive stars ends with a supernova explosion. During the collapse, the core of the star becomes a neutron star or a black hole. Recent calculations which implement multidimensional hydrodynamics and refined neutrino transport suggest that core neutrino emission is the main cause of the explosion. However, it is generally found that the neutron richness of the neutrino-wind ejecta is not enough to produce a complete r-process abundance pattern, that is one reaching $A \sim 210$. That is the case of trajectories produced by Bliss et al. [Bli18], which correspond to neutrino-driven supernova jets. The corresponding r-process path proceeds close to stability and the nuclei studied in this Thesis work are never reached, so no impact is found.

An additional mechanism, which requires strong magnetic fields and a high spin rate, can produce a polar ejection. The material is expelled before neutrinos decrease the neutron-to-seed ratio, and therefore a complete r-process nucleosynthesis can be achieved according to numerical simulations. This mechanism was studied only recently, when computing power was enough to run 2D and 3D magneto-hydrodynamical calculations.

The impact of experimental half-lives and neutron emission probabilities presented in Chap. 4 is evaluated for three different trajectories corresponding to a magneto-rotationally driven supernova explosion. One of them correspond to the work which was carried out by Winteler et al. [Win12]. In this case, r-process starts close to the nuclei studied in this Thesis. The heaviest isotopes of nickel and zinc are present briefly when temperature is still around 3 GK, but then matter flows towards heavier nuclei as temperature drops. Final abundances, which are shown in Fig. 5.32, reproduce the structure between the second and third r-process peaks around mass 130 and 190 respectively, but underproduce elements lighter than mass 130. The relative difference of the abundance pattern produced using the default REACLIB database and the one updated with our BRIKEN experimental values is shown in the lower panel of Fig. 5.32, calculated as in Eq. 5.2.

$$\Delta_A = \frac{Y_A^{BRIKEN} - Y_A^{REACLIB}}{Y_A^{REACLIB}} \quad (5.2)$$

The process path proceeds further away from the stability than the nuclei studied in this Thesis work, and therefore their impact is limited to a local redistribution of the final abundances at masses $A = 75 - 95$, as can be seen in the lower panel of Fig. 5.32.

The other two trajectories correspond also to magneto-rotationally driven supernova explosion, calculated by Obergaulinger [Obe17]. This work includes an improved treatment of several key features, namely neutrino transport, magneto-hydrodynamics and the relativistic gravitational potential. However, magneto-hydrodynamic simulations are modeled in two dimensions, and it may affect the result. Both trajectories corresponds to a progenitor mass of $28 M_\odot$, with

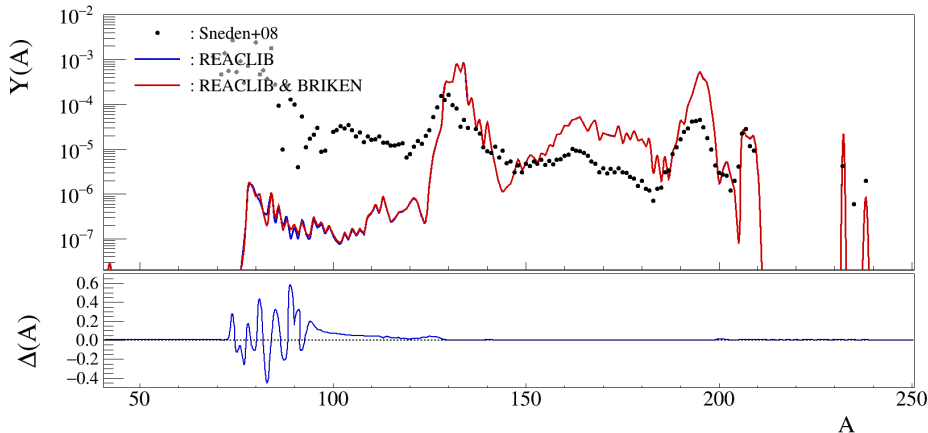


Figure 5.32: Abundance pattern corresponding to the representative trajectory studied in [Win12], and calculated using the default REACLIB (*REACLIB*) and the REACLIB database updated with the results presented in this Thesis (*REACLIB & BRIKEN*).

a non-convective iron core whose mass is $2.1 M_{\odot}$, and a very strong magnetic field of 10^{12} G. Given the combination of such strong magnetic field and rapid rotation, the supernova explosion is not driven by neutrinos, but magneto-rotationally. The relativistic jets are expelled on polar directions. One of the trajectories produce a complete r-process abundance pattern, as it is shown in Fig. 5.33. Similarly to the previous trajectory the contribution to the nucleosynthesis below the second peak is very small: some of the nuclei of interest appear briefly at the beginning of the simulation, but then the process moves to heavier elements. However, as seen in the lower panel of Fig. 5.33 the impact of our data on abundances is larger than in the previous case and extends to higher masses, between mass 75 and 130.

Fig. 5.34 represents the elemental abundance pattern calculated following another trajectory from the same astrophysical event aforementioned. In this case, temperature is higher at the beginning, and the r-process path starts between the stability and the nuclei studied in this Thesis work. As before, the neutron capture process move towards heavier masses when temperature goes below 3 GK, and only the lighter nuclei of interest are produced for a short time, some of them at the very end. As it can be seen in Fig. 5.34, the final abundances reproduce well SS r-process residuals for elements of the first r-process peak and up to mass $A \sim 130$ but fails to synthesize elements beyond. These are the typical characteristics of a so-called weak r-process. The relative differences between using the default nuclear database and the one updated with experimental values from Chap. 4 are shown in the lower panel of Fig. 5.34. As in the previous trajectory, there is a significant

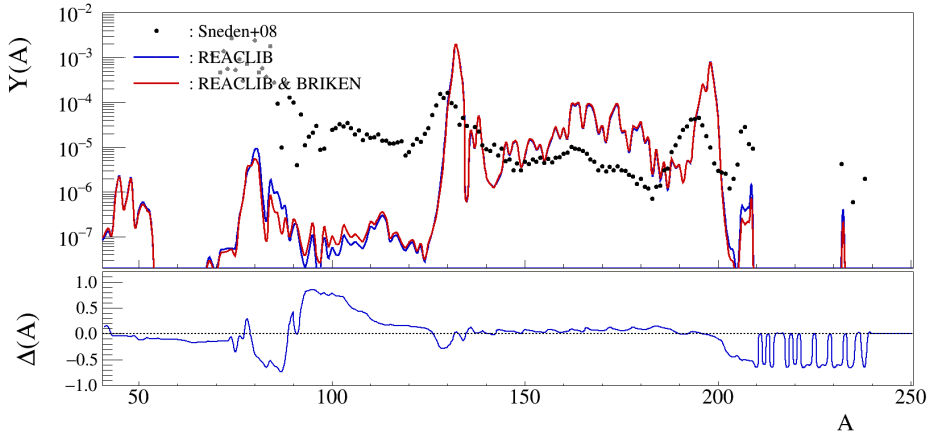


Figure 5.33: R-process abundance pattern calculated in the astrophysical scenario named *350C-RS*, from [Obe17]. The pattern labeled as *REACLIB* is calculated using the default REACLIB, and the one tagged with *REACLIB & BRIKEN* corresponds to REACLIB database updated with the results presented in this Thesis.

increase in the final yields for elements with mass between 90 and 130 when our data is used.

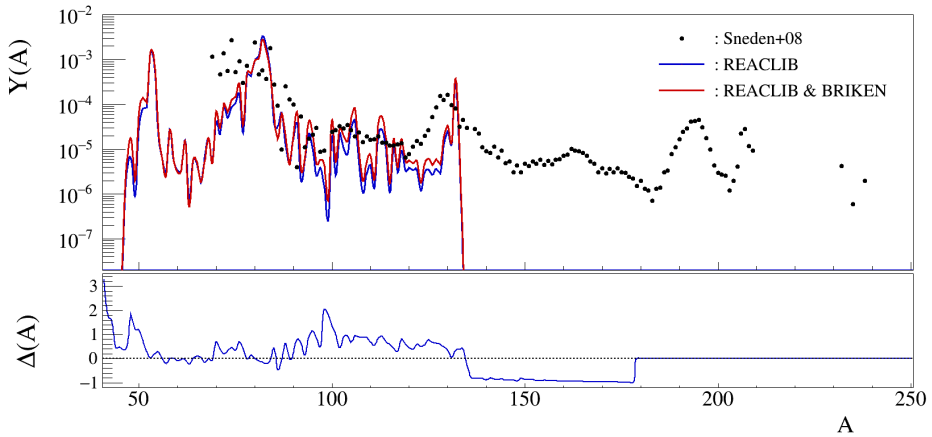


Figure 5.34: Weak r-process abundance pattern produced by the astrophysical scenario named *350C-RS*, from [Obe17].

5.2.2 Neutron star mergers

A neutron star is the remnant of a massive star core after its supernova explosion. A binary system made up of two neutron star loses energy in form of gravitational waves, and eventually merges. Before colliding, stars may be teared apart by tidal forces, and cold neutron-rich material may be expelled. Trajectories corresponding to this cold dynamical ejecta push abundance evolution to the neutron drip line and lighter r-process elements are marginally produced. A representative trajectory of this ejecta was investigated by Korobkin et al. [Kor12b]. The nuclei studied in this Thesis work are never synthesized during the r-process trajectory, hence no impact is found. When neutron stars make contact, a huge amount of hot and very neutron-rich matter is also ejected. These kind of ejecta, so called hot dynamical ejecta, are studied by Bovard et al. [Bov17]. Their calculations implement a fully relativistic treatment of hydrodynamic evolution, and adopt the so-called neutrino leakage scheme, which reproduce neutrino cooling but disregards its interaction with matter. Two trajectories from this work are used to investigate the impact of the experimental values of half-lives and neutron emission probabilities obtained in this Thesis. One of them, numbered as #517, correspond to very hot dynamically ejected matter. As it can be seen in Fig. 5.35 the nucleosynthesis reaches the heaviest elements although the contribution of elements with mass below $A \sim 130$ is very small. The impact of our data is quite low and restricted to elements in the mass region $A = 75 - 95$. In this case, the r-process proceeds further away from the stability than the nuclei studied in this Thesis work. However, these nuclei have a secondary role once the neutron capture ends while all the produced nuclei decay back to stability, causing a local redistribution of the final abundances. This local effect on elements with mass between 75 and 95, which is caused when the r-process path proceeds further from stability than the nuclei studied in this Thesis, is also observed in other previously presented calculations, like the one from Winteler et al. [Win12] shown in Fig. 5.32.

Another trajectory from [Bov17], numbered as #651, corresponds also to dynamical ejecta. The initial temperature is lower than in the previous trajectory, so the r-process can start further from the stability. Elements from the first to the third abundance peak are produced and the shape of final abundance distribution resembles the SS residuals. As before, the r-process path proceeds through nuclei which are more exotic than the ones studied in this Thesis work, and therefore the impact of our data is restricted to elements with mass $A = 75 - 95$, as it is shown in the lower panel of Fig. 5.36.

After the merger, an accretion disk is formed around the central object. This central object may be another neutron star or an hyper massive neutron star, which eventually collapse to a black hole. Viscous effects inside the disk, in addition to neutrino-winds coming from the central neutron star, can be an efficient ejection mechanism. Nucleosynthesis in neutrino-wind ejecta is studied by Martin et al. [Mar15]. A three dimensional hydrodynamic simulation is used to obtain the

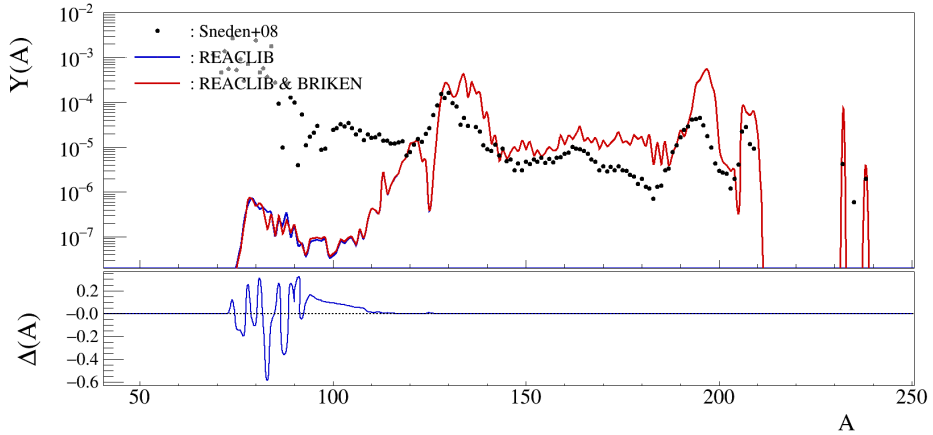


Figure 5.35: Abundance pattern produced by dynamic ejecta, trajectory number #517 from [Bov17].

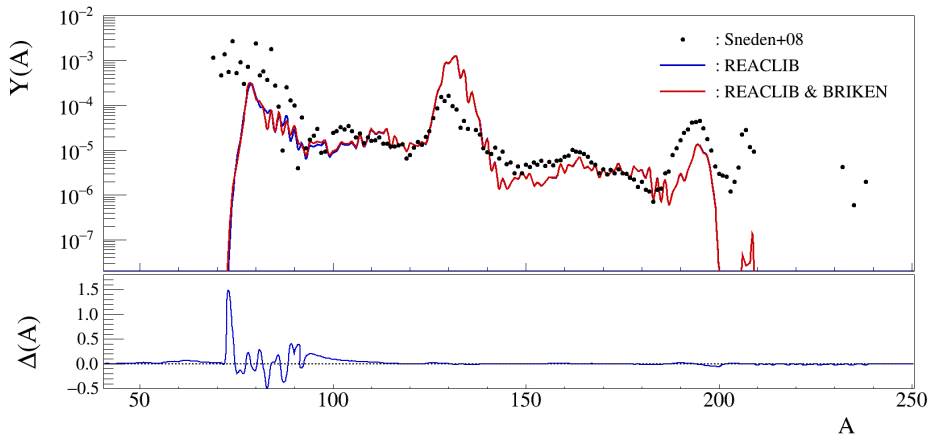


Figure 5.36: Abundance pattern produced by dynamic ejecta, trajectory number #651 from [Bov17].

thermodynamical trajectories. The neutrino-matter interactions are included by using the multiflavour Advanced Spectral Leakage scheme. Given the opacity of the disk, the neutrino luminosity is three time larger in the polar direction than in the equator, and therefore the neutrino-wind ejecta is expelled for latitudes larger than 30° . Given the angular distribution, hydrodynamical trajectories are grouped in four angular bins, as it is shown in Fig. 5.37. The impact of experimental results is evaluated for each angular bin representative trajectory. Each trajectory has

different properties. For example, neutron richness increase for material ejected further from the polar directions, and thus heavier elements can be synthesized.

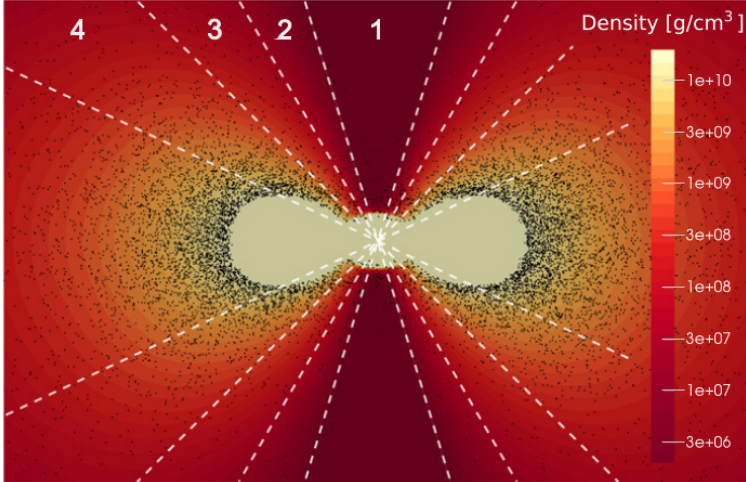


Figure 5.37: Density profile in $x - z$ plane at the beginning of the simulation. One representative thermodynamic trajectory is chosen for each angular bin (Fig. 2 from [Mar15]).

The most neutron-rich ejecta corresponds to the representative trajectory of the fourth bin. Among the nuclei studied in this Thesis work, only the less exotic isotopes between nickel and gallium are synthesized briefly at the beginning of the process. The final abundances using the default input and the updated one, as well as the relative differences, is shown in Fig. 5.38. The yield variation at mass 86 is caused by the lighter isotopes of germanium, which are on the border of r-process path, and the lighter isotopes of arsenic which are produced at the very end.

The third bin trajectory is less neutron rich, so neutrons are exhausted before synthesizing nuclei with $N=82$ and therefore second abundance peak is not formed. The path settles on the gallium and germanium isotopes studied in this Thesis work. In addition, once the neutron capture ends and the produced nuclei decay back to stability, arsenic isotopes appear and have a secondary function redistributing the final abundances. Elemental abundances corresponding to this trajectory are shown in Fig. 5.39. As it can be seen in the lower panel, the impact of our experimental data extends up to mass 130, mainly because some of the updated nuclei are part of the r-process path.

Elemental abundances produced during the second angular bin representative trajectory are shown in Fig. 5.39. Similarly to the previous case, r-process path crosses some of the nuclei studied in the present work, particularly germanium and arsenic isotopes, which cause an increment in the final yields by a factor 3 for nuclei

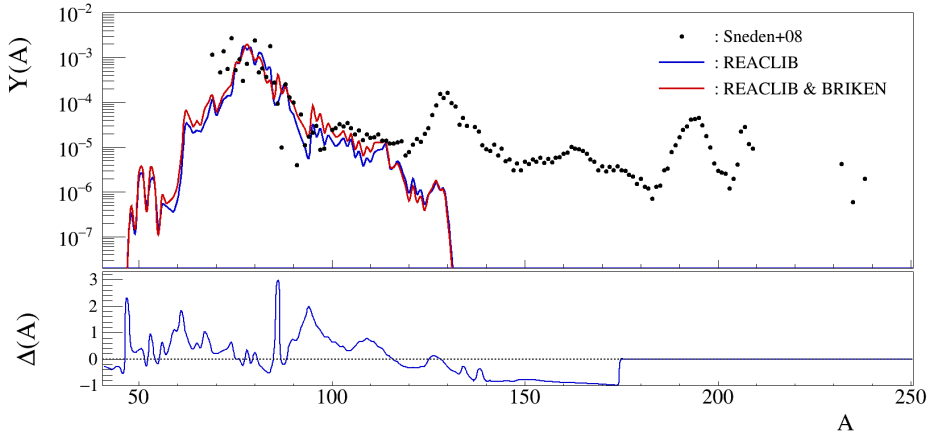


Figure 5.38: Abundance pattern produced by neutrino-wind ejecta in the aftermath of a two neutron star merger [Mar15], trajectory corresponding to fourth angular bin in Fig. 5.37.

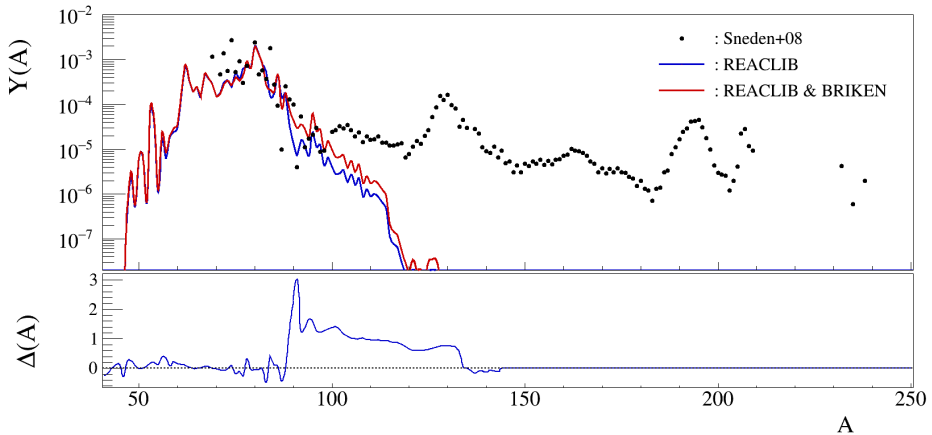


Figure 5.39: Abundance pattern produced by neutrino-wind ejecta in the aftermath of a two neutron star merger [Mar15], trajectory corresponding to third angular bin in Fig. 5.37.

with mass larger than 90. The last trajectory, corresponding to the first angular bin, is the least neutron rich, and nuclei up to mass 80 are synthesized, so the r-process does not reach the nuclei of interest and the impact is negligible.

There is another mechanism capable of ejecting material, in addition to neutron-winds and dynamical ejecta before and during the merger itself. After two

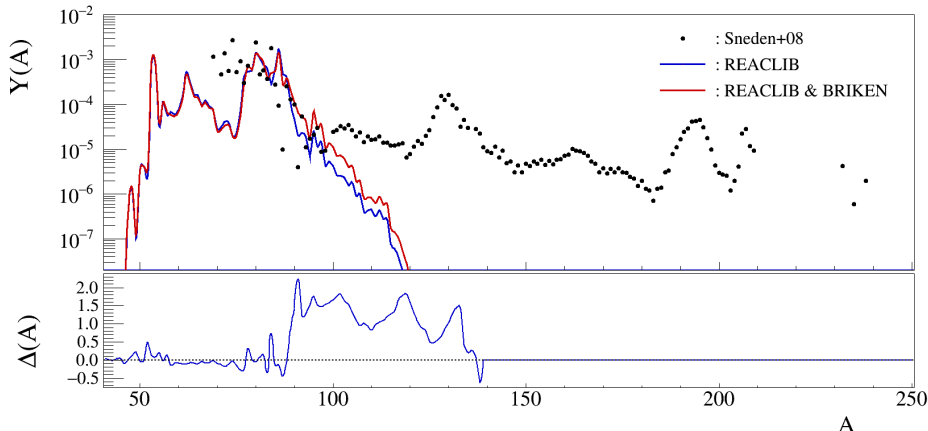


Figure 5.40: Abundance pattern produced by neutrino-wind ejecta in the aftermath of a two neutron star merger [Mar15], trajectory corresponding to second angular bin in Fig. 5.37.

neutron star or a neutron star and a black hole merge, an accretion disk is formed around the resulting central object. If this central object is a hypermassive neutron star, it may collapse into a black hole after a certain amount of time. Viscous effects can eject some material from the accretion disk, as studied by Lippuner et al. [Lip17]. Two-dimensional hydrodynamical calculations were performed to obtain the thermodynamical trajectory of these postmerger outflows. Gravity was included as a pseudo-Newtonian potential, and neutrino cooling is implemented following the leakage scheme. A strong correlation is found between the neutron richness of the ejected material and the life-time of the central massive neutron star. In addition, the longer its life, the larger amount of ejected material from the accretion disk. The impact of new experimental values presented in this Thesis work was explored in two trajectories corresponding to disk ejecta from [Lip17]. In one of them, the impact is negligible since r-process path runs very close to stability. On the contrary, the impact on the final abundances when the other trajectory is followed has some interesting features, as it can be seen in Fig. 5.41. First, a local redistribution of the final abundances in the mass region $A = 85 - 95$ is caused by the updated lighter germanium and arsenic isotopes. Secondly, the production of heavy nuclei with mass between 130 and 200 is increased by a factor 2. This global impact is originated because r-process path starts very close to the nuclei which are updated by the experimental results of the present work. Further details about the impact of our experimental values on the abundance evolution during this particular trajectory is presented in Appendix D.

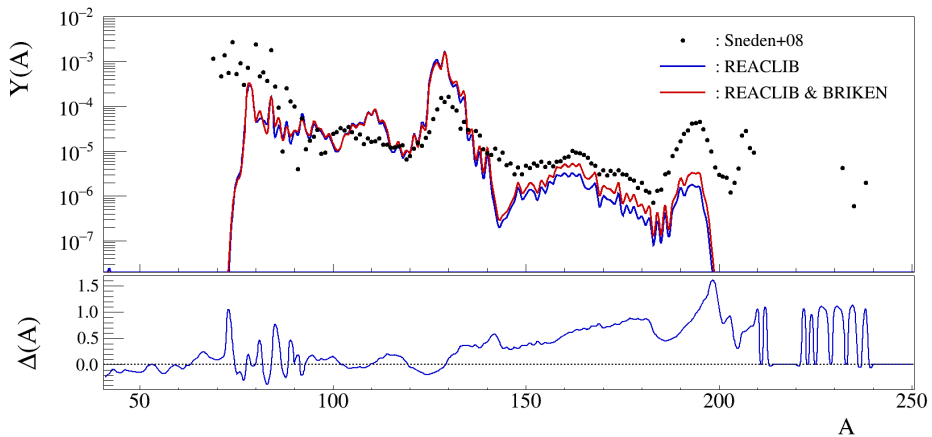


Figure 5.41: Abundance pattern produced by disk ejecta in the aftermath of a two neutron star merger, trajectory from [Lip17].

5.2.3 Summary

We have evaluated the impact of the new experimental half-lives and P_{xn} values of nuclei studied in this Thesis on the final abundances calculated using several thermodynamical trajectories corresponding to different ejecta from supernova explosions and neutron star mergers

There is a number of possible thermodynamical trajectories where our experimental data show an impact. If the isobaric progenitors of the nuclei of interest are synthesized during the r-process, a local redistribution of the final elemental abundances is found, in our case in the mass range (75, 95). This effect appears in all the cases presented in the previous section. This is important to reduce uncertainties of yields around mass 90, which are found in large different proportions in stars [Sne08].

The biggest impact happens when the measured nuclei are part of the r-process path. Changing their half-lives and P_{xn} modify how matter flows towards heavier nuclei, shifting the path itself. One example are Obergaulinger [Obe17] trajectories corresponding to magneto-rotationally driven supernova explosions, where our measured nuclei (with mass between 75 and 94) have an impact up to mass 130. The other example is the trajectory corresponding to a disk ejecta, calculated by Lippuner et al. [Lip17], where the final abundances of elements with mass between 130 and 200 are increased by a factor 2.

Chapter 6

Conclusions

The lack of experimental data limits our knowledge of the beta-delayed neutron emission. Few data is available to fully benchmark theoretical models. According to the last evaluation [BdN-IAEA], 270 P_{1n} have been measured, of which 92 correspond to nuclei lighter than nickel ($Z=28$). In addition, the site where rapid neutron capture (r -process) takes place is still not well determined, and the simulations which are used to constraint the astrophysical environment rely on theoretical models.

The aim of Beta-delayed neutrons at RIKEN (BRIKEN) collaboration is the precise measurement of neutron emission probabilities and half-lives of very neutron-rich nuclei. In the present work we have studied 37 beta-delayed neutron emitters in the mass range $A=75-94$. We have measured 39 P_{1n} , of which 12 are determined for the first time including the P_{1n} of the doubly-magic ^{78}Ni , and we have improved importantly the uncertainty of the rest. Some of the nuclei are also multi-neutron emitters, and 17 P_{2n} were measured, of which 15 are new values and we improve greatly the other two previously measured ones. This work confirm the half-lives from the last evaluation [BdN-IAEA] of 25 isotopes, and report 14 half-lives of which 7 are completely new, improving significantly the uncertainty for the rest.

The comparison with theoretical estimates show that there is no model consistent with the full set of experimental values, which should motivate a review of the nuclear models mentioned. This proves the reduced predictive power of the state-of-the-art models and the necessity of more experimental measurements.

In addition, we studied the astrophysical impact of the newly measured half-lives and neutron emission probabilities in abundance calculations of the rapid neutron capture (r -process). Half-lives and neutron emission probabilities determine the r -process path, and changes in the measured nuclei in the mass range $A=75-94$ can have an impact on the final abundances of all the elements. In particular it causes a local redistribution of abundances, while the very neutron-rich nuclei which have been synthesized during the r -process decay to stability. This is important to reduce uncertainties of yields around mass 90, which are found in large different proportions in stars [Sne08].

Appendices

Chapter A
General results

Table A.1: Number of implants of each isotope N_i , and its number of beta decays N_0 obtained from the simultaneous fit of beta and neutron-beta decay curves. ε_β is the ratio of number of decays and the number of implants.

Nuc.	N_i	N_0	$\varepsilon_\beta [\%]$	$Q_\beta [MeV]$
^{75}Co	$2.08 \cdot 10^3$	$2.46 \cdot 10^2$	11.83	10.74
^{75}Ni	$6.94 \cdot 10^4$	$1.32 \cdot 10^4$	19.05	3.91
^{76}Ni	$1.34 \cdot 10^5$	$1.85 \cdot 10^4$	13.80	4.77
^{77}Ni	$6.36 \cdot 10^4$	$1.31 \cdot 10^4$	20.55	6.11
^{78}Ni	$7.17 \cdot 10^3$	$1.64 \cdot 10^3$	22.87	6.66
^{76}Cu	$1.08 \cdot 10^5$	$2.77 \cdot 10^4$	25.74	3.51
^{77}Cu	$4.99 \cdot 10^5$	$8.69 \cdot 10^4$	17.40	5.61
^{78}Cu	$2.12 \cdot 10^6$	$5.57 \cdot 10^5$	26.23	6.22
^{79}Cu	$7.37 \cdot 10^5$	$1.84 \cdot 10^5$	25.00	7.67
^{80}Cu	$4.96 \cdot 10^4$	$1.19 \cdot 10^4$	23.97	9.16
^{81}Cu	$7.35 \cdot 10^3$	$1.78 \cdot 10^3$	24.26	12.16
^{79}Zn	$8.07 \cdot 10^5$	$2.39 \cdot 10^5$	29.59	2.20
^{80}Zn	$4.04 \cdot 10^6$	$1.13 \cdot 10^6$	28.04	2.83
^{81}Zn	$2.74 \cdot 10^6$	$6.56 \cdot 10^5$	23.95	4.95
^{82}Zn	$7.84 \cdot 10^5$	$1.92 \cdot 10^5$	24.45	7.24
^{83}Zn	$5.66 \cdot 10^4$	$1.36 \cdot 10^4$	24.10	8.57
^{84}Zn	$5.24 \cdot 10^3$	$1.17 \cdot 10^3$	22.39	9.26
^{82}Ga	$2.57 \cdot 10^5$	$6.55 \cdot 10^4$	25.47	5.29
^{83}Ga	$5.07 \cdot 10^6$	$1.38 \cdot 10^6$	27.20	8.09

Continued on next page

Appendix A. General results

Table A.1 – continued from previous page

Nuc.	N_i	N_0	$\varepsilon_\beta [\%]$	$Q_\beta [MeV]$
^{84}Ga	$2.41 \cdot 10^6$	$5.33 \cdot 10^5$	22.13	8.82
^{85}Ga	$5.69 \cdot 10^5$	$1.35 \cdot 10^5$	23.72	10.23
^{86}Ga	$3.12 \cdot 10^4$	$7.53 \cdot 10^3$	24.17	10.97
^{87}Ga	$2.60 \cdot 10^3$	$6.39 \cdot 10^2$	24.56	12.08
^{85}Ge	$8.05 \cdot 10^4$	$2.07 \cdot 10^4$	25.68	4.66
^{86}Ge	$6.10 \cdot 10^6$	$1.53 \cdot 10^6$	25.13	5.72
^{87}Ge	$1.37 \cdot 10^6$	$3.35 \cdot 10^5$	24.47	6.81
^{88}Ge	$1.98 \cdot 10^5$	$4.91 \cdot 10^4$	24.80	7.41
^{89}Ge	$5.70 \cdot 10^3$	$1.38 \cdot 10^3$	24.27	8.92
^{88}As	$1.57 \cdot 10^5$	$4.29 \cdot 10^4$	27.39	7.64
^{89}As	$2.27 \cdot 10^6$	$5.98 \cdot 10^5$	26.30	9.02
^{90}As	$2.12 \cdot 10^5$	$5.40 \cdot 10^4$	25.44	9.59
^{91}As	$2.91 \cdot 10^4$	$7.56 \cdot 10^3$	25.96	10.83
^{92}As	$6.58 \cdot 10^2$	$1.64 \cdot 10^2$	24.92	11.53
^{91}Se	$5.27 \cdot 10^4$	$1.40 \cdot 10^4$	26.59	5.35
^{92}Se	$2.98 \cdot 10^5$	$8.46 \cdot 10^4$	28.34	6.31
^{93}Se	$1.47 \cdot 10^4$	$3.97 \cdot 10^3$	27.03	7.45
^{94}Br	$3.03 \cdot 10^3$	$3.90 \cdot 10^2$	12.87	8.67

Table A.2: Number of beta, $\beta 1n$ and $2n$ -beta decays of all isotopes (background subtracted), and its ratio to background. The total background is formed by an uncorrelated background, that is originated by accidental time-correlations of an implant with non-physically correlated decay events, plus a correlated background in case of beta-one-neutron or beta-two-neutron decay curves, which is caused by correlation of a beta decay with one or more neutrons that do not come from the decay (see Sec. 3.7.2 for further details).

Nuc.	N_β	$N_{\beta 1n}$	$N_{\beta 2n}$	$(\frac{N}{B})_\beta$	$(\frac{N}{B})_{\beta 1n}$	$(\frac{N}{B})_{\beta 2n}$
^{75}Co	$8.1 \cdot 10^2$	$3.8 \cdot 10^1$	—	0.24	0.12	—
^{75}Ni	$3.1 \cdot 10^4$	$6.9 \cdot 10^2$	—	0.21	0.14	—
^{76}Ni	$4.9 \cdot 10^4$	$1.7 \cdot 10^3$	—	0.20	0.09	—

Continued on next page

Table A.2 – continued from previous page

Nuc.	N_β	$N_{\beta 1n}$	$N_{\beta 2n}$	$(\frac{N}{B})_\beta$	$(\frac{N}{B})_{\beta 1n}$	$(\frac{N}{B})_{\beta 2n}$
⁷⁷ Ni	$3.9 \cdot 10^4$	$3.4 \cdot 10^3$	—	0.31	0.36	—
⁷⁸ Ni	$5.5 \cdot 10^3$	$6.1 \cdot 10^2$	—	0.31	0.45	—
⁷⁶ Cu	$4.8 \cdot 10^4$	$1.1 \cdot 10^3$	—	0.18	0.14	—
⁷⁷ Cu	$1.8 \cdot 10^5$	$1.5 \cdot 10^4$	—	0.15	0.17	—
⁷⁸ Cu	$1.4 \cdot 10^6$	$1.3 \cdot 10^5$	—	0.31	0.39	—
⁷⁹ Cu	$5.1 \cdot 10^5$	$6.5 \cdot 10^4$	—	0.28	0.45	—
⁸⁰ Cu	$3.6 \cdot 10^4$	$3.9 \cdot 10^3$	$1.1 \cdot 10^1$	0.29	0.38	0.03
⁸¹ Cu	$5.7 \cdot 10^3$	$8.1 \cdot 10^2$	$1.4 \cdot 10^1$	0.31	0.48	0.22
⁷⁹ Zn	$4.9 \cdot 10^5$	$1.0 \cdot 10^3$	—	0.23	0.02	—
⁸⁰ Zn	$2.4 \cdot 10^6$	$1.6 \cdot 10^4$	—	0.19	0.02	—
⁸¹ Zn	$1.6 \cdot 10^6$	$1.2 \cdot 10^5$	—	0.21	0.17	—
⁸² Zn	$5.0 \cdot 10^5$	$8.9 \cdot 10^4$	—	0.23	0.44	—
⁸³ Zn	$3.9 \cdot 10^4$	$8.3 \cdot 10^3$	$1.1 \cdot 10^2$	0.25	0.56	0.19
⁸⁴ Zn	$3.7 \cdot 10^3$	$8.8 \cdot 10^2$	$6.1 \cdot 10^0$	0.27	0.64	0.11
⁸² Ga	$1.2 \cdot 10^5$	$9.8 \cdot 10^3$	—	0.18	0.41	—
⁸³ Ga	$2.5 \cdot 10^6$	$5.4 \cdot 10^5$	—	0.18	0.40	—
⁸⁴ Ga	$1.4 \cdot 10^6$	$1.3 \cdot 10^5$	$3.3 \cdot 10^3$	0.19	0.19	0.15
⁸⁵ Ga	$3.6 \cdot 10^5$	$6.8 \cdot 10^4$	$8.3 \cdot 10^2$	0.22	0.44	0.15
⁸⁶ Ga	$1.9 \cdot 10^4$	$4.0 \cdot 10^3$	$2.5 \cdot 10^2$	0.23	0.47	0.82
⁸⁷ Ga	$1.8 \cdot 10^3$	$4.4 \cdot 10^2$	$2.3 \cdot 10^1$	0.27	0.69	0.91
⁸⁵ Ge	$4.1 \cdot 10^4$	$8.5 \cdot 10^3$	—	0.14	0.33	—
⁸⁶ Ge	$3.4 \cdot 10^6$	$6.1 \cdot 10^5$	—	0.21	0.40	—
⁸⁷ Ge	$8.0 \cdot 10^5$	$1.9 \cdot 10^5$	$3.3 \cdot 10^2$	0.24	0.59	0.03
⁸⁸ Ge	$1.4 \cdot 10^5$	$2.9 \cdot 10^4$	$8.7 \cdot 10^1$	0.29	0.64	0.05
⁸⁹ Ge	$4.4 \cdot 10^3$	$9.4 \cdot 10^2$	$1.2 \cdot 10^1$	0.31	0.70	0.22
⁸⁸ As	$8.5 \cdot 10^4$	$1.4 \cdot 10^4$	$7.9 \cdot 10^1$	0.19	0.36	0.06
⁸⁹ As	$1.4 \cdot 10^6$	$3.1 \cdot 10^5$	$5.6 \cdot 10^2$	0.29	0.69	0.03
⁹⁰ As	$1.5 \cdot 10^5$	$2.9 \cdot 10^4$	$1.1 \cdot 10^3$	0.33	0.66	0.46
⁹¹ As	$2.3 \cdot 10^4$	$4.9 \cdot 10^3$	$5.9 \cdot 10^1$	0.39	0.87	0.17
⁹² As	$5.5 \cdot 10^2$	$9.9 \cdot 10^1$	$1.3 \cdot 10^1$	0.45	0.71	3.72

Continued on next page

Table A.2 – continued from previous page

Nuc.	N_β	$N_{\beta 1n}$	$N_{\beta 2n}$	$(\frac{N}{B})_\beta$	$(\frac{N}{B})_{\beta 1n}$	$(\frac{N}{B})_{\beta 2n}$
^{91}Se	$3.3 \cdot 10^4$	$3.9 \cdot 10^3$	–	0.26	0.34	–
^{92}Se	$2.5 \cdot 10^5$	$3.1 \cdot 10^4$	–	0.42	0.57	–
^{93}Se	$1.4 \cdot 10^4$	$2.0 \cdot 10^3$	$1.2 \cdot 10^1$	0.50	0.72	0.06
^{94}Br	$1.1 \cdot 10^3$	$1.7 \cdot 10^2$	–	0.15	0.27	–

Neutron detection efficiency for each isotope

A simple model was presented in Sec. 3.6 to account for a isotope dependent neutron detection efficiency. The values corresponding to individual isotopes, which appear in one or more decay chains, are presented in Tab. B.1-B.2. Although the central value of the efficiency does not deviates severely from the nominal value 66.8% even for the largest $Q_{\beta 1n}$, the ample error bars should ensure that any isotope dependency is within the error band. The neutron detection efficiency for $^{83,84}\text{Ga}$ isotopes is not presented in this table because the value which was used is calculated using measured neutron energy spectra [Mad16] and Monte Carlo simulated efficiency as a function of E_n .

Table B.1: Neutron efficiency estimated from $Q_{\beta 1n}$.

Nuclide	$Q_{\beta 1n}$ [MeV]	ε_v [%]	σ^- [%]	σ^+ [%]
^{92}Rb	0.81	67.47	0.09	0.03
^{92}Kr	0.90	67.46	0.11	0.04
^{87}Se	1.13	67.45	0.16	0.04
^{79}Ga	1.24	67.44	0.19	0.04
^{87}Br	1.30	67.44	0.20	0.04
^{84}As	1.42	67.43	0.24	0.05
^{88}Br	1.92	67.37	0.50	0.10
^{88}Se	1.94	67.37	0.50	0.10
^{93}Rb	2.18	67.33	0.64	0.12
^{79}Zn	2.20	67.33	0.65	0.13
^{80}Ga	2.23	67.33	0.67	0.13
^{93}Kr	2.57	67.28	0.88	0.17
^{80}Zn	2.83	67.25	1.06	0.20

Continued on next page

Table B.1 – continued from previous page

Nuclide	$Q_{\beta 1n}$ [MeV]	ε_v [%]	σ^- [%]	σ^+ [%]
^{94}Kr	3.20	67.17	1.31	0.25
^{75}Cu	3.21	67.17	1.32	0.25
^{89}Br	3.35	67.13	1.41	0.29
^{84}Ge	3.45	67.09	1.48	0.32
^{94}Rb	3.45	67.09	1.48	0.32
^{76}Cu	3.51	67.07	1.52	0.33
^{89}Se	3.65	67.02	1.61	0.37
^{81}Ga	3.84	66.96	1.74	0.42
^{75}Ni	3.91	66.93	1.78	0.44
^{90}Se	4.40	66.76	2.06	0.58
^{90}Br	4.46	66.74	2.09	0.60
^{85}Ge	4.66	66.67	2.20	0.65
^{85}As	4.69	66.66	2.21	0.66
^{76}Ni	4.77	66.63	2.26	0.69
^{81}Zn	4.95	66.56	2.37	0.75
^{82}Ga	5.29	66.43	2.57	0.86
^{91}Se	5.35	66.40	2.61	0.88
^{86}As	5.38	66.39	2.62	0.89
^{77}Cu	5.61	66.30	2.76	0.97
^{86}Ge	5.72	66.25	2.84	1.00
^{91}Br	5.78	66.23	2.88	1.02
^{77}Ni	6.11	66.10	3.13	1.14
^{78}Cu	6.22	66.06	3.22	1.17
^{92}Se	6.31	66.02	3.28	1.20
^{78}Ni	6.66	65.86	3.47	1.32
^{92}Br	6.67	65.85	3.48	1.32
^{87}Ge	6.81	65.78	3.53	1.37
^{87}As	6.81	65.78	3.54	1.37
^{82}Zn	7.24	65.56	3.71	1.51
^{88}Ge	7.41	65.48	3.83	1.57

Continued on next page

Table B.1 – continued from previous page

Nuclide	$Q_{\beta 1n}$ [MeV]	ε_v [%]	σ^- [%]	σ^+ [%]
⁹³ Se	7.45	65.46	3.85	1.58
⁸⁸ As	7.64	65.36	3.99	1.64
⁷⁹ Cu	7.67	65.35	4.01	1.65
⁹³ Br	7.81	65.27	4.12	1.70
⁸³ Zn	8.57	64.91	4.52	1.93
⁹⁴ Br	8.67	64.87	4.55	1.96
⁸⁹ Ge	8.92	64.76	4.63	2.03
⁸⁹ As	9.02	64.71	4.65	2.06
⁸⁰ Cu	9.16	64.65	4.64	2.09
⁸⁴ Zn	9.26	64.60	4.64	2.12
⁹⁰ As	9.59	64.46	4.63	2.21
⁸⁵ Ga	10.23	64.15	4.98	2.39
⁷⁵ Co	10.74	63.90	5.30	2.55
⁹¹ As	10.83	63.85	5.26	2.57
⁸⁶ Ga	10.97	63.78	5.20	2.61
⁹² As	11.53	63.50	4.96	2.78
⁸⁷ Ga	12.08	63.19	4.90	2.99
⁸¹ Cu	12.16	63.14	4.90	3.02

Table B.2: Neutron efficiency estimated from $Q_{\beta 2n}$.

Nuclide	$Q_{\beta 2n}$ [MeV]	ε_v [%]	σ^- [%]	σ^+ [%]
⁸⁸ Ge	2.68	67.27	0.96	0.18
⁸⁷ Ge	2.97	67.23	1.16	0.21
⁸⁹ As	3.49	67.08	1.50	0.33
⁸⁸ As	3.64	67.03	1.61	0.37
⁹³ Se	4.25	66.81	1.98	0.54
⁸⁴ Zn	4.86	66.60	2.32	0.72
⁸⁵ Ga	4.98	66.55	2.39	0.76
⁸⁰ Cu	5.14	66.49	2.48	0.81

Continued on next page

Table B.2 – continued from previous page

Nuclide	$Q_{\beta 2n}$ [MeV]	ε_v [%]	σ^- [%]	σ^+ [%]
^{84}Ga	5.18	66.47	2.51	0.83
^{83}Zn	5.20	66.46	2.52	0.83
^{89}Ge	5.75	66.24	2.86	1.01
^{81}Cu	5.87	66.19	2.95	1.05
^{91}As	5.95	66.16	3.01	1.08
^{90}As	6.41	65.98	3.35	1.23
^{87}Ga	7.73	65.32	4.06	1.67
^{86}Ga	7.93	65.21	4.21	1.74
^{92}As	8.68	64.86	4.55	1.96

Fits of beta decay and neutron-beta decay curves

The experimental results of this Thesis work are gathered at the end of Chap. 4. This chapter shows the plots of the simultaneous fit of β -decay and $\beta 1n$ -decay (and $\beta 2n$ -decay if corresponds) curves of the 37 nuclides investigated in this Thesis. Relative deviations of the fit with respect to the data are shown below each each fit plot. This deviations are calculated as in Eq. C.1, where $f(t)$ is the fit function and $\{t_i, y_i\}$ the experimental decay curve.

$$\text{rel. dev.} = \frac{f(t_i) - y_i}{f(t_i)} \quad (\text{C.1})$$

C.1 Fit of ^{75}Co decay curves

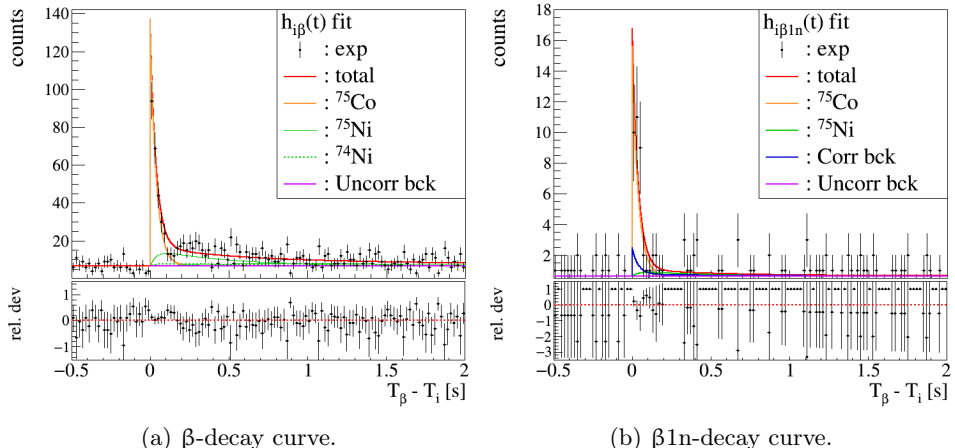


Figure C.1: Result of the simultaneous fit of β -decay and $\beta 1n$ -decay curves of ^{75}Co .

C.2 Fit of ^{75}Ni decay curves

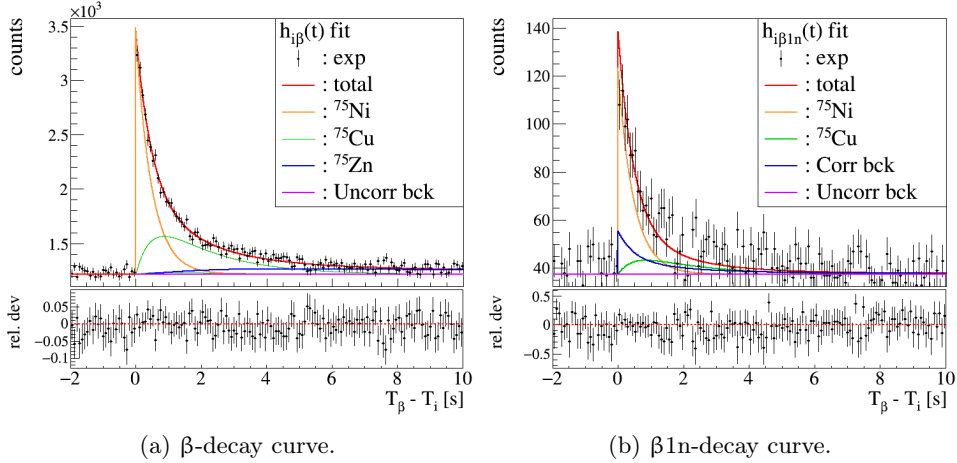


Figure C.2: Result of the simultaneous fit of β -decay and $\beta\text{1}n$ -decay curves of ^{75}Ni .

C.3 Fit of ^{76}Ni decay curves

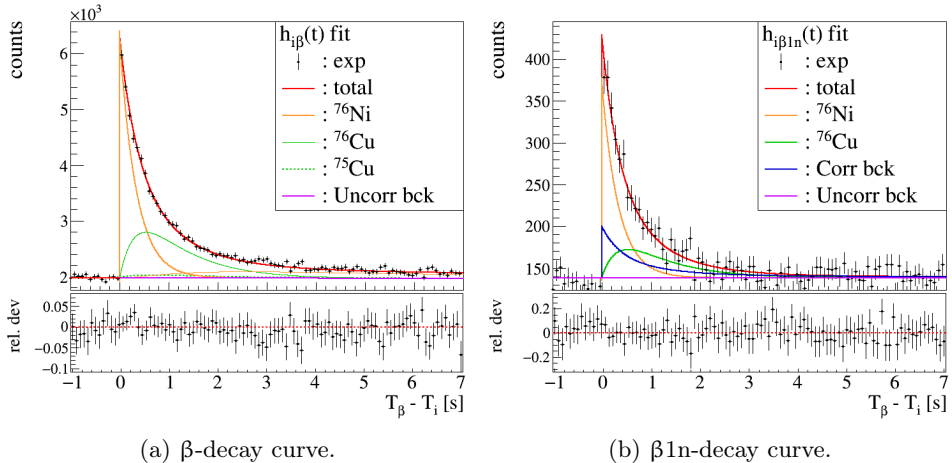


Figure C.3: Result of the simultaneous fit of β -decay and $\beta\text{1}n$ -decay curves of ^{76}Ni .

C.4 Fit of ^{77}Ni decay curves

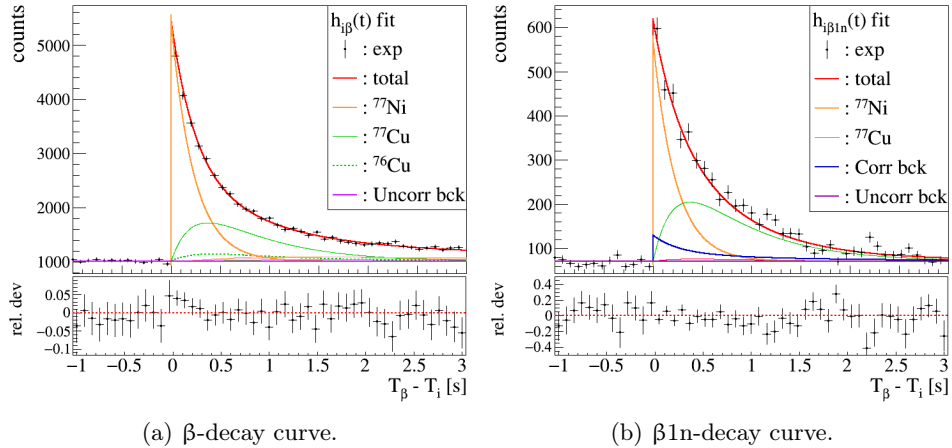


Figure C.4: Result of the simultaneous fit of β -decay and $\beta 1n$ -decay curves of ^{77}Ni .

C.5 Fit of ^{78}Ni decay curves

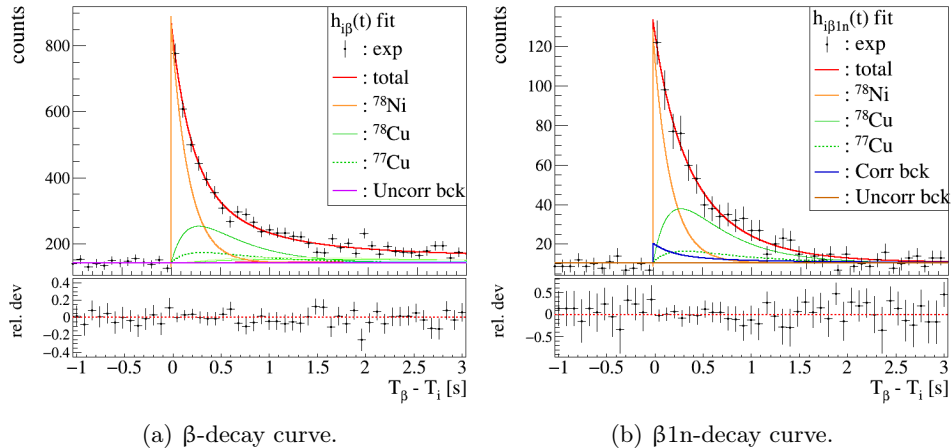


Figure C.5: Result of the simultaneous fit of β -decay and $\beta 1n$ -decay curves of ^{78}Ni .

C.6 Fit of ^{76}Cu decay curves

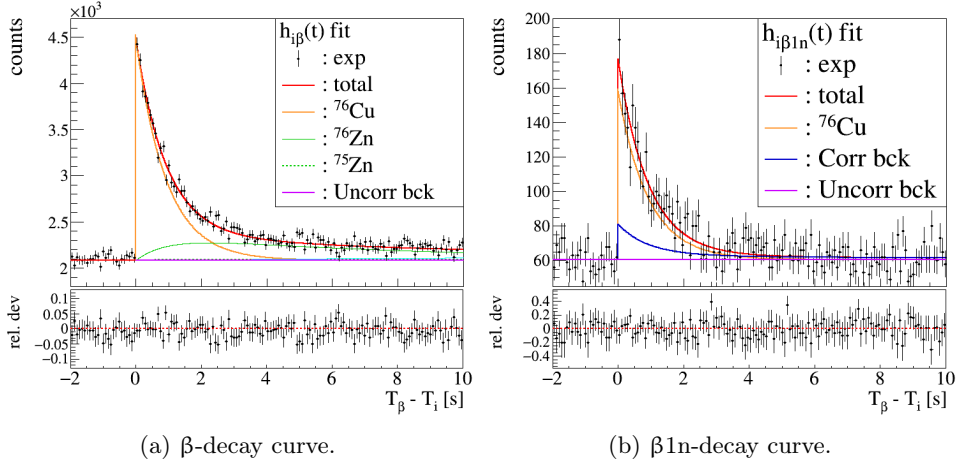


Figure C.6: Result of the simultaneous fit of β -decay and $\beta 1n$ -decay curves of ^{76}Cu .

C.7 Fit of ^{77}Cu decay curves

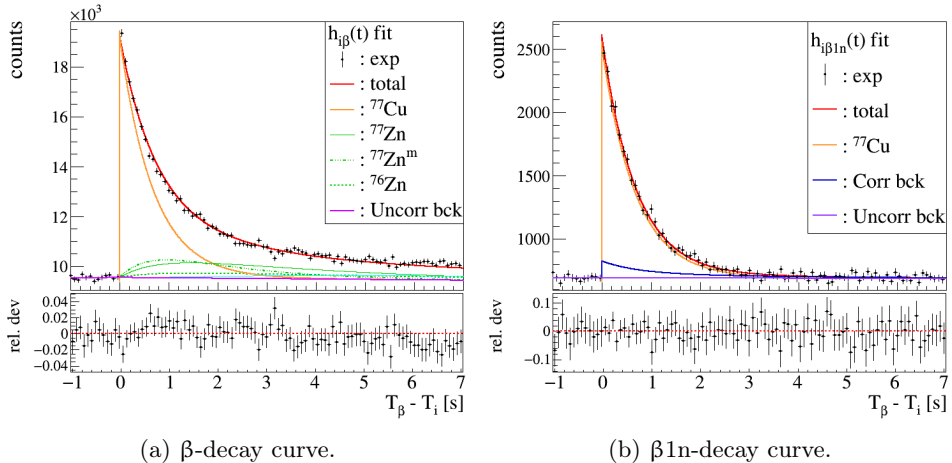


Figure C.7: Result of the simultaneous fit of β -decay and $\beta 1n$ -decay curves of ^{77}Cu .

C.8 Fit of ^{78}Cu decay curves

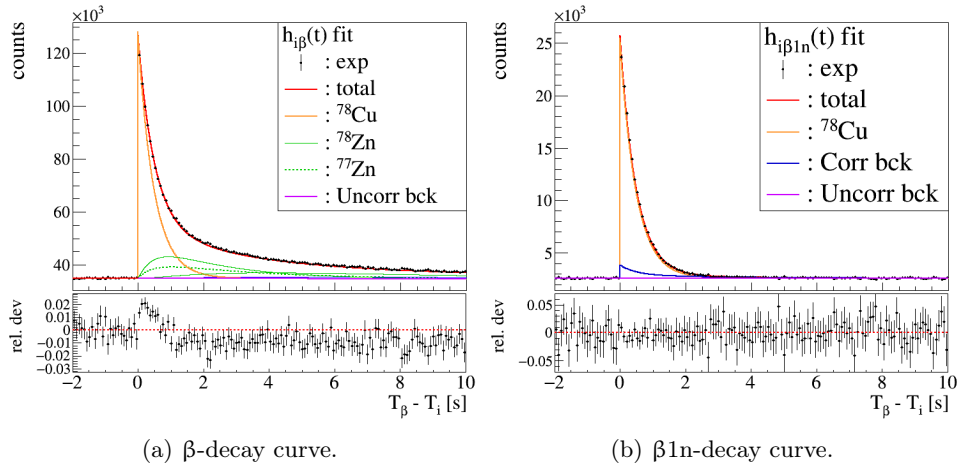


Figure C.8: Result of the simultaneous fit of β -decay and $\beta 1n$ -decay curves of ^{78}Cu .

C.9 Fit of ^{79}Cu decay curves

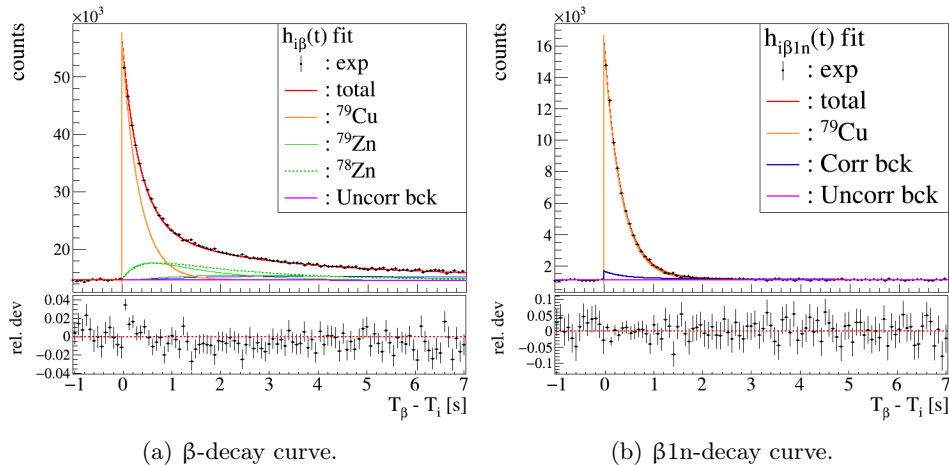


Figure C.9: Result of the simultaneous fit of β -decay and $\beta 1n$ -decay curves of ^{79}Cu .

C.10 Fit of ^{80}Cu decay curves

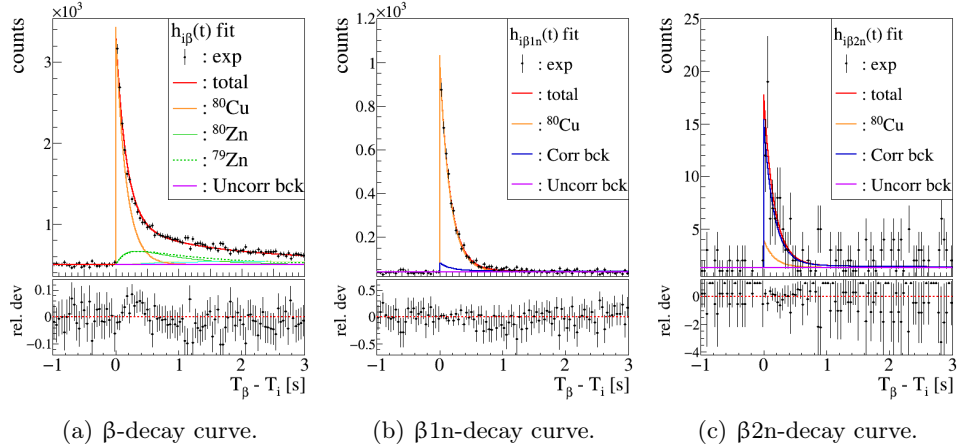


Figure C.10: Result of simultaneous fit of β , $\beta 1n$ and $\beta 2n$ -decay curves of ^{80}Cu .

C.11 Fit of ^{81}Cu decay curves

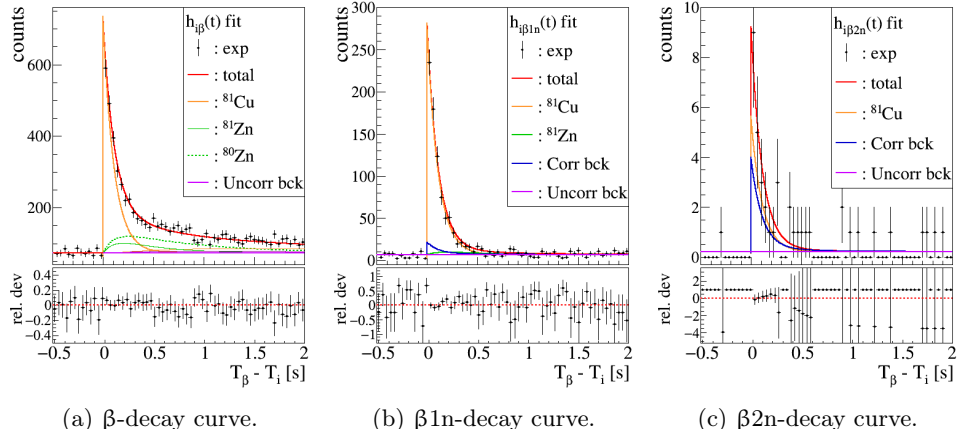


Figure C.11: Result of simultaneous fit of β , $\beta 1n$ and $\beta 2n$ -decay curves of ^{81}Cu .

C.12 Fit of ^{79}Zn decay curves

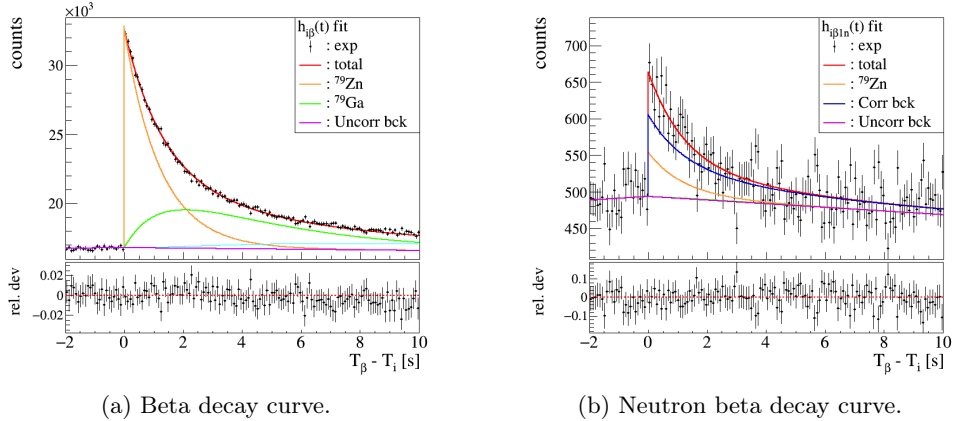


Figure C.12: Result of the simultaneous fit of β and $\beta1n$ -decay curves of ^{79}Zn .

C.13 Fit of ^{80}Zn decay curves

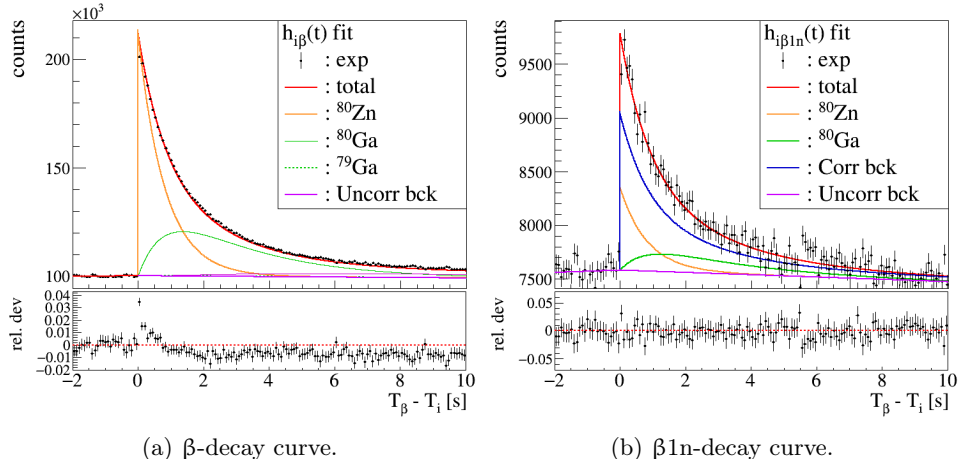


Figure C.13: Result of the simultaneous fit of β and $\beta1n$ -decay curves of ^{80}Zn .

C.14 Fit of ^{81}Zn decay curves

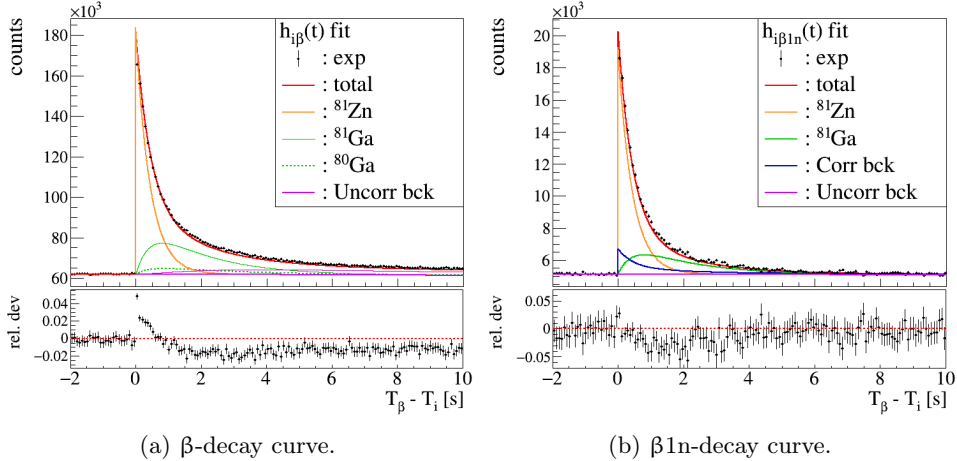


Figure C.14: Result of the simultaneous fit of β and β1n -decay curves of ^{81}Zn .

C.15 Fit of ^{82}Zn decay curves

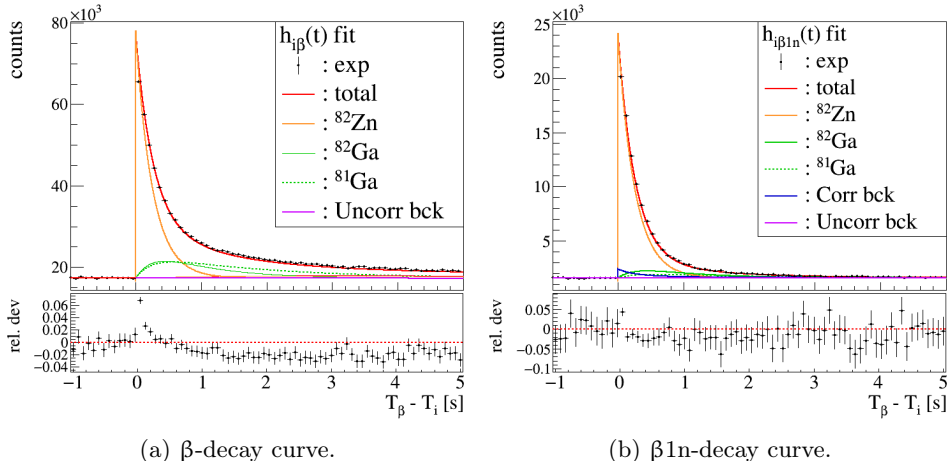


Figure C.15: Result of the simultaneous fit of β and β1n -decay curves of ^{82}Zn .

C.16 Fit of ^{83}Zn decay curves

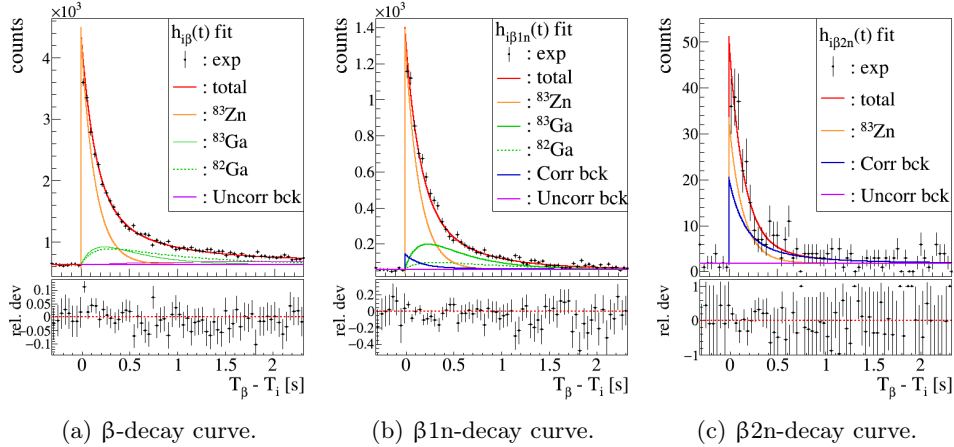


Figure C.16: Result of the simultaneous fit of β , $\beta 1n$ and $\beta 2n$ -decay curves of ^{83}Zn .

C.17 Fit of ^{84}Zn decay curves

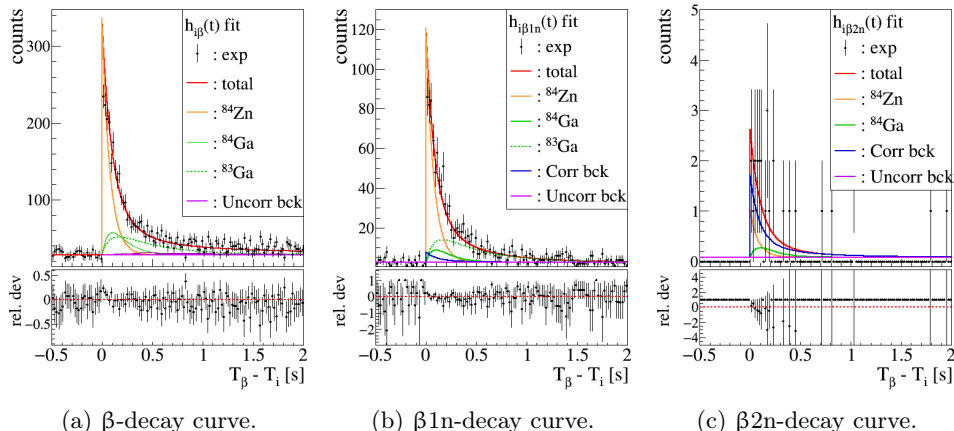


Figure C.17: Result of the simultaneous fit of β , $\beta 1n$ and $\beta 2n$ -decay curves of ^{84}Zn .

C.18 Fit of ^{82}Ga decay curves

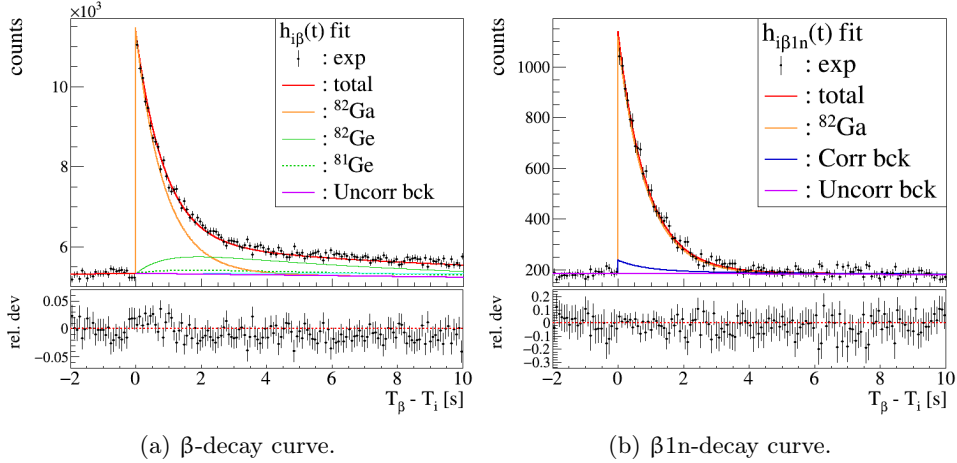


Figure C.18: Result of the simultaneous fit of β and $\beta\text{1}n$ -decay curves of ^{82}Ga .

C.19 Fit of ^{83}Ga decay curves

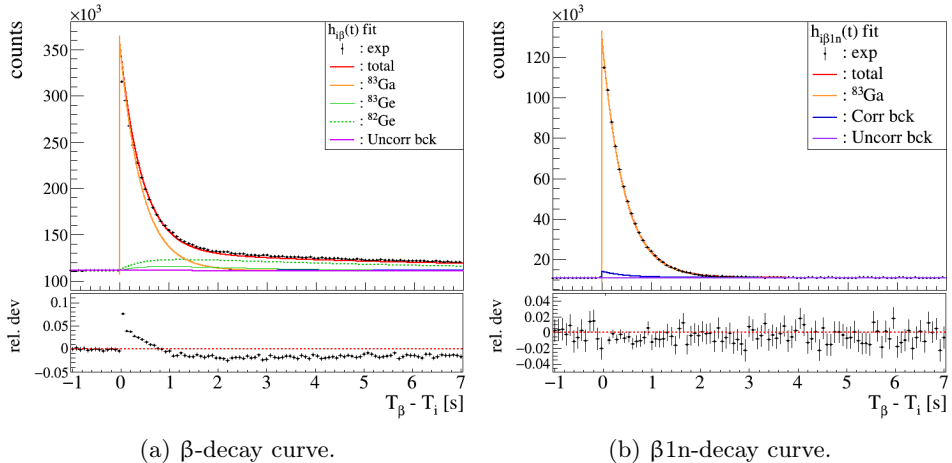


Figure C.19: Result of the simultaneous fit of β and $\beta\text{1}n$ -decay curves of ^{83}Ga .

C.20 Fit of ^{84}Ga decay curves

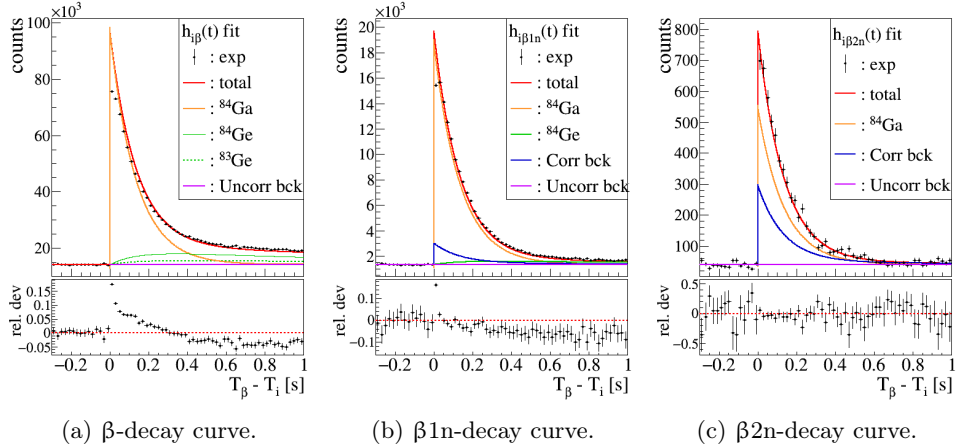


Figure C.20: Result of simultaneous fit of β , $\beta 1n$ and $\beta 2n$ -decay curves of ^{84}Ga .

C.21 Fit of ^{85}Ga decay curves

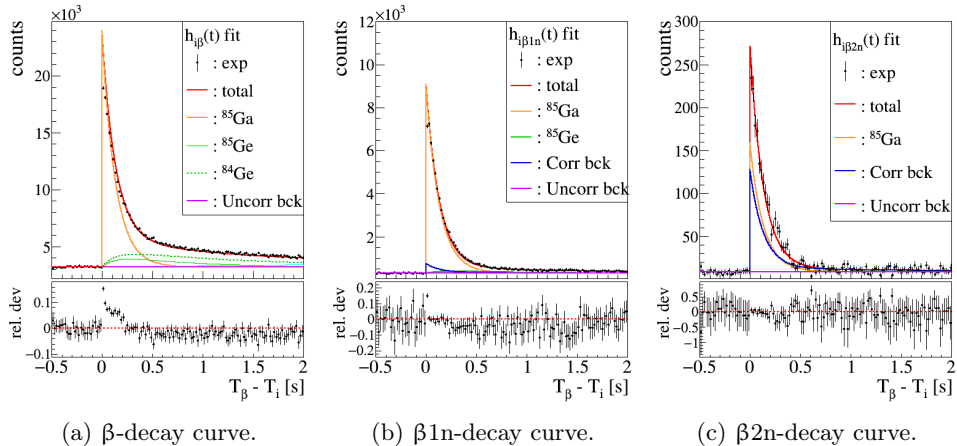


Figure C.21: Result of simultaneous fit of β , $\beta 1n$ and $\beta 2n$ -decay curves of ^{85}Ga .

C.22 Fit of ^{86}Ga decay curves

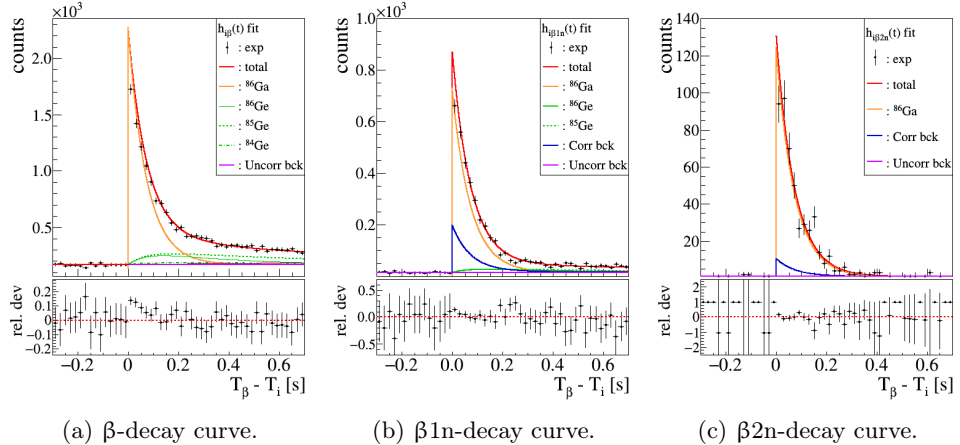


Figure C.22: Result of simultaneous fit of β , $\beta 1n$ and $\beta 2n$ -decay curves of ^{86}Ga .

C.23 Fit of ^{87}Ga decay curves

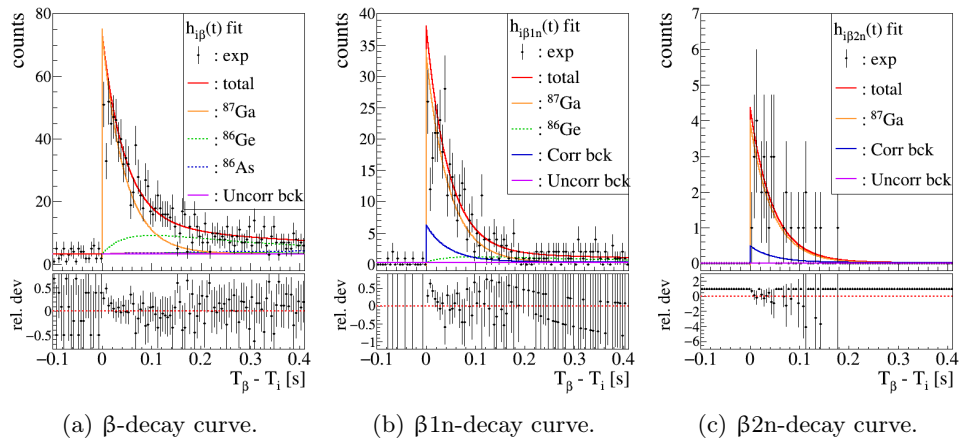


Figure C.23: Result of simultaneous fit of β , $\beta 1n$ and $\beta 2n$ -decay curves of ^{87}Ga .

C.24 Fit of ^{85}Ge decay curves

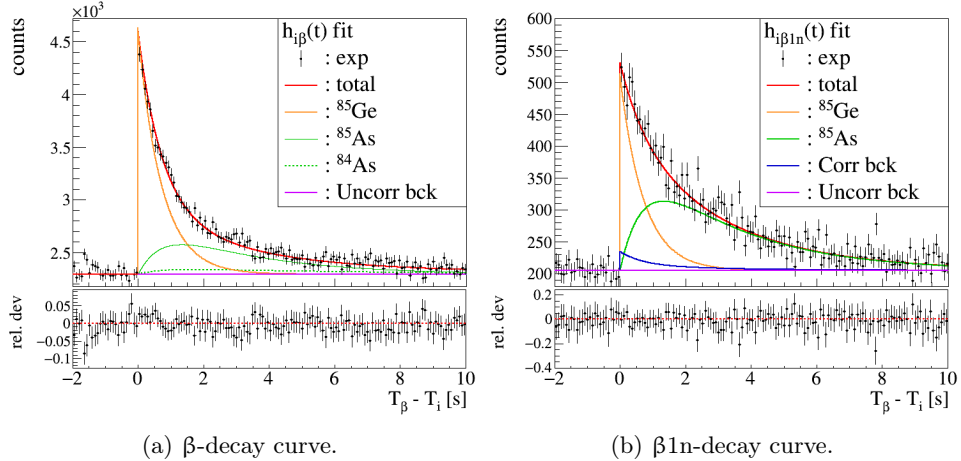


Figure C.24: Result of the simultaneous fit of β and $\beta 1n$ -decay curves of ^{85}Ge .

C.25 Fit of ^{86}Ge decay curves

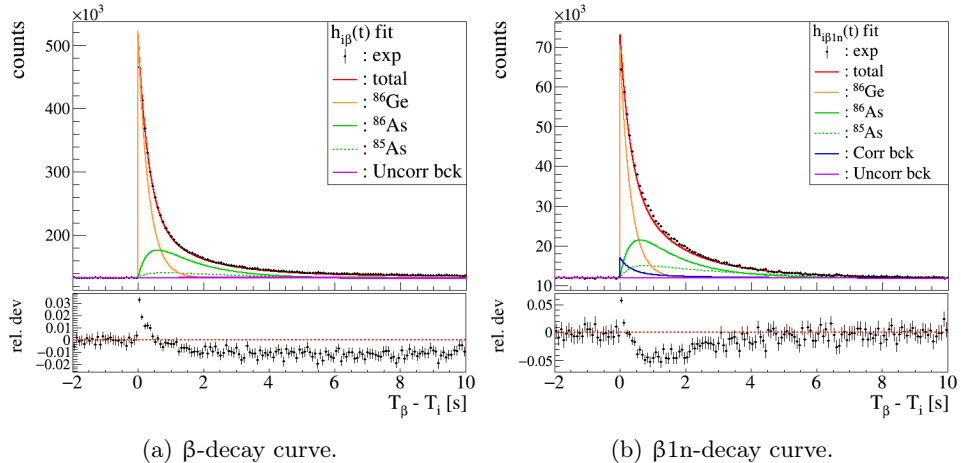


Figure C.25: Result of the simultaneous fit of β and $\beta 1n$ -decay curves of ^{86}Ge .

C.26 Fit of ^{87}Ge decay curves

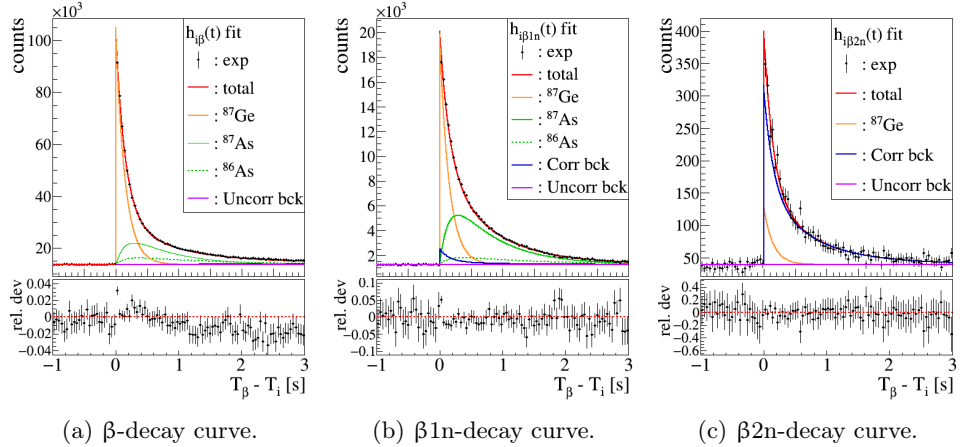


Figure C.26: Result of simultaneous fit of β , $\beta 1n$ and $\beta 2n$ -decay curves of ^{87}Ge .

C.27 Fit of ^{88}Ge decay curves

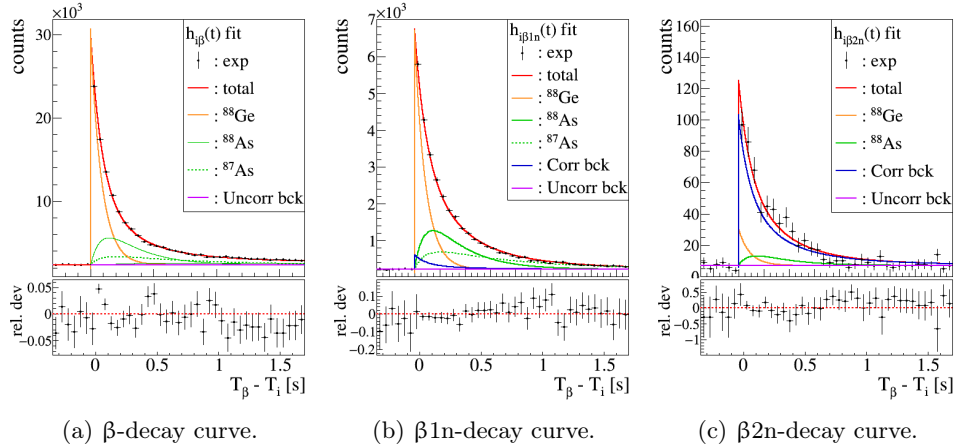


Figure C.27: Result of simultaneous fit of β , $\beta 1n$ and $\beta 2n$ -decay curves of ^{88}Ge .

C.28 Fit of ^{89}Ge decay curves

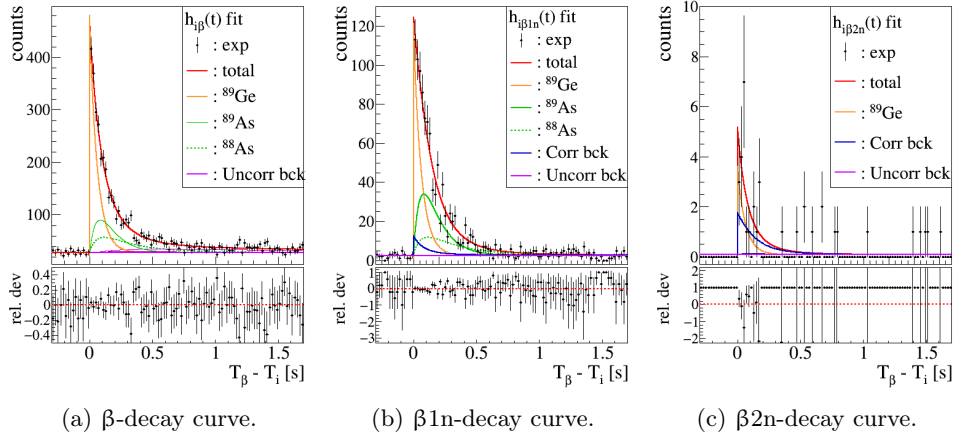


Figure C.28: Result of simultaneous fit of β , $\beta 1n$ and $\beta 2n$ -decay curves of ^{89}Ge .

C.29 Fit of ^{88}As decay curves

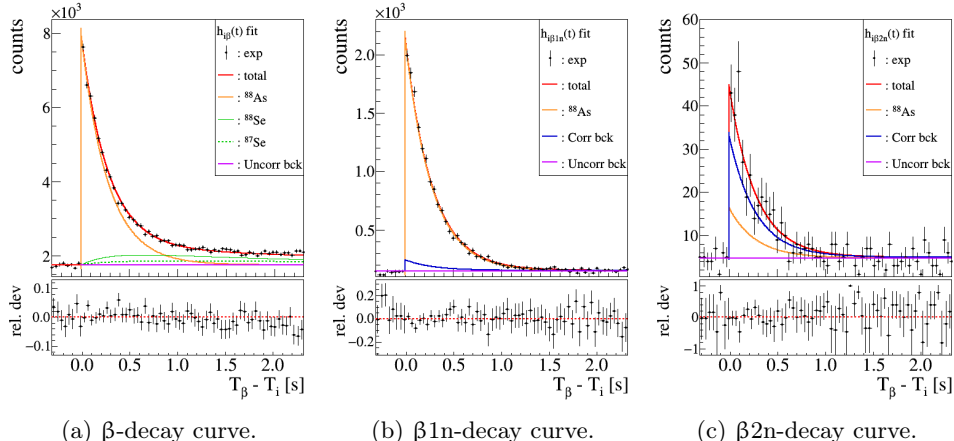


Figure C.29: Result of simultaneous fit of β , $\beta 1n$ and $\beta 2n$ -decay curves of ^{88}As .

C.30 Fit of ^{89}As decay curves

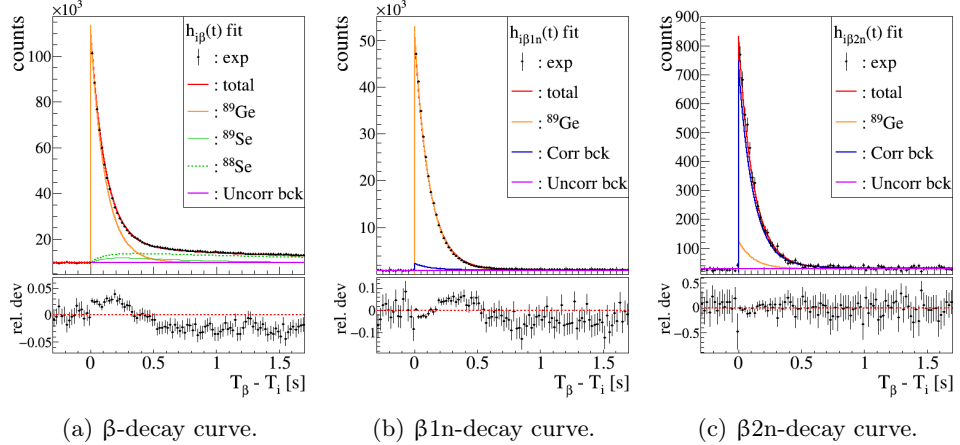


Figure C.30: Result of simultaneous fit of β , $\beta 1n$ and $\beta 2n$ -decay curves of ^{89}As .

C.31 Fit of ^{90}As decay curves

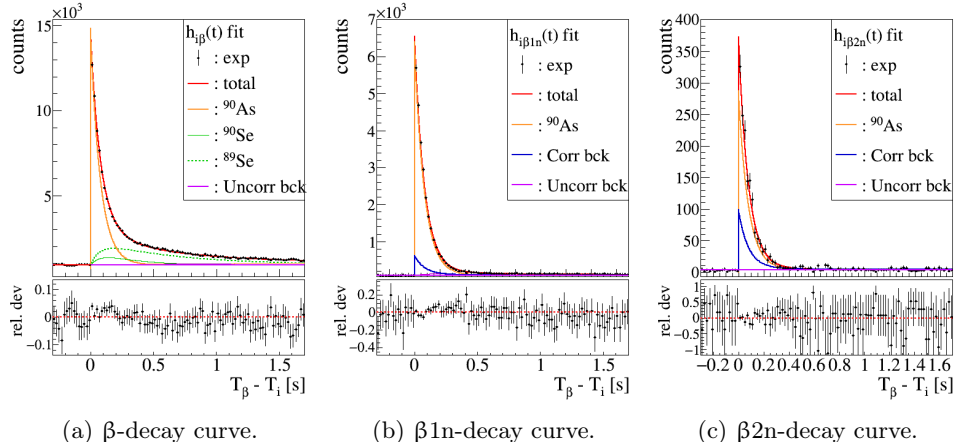


Figure C.31: Result of simultaneous fit of β , $\beta 1n$ and $\beta 2n$ -decay curves of ^{90}As .

C.32 Fit of ^{91}As decay curves

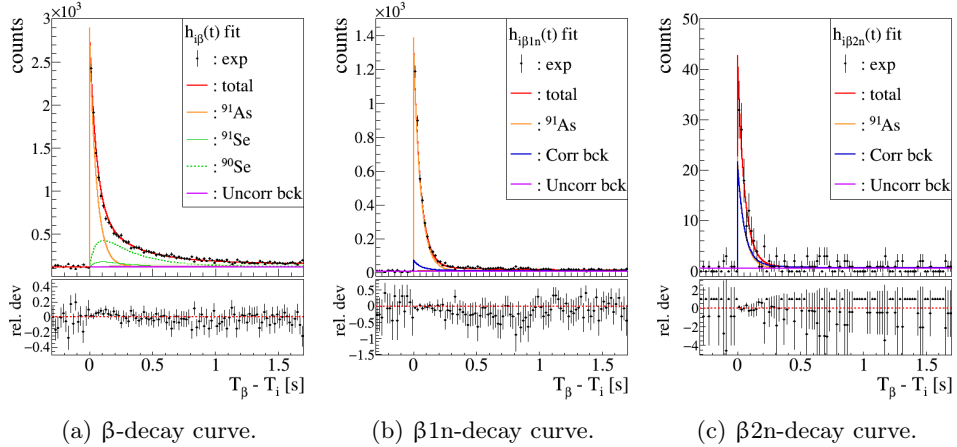


Figure C.32: Result of simultaneous fit of β , $\beta 1n$ and $\beta 2n$ -decay curves of ^{91}As .

C.33 Fit of ^{92}As decay curves

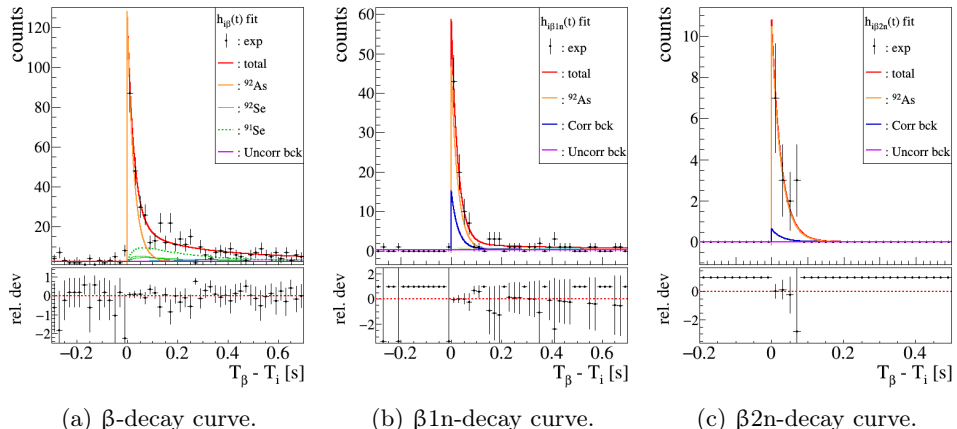


Figure C.33: Result of simultaneous fit of β , $\beta 1n$ and $\beta 2n$ -decay curves of ^{92}As .

C.34 Fit of ^{91}Se decay curves

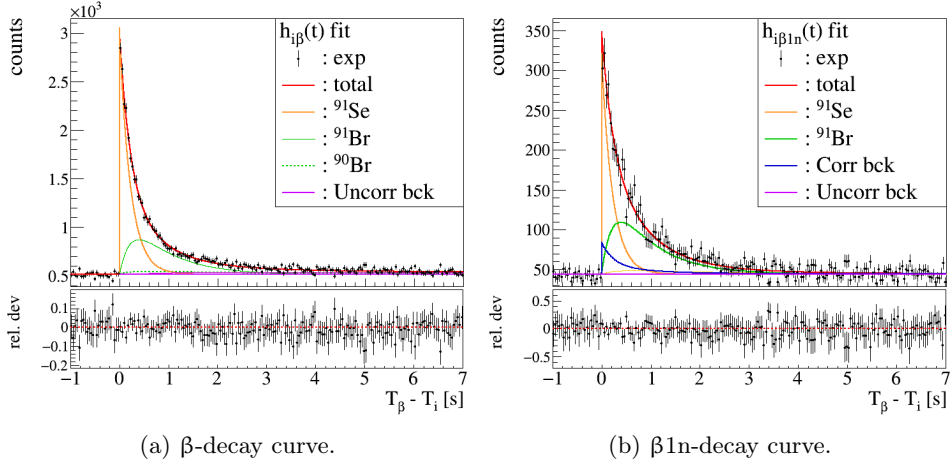


Figure C.34: Result of the simultaneous fit of β and $\beta\text{1}n$ -decay curves of ^{91}Se .

C.35 Fit of ^{92}Se decay curves

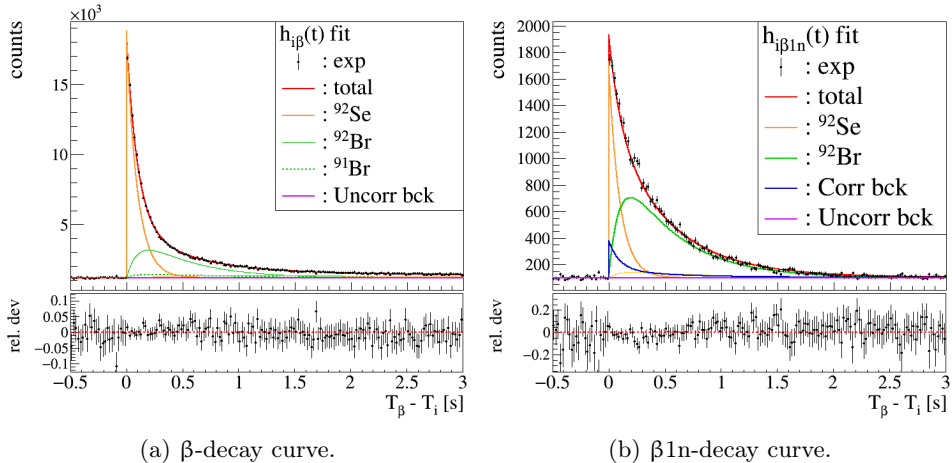


Figure C.35: Result of the simultaneous fit of β and $\beta\text{1}n$ -decay curves of ^{92}Se .

C.36 Fit of ^{93}Se decay curves

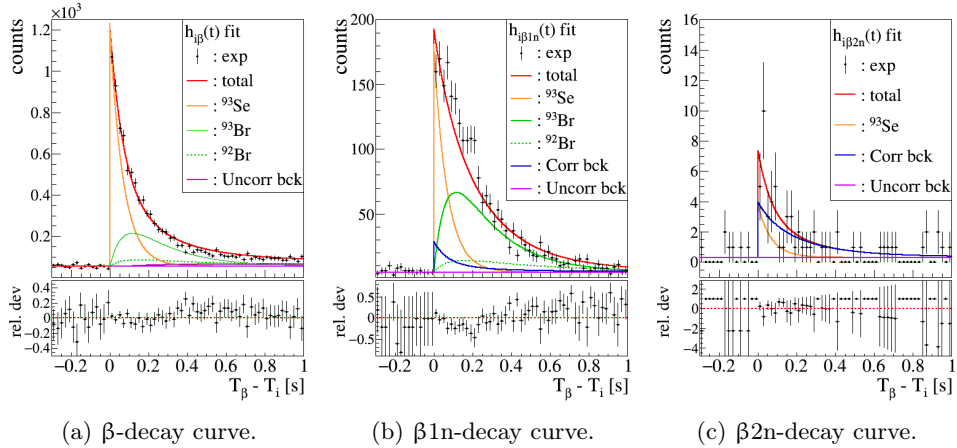


Figure C.36: Result of simultaneous fit of β , $\beta 1n$ and $\beta 2n$ -decay curves of ^{93}Se .

C.37 Fit of ^{94}Br decay curves

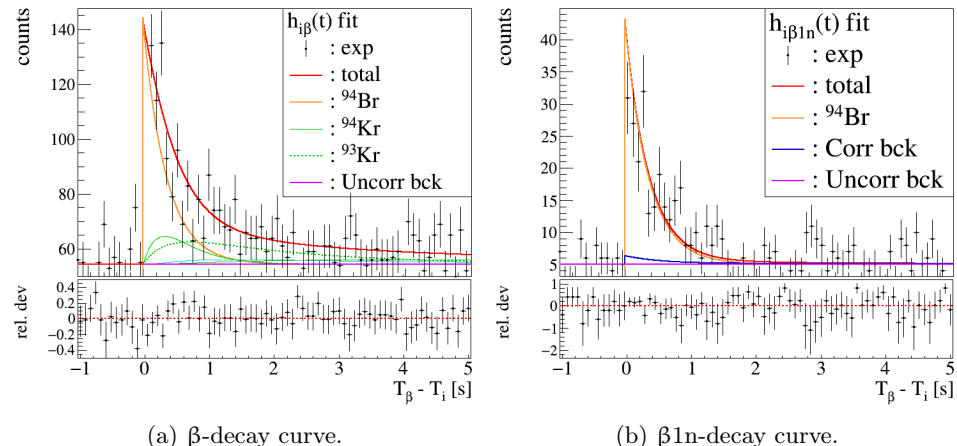


Figure C.37: Result of the simultaneous fit of β and $\beta 1n$ -decay curves of ^{94}Br .

Post neutron star merger nucleosynthesis. Disk ejecta

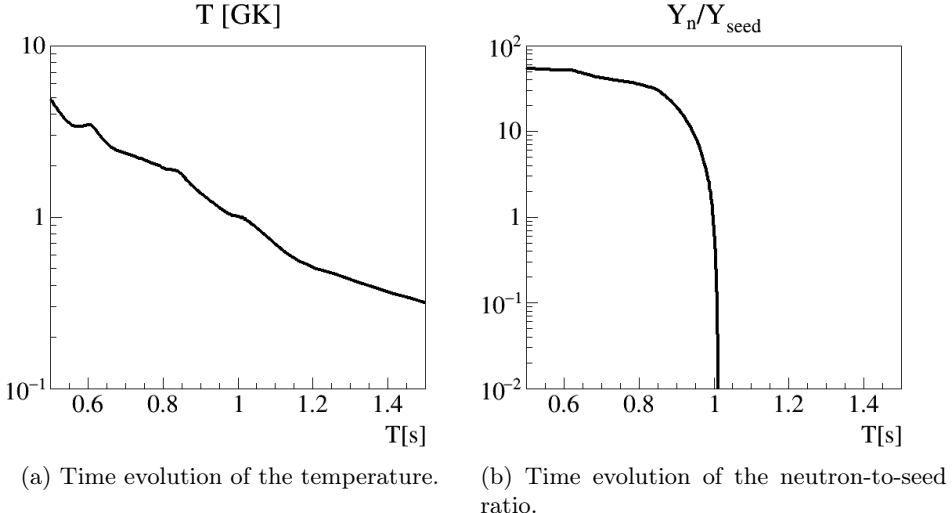
The impact of our experimental results in the rapid neutron capture (*r*-process) calculated final abundances at different astrophysical conditions of a neutron star merger (NSM) is presented in Sec. 5.2.2. The nuclear reaction net program [Win13, Win12] calculates the evolution of the abundances of more than 5000 nuclei, following a given thermodynamical trajectory and a nuclear database. Two databases are prepared: the default version of REACLIB, and a version of REACLIB updated with our P_{xn} and $T_{1/2}$ values. The nuclear reaction net program runs using each one, and the impact of our experimental data is reflected on the differences of the final abundances.

One of the trajectories, the number #991 of [Lip17] corresponds to ejecta from the accretion disk. It leads to the nucleosynthesis up to the heaviest elements, and the impact of our experimental data is not constraint to a redistribution of the final abundances in the mass region $A=75\text{--}95$, but also they cause an increment of a factor 2 in the final abundances of elements from mass 130 to 210. To better understand how this changes are possible, it is necessary to look at the time evolution of the abundances during the *r*-process.

In Fig. D.1a it is shown the time evolution of the temperature of this thermodinamic trajectory. Before $t=0.5$ s, temperature is so high that *r*-process can not start. Once the temperature drops below 5 GK, nuclei far from stability can be formed and the nucleosynthesis proceed. The neutron capture is kept while $Y_n/Y_{seed} > 1$. As it can be seen in Fig. D.1b, after $t=1$ s there are no more neutrons to be captured by seed nuclei and the *r*-process freeze-out is reached.

In the following, a pair of pictures are shown corresponding to different times of the *r*-process. One of them represent the abundances at a given time calculated with the default nuclear database REACLIB. The other one corresponds to the relative difference of the abundances using the nuclear database updated with our experimental values and the default one.

At the beginning of the *r*-process, at $t=0.52$ s, temperature starts to drop enough to allow neutron captures and move the abundances far from stability as it can be seen in Fig. D.2. The nuclei studied in this Thesis has not been synthesized



(a) Time evolution of the temperature.

(b) Time evolution of the neutron-to-seed ratio.

Figure D.1: Time evolution of the temperature and the neutron-to-seed ratio during the trajectory number #991 of [Lip17].

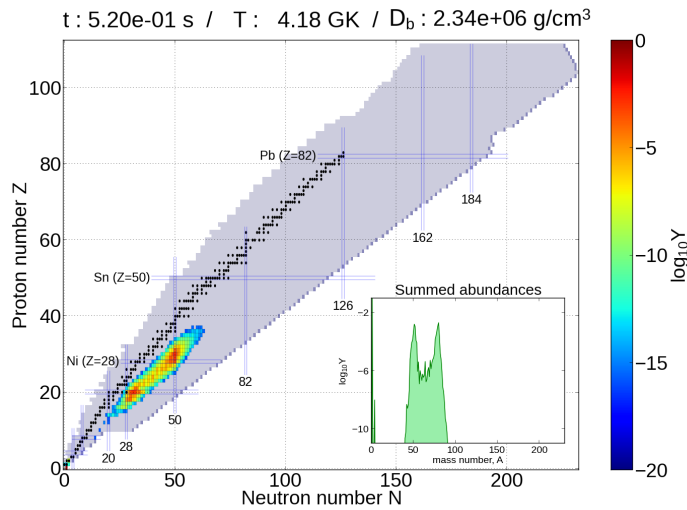
yet, and there is no differences between using the default nuclear database or the one updated with our values.

As the temperature is going down, the r-process proceeds towards heavier isotopes as shown in Fig. D.3a. At this point, our nuclei have been synthesized and are part of the path. As it can be seen in Fig. D.3b, the nuclei with larger Z are more abundant at this moment $t=669 \text{ ms}$ when the nuclear database updated with our experimental values is used. Once the r-process path crosses the nuclei that are updated by our results, the material flows faster towards heavier masses.

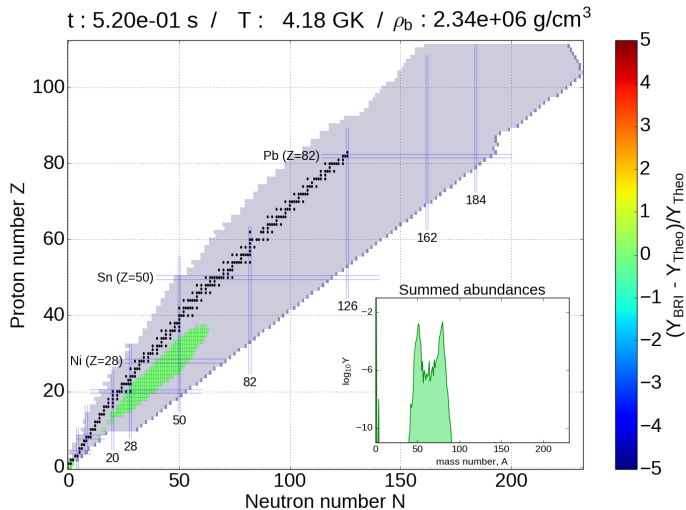
When the r-process reaches the closed shell nuclei with $N=82$, around $t=0.80 \text{ s}$, the process progresses closer to stability in case of the calculation which uses the nuclear database updated with our experimental values instead the default one, as it can be seen in Fig. D.4b. In addition, the relative differences show that nuclei around $N=82$ are more produced when the BRIKEN values are used.

At $t=934 \text{ ms}$ the nuclei with closed shell $N=126$ are reached, as it is shown in Fig. D.5a. At this moment of the nucleosynthesis, isotopes around between $Z=45$ and $Z=60$ are more produced by the abundance calculation which uses the updated experimental values. There is little difference for nuclei between $N=50$ and $N=82$ except for the lightest isotopes of gallium ($Z=31$) and germanium ($Z=32$) which are in fact updated by the experimental values obtained in this Thesis work.

At $t=998 \text{ ms}$ the r-process freeze-out happens, when neutrons are exhausted (see Fig. D.1b). From this moment, all the neutron rich nuclei have to decay back to stability. As it is shown in Fig. D.6a, this trajectory leads to the nucleosynthesis



(a) Abundances at the beginning of the r-process, $t=0.52$ s.



(b) Relative abundance difference at the beginning of the r-process,
 $t=0.52$ s.

Figure D.2: Abundances (top) and relative abundance difference (bottom) at the beginning of the r-process, $t=0.52$ s.

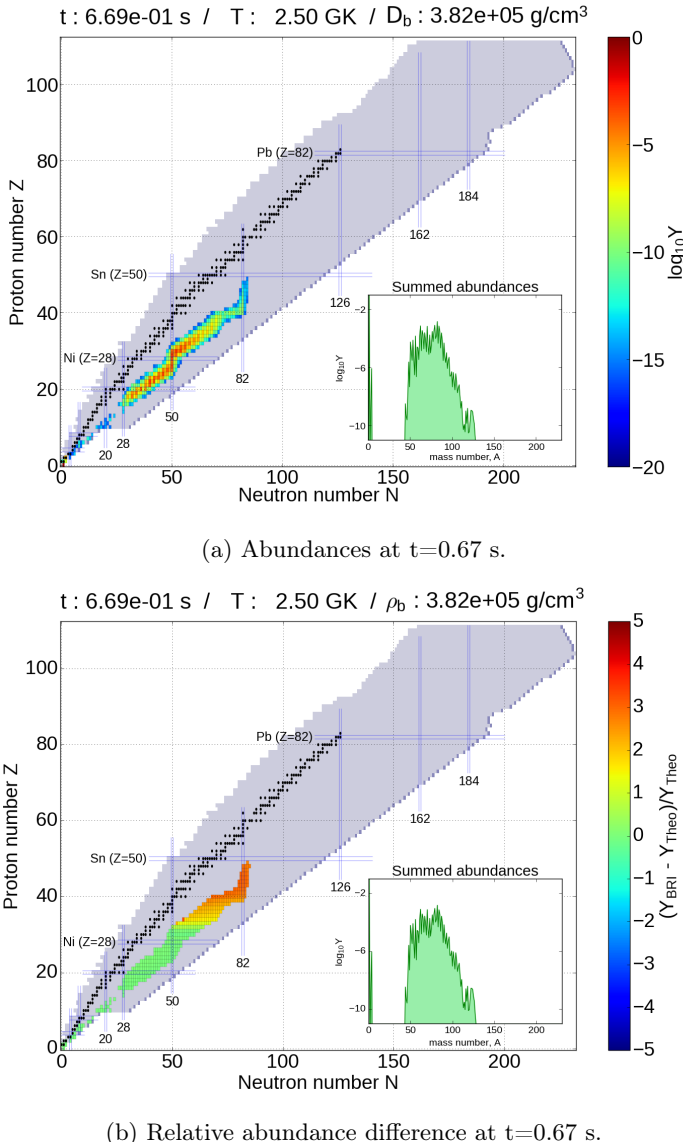


Figure D.3: Abundances (top) and relative abundance difference (bottom) at $t=0.67$ s.

of heavy elements beyond $N=126$. The relative differences of abundances, when the nuclear database updated with our values is used instead of the default one,

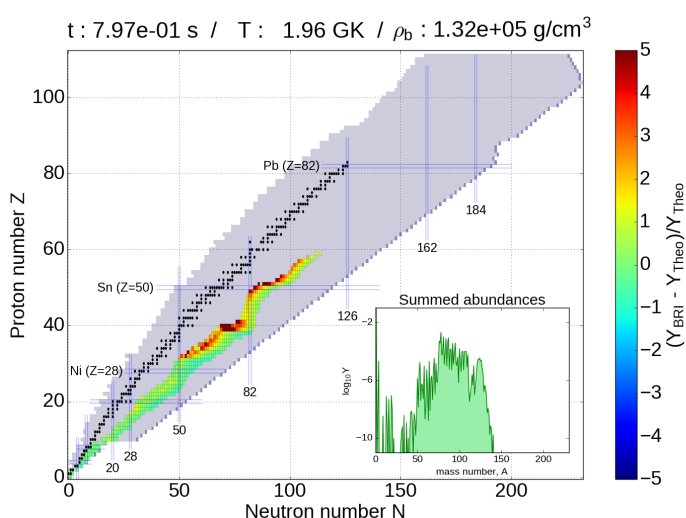
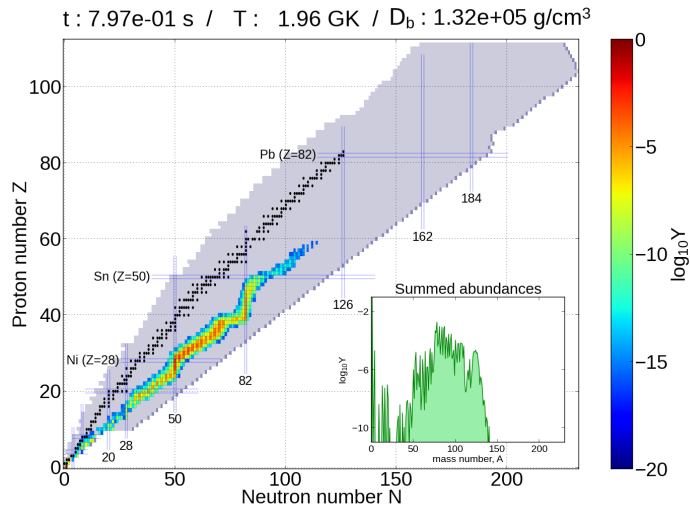


Figure D.4: Abundances (top) and relative abundance difference (bottom) at $t=0.80 \text{ s}$.

is presented in Fig. D.6b. There is an increase in the abundances for nuclei with $A>130$ ($Z>50$ and $N>82$), and this excess is also present in the final abundances.

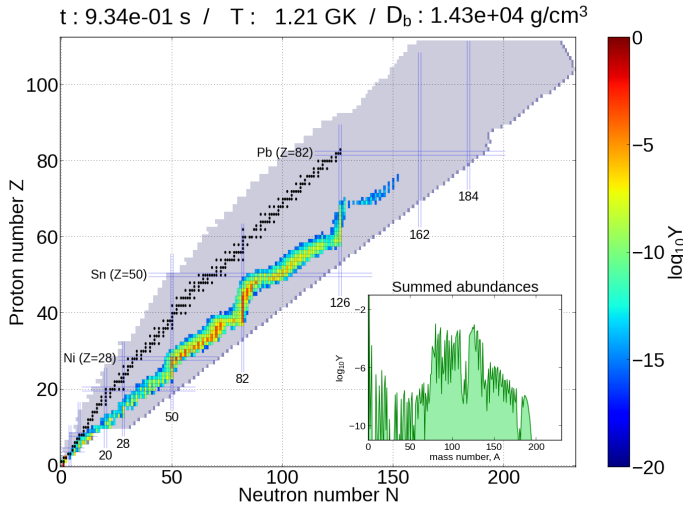
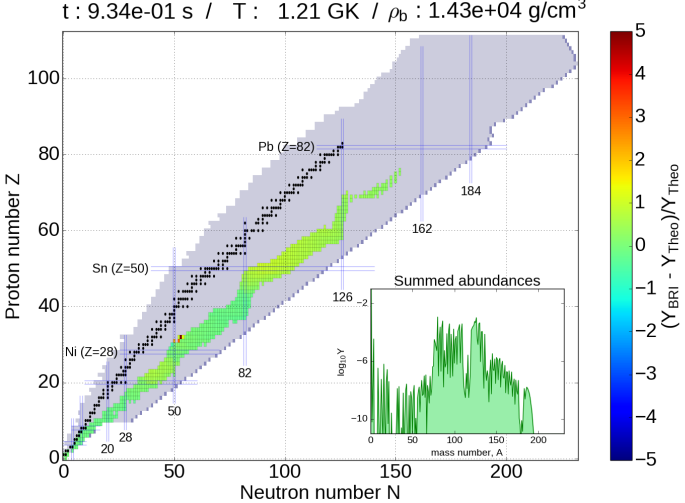
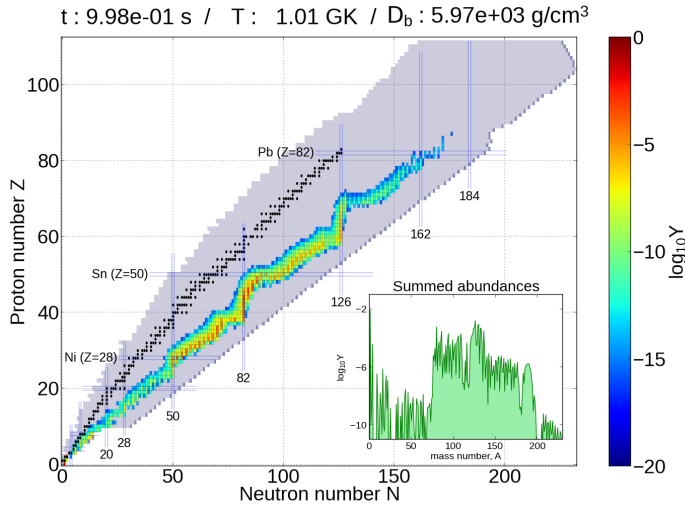

 (a) Abundances at $t=0.93$ s.

 (b) Relative abundance difference at $t=0.93$ s.

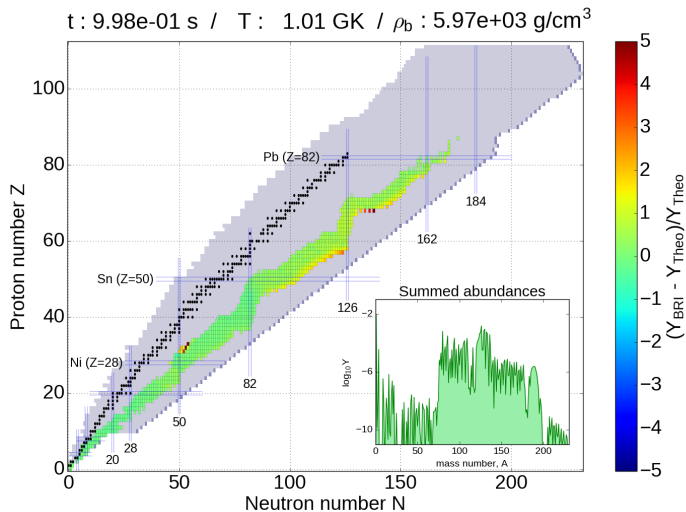
 Figure D.5: Abundances (top) and relative abundance difference (bottom) at $t=0.93$ s.

It is worth to notice the strong oscillations in the elemental abundances (secondary panel in the bottom right of Fig. D.6a) that are present at the moment of r-process

freeze-out but that are smoothed as the nuclei decay back to stability.



(a) Abundances at the r-process freeze-out, $t=0.998$ s.



(b) Relative abundance difference at the r-process freeze-out, $t=0.998$ s.

Figure D.6: Abundances (top) and relative abundance difference (bottom) at the r-process freeze-out, $t=0.998$ s.

To sum up, we have shown that the nuclei studied in this Thesis, in the mass range $A=75\text{--}95$, have an impact on the r-process path and the synthesis of elements beyond $A=95$, in particular for the trajectory number #991 of [Lip17], which corresponds to ejecta from the accretion disk. In addition, we find a local redistribution of the final abundances in the mass region $A=75\text{--}95$ caused by the nuclei, which are formed during the r-process, as they decay to stability.

Chapter E
Resumen en castellano

E.1 Motivación

La emisión de neutrones retardada por desintegración beta es una forma de desintegración radioactiva en la que se emite una pareja de un electrón y un antineutrino, y que además puede estar acompañada de uno o más neutrones. Este tipo de desintegración fue descubierta en 1939 por Roberts y col. [Rob39a, Rob39b] mientras estudiaban la radioactividad de los fragmentos de fisión del uranio y del torio. Desde entonces se han identificado 270 núcleos emisores de neutrones retardados, de los cuales 92 corresponden a elementos más ligeros que el níquel ($Z = 28$), de acuerdo a la última evaluación [BdN-IAEA]. Este proceso es característico de núcleos con exceso de neutrones, si al desintegrarse beta se pueblan estados excitados en el núcleo hijo por encima de su energía de separación de neutrón S_{xn} , como se muestra en la Fig. E.1. A la probabilidad de emisión de x -neutrones se llama P_{xn} .

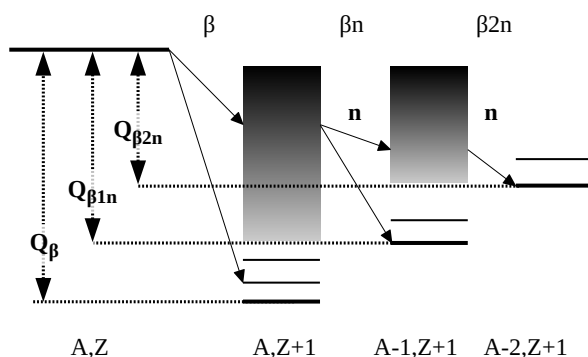


Figura E.1: Representación esquemática de la emisión retardada de neutrones.

E.1.1 Estructura nuclear de la desintegración beta

Existen diferentes teorías capaces de hacer predicciones sobre las vidas medias $T_{1/2}$ y las probabilidades de emisión de neutrón P_{xn} , desde modelos macro-microscópicos hasta modelos ab initio, pasando por modelos puramente microscópicos. Todos ellos tienen dos ingredientes básicos: modelo de masas y la forma de calcular la probabilidad de que el estado excitado a energía E_x del núcleo hijo sea poblado por desintegración beta del núcleo padre. Una vez que las probabilidades de transición son calculadas, la vida media puede obtenerse según la Eq. E.1 donde f es la función de Fermi, S_β la función de beta-strength, y $[0, Q_\beta]$ la ventana de energía del proceso de desintegración beta.

$$1/T_{1/2} = \int_0^{Q_\beta} S_\beta(E_x) f(Z, A, Q_\beta - E_x) dE_x \quad (\text{E.1})$$

Si los estados poblados por la desintegración beta están por encima de la energía de separación de x-neutrones S_{xn} , la probabilidad de emisión de x-neutrones se puede calcular según la Eq. E.2.

$$P_{xn} = \frac{\int_{S_{xn}}^{Q_\beta} S_\beta(E_x) f(Z, R, Q_\beta - E_x) p_{xn}(E_x) dE_x}{\int_0^{Q_\beta} S_\beta(E_x) f(Z, R, Q_\beta - E_x) dE_x} \quad (\text{E.2})$$

El término $p_{xn}(E_x)$ es la probabilidad de emisión de una partícula desde un nivel excitado a energía E_x en el núcleo hijo, expresado en la Eq. E.3 en función de la anchura de escape gamma Γ_γ y anchura de escape de neutrón $\Gamma_n = \sum_x \Gamma_{xn}$.

$$p_{xn}(E_x) = \frac{\Gamma_{xn}(E_x)}{\Gamma_n(E_x) + \Gamma_\gamma(E_x)} \quad (\text{E.3})$$

En general se asume que $\Gamma_n \gg \Gamma_\gamma$, y por lo tanto $p_{xn} \approx 1$, de forma que la fórmula para calcular por ejemplo el P_{1n} se podría simplificar a la Eq. E.4. Esta aproximación ignora la competición de emisión de rayos gamma frente a la emisión de neutrón, y por tanto los valores de P_{xn} así calculados pueden resultar sobreestimados.

$$P_{1n} = \frac{\int_{S_{1n}}^{Q_\beta} S_\beta(E_x) f(Z, R, Q_\beta - E_x) dE_x}{\int_0^{Q_\beta} S_\beta(E_x) f(Z, R, Q_\beta - E_x) dE_x} \quad (\text{E.4})$$

Las predicciones teóricas calculadas por Möller y col. [Möll03] están basadas en cálculos de Quasiparticle Random Phase Approximation (QRPA) sobre un modelo macro-microscópico de masas Finite Range Droplet Model (FRDM) [Möll95].

Recientemente se ha publicado una versión evolucionada del modelo [Mö19], la cual actualiza el modelo de masas FRDM(2012) [Mö16] y que incluye la competición gamma/1-neutrón/2-neutrones/... en el cálculo de P_{xn} (Eq. E.2). Otro modelo teórico macro-microscópico está basado en el cálculo estadístico de Gross Theory [Tac90] sobre el modelo de masas de Koura y col. [KTUY05].

Entre los modelos microscópicos basados en interacciones efectivas mencionaremos tres modelos. El modelo desarrollado por Marketin y col. [Mar16] está basado en relativistic Hartree Bogoliubov (RHB) para el cálculo del estado fundamental del nucleo hijo, y el uso del mismo funcional de la densidad para la descripción mediante proton-neutron relativistic Quasiparticle Random Phase Approximation (pn-RQRPA) de los estados excitados y la probabilidad de ser poblados por la desintegración beta del progenitor manteniendo así la auto-consistencia del cálculo. Otro modelo microscópico auto-consistente ha sido desarrollado por Borzov [Bor05], utilizando el funcional de la densidad de Fayans para la descripción del estado fundamental del núcleo hijo, además de una interacción nucleón-nucleón efectiva universal y continuous-QRPA para el cálculo de los estados excitados y la probabilidad de ser poblados en la desintegración beta del núcleo padre. Por último, Zhi y col. [Zhi13] implementa un modelo de capas interactuante, mejorando el tratamiento de las correlaciones nucleón-nucleón, pero que por limitaciones de computación sólo puede estudiar núcleos de capa cerrada.

En general, el tratamiento de la emisión de neutrón está simplificado y los modelos [Mö03] y [Mar16] asumen que todos los estados del nucleo hijo entre S_{xn} y $S_{(x+1)n}$ darán lugar a la emisión de x-neutrones, calculando los valores P_{xn} según la fórmula dada en la Eq. E.4. Una forma de abordar la competición de emisión de partículas, gamma-neutrón y neutrón-neutrón, ha sido desarrollada por [Kaw08], asumiendo una emisión secuencial de éstos. La competición gamma-neutrón ha sido implementada en modelos de desintegración beta recientes como [Mum16a, Mö19]. Con todo, más datos experimentales son necesarios para poder desarrollar estos modelos, y que puedan describir apropiadamente la emisión multiple de neutrones de los núcleos más exóticos.

Además de estos modelos sofisticados, existen predicciones basadas en ajustes empíricos globales. El modelo propuesto por McCutchan y col. [McC12] estudia la correlación entre el ratio de la probabilidad total de emisión de neutrón P_n ($\sum_x P_{xn}$) y la vida media de un núcleo $T_{1/2}$, y su ventana de energía de desintegración $Q_{\beta 1n}$, según la Eq. E.5.

$$\frac{P_n}{T_{1/2}} = c Q_{\beta 1n}^d \quad (\text{E.5})$$

Los coeficientes de la Eq. E.5, $c = 0,0097(9)$ y $d = 4,87(7)$, se obtuvieron del ajuste de los datos experimentales disponibles en aquel momento para núcleos con $28 \leq Z \leq 43$ [McC12], mostrados en la Fig. E.2.

Otro modelo fenomenológico, propuesto por Miernik [Mie14] calcula las

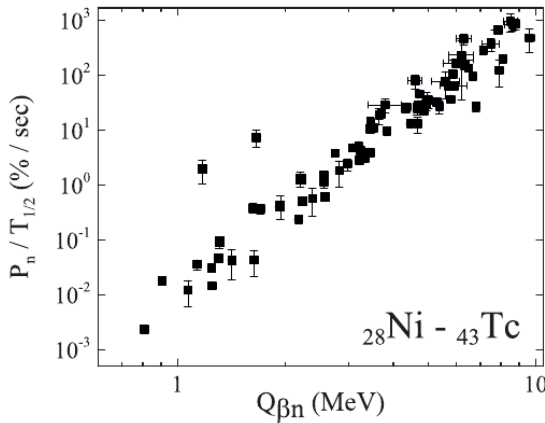


Figura E.2: Cociente de los valores experimentales de la probabilidad total de emisión de neutrón P_n y vida media $T_{1/2}$ en función de $Q_{\beta n}$ para núcleos con $28 \leq Z \leq 43$ [McC12]

probabilidades de emisión de neutrón asumiendo que la función de beta-strength es proporcional a una densidad de niveles efectiva, dada en la Eq. E.6, sobre un modelo de masas previamente calculado por Goriely y col. [Gor10].

$$S_\beta(E_x) \sim \rho(E_x) = \frac{\exp(a_d \sqrt{E_x})}{E_x^{3/2}} \quad (\text{E.6})$$

E.1.2 Astrofísica del proceso de captura rápida de neutrones

Dado que la emisión retardada de neutrones es una forma de desintegración característica de núcleos más exóticos entre el valle de la estabilidad beta y la línea de goteo de neutrones, juega un papel esencial en la síntesis de elementos más pesados que el hierro mediante el proceso de captura rápida de neutrones o proceso-r [B²HF]. La vida media y P_{xn} determinan las abundancias iniciales del proceso, por lo que núcleos de masa 80 pueden afectar la síntesis del resto de elementos. Una vez cesa la captura de neutrones, los núcleos inestables formados durante el proceso-r se desintegran hacia la estabilidad y la emisión retardada de neutrones produce redistribuciones de las abundancias finales hacia masas menores. Para poder reproducir este proceso se recurre a simulaciones de los eventos astrofísicos donde pueden darse las altas densidades de neutrón requeridas por el proceso-r.

Estas simulaciones constan de dos partes. En una primera simulación se sigue la evolución termodinámica (temperatura, presión, densidad, etc) de las

masas eyectadas durante un cierto evento astrofísico. Para agilizar el cálculo, la composición de este material se reduce a unas pocas especies nucleares (n , p , 4He , ${}^{56}Ni$). A continuación, se procede al cálculo de la evolución de abundancias de los núcleos según esa trayectoria termodinámica. En este segundo cálculo se incluyen más de 5000 especies nucleares distintas. Estas simulaciones requieren una gran cantidad de información sobre estos núcleos como sus masas, vidas medias y formas de desintegración, interacción con neutrinos, y velocidades de reacción, recopiladas en la base de datos JINA REACLIB [Cyb10, REACLIB]. Muy pocos núcleos involucrados en el proceso-r son accesibles experimentalmente, y por tanto sus vidas medias y P_{xn} no se han podido medir. Por ello, las simulaciones utilizan predicciones teóricas para los núcleos no medidos, las cuales introducen grandes incertidumbres en sus resultados. Para utilizar los resultados de las simulaciones, en particular las abundancias finales, a la hora de determinar los sitios astronómicos donde ocurre el proceso-r y en cálculos de evolución química galáctica se requiere reducir las incertidumbres de vidas medias y P_{xn} de los núcleos ricos en neutrones [Hor19].

E.2 Experimento

La colaboración Beta-delayed-neutron-measurements at RIKEN (BRIKEN) se fundó con la idea de aumentar enormemente el número de medidas de alta precisión de vidas medias y P_{xn} de núcleos con exceso de neutrones. Estas medidas ayudarán a mejorar los modelos nucleares existentes y tendrán un impacto directo en los cálculos de astrofísica, en particular de nucleosíntesis mediante proceso-r.

El montaje experimental consta de dos sistemas diferentes. El primero consiste en una pila de detectores de silicio altamente segmentados, llamado Advanced Implantation Detector Array (AIDA). Este detector se encuentra en el centro de un detector de neutrones 4π . Este montaje se encuentra en la Fábrica de Haces de Isótopos Radioactivos (Radioactive Isotope Beam Factory, RIBF) del RIKEN Nishina Center (Japón), que actualmente provee de los haces de isótopos más exóticos producidos por fisión en vuelo de un intenso haz primario de uranio. Se han realizado exitosamente cuatro campañas experimentales que cubren isótopos desde las tierras raras hasta el níquel, estando esta tesis dedicada al estudio de los núcleos producidos en torno al núcleo doblemente mágico ${}^{78}Ni$ producidos durante el experimento RIBF127.

E.2.1 Separación e identificación de los iones radioactivos. BigRIPS

El separador BigRIPS [BigRIPS] está compuesto de dos partes, como se indica en la Fig. E.3. En el primer plano focal F0 se produce el haz secundario radioactivo por fisión al colisionar un haz primario de uranio acelerado al 70 % de la velocidad

de la luz con un blanco de berilio. En una primera sección, desde el plano focal F0 hasta el plano F2, se lleva a cabo una separación grosera del haz secundario. En una segunda parte, entre los planos focales F3 y F7 se mide el tiempo de vuelo de cada núcleo mediante detectores plásticos de centelleo, su posición XY en los diferentes planos focales mediante detectores PPAC [Kum13], y su pérdida de energía en detectores MUSIC [Car15]. De estas mediciones se pueden derivar su ratio de masa-carga A/Q y un número atómico Z (características de cada núcleo), permitiendo así su identificación [Fuk13].

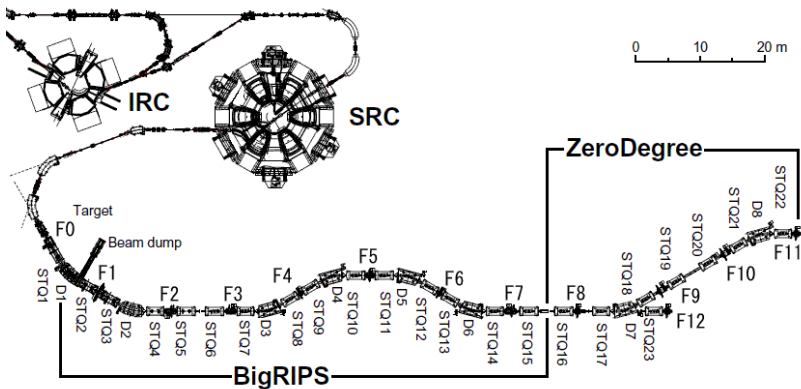


Figura E.3: Esquema del separador BigRIPS y ZeroDegree [Kub12]. El contador de neutrones de BRIKEN y el detector de implantes y desintegraciones AIDA se encuentran en el plano focal F11, al final de la línea del separador ZeroDegree.

E.2.2 Dector de implantaciones y desintegraciones. AIDA

Los isótopos radioactivos identificados por el separador BigRIPS, tras atravesar el separador ZeroDregree y se implantan en los detectores de silicio de AIDA [AIDA], localizada tras el último plano focal F11 del separador. Estos detectores registran tanto la implantación de los núcleos radioactivos como sus posteriores desintegraciones gracias al uso de dos ramas de su sistema de adquisición [Bra11]. La alta segmentación de estos detectores de silicio permite una precisa reconstrucción espacial de los eventos, que junto con un sistema de adquisición de datos (DAQ) digital garantizan una alta eficiencia. Para ajustar la profundidad de implantación en la pila de detectores se utilizaron un conjunto de láminas de aluminio, dispuestas entre el final de la línea del acelerador y AIDA.

E.2.3 Detector de neutrones beta retardados. BRIKEN

El detector de neutrones 4π que rodea a AIDA consiste en un conjunto de 140 tubos proporcionales de ${}^3\text{He}$, embebidos en una matriz de polietileno (PE) y distribuidos como se muestra en la Fig. E.4. Se desarrolló un algoritmo paramétrico Monte Carlo para optimizar la distribución de los tubos dentro de la matriz, y conseguir una alta eficiencia lo más plana posible hasta una energía de neutrón de 1 MeV [Tar17]. La matriz está rodeada en los laterales por unos bloques extra de polietileno y una fina lámina de cadmio, con el fin de atenuar el fondo de neutrones exterior. Se añadió un bloque grueso de polietileno con agujero central en el frontal del montaje, para blindar el detector frente a los neutrones que acompañan al haz.

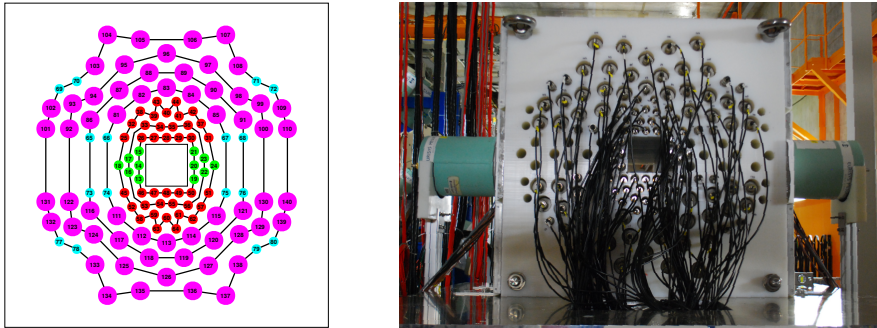


Figura E.4: A la izquierda, esquema de la distribución de los tubos proporcionales en la matriz. Los tubos se agrupan por distancia al centro en siete anillos (líneas continuas). A la derecha, una foto del montaje.

Los neutrones que acompañan a las desintegraciones beta son termalizados mediante colisiones elásticas en el plástico de la matriz y posteriormente detectados por los tubos. El ${}^3\text{He}$ del interior de los tubos captura los neutrones térmicos, dando lugar a una reacción exotérmica que libera 764 keV a repartir entre un protón y un tritón, los cuales son detectados por el tubo proporcional [Leo87]. Esta reacción nuclear en el tubo da lugar a una señal eléctrica que es amplificada en un preamplificador Mesytec [Mesytec] y registrada por un sistema de adquisición (DAQ) digital formado por siete digitalizadores SIS3316 y siete digitalizadores SIS3302 [SYS], controlado por el software GASIFIC 7.0 desarrollado en el IFIC (Valencia) [Agr16, Agr18]. Los preamplificadores se encargan también de distribuir el alto voltaje los tubos proporcionales, e introducen un pulso de test en todos los canales, que es usado durante la etapa de análisis para determinar el tiempo vivo del sistema de adquisición.

El modelo de matriz que finalmente se utiliza incluye dos detectores de rayos gamma tipo CLOVER, con cuatro cristales de germanio de alta pureza cada uno, los cuales añaden la capacidad de espectroscopía gamma de alta resolución. La señal de

estos detectores de rayos gamma, así como la señal de otros detectores auxiliares es registrada por el sistema de adquisición del contador de neutrones. Los detectores auxiliares consisten en detectores plásticos de centelleo, dispuestos sobre la línea del haz antes y después de la pila de detectores de AIDA, y otros dos dispuestos alrededor del agujero del blindaje frontal de polietileno, utilizados durante la etapa de análisis para suprimir eficazmente el fondo de neutrones inducido por el acelerador. Además, se incorporó un detector de silicio en el agujero del blindaje frontal para una identificación precisa del número atómico de los iones radioactivos que se implantan en AIDA. La Fig. E.5 representa un esquema de la distribución de los detectores.

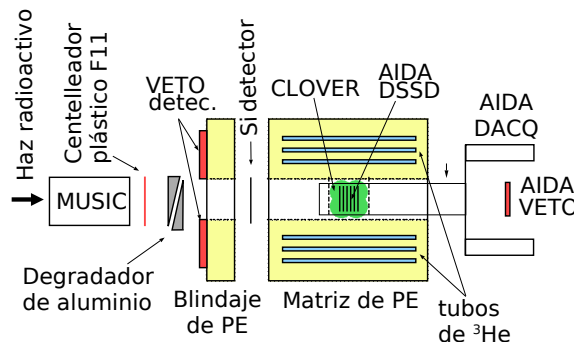


Figura E.5: Esquema del montaje experimental (vista lateral).

Los sistemas de adquisición del separador BigRIPS, del detector de implantaciones y desintegraciones AIDA y del contador de neutrones funcionan independientemente. Sin embargo, es necesario que los tres sistemas estén sincronizados, de forma que sus datos puedan correlacionarse temporalmente en la etapa de análisis. Para ello, se distribuye una señal común de 25 MHz a los tres sistemas y se establece un origen común de tiempos.

E.2.4 Condiciones del experimento

El experimento RIBF127 tuvo una duración efectiva de 83.2 h, y un número total de 30 millones de implantes, de los cuales 7200 corresponden al ${}^{78}\text{Ni}$. En la parte superior de la Fig. E.6 se muestra una foto del montaje experimental, distinguiendo el detector AIDA y su electrónica en la parte izquierda, y el contador de neutrones y su electrónica en la parte derecha. La fotografía de la parte inferior se corresponde al montaje visto desde el último plano focal F11 del separador ZeroDegree, donde se pueden ver todos los detectores auxiliares salvo el plástico centelleador localizado tras la pila de detectores de AIDA.

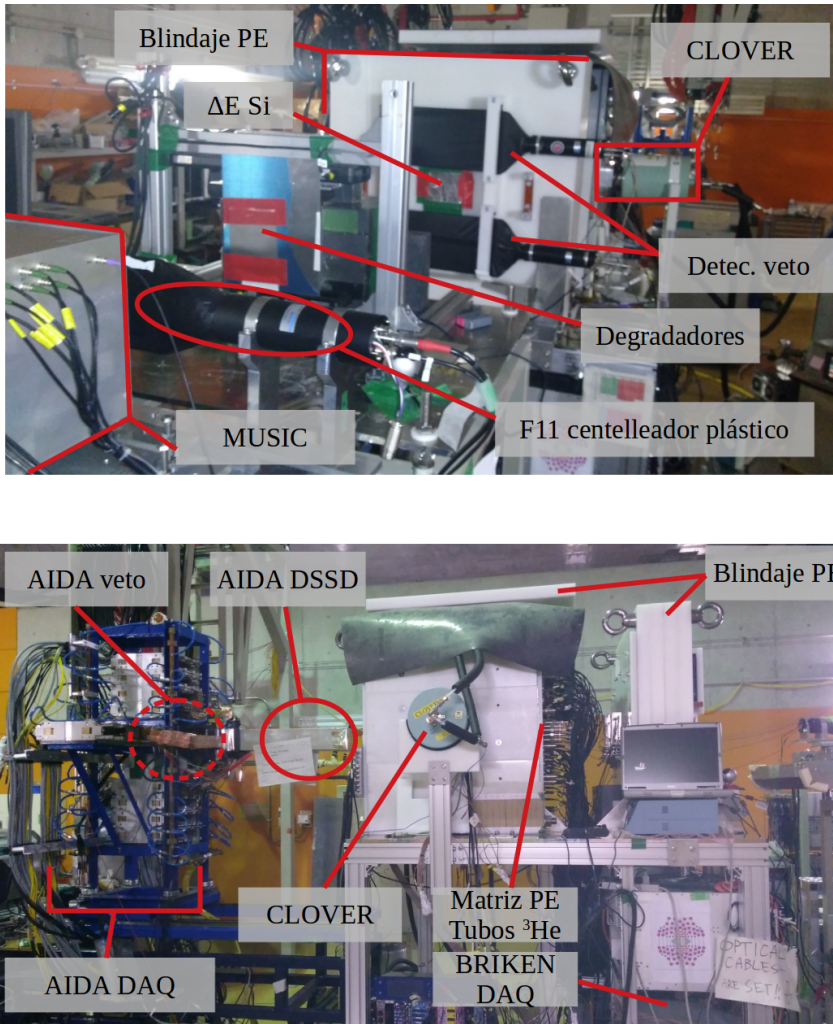


Figura E.6: Vista lateral (arriba) y frontal (abajo) del montaje experimental.

E.3 Método de análisis

E.3.1 Procesado de datos

Durante la etapa de análisis, los datos registrados por los respectivos sistemas de adquisición son convertidos a eventos físicos y guardados en formato TTree [Bru97]. Todos los eventos tienen al menos una marca de tiempo, que permite

relacionarlos temporalmente con eventos de otros sistemas. Los eventos de BigRIPS contienen la información necesaria para identificar al isótopo correspondiente, el ratio masa-carga A/Q y el número atómico Z, así como otra información que puede ser necesaria posteriormente, como la velocidad de vuelo β . Esta información se obtiene a partir de las medidas de los diferentes detectores a lo largo de la línea del separador BigRIPS según se explica en [Fuk13]. Para el preprocesado y conversión de los datos de AIDA se utilizó el programa AIDASort [Hal18], el cual genera eventos de implantación y desintegración beta caracterizados por un cierto número de píxeles activados dentro de un cierto detector de silicio y una energía total depositada. Los eventos correspondientes a eventos de detección de neutrones, o procedentes de detectores auxiliares, están caracterizados por su energía y por un número que identifica al detector, además de la correspondiente marca de tiempo común.

Una vez que tenemos los eventos físicos de los tres sistemas, se procede a ordenar y agrupar temporalmente los eventos en un solo flujo de datos mediante un software dedicado *Merger*, desarrollado en el IFIC (Valencia) [Merger, Agr18]. En la Fig. E.7 se muestran los pasos seguidos hasta este punto.

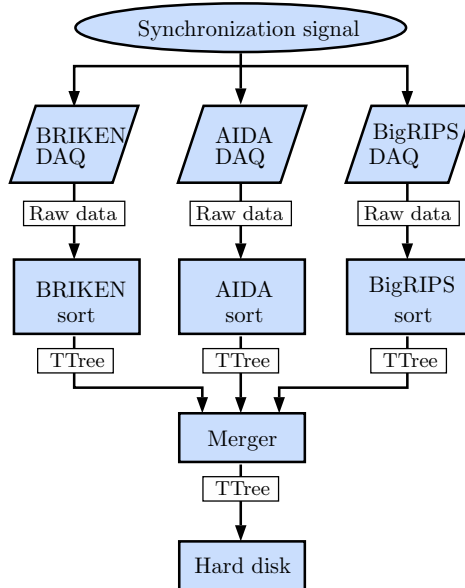


Figura E.7: Diagrama de flujo que resume el procesamiento de los datos.

Dado que la ventana de tiempo para relacionar eventos de desintegración con eventos de implantación es del orden de segundos, pero la ventana con eventos de neutrón o gamma es ordenes de magnitud más corta, se elige utilizar los eventos

de desintegración beta como origen de tiempos en la agrupación temporal del resto de eventos. Así, cada evento de desintegración tendrá asociada un conjunto de implantes, otro conjunto de neutrones, etc. La ventana temporal para esta agrupación es distinta dependiendo del tipo de evento (implante, neutrón, etc). El propio programa de *Merger* aplica una correlación espacial entre eventos beta e implantes que es necesaria para reducir las correlaciones accidentales.

E.3.2 Construcción de las curvas de desintegración

Además de ordenar temporalmente los datos de entrada, el programa de *Merger* realiza una serie de asociaciones necesarias en la estapa de análisis. Una de ellas consiste en la asignación de una pareja de valores (A/Q , Z) de un ión radioactivo identificado a su paso por BigRIPS a su evento de implantación detectado en AIDA. En la Fig. E.8 se puede ver la identificación de los isótopos implantados en AIDA durante el experimento RIBF127.

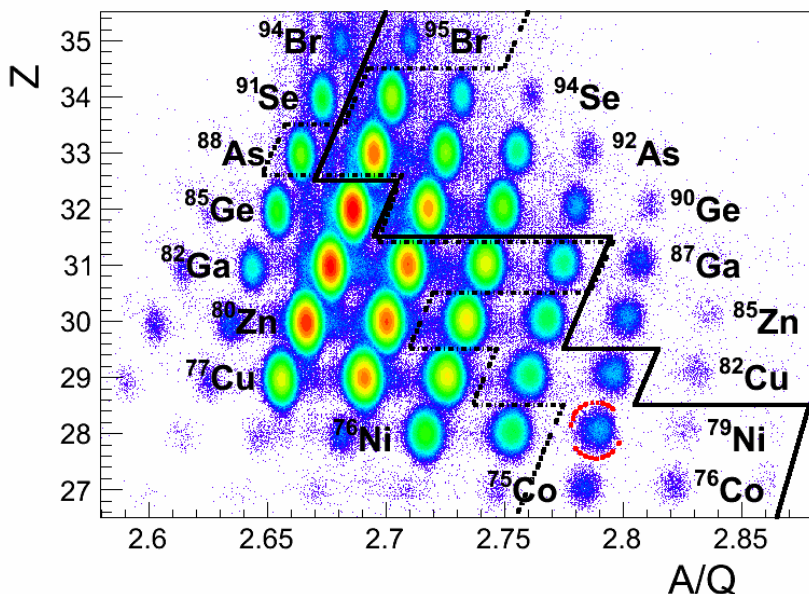


Figura E.8: Indetificación de los isótopos implantados durante el experimento RIBF127.

Como se decía en el apartado anterior, este programa agrupa temporalmente eventos de implantación previamente identificados, y de detección de neutrón, con cada evento de desintegración registrado en AIDA, de forma que el flujo

de datos de salida se puede utilizar directamente para construir las curvas de desintegración de cada núcleo.

La curva de desintegración beta resulta de las diferencias temporales entre los eventos de implantación de un cierto núcleo y sus desintegraciones beta. También se construyen las curvas de desintegración correspondientes a la emisión de x-neutrones, exigiendo que dentro de una ventana temporal de 200 μs tras el evento beta aparezcan x-neutrones. En la Fig. E.9 se muestran las curvas de desintegración del ^{86}Ga .

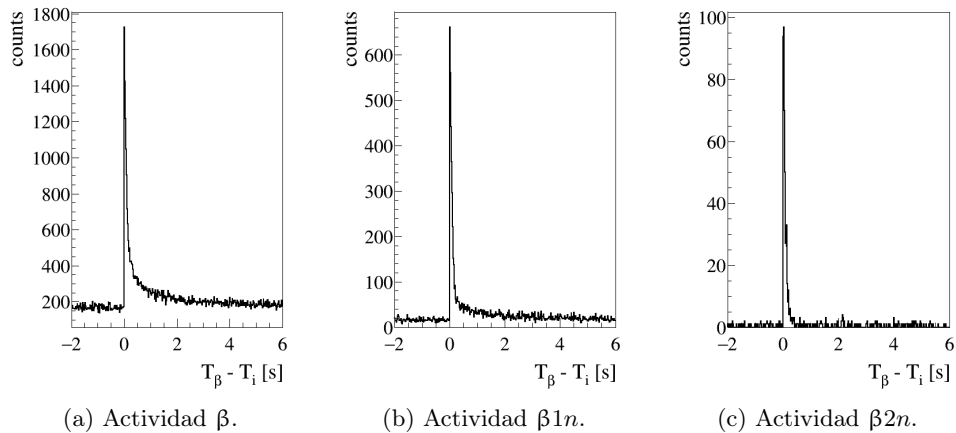


Figura E.9: Curvas de desintegración beta, beta-1-neutrón y beta-2-neutrones correspondientes al isótopo ^{86}Ga .

Alguno de esos x-neutrones puede no venir de la desintegración que se está estudiando, y formar así un fondo correlacionado en las curvas de actividad beta-neutrón. Una correcta determinación de este fondo correlacionado, o bien experimentalmente o bien calculado, es crucial en los casos límite de baja estadística o P_{xn} pequeños [Tol19].

E.3.3 Dependencia isotópica de la eficiencia de detección de neutrón

La eficiencia total simulada [Tar17] se muestra en la Fig. E.10. Como se puede ver, es prácticamente plana para energías de neutrón por debajo de 1 MeV, teniendo un valor absoluto de 66.8(20) %. Sin embargo, disminuye moderadamente para energías mayores. La simulación fue validada para una fuente de neutrones ^{252}Cf . La eficiencia de detección para esta fuente fue determinada experimentalmente mediante el método de las multiplicidades [Cro12, San08], encontrando un valor de 61.72(20) %. La eficiencia para esta fuente, calculada a partir del espectro de

neutrinos de la fuente ^{252}Cf [NDS-IAEA] y de la simulación Monte Carlo, es de 62.0(18) %, muy cercano al experimental y dentro del error, validando por tanto la simulación de la eficiencia total.

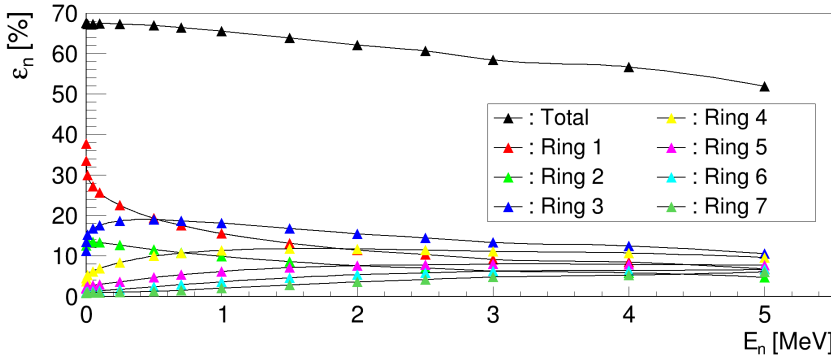


Figura E.10: Eficiencia de detección en función de la energía de neutrón, simulada mediante GEANT4. Se muestra tanto la eficiencia total (en negro), como la eficiencia de cada anillo.

El espectro de energía de los neutrones retardados beta de los núcleos $^{83-84}\text{Ga}$, producidos durante el experimento RIBF127, fue medido previamente por Madurga y col. [Mad16]. La correspondiente eficiencia de detección, calculada a partir de la eficiencia simulada Monte Carlo, es un 10 % menor que la eficiencia nominal para energías de neutrón por debajo de 1 MeV. Dado que los núcleos medidos tienen unas ventanas de energía $Q_{\beta 1n}$ incluso mayores que las de $^{83-84}\text{Ga}$, los neutrones pueden incluso tener una energía mayor, y por tanto su eficiencia de detección puede ser menor. Para poder extrapolar la eficiencia de detección de los neutrones retardados a esos núcleos con grandes ventanas $Q_{\beta 1n}$ recurrimos a dos simplificaciones. La primera consiste en aproximar que la eficiencia correspondiente a un espectro de neutrones por la eficiencia correspondiente a la energía promedio de neutrón, según la Eq. E.7.

$$\langle \varepsilon_n(E_n) \rangle \approx \varepsilon_n(\langle E_n \rangle) \quad (\text{E.7})$$

En la Fig. E.11 se muestran las eficiencias calculadas según esta aproximación, correspondientes a 36 espectros de neutrones retardados que han sido medidos [Bra89, Mad16] y al espectro de neutrones de la fuente de ^{252}Cf . La eficiencia de detección en función de la energía de neutrón (ε_n vs E_n) se muestra también en la misma figura. Como puede observarse, la desviación máxima es de 0.5 %, validando así esta aproximación.

La segunda aproximación consiste en relacionar la energía promedio de neutrón beta retardado de un cierto núcleo con su valor $Q_{\beta 1n}$. Asumiendo que la función

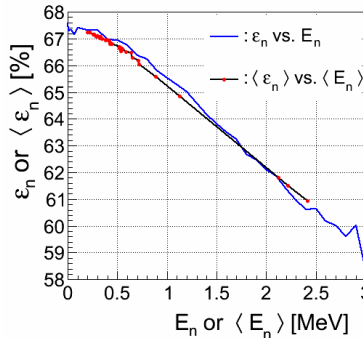


Figura E.11: Comparación de la eficiencia de detección en función de la energía de neutrón (línea azul), y la eficiencia calculada para algunos núcleos cuyo espectro de neutrones ha sido medido en función de la energía promedio de neutrón (puntos rojos).

de beta-strength es constante por encima de la energía de separación de neutrón S_{1n} [Pap72], y que todos los estados excitados a una energía E_x por encima de S_{1n} decaen mediante emisión de neutrón al estado fundamental del estado final con energía $E_n = E_x - S_{1n}$, se puede calcular la energía promedio de los neutrones retardados según la Eq. E.8.

$$\langle E_n \rangle \approx \frac{\int_{S_{1n}}^{Q_\beta} (E_x - S_{1n}) f(Z, Q_\beta - E_x) dE_x}{\int_{S_{1n}}^{Q_\beta} f(Z, Q_\beta - E_x) dE_x} = \langle E_n \rangle (Q_{\beta 1n}) \quad (\text{E.8})$$

La Fig. E.12 representa la energía promedio de neutrón calculada según la fórmula dada en la Eq. E.8 (puntos azules) mostrando que su dependencia con el valor $Q_{\beta 1n}$ está bien aproximada por una relación lineal (línea verde). Además, en la misma figura se muestra también el valor real (puntos rojos) calculados con los espectros de neutrones experimentales de los 36 emisores retardados- β antes mencionados [Bra89, Mad16]. Se observa que los valores están distribuidos alrededor de esta línea roja pero todos ellos contenidos dentro de la línea punteada verde que representa un factor 2 arriba o abajo con respecto del modelo. Esta observación es la base del modelo para extraer la eficiencia de neutrón para aquellos núcleos que no tienen un espectro de neutrones retardados medido.

Utilizando la eficiencia calculada mediante GEANT4, junto con las dos aproximaciones anteriores expuestas, podemos calcular la eficiencia de detección para los neutrones beta-retardados de un cierto núcleo como función de su $Q_{\beta 1n}$, mostrada en la Fig. E.13. El valor central de la eficiencia se corresponde con la línea continua, mientras que el área sombreada en gris marca los errores mínimo/máximo. Para

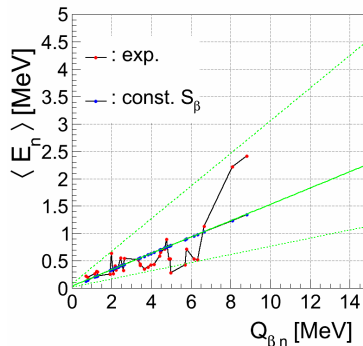


Figura E.12: Valores experimentales de las energías promedio de neutrón [Bra89, Mad16] en función del $Q_{\beta 1n}$. Los valores reales muestran una desviación con respecto del modelo dado en la Eq. E.8 contenida en un factor 2.

los núcleos $^{83-84}\text{Ga}$ utilizamos el valor obtenido a partir de la curva simulada mediante GEANT4 y los espectros de neutrón medidos [Mad16], indicados con un punto verde.

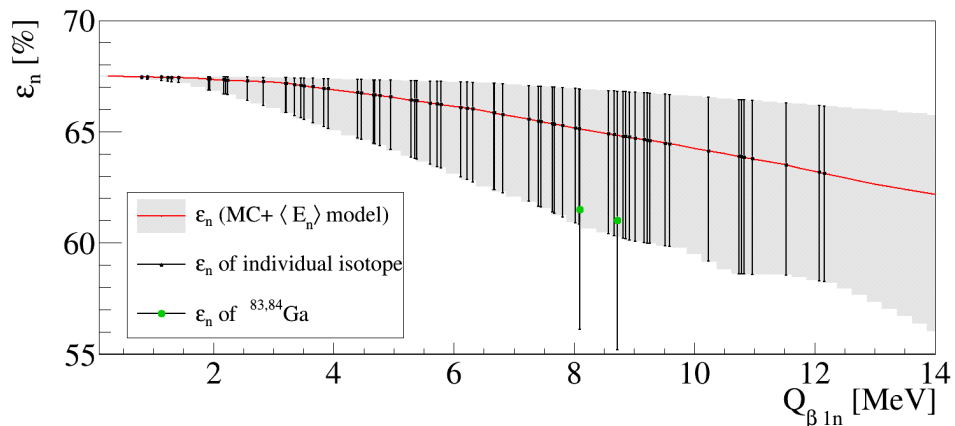


Figura E.13: Eficiencia de detección de neutrón en función del $Q_{\beta 1n}$, calculada según las aproximaciones expuestas en esta sección. Cada punto corresponde a un isótopo que aparece en una o varias cadenas de desintegración de los isótopos implantados. La banda de error, sombreada en gris, se deriva de la incertidumbre del modelo que relaciona la energía promedio de neutrón y el $Q_{\beta 1n}$, mostrado en Fig. E.12. Los dos puntos verdes se corresponden con la eficiencia de detección para los núcleos $^{83,84}\text{Ga}$.

E.3.4 Ajuste de las curvas de desintegración

Las ecuaciones de Bateman [Bat10] son un sistema de ecuaciones diferenciales que describe la evolución temporal de la cantidad de núcleos de cada especie en una cadena de desintegración. Su solución generalizada [Skr74] puede ser simplificada a la Eq. E.9 si inicialmente sólo se tiene una cierta cantidad de núcleos del primer núcleo de la cadena de desintegración. El símbolo λ representa la constante de desintegración y $b_{j,j+1}$ la probabilidad de que el núcleo i -ésimo se desintegre en el siguiente.

$$N_n(t) = N_1(0) \prod_{j=1}^{n-1} (\lambda_j b_{j,j+1}) \sum_{i=1}^n \sum_{j=i}^n \left(\frac{e^{-\lambda_j t}}{\prod_{p=i, p \neq j}^n (\lambda_p - \lambda_j)} \right) \quad (\text{E.9})$$

Dado que la actividad se define como $A_i(t) = \lambda N_i(t)$, la función modelo de nuestras curvas de desintegración beta y desintegración beta-x-neutrón vienen dada por las Eqs. (E.10a)-(E.10c).

$$A_\beta(t) = \sum_{i \in \beta} \overline{\varepsilon_i^\beta} \lambda_i N_i(t) \quad (\text{E.10a})$$

$$A_{\beta 1n}(t) = \sum_{i \in \beta 1n} \overline{\varepsilon_i^\beta} \overline{\varepsilon_i^{1n}} P_i^{1n} \lambda_i N_i(t) \quad (\text{E.10b})$$

$$A_{\beta 2n}(t) = \sum_{i \in \beta 2n} \overline{\varepsilon_i^\beta} \overline{\varepsilon_i^{2n}} P_i^{2n} \lambda_i N_i(t) \quad (\text{E.10c})$$

El fondo correlacionado que aparece en las curvas de desintegración beta-x-neutrón se puede calcular a partir de las actividades beta y beta-x-neutrón dadas en la ecuación anterior [Tol19]. Las curvas de desintegración están montadas sobre un fondo descorrelacionado. En los casos donde hay más estadística se puede comprobar que este fondo no es completamente plano. En esos casos, se ajusta a una recta en la región $-10 \text{ s} < t_b - t_i < 0 \text{ s}$, y se simetriza en la región de fit, $0 \text{ s} < t_b - t_i < 10 \text{ s}$. El origen de la forma no planar del fondo descorrelacionado está en las numerosas interrupciones del haz, y en general en sus variaciones de intensidad. En los casos de menor estadística, se asume un fondo plano y se extrapola a la región de fit. Finalmente, las funciones que modelizan las curvas de desintegración en la región $0 \text{ s} < t_b - t_i < 10 \text{ s}$ están dadas en la Eq. E.11.

$$f_\beta(t) = A_\beta(t) + bck_\beta^u(t) \quad (\text{E.11a})$$

$$f_{\beta 1n}(t) = a_0 A_\beta(t) + a_1 A_{\beta 1n}(t) + a_2 A_{\beta 2n}(t) + bck_{\beta 1n}^u(t) \quad (\text{E.11b})$$

$$f_{\beta 2n}(t) = b_0 A_\beta(t) + b_1 A_{\beta 1n}(t) + b_2 A_{\beta 2n}(t) + bck_{\beta 2n}^u(t) \quad (\text{E.11c})$$

Estas funciones dan cuenta de la actividad del núcleo padre y de todos los descendientes hasta la estabilidad, así como los fondos antes mencionados. En

general, los parámetros de estas funciones son fijos, salvo las probabilidades de emisión del padre P_{xn} y su número de desintegraciones. Las vidas medias y P_{xn} de los descendientes suelen ser bien conocidas, y sólo en algunos casos se ajusta la vida media del padre, obtenida simultáneamente junto con sus valores P_{xn} .

La eficiencia de neutrón correspondiente a cada isótopo viene dada por el modelo presentado en la sección anterior. Esta eficiencia de detección es escalada por el tiempo vivo del sistema de adquisición, y dos factores que provienen de la etapa análisis. Uno de estos factores es el tiempo muerto inducido por el voto que se aplica para reducir el fondo de neutrones inducido por el acelerador. El otro factor proviene de la ventana finita que se utiliza para asociar x-neutrones a cada desintegración beta.

La eficiencia beta se asume que es igual para todos los isótopos. Sin embargo, se observa en todos los casos que la curva teórica sobreestima los datos experimentales en las primeras décimas de segundo. En un trabajo previo [Tol19] se propuso que este efecto está causado por una diferencia de la eficiencia beta del núcleo padre con respecto a sus descendientes, y por tanto habría que ajustar esa eficiencia junto sus probabilidades de emisión de neutrón P_{xn} . Un experimento posterior, en el que se usó otro detector de implantación y desintegraciones beta y en el que se produjeron núcleos comunes con el del experimento RIBF127, se encontró que el ajuste simultaneo de la eficiencia beta del núcleo padre y de P_{xn} introduce un efecto sistemático, y que los valores eran consistentes entre ambos experimentos si no se ajusta dicha eficiencia beta.

Las probabilidades de emisión de neutrón y el número de desintegraciones del padre (y la vida media del padre si procede) se obtienen ajustando simultáneamente la curva de desintegración beta y las curvas de desintegración beta-x-neutrón mediante un minimizador común construido como suma de los estimadores de máxima verosimilitud de cada pareja de curva y función modelo. El algoritmo utilizado para encontrar el mínimo fue MIGRAD, del paquete Minuit. El error estadístico es calculado a partir del minimizador utilizando el paquete MINOS. El error sistemático, causado por las incertidumbres de los parámetros fijos durante el ajuste, es calculado mediante un método Monte Carlo, repitiendo el ajuste variando los parámetros fijos dentro de su incertidumbre.

E.4 Resultados

Los datos presentados en esta Tesis corresponden a vidas medias $T_{1/2}$ y P_{xn} de núcleos en la zona del ^{78}Ni , implantados durante el experimento RIBF127, y del reanálisis de cuatro núcleos que fueron implantados en mayor número durante el experimento parásito previo RIBF123. De los 39 P_{1n} que reportamos en esta tesis, 12 son medidos por primera vez y mejoramos considerablemente las incertidumbres del resto. Los valores de la evaluación [BdN-IAEA] para el P_{1n} del ^{87}As y al ^{92}Br desvirtuan los ajustes y por tanto los consideramos erroneos, así que son obtenidos

junto con el P_{xn} de sus progenitores el ^{87}Ge y el ^{92}Se respectivamente. En la Fig. E.14 se muestran los P_{1n} obtenidos en esta Tesis.

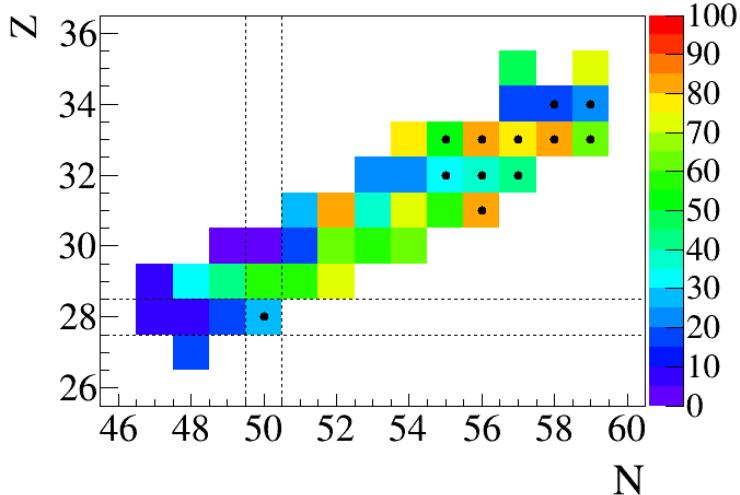


Figura E.14: Valores experimentales de los P_{1n} (en %) obtenidos en esta Tesis. Los puntos marcan los núcleos cuyo P_{1n} ha sido medido por primera vez en este trabajo de Tesis.

De los 17 P_{2n} que reportamos, 15 son completamente nuevos y mejoramos de forma importante la incertidumbre de dos que habían sido medidos previamente. Los P_{2n} obtenidos en esta Tesis se muestran en la Fig. E.15. Se pueden observar grandes oscilaciones para los P_{2n} dentro de las cadenas isotópicas del galio y del arsénico, y en menor medida en la cadena del cobre. Nótese que los máximos de esas oscilaciones en el caso de P_{1n} ocurren para núcleos con masa impar, y los del P_{2n} para núcleos con masa par.

En general, las vidas medianas de los núcleos estudiados por esta tesis han sido medidas previamente, y sólo reportamos valores nuevos en caso de poder mejorar la incertidumbre de las medidas existentes, confirmando el valor de la evaluación [BdN-IAEA] en el resto de casos. En el caso del ^{78}Cu y del ^{83}Ga , la vida media se obtuvo mediante el ajuste a la actividad beta-1-neutrón, ya que los padres son los únicos emisores de neutrón en sus respectivas cadenas. En el resto de casos donde se reporta la vida media, se obtuvo junto con el P_{xn} mediante un ajuste simultáneo a las curvas beta y beta-x-neutrón.

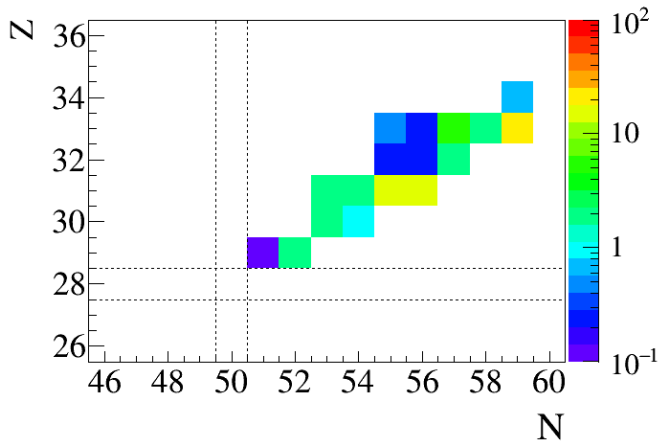


Figura E.15: Valores experimentales de los P_{2n} (en %) obtenidos en esta Tesis.

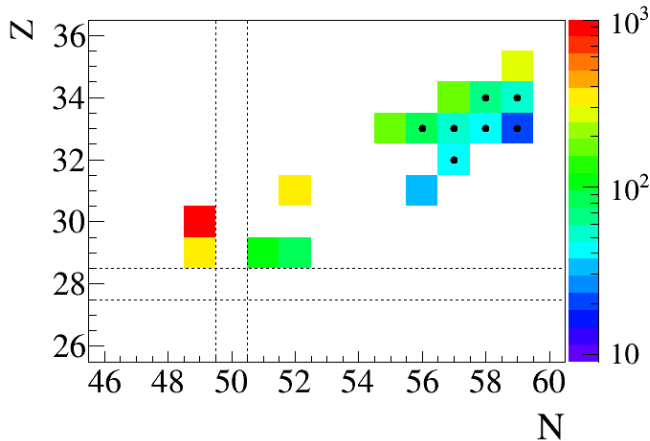


Figura E.16: Valores experimentales de las vidas medias $T_{1/2}$ (en milisegundos) obtenidos en este trabajo de Tesis. Un marcador identifica los núcleos cuya vida media ha sido medida por primera vez en este trabajo de tesis.

E.5 Discusión de los resultados

Esta sección está dedicada a la comparación de las predicciones teóricas de varios modelos para los resultados experimentales obtenidos en este trabajo de Tesis. En una segunda parte, se muestra el impacto de nuestros datos experimentales en cálculos de abundancias en diferentes entornos astrofísicos.

E.5.1 Comparación con predicciones teóricas

En la Fig. E.17 se presenta una comparación de los valores obtenidos en este trabajo de Tesis y las predicciones de los modelos descritos en la introducción. En general, [Möll03], [Möll19] y [Mar16] tienden a subestimar los valores experimentales para núcleos con $N > 50$, $Z > 28$. Koura tiende a predecir valores más bajos que los experimentales para núcleos con $N \sim 50$ y $Z \sim 28$. El isótopo ^{80}Zn es un caso particular, cuyo P_{1n} es sobre estimado por los modelos que implementan QRPA y subestimado por el modelo que implementa GT.

En la Fig. E.18 se muestra una comparación del modelo empírico de Miernik [Mie14] y los valores P_{1n} obtenidos en esta Tesis. Aunque subestima los valores correspondientes a los núcleos más ligeros, las predicciones teóricas se acercan a los valores experimentales especialmente para los isótopos más pesados excepto

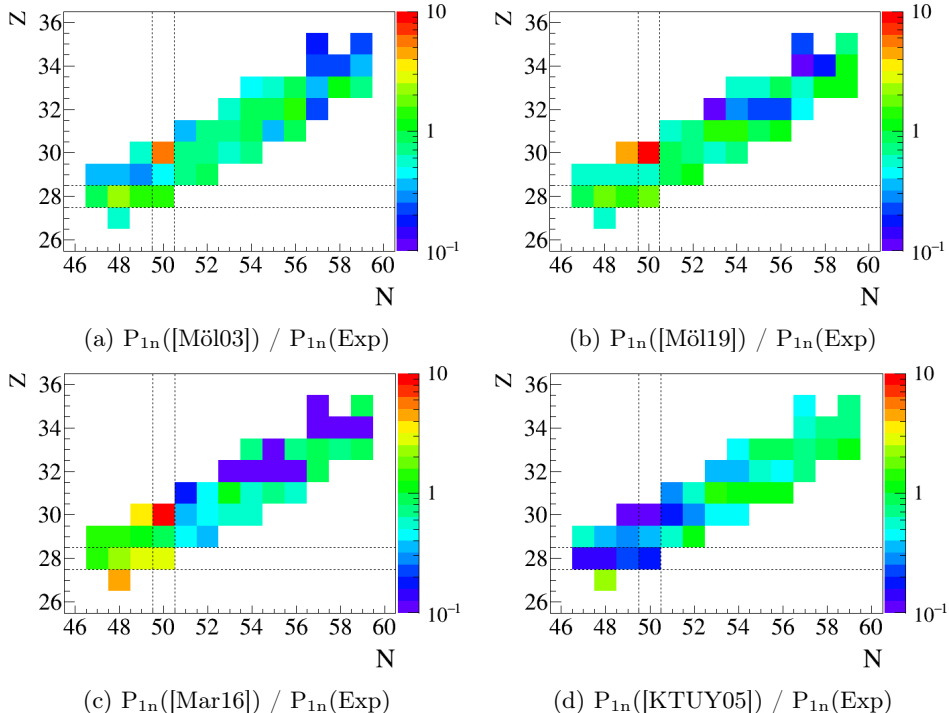


Figura E.17: Cociente de los valores P_{1n} calculados por diferentes modelos teóricos, y los valores experimentales obtenidos en este trabajo de Tesis. En el panel superior izquierdo se corresponde a la comparación de las predicciones de Möller y col. [Möll03], la superior derecha a Möller y col. [Möll19], la inferior izquierda a Marketin y col. [Mar16], y la inferior derecha a Koura y col. [KTUY05].

los del bromo. Como en el caso de los modelos microscópicos, el P_{1n} del ^{80}Zn es subestimado también por este modelo empírico.

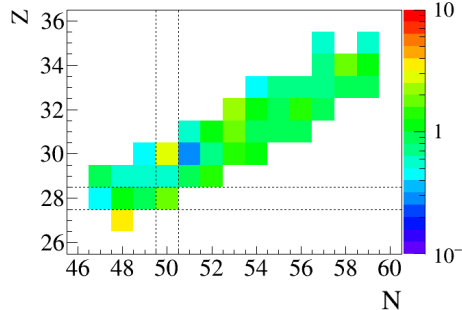


Figura E.18: Cociente de los valores experimentales P_{1n} obtenidos en esta Tesis y las predicciones teóricas del modelo empírico de Miernik [Mie14].

En la Fig. E.19 se muestra una comparación de las medidas de P_{2n} reportadas en la presente tesis y las predicciones de diferentes modelos. Las predicciones de [Möll03] se acercan más a los valores medidos para los isótopos más pesados de cada elemento, pero tiende a sobreestimar los valores pequeños correspondientes a los núcleos más ligeros. La versión más moderna de este modelo [Möll19] da valores en general más bajos o en algunos casos nulos. Los valores teóricos de Marketin [Mar16] reproducen bien los P_{2n} de los isótopos más ligeros pero subestima los valores correspondientes a isótopos más pesados, en particular con un número impar de protones. El modelo fenomenológico de [Mie14] da resultados cercanos a los valores experimentales, particularmente para los núcleos con N impar, pero subestima los P_{2n} de los núcleos ^{88}Ge y ^{89}As .

La Fig. E.20 muestra los valores teóricos de vidas medias calculados mediante los cuatro modelos globales presentados en la introducción comparados con los valores obtenidos en esta Tesis. Recuérdese que en el presente trabajo sólo se reportan los valores de vidas medias que mejoran medidas previas o que son nuevos. En el resto de casos, confirmamos los valores de la última evaluación. En general, [Möll03] predice vidas medias más largas, aunque los valores de la versión más reciente [Möll19] están más cerca de los valores experimentales. [KTUY05] predice valores de vidas medias en general por debajo de los valores experimentales, pero que reproducen las tendencias, especialmente para los isótopos más pesados. Los valores teóricos de [Mar16] son en general próximos o menores que los valores experimentales para núcleos con $N > 50$, y demasiado grandes para núcleos $N < 50$.

Además de estos modelos microscópicos sofisticados existen modelos empíricos que relacionan magnitudes macroscópicas de los núcleos. El modelo de McCutchan y col. [McC12] establece una correlación entre el cociente de la probabilidad de emisión total de neutrón y la vida media de un determinado núcleo y su $Q_{\beta 1n}$,

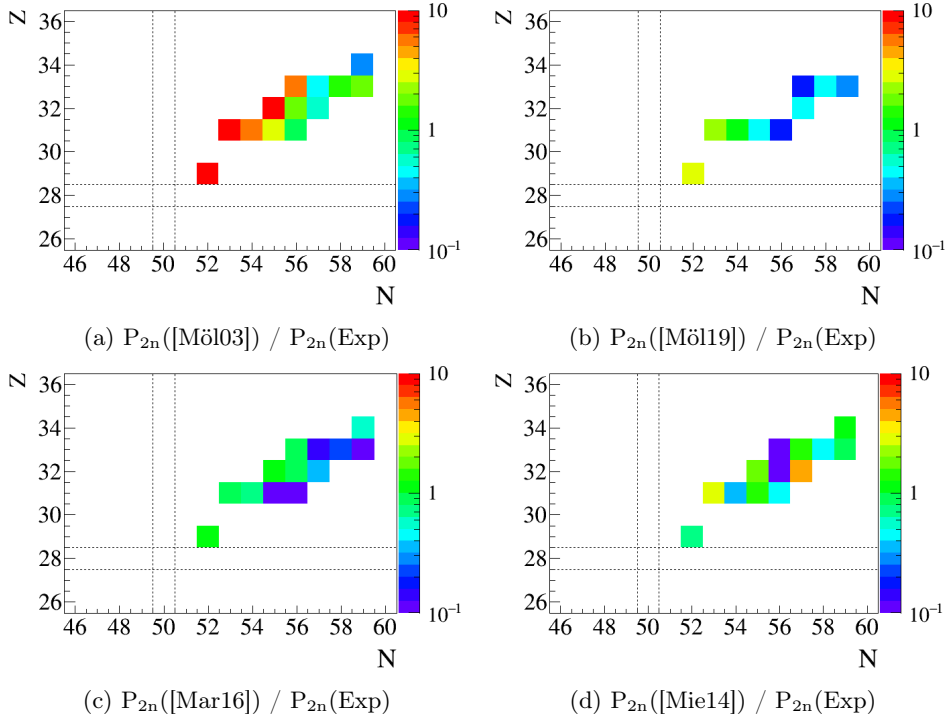


Figura E.19: Cociente de los valores P_{2n} calculados por diferentes modelos teóricos, y los valores experimentales obtenidos en este trabajo de Tesis. En el panel superior izquierdo se corresponde a la comparación de las predicciones de Möller y col. [Möll03], la superior derecha a Möller y col. [Möll19], la inferior izquierda a Marketin y col. [Mar16], y la inferior derecha a Miernik [Mie14].

según $P_n/T_{1/2} = cQ_{\beta 1n}^d$. Los parámetros fueron obtenidos de un ajuste a los datos experimentales disponibles en aquel momento, para núcleos con $28 \leq Z \leq 43$, encontrando $c = 0,0097(9)$ y $d = 4,87(7)$ [McC12]. En la Fig. E.21, los diferentes marcadores se corresponden con los cocientes de los valores experimentales P_n y $T_{1/2}$ de los núcleos estudiados en esta Tesis, en función del $Q_{\beta 1n}$; la línea roja se corresponde al modelo [McC12]. Se puede observar que la mayor parte de los puntos experimentales aparecen por encima de la línea roja (modelo), aunque la correlación lineal (en escala doble-logarítmica) es clara, en especial para las diferentes series isotópicas.

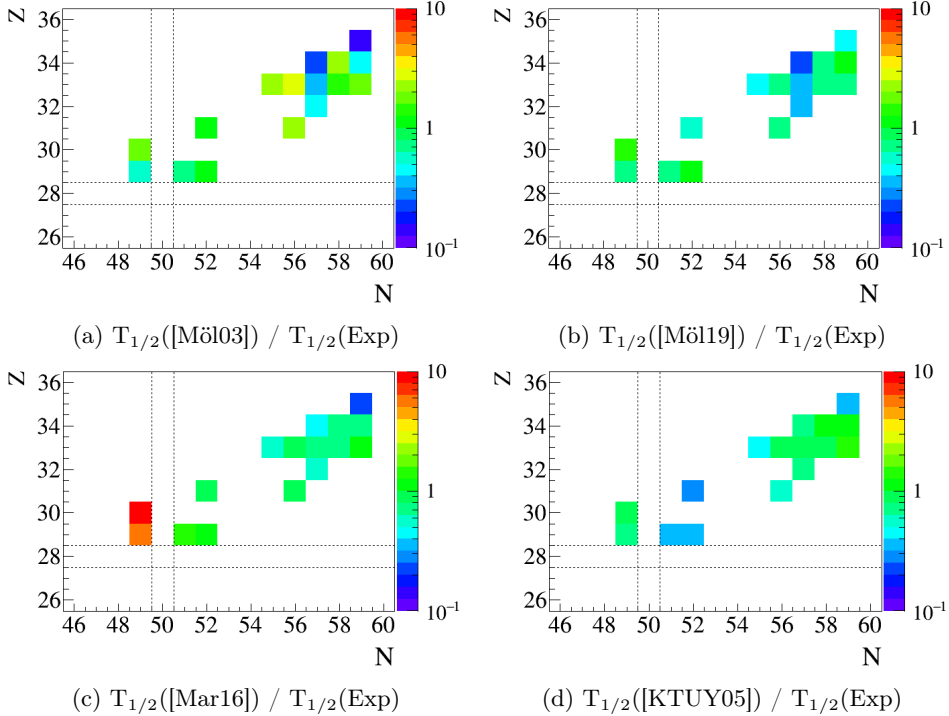


Figura E.20: Cociente de las vidas medias $T_{1/2}$ calculadas por diferentes modelos teóricos, y los valores experimentales obtenidos en este trabajo de Tesis. En el panel superior izquierdo se corresponde a la comparación de las predicciones de Möller y col. [Möll03], la superior derecha a Möller y col. [Möll19], la inferior izquierda a Marketin y col. [Mar16], y la inferior derecha a Koura y col. [KTUY05].

E.5.2 Impacto astrofísico

Como se explicaba al comienzo de este resumen, las simulaciones astrofísicas que calculan las abundancias producidas durante la nucleosíntesis mediante proceso-r constan de dos partes. Una primera donde se calcula la trayectoria termodinámica, y una segunda donde se calcula la evolución de las abundancias siguiendo la trayectoria antes calculada. Para este segundo cálculo se usó un programa que implementa una gran red de reacciones nucleares [Win13, Win12] de todos los núcleos registrado en la base de datos REACLIB. El impacto astrofísico se evalúa comparando el cálculo de las abundancias usando la versión estandar de la REACLIB, y una versión actualizada por nuestras medidas. En esta sección se mostrará el impacto en varias trayectorias correspondientes a explosiones supernova y a diferentes eyectas asociados a colisiones de estrellas de neutrones.

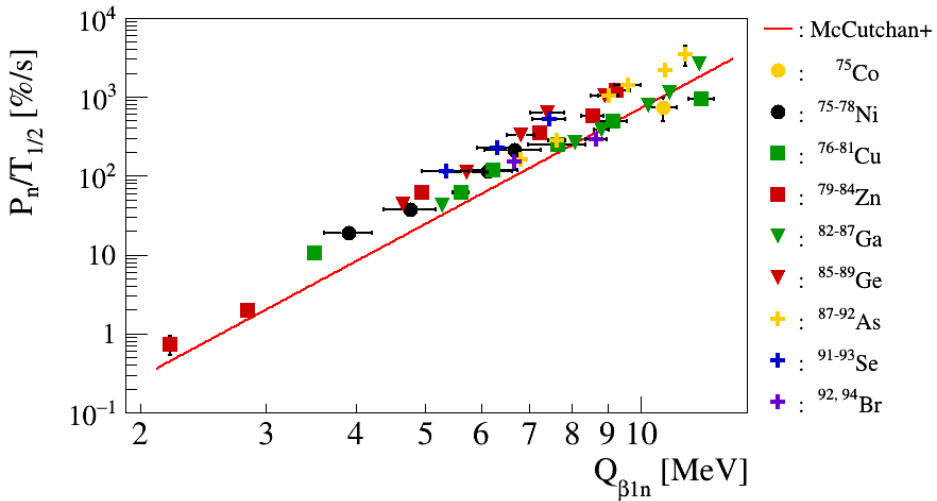


Figura E.21: Cociente de los valores experimentales $P_n/T_{1/2}$ en función de $Q_{\beta_{1n}}$. Cada punto se corresponde con un núcleo estudiado en este trabajo de Tesis. Los valores $Q_{\beta_{1n}}$ están tomados de la última evaluación [BdN-IAEA]. La línea roja se corresponde con la fórmula $P_n/T_{1/2} = cQ_{\beta_{1n}}^d$, con parámetros $c = 0,0097(9)$ y $d = 4,87(7)$ [McC12].

De acuerdo a las simulaciones más recientes, las explosiones supernova impulsadas por vientos de neutrinos dan lugar a un proceso-r débil, ya que los grandes flujos de neutrinos reducen la riqueza en neutrones y los elementos más pesados no llegan a sintetizarse. El impacto de los núcleos estudiados en esta tesis en tales entornos, evaluado en las trayectorias calculadas por [Bliss] es inexistente, porque el proceso-r discurre muy cerca de la estabilidad y los núcleos de interés nunca llegan a ser sintetizados. Sin embargo, bajo ciertas condiciones especiales como intensos campos magnéticos y altas velocidades de rotación de la estrella progenitora, parte del material puede ser eyectado antes de ser expuesto a los altos flujos de neutrinos y así conseguir un proceso-r en el que se sintetizan hasta los elementos más pesados. En estos casos, la evolución del proceso-r discurre más lejos de la estabilidad. En la Fig. E.22 se muestra el caso de las abundancias finales siguiendo la trayectoria presentada en [Win12]. Estas abundancias elementales $Y(A)$ se obtienen a partir de la densidad másica total ρ_{tot} y de la densidad másica elemental $\rho(A)$ como en la Eq. E.12. Las abundancias calculadas están normalizadas según $\sum Y_i A_i = 1$. En las siguientes figuras, se añade como referencia el patrón de abundancias del proceso-r observado en el Sistema Solar abundances, calculado

por Sneden y col. [Sne08], estando normalizado a 100 átomos para el silicio.

$$Y(A) = \frac{1}{A} \frac{\rho(A)}{\rho_{tot}} \quad (\text{E.12})$$

En el panel inferior de la Fig. E.22 se presentan las diferencias relativas de abundancias utilizando la base de datos estandar REACLIB o utilizando esa base de datos actualizada por nuestras medidas. Los núcleos estudiados en el presente trabajo tienen un impacto local en la región de masas 75-95, redistribuyendo las abundancias finales una vez que el proceso de captura termina y los núcleos así producidos se desintegran beta.

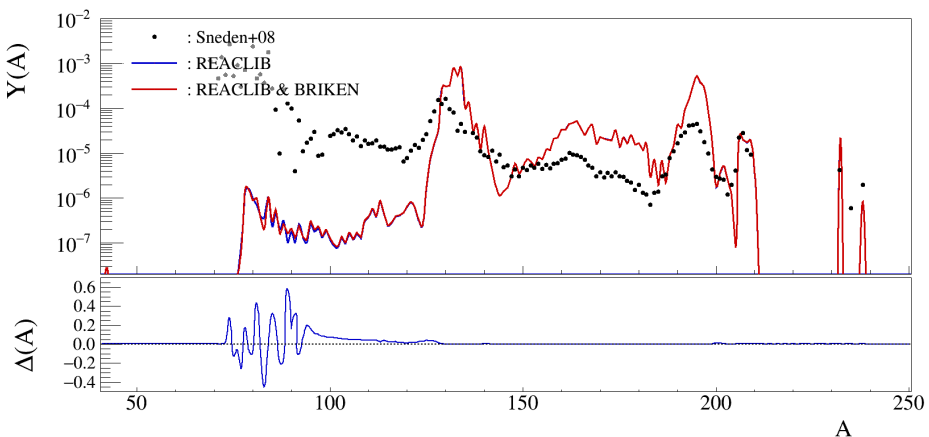


Figura E.22: Patrón de abundancias calculado, siguiendo la trayectoria termodinámica representativa mostrada en [Win12], usando la base de datos REACLIB (*REACLIB*) y esta base de datos actualizada por los resultados experimentales presentado en este trabajo de Tesis (*REACLIB & BRIKEN*).

En el caso de las trayectorias calculadas por [Obe17], correspondientes también a una explosión supernova con presencia de intensos campos magnéticos, el proceso-r comienza cerca de los núcleos estudiados aquí, por lo que el impacto en las abundancias finales se extiende a masas mayores, como puede verse en el panel inferior de la Fig. E.23 correspondiente a una de las trayectorias.

El otro candidato para la producción de elementos pesados mediante captura rápida de neutrones son las colisiones de dos estrellas de neutrones. Los sistemas binarios de estrellas de neutrones pierden energía mediante la emisión de ondas gravitacionales, y las intensas fuerzas de marea entre ellas pueden desgarrar parte de su compañera. La materia eyectada de esta forma, llamado eyecta dinámico frío, conserva la riqueza en neutrones de la estrella, y la nucleosíntesis hasta los elementos más pesados mediante proceso-r puede ocurrir. En el caso de la

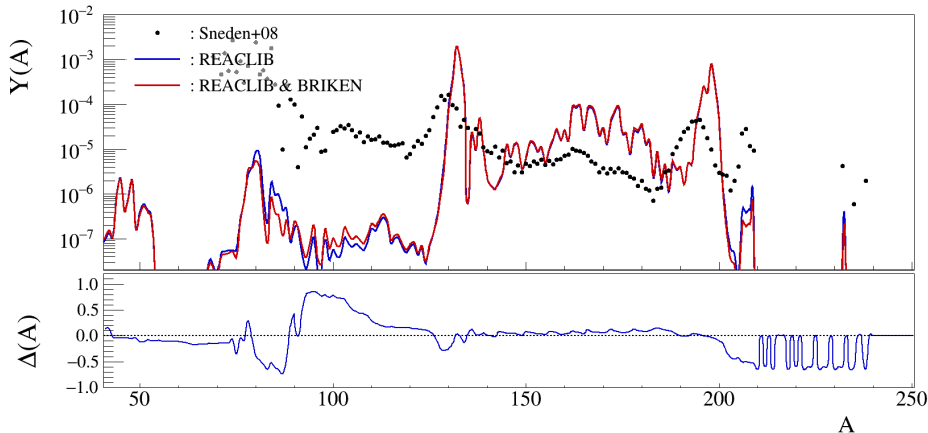


Figura E.23: Patrón de abundancias calculado, siguiendo la trayectoria termodinámica llamada *350C-RS*, presentada en [Obe17]. Las abundancias etiquetadas como *REACLIB* están calculadas usando la base de datos REACLIB, y las abundancias marcadas como *REACLIB & BRIKEN* resultan de usar la base de datos REACLIB actualizada con nuestras medidas experimentales.

trayectoria termodinámica estudiada por [Kor12b], el proceso-r discurre sobre la línea de goteo de neutrones, de forma que los núcleos estudiados son sintetizados marginalmente una vez terminado el proceso de captura, por lo que el impacto es muy reducido.

Se llama eyecta dinámico caliente al material desprendido durante la colisión de dos estrellas de neutrones. Se parece al proceso anterior, salvo por una temperatura más alta que obliga al proceso-r a discurrir más cerca de la estabilidad. El impacto en este tipo de entornos fue evaluado en las trayectorias calculadas por [Bov17]. En la Fig. E.24 se presentan las abundancias finales, y en el panel inferior las diferencias relativas al usar nuestros datos experimentales. Como en las trayectorias correspondientes a explosiones supernova impulsadas por inestabilidades magneto-rotacionales, el proceso-r discurre sobre núcleos más exóticos que los investigados en esta tesis, y se encuentra que nuestros datos experimentales tienen un papel en la redistribución local de las abundancias finales de elementos con masas entre 75 y 95, una vez que el proceso de captura termina.

Tras la colisión, los escombros se agrupan en un disco de acreción en torno al remanente de la fusión de las dos estrellas de neutrones. Si el objeto resultante tiene masa suficiente, puede eventualmente colapsar a un agujero negro. Si el objeto central no colapsa inmediatamente a un agujero negro, un viento de neutrinos puede arrastrar parte del material circundante a la estrella de neutrones hipermasiva, y puede darse la nucleosíntesis por proceso-r. La opacidad del disco causa una

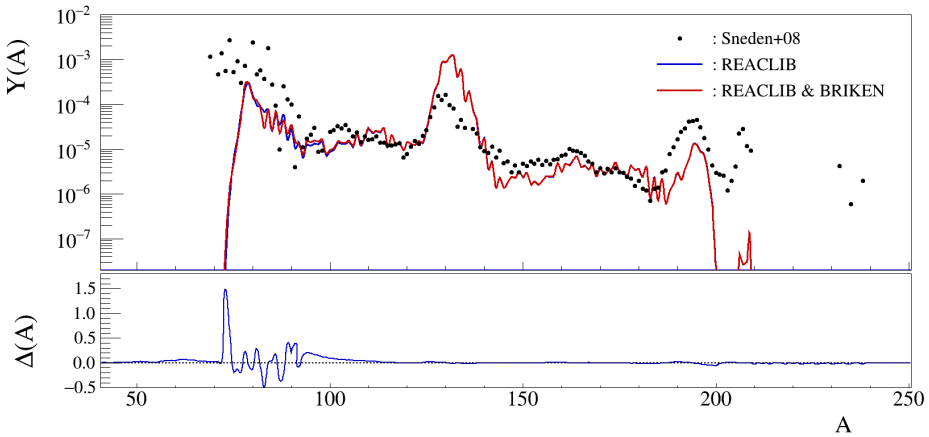


Figura E.24: Patrón de abundancias de un eyecta dinámico caliente, calculado siguiendo la trayectoria número #651 de [Bov17].

dependencia angular en el flujo de neutrinos. Como en el caso de las explosiones supernova, un flujo extremadamente alto puede disminuir la riqueza en neutrones del material y evitar que la nucleosíntesis alcance los elementos más pesados. Para evaluar el impacto de nuestros nucleos bajo estas condiciones, se siguió cada una de las cuatro trayectorias representativas dadas en [Mar15], correspondientes a cada rango de latitudes como se muestra en la Fig. E.25.

En el caso de la trayectorias correspondientes al segundo, tercer y cuarto rango de latitudes, el proceso-r discurre cerca de los núcleos estudiados en esta tesis, y se encuentra que el impacto se extiende a masas 130. En la Fig. E.26 se muestran las abundancias finales correspondientes a la trayectoria correspondiente al tercer rango de latitudes. En el caso de la trayectoria correspondiente al primer rango de latitudes, es la menos rica en neutrones y sólo se sintetizan elementos hasta masa 80, de forma que nuestros núcleos tienen un impacto reducido.

Efectos viscosos, causados por los altos campos magnéticos, y efectos de rotación diferencial pueden ser capaces de eyectar material del disco de acreción. Nuestros datos experimentales tienen un impacto inesperado en las abundancias finales calculadas según una de las trayectorias investigadas en [Lip17], como se puede ver en la Fig. E.27. En el panel inferior se observa el impacto por la redistribución de las abundancias finales de los elementos con masas entre 75 y 95, como ocurre en otros casos antes mencionados. Adicionalmente, se encuentra que los elementos con masa entre 150 y 210 son producidos en mayor cantidad en el cálculo que utiliza nuestros datos, con respecto del cálculo que utiliza la base de datos REACLIB. Aunque los núcleos medidos en esta tesis tienen una masa menor, forman parte del proceso-r y la evolución de las abundancias durante el proceso de captura cambia

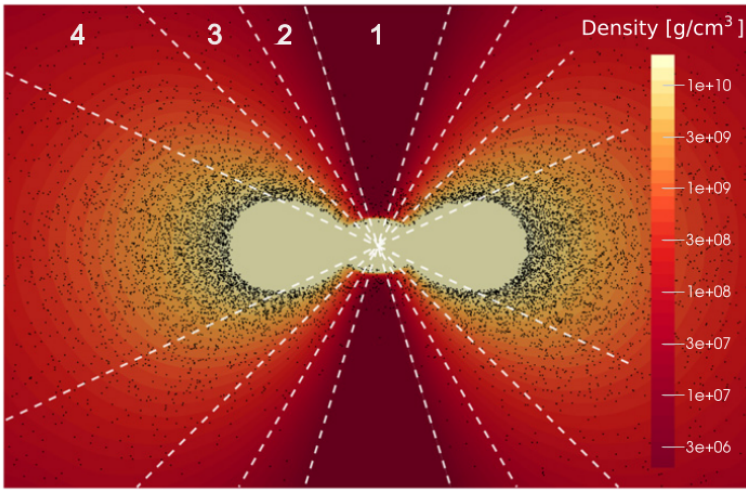


Figura E.25: Perfil de densidad en el plano $x - z$ al comienzo de la simulación. Se eligió una trayectoria representativa para cada región angular (Fig. 2 de [Mar15]).

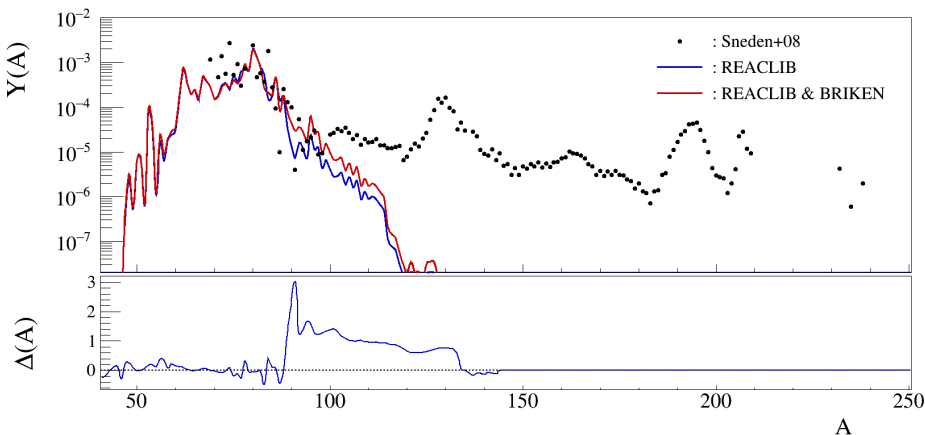


Figura E.26: El patrón de abundancias causado por los eyectas del viento de neutrinos tras una colisión de dos estrellas de neutrones [Mar15], calculado según la trayectoria correspondiente al tercer rango de latitudes en Fig. E.25.

lo suficiente como para reflejarse en las abundancias finales.

En esta sección se ha mostrado que los núcleos estudiados en este trabajo de Tesis tienen un impacto en las abundancias finales de la nucleosíntesis mediante proceso- r , evaluado en diferentes trayectorias termodinámicas correspondientes a

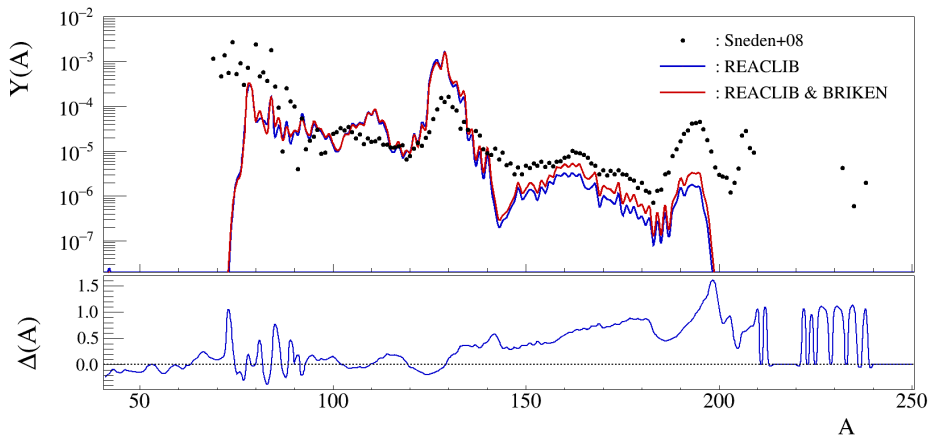


Figura E.27: Patrón de abundancias producido en un eyecta de disco de acreción resultante de la colisión de dos estrellas de neutrones, siguiendo la trayectoria dada en [Lip17].

diferentes eventos astrofísicos. Nuestros núcleos pueden tener un impacto local, en elementos con masas entre 75 y 95, o un impacto en núcleos de masas mayores. En el caso del primero, consiste en una redistribución local de las abundancias finales, que ocurre mientras los núcleos sintetizados durante el proceso de captura de neutrones una vez que éste termina. Este efecto se puede observar en todas los casos aquí presentados. El segundo caso, donde se encuentra un impacto en las abundancias finales de elementos con masa mayor de 95, se debe a que el proceso-r discurre por alguno de los núcleos estudiados por este trabajo de Tesis. Esto causa un reajuste en la evolución posterior del proceso, que se traduce en un cambio en las abundancias finales que se extiende a elementos más pesados que los núcleos aquí estudiados.

Bibliography

- [Abb16] B. P. Abbott et al. “Observation of Gravitational Waves from a Binary Black Hole Merger”. In: *Phys. Rev. Lett.* 116 (6 Feb. 2016), p. 061102. DOI: [10.1103/PhysRevLett.116.061102](https://doi.org/10.1103/PhysRevLett.116.061102).
- [Abb17a] B. P. Abbott et al. “GW170817: Observation of Gravitational Waves from a Binary Neutron Star Inspiral”. In: *Phys. Rev. Lett.* 119 (16 Oct. 2017), p. 161101. DOI: [10.1103/PhysRevLett.119.161101](https://doi.org/10.1103/PhysRevLett.119.161101).
- [Abb17b] B. P. Abbott et al. “Multi-messenger Observations of a Binary Neutron Star Merger”. In: *ApJ* 848.2 (Oct. 2017), p. L12. DOI: [10.3847/2041-8213/aa91c9](https://doi.org/10.3847/2041-8213/aa91c9).
- [Abb19] B. P. Abbott et al. “GWTC-1: A Gravitational-Wave Transient Catalog of Compact Binary Mergers Observed by LIGO and Virgo during the First and Second Observing Runs”. In: *Phys. Rev. X* 9 (3 Sept. 2019), p. 031040. DOI: [10.1103/PhysRevX.9.031040](https://doi.org/10.1103/PhysRevX.9.031040).
- [Agr16] J. Agramunt et al. “Characterization of a neutron-beta counting system with beta-delayed neutron emitters”. In: *Nucl. Instrum. Methods Phys. Res. A* 807 (2016), pp. 69–78. DOI: <https://doi.org/10.1016/j.nima.2015.10.082>.
- [Agr18] J. Agramunt et al. *Data integration for experiments with independent setups, BRIKEN approach*. Nuclear physics in stellar explosions Workshop ’18, (p. 56). Hungary: Institute for Nuclear Research of the Hungarian Academy of Sciences. 2018. URL: https://inis.iaea.org/search/search.aspx?orig_q=RN:50024427.
- [AIDA] T. Davinson. *Web of AIDA Collaboration*. 2019. URL: <http://www2.ph.ed.ac.uk/~td/AIDA/welcome.html>.
- [Als16] M. F. Alshudifat et al. “Reexamining Gamow-Teller decays near ^{78}Ni ”. In: *Phys. Rev. C* 93 (4 Apr. 2016), p. 044325. DOI: [10.1103/PhysRevC.93.044325](https://doi.org/10.1103/PhysRevC.93.044325).

Bibliography

- [Arc11] A. Arcones et al. “Dynamical r -process studies within the neutrino driven wind scenario and its sensitivity to the nuclear physics input”. In: *Phys. Rev. C* 83 (4 Apr. 2011), p. 045809. DOI: 10.1103/PhysRevC.83.045809.
- [Asg75] M. Asghar et al. “The Pn values of the ^{235}U (nth, f) produced precursors in the mass chains 90, 91, 93–95, 99, 134 and 137–139”. In: *Nuclear Physics A* 247.2 (1975), pp. 359–376. DOI: [https://doi.org/10.1016/0375-9474\(75\)90642-9](https://doi.org/10.1016/0375-9474(75)90642-9).
- [B²HF] E. Margaret Burbidge et al. “Synthesis of the Elements in Stars”. In: *Rev. Mod. Phys.* 29 (4 Oct. 1957), pp. 547–650. DOI: 10.1103/RevModPhys.29.547.
- [Bab09] Hidekada Baba. *Logic Unit for Programmable Operation (LUPO) web page*. 2009. URL: <https://ribf.riken.jp/RIBFDAQ/index.php?DAQ/Information/Module/LUPO>.
- [Bab10] H. Baba et al. “New data acquisition system for the RIKEN Radioactive Isotope Beam Factory”. In: *Nucl. Instrum. Methods Phys. Res. A* 616.1 (2010), pp. 65–68. DOI: <https://doi.org/10.1016/j.nima.2010.02.120>.
- [Bat10] H. Bateman. “The solution of a system of differential equations occurring in the theory of radioactive transformations”. In: *Proc. Cambridge Philos. Soc* 15(V) (1910), pp. 423–427.
- [BdN-IAEA] Beta-Delayed Neutron Emission Reference Database. URL: <https://www-nds.iaea.org/relnsd/delayedn/delayedn.html> (visited on 12/2019).
- [Bec96] Henri Becquerel. “On the rays emitted by phosphorescence”. In: *Compt. Rend. Hebd. Séances Acad. Sci.* 122.8 (1896), pp. 420–421.
- [Ben03] M. Bender et al. “Self-consistent mean-field models for nuclear structure”. In: *Rev. Mod. Phys.* 75 (1 Jan. 2003), pp. 121–180. DOI: 10.1103/RevModPhys.75.121.
- [BigRIPS] *BigRIPS Technical information*. Feb. 2019. URL: <https://ribf.riken.jp/BigRIPSInfo/>.
- [Bli18] J. Bliss et al. “Survey of Astrophysical Conditions in Neutrino-driven Supernova Ejecta Nucleosynthesis”. In: *ApJ* 855.2 (Mar. 2018), p. 135. DOI: 10.3847/1538-4357/aaadbe.
- [Bor05] I. N. Borzov. “ β -delayed neutron emission in the ^{78}Ni region”. In: *Phys. Rev. C* 71 (6 June 2005), p. 065801. DOI: 10.1103/PhysRevC.71.065801.
- [Bor12] Borzov, I. N. “Evolution of single-particle structure and beta-decay near ^{78}Ni ”. In: *EPJ Web of Conferences* 38 (2012), p. 12002. DOI: 10.1051/epjconf/20123812002.

- [Bor16] I. N. Borzov. “Self-consistent approach to beta decay and delayed neutron emission”. In: *Physics of Atomic Nuclei* 79.6 (Nov. 2016), pp. 910–923. DOI: [10.1134/S1063778816060041](https://doi.org/10.1134/S1063778816060041).
- [Bov17] Luke Bovard et al. “*r*-process nucleosynthesis from matter ejected in binary neutron star mergers”. In: *Phys. Rev. D* 96 (12 Dec. 2017), p. 124005. DOI: [10.1103/PhysRevD.96.124005](https://doi.org/10.1103/PhysRevD.96.124005).
- [Bra11] D. Braga et al. “AIDA: A 16-channel amplifier ASIC to read out the Advanced Implantation Detector Array for experiments in nuclear decay spectroscopy”. In: *2011 2nd International Conference on Advancements in Nuclear Instrumentation, Measurement Methods and their Applications*. June 2011, pp. 1–5. DOI: [10.1109/ANIMMA.2011.6172853](https://doi.org/10.1109/ANIMMA.2011.6172853).
- [Bra89] M. C. Brady. “Evaluation and Application of Delayed Neutron Precursor Data”. PhD thesis. 1989.
- [BRIKEN] *Web of BRIKEN (Beta-delayed neutrons at RIKEN) Collaboration*. URL: <https://www.wiki.ed.ac.uk/display/BRIKEN/Home>.
- [Bru97] R. Brun et al. “ROOT — An object oriented data analysis framework”. In: *Nucl. Instrum. Methods Phys. Res. A* 389.1 (1997), pp. 81–86. DOI: [https://doi.org/10.1016/S0168-9002\(97\)00048-X](https://doi.org/10.1016/S0168-9002(97)00048-X).
- [Cam57] A. G. W. Cameron. “Nuclear Reactions in Stars and Nucleogenesis”. In: *Publications of the Astronomical Society of the Pacific* 69 (June 1957), p. 201. DOI: [10.1086/127051](https://doi.org/10.1086/127051).
- [Car15] P.F.F. Carnelli et al. “Multi-Sampling Ionization Chamber (MUSIC) for measurements of fusion reactions with radioactive beams”. In: *Nucl. Instrum. Methods Phys. Res. A* 799 (2015), pp. 197–202. DOI: <https://doi.org/10.1016/j.nima.2015.07.030>.
- [Cow04] J. J. Cowan et al. “R-Process Nucleosynthesis in Supernovae”. In: *Physics Today* 57 (10 2004), pp. 47–53. DOI: [10.1063/1.1825268](https://doi.org/10.1063/1.1825268).
- [Cra78] J. Crancon et al. “Half-Lives and P(n) Values of Delayed-Neutron Precursors in the Mass Chains 85-87, 92, 135, 136 and 145”. In: *Z. Phys. A* 287 (1978), p. 45.
- [Cro12] S. Croft et al. “Extraction of correlated count rates using various gate generation techniques: Part I theory”. In: *Nucl. Instrum. Methods Phys. Res. A* 691 (2012), pp. 152–158. DOI: <https://doi.org/10.1016/j.nima.2012.06.011>.
- [Cyb10] Richard H. Cyburt et al. “The JINA REACLIB database: its recent updates and impact on type-I x-ray bursts”. In: *ApJS* 189.1 (June 2010), pp. 240–252. DOI: [10.1088/0067-0049/189/1/240](https://doi.org/10.1088/0067-0049/189/1/240).

Bibliography

- [Eks86] B. Ekstrom et al. “Decay Properties of $^{75-80}\text{Zn}$ and Q(β)-Values of Neutron-Rich Zn and Ga Isotopes”. In: *Phys.Scr.* 34 (1986), p. 614.
- [Ewa84] G. T. Ewan et al. “Intense Mass-Separated Beams of Halogens and Beta-Delayed Neutron Emission from Heavy Bromine Isotopes”. In: *Z.Phys.* A318 (1984), p. 309.
- [Fay00] S.A. Fayans et al. “Nuclear isotope shifts within the local energy-density functional approach”. In: *Nuclear Physics A* 676.1 (2000), pp. 49–119. DOI: [https://doi.org/10.1016/S0375-9474\(00\)00192-5](https://doi.org/10.1016/S0375-9474(00)00192-5).
- [Fuk13] N. Fukuda et al. “Identification and separation of radioactive isotope beams by the BigRIPS separator at the RIKEN RI Beam Factory”. In: *Nucl. Instrum. Methods Phys. Res. B* 317 (2013), pp. 323–332. DOI: <https://doi.org/10.1016/j.nimb.2013.08.048>.
- [Gor10] S. Goriely et al. “Further explorations of Skyrme-Hartree-Fock-Bogoliubov mass formulas. XII. Stiffness and stability of neutron-star matter”. In: *Phys. Rev. C* 82 (3 Sept. 2010), p. 035804. DOI: [10.1103/PhysRevC.82.035804](https://doi.org/10.1103/PhysRevC.82.035804).
- [Gra74] B. Grapengiesser et al. “Survey of short-lived fission products obtained using the isotope-separator-on-line facility at Studsvik”. In: *Journal of Inorganic and Nuclear Chemistry* 36.11 (1974), pp. 2409–2431. DOI: [https://doi.org/10.1016/0022-1902\(74\)80448-3](https://doi.org/10.1016/0022-1902(74)80448-3).
- [Gri19] Christopher Griffin. “ β -decay studies of r-process nuclei using the Advanced Implantation Detector Array (AIDA)”. PhD thesis. July 2019.
- [Gro00] C.J Gross et al. “Performance of the Recoil Mass Spectrometer and its detector systems at the Holifield Radioactive Ion Beam Facility”. In: *Nucl. Instrum. Methods Phys. Res. A* 450.1 (2000), pp. 12–29. DOI: [https://doi.org/10.1016/S0168-9002\(00\)00159-5](https://doi.org/10.1016/S0168-9002(00)00159-5).
- [Hal18] Oscar Hall. *AIDA Sort*. Dec. 2018. URL: <https://github.com/ohall1/AIDASort>.
- [Hal20] Oscar Hall. “(to be published)”. PhD thesis. Feb. 2020.
- [Hor19] C J Horowitz et al. “r-process nucleosynthesis: connecting rare isotope beam facilities with the cosmos”. In: *J. Phys. G* 46.8 (July 2019), p. 083001. DOI: [10.1088/1361-6471/ab0849](https://doi.org/10.1088/1361-6471/ab0849).
- [Hos10] P. Hosmer et al. “Half-lives and branchings for β -delayed neutron emission for neutron-rich Co–Cu isotopes in the *r*-process”. In: *Phys. Rev. C* 82 (2 Aug. 2010), p. 025806. DOI: [10.1103/PhysRevC.82.025806](https://doi.org/10.1103/PhysRevC.82.025806).

- [Ily09] S. V. Ilyushkin et al. “ β decay of the $\pi f_{5/2}$ ground state of ^{77}Cu studied with 225 MeV and 0.2 MeV purified radioactive beams”. In: *Phys. Rev. C* 80 (5 Nov. 2009), p. 054304. DOI: [10.1103/PhysRevC.80.054304](https://doi.org/10.1103/PhysRevC.80.054304).
- [Iso13] T. Isobe. “Anaroot: new online/offline framework for ribf data analysis based on ROOT”. In: *RIBF User meeting*. 2013.
- [Kal12] Jason S. Kalirai. “The age of the Milky Way inner halo”. In: *Nature* 486.7401 (June 2012), pp. 90–92. DOI: [10.1038/nature11062](https://doi.org/10.1038/nature11062).
- [Kaw08] T. Kawano et al. “Calculation of delayed-neutron energy spectra in a quasiparticle random-phase approximation–Hauser–Feshbach model”. In: *Phys. Rev. C* 78 (5 Nov. 2008), p. 054601. DOI: [10.1103/PhysRevC.78.054601](https://doi.org/10.1103/PhysRevC.78.054601).
- [Kor12a] A. Korgul et al. “ β - γ and β -delayed neutron- γ decay of neutron-rich copper isotopes”. In: *Phys. Rev. C* 86 (2 Aug. 2012), p. 024307. DOI: [10.1103/PhysRevC.86.024307](https://doi.org/10.1103/PhysRevC.86.024307).
- [Kor12b] O. Korobkin et al. “On the astrophysical robustness of the neutron star merger r-process”. In: *Mon. Notices Royal Astron. Soc.* 426.3 (Nov. 2012), pp. 1940–1949. DOI: [10.1111/j.1365-2966.2012.21859.x](https://doi.org/10.1111/j.1365-2966.2012.21859.x).
- [Kos00] U. Koster. *Ausbeuten und Spektroskopie radioaktiver Isotope bei LOHENGRIN und ISOLDE*. PhD thesis. Technischen Univ. Munchen, Germany., 2000.
- [Kra88] K.-L. Kratz et al. “Onset of Deformation in Neutron-Rich Krypton Isotopes”. In: *Z. Phys.* A330 (1988), p. 229.
- [Kra91] K. -L. Kratz et al. “Neutron-Rich Isotopes Around the r-Process ’Waiting-Point’ Nuclei $^{79}_{29}\text{Cu}_{50}$ and $^{80}_{30}\text{Zn}_{50}$ ”. In: *Z.Phys.* A340 (1991), p. 419.
- [KTUY00] H. Koura et al. “Nuclear mass formula with shell energies calculated by a new method”. In: *Nuclear Physics A* 674.1 (2000), pp. 47–76. DOI: [https://doi.org/10.1016/S0375-9474\(00\)00155-X](https://doi.org/10.1016/S0375-9474(00)00155-X).
- [KTUY05] H. Koura et al. “Nuclidic Mass Formula on a Spherical Basis with an Improved Even-Odd Term”. In: *Prog. Theor. Phys.* 113.2 (Feb. 2005), pp. 305–325. DOI: [10.1143/PTP.113.305](https://doi.org/10.1143/PTP.113.305).
- [Kub12] T. Kubo et al. “BigRIPS separator and ZeroDegree spectrometer at RIKEN RI Beam Factory”. In: *Prog. Theor. Exp. Phys.* 2012.1 (Dec. 2012). DOI: [10.1093/ptep/pts064](https://doi.org/10.1093/ptep/pts064).
- [Kum13] H. Kumagai et al. “Development of Parallel Plate Avalanche Counter (PPAC) for BigRIPS fragment separator”. In: *Nucl. Instrum. Methods Phys. Res. B* 317 (2013), pp. 717–727. DOI: <https://doi.org/10.1016/j.nimb.2013.08.050>.

Bibliography

- [LabJack] *LabJack*. URL: <https://labjack.com/> (visited on 12/2016).
- [Leo87] W. R. Leo. *Techniques for Nuclear and Particle Physics Experiments: A How to Approach*. 1987.
- [Lic14] R. Lică et al. “Low-lying isomeric states in ^{80}Ga from the β^- decay of ^{80}Zn ”. In: *Phys. Rev. C* 90 (1 July 2014), p. 014320. DOI: 10.1103/PhysRevC.90.014320.
- [Lip17] J. Lippuner et al. “Signatures of hypermassive neutron star lifetimes on r-process nucleosynthesis in the disc ejecta from neutron star mergers”. In: *Mon. Notices Royal Astron. Soc.* 472.1 (Aug. 2017), pp. 904–918. DOI: 10.1093/mnras/stx1987.
- [Liu11] Min Liu et al. “Further improvements on a global nuclear mass model”. In: *Phys. Rev. C* 84 (1 July 2011), p. 014333. DOI: 10.1103/PhysRevC.84.014333.
- [Mad16] M. Madurga et al. “Evidence for Gamow-Teller Decay of ^{78}Ni Core from Beta-Delayed Neutron Emission Studies”. In: *Phys. Rev. Lett.* 117 (9 Aug. 2016), p. 092502. DOI: 10.1103/PhysRevLett.117.092502.
- [Mar] Dirk Martin. *Priv. comm.*
- [Mar07] T. Marketin et al. “Calculation of β -decay rates in a relativistic model with momentum-dependent self-energies”. In: *Phys. Rev. C* 75 (2 Feb. 2007), p. 024304. DOI: 10.1103/PhysRevC.75.024304.
- [Mar15] D. Martin et al. “Neutrino-driven winds in the aftermath of a neutron star merger: nucleosynthesis and electromagnetic transients”. In: *ApJ* 813.1 (Oct. 2015), p. 2. DOI: 10.1088/0004-637x/813/1/2.
- [Mar16] T. Marketin et al. “Large-scale evaluation of β -decay rates of r-process nuclei with the inclusion of first-forbidden transitions”. In: *Phys. Rev. C* 93 (2 Feb. 2016), p. 025805. DOI: 10.1103/PhysRevC.93.025805.
- [Maz13] C. Mazzocchi et al. “New half-life measurements of the most neutron-rich arsenic and germanium isotopes”. In: *Phys. Rev. C* 87 (3 Mar. 2013), p. 034315. DOI: 10.1103/PhysRevC.87.034315.
- [McC12] E. A. McCutchan et al. “Improving systematic predictions of β -delayed neutron emission probabilities”. In: *Phys. Rev. C* 86 (4 Oct. 2012), p. 041305. DOI: 10.1103/PhysRevC.86.041305.
- [Merger] J. Agramunt et al. *BRIKEN Merger*. 2018. URL: <http://isvn.ific.uv.es/repos/BrikenTools/Merger>.
- [Mesytec] *Mesytec*. URL: <https://www.mesytec.com/> (visited on 12/2019).

- [Met10] B. D. Metzger et al. “Electromagnetic counterparts of compact object mergers powered by the radioactive decay of r-process nuclei”. In: *Mon. Notices Royal Astron. Soc.* 406.4 (Aug. 2010), pp. 2650–2662. DOI: [10.1111/j.1365-2966.2010.16864.x](https://doi.org/10.1111/j.1365-2966.2010.16864.x).
- [MIDAS] *Multi Instance Data Acquisition System, MIDAS package*. URL: <http://npg.dl.ac.uk/MIDAS/>.
- [Mie13a] K. Miernik et al. “ β -decay study of neutron-rich bromine and krypton isotopes”. In: *Phys. Rev. C* 88 (1 July 2013), p. 014309. DOI: [10.1103/PhysRevC.88.014309](https://doi.org/10.1103/PhysRevC.88.014309).
- [Mie13b] K. Miernik et al. “Large β -Delayed One and Two Neutron Emission Rates in the Decay of ^{86}Ga ”. In: *Phys. Rev. Lett.* 111 (13 Sept. 2013), p. 132502. DOI: [10.1103/PhysRevLett.111.132502](https://doi.org/10.1103/PhysRevLett.111.132502).
- [Mie13c] K. Miernik et al. “Large β -Delayed One and Two Neutron Emission Rates in the Decay of ^{86}Ga ”. In: *Phys. Rev. Lett.* 111 (13 Sept. 2013), p. 132502. DOI: [10.1103/PhysRevLett.111.132502](https://doi.org/10.1103/PhysRevLett.111.132502).
- [Mie14] K. Miernik. “ β -delayed multiple-neutron emission in the effective density model”. In: *Phys. Rev. C* 90 (5 Nov. 2014), p. 054306. DOI: [10.1103/PhysRevC.90.054306](https://doi.org/10.1103/PhysRevC.90.054306).
- [Mie18] K. Miernik et al. “ β -delayed neutron emission from ^{85}Ga ”. In: *Phys. Rev. C* 97 (5 May 2018), p. 054317. DOI: [10.1103/PhysRevC.97.054317](https://doi.org/10.1103/PhysRevC.97.054317).
- [MINOS] Fred James et al. “MINUIT User’s Guide”. In: (June 2004).
- [Möл03] P. Möller et al. “New calculations of gross β -decay properties for astrophysical applications: Speeding-up the classical r process”. In: *Phys. Rev. C* 67 (5 May 2003), p. 055802. DOI: [10.1103/PhysRevC.67.055802](https://doi.org/10.1103/PhysRevC.67.055802).
- [Möл16] P. Möller et al. “Nuclear ground-state masses and deformations: FRDM(2012)”. In: *At. Data Nucl. Data Tables* 109-110 (2016), pp. 1–204. DOI: <https://doi.org/10.1016/j.adt.2015.10.002>.
- [Möл19] P. Möller et al. “Nuclear properties for astrophysical and radioactive ion beam applications (II)”. In: *At. Data Nucl. Data Tables* 125 (2019), pp. 1–192. DOI: <https://doi.org/10.1016/j.adt.2018.03.003>.
- [Möл95] P. Möller et al. “Nuclear Ground-State Masses and Deformations”. In: *At. Data Nucl. Data Tables* 59.2 (1995), pp. 185–381. DOI: <https://doi.org/10.1006/adnd.1995.1002>.
- [Mon08] L. Moneta et al. “Recent improvements of the ROOT fitting and minimization classes”. In: *PoS* (2008), p. 075.

Bibliography

- [MPOD] *MPOD Universal Low and High Voltage Power Supply System, Wiener.* URL: <http://www.wiener-d.com/sc/power-supplies/mpod--lvhv/> (visited on 12/2017).
- [Mum16a] M. R. Mumpower et al. “Neutron- γ competition for β -delayed neutron emission”. In: *Phys. Rev. C* 94 (6 Dec. 2016), p. 064317. DOI: [10.1103/PhysRevC.94.064317](https://doi.org/10.1103/PhysRevC.94.064317).
- [Mum16b] M. R. Mumpower et al. “The impact of individual nuclear properties on r-process nucleosynthesis”. In: *Prog. Part. Nucl. Phys.* 86 (2016), pp. 86–126. DOI: <https://doi.org/10.1016/j.ppnp.2015.09.001>.
- [NDS-IAEA] Vienna (Austria) Nuclear Data Section International Atomic Energy Agency. *Cf-252 neutron spectrum*. Tech. rep. 1987, p. 44.
- [Nis13] S. Nishimura et al. *WAS3ABi: The beta-counting system for the EURICA project*. 2013.
- [Obe17] M. Obergaulinger et al. “Protomagnetar and black hole formation in high-mass stars”. In: *Mon. Notices Royal Astron. Soc. Letters* 469.1 (Mar. 2017), pp. L43–L47. DOI: [10.1093/mnrasl/slx046](https://doi.org/10.1093/mnrasl/slx046).
- [Pad10] S. Padgett et al. “ β decay of ^{81}Zn and migrations of states observed near the $N = 50$ closed shell”. In: *Phys. Rev. C* 82 (6 Dec. 2010), p. 064314. DOI: [10.1103/PhysRevC.82.064314](https://doi.org/10.1103/PhysRevC.82.064314).
- [Pan05] I.V. Panov et al. “Calculations of fission rates for r-process nucleosynthesis”. In: *Nucl. Phys.* 747.2 (2005), pp. 633–654. DOI: <https://doi.org/10.1016/j.nuclphysa.2004.09.115>.
- [Pan10] I. V. Panov et al. “Neutron-induced astrophysical reaction rates for translead nuclei*”. In: *A&A* 513 (2010), A61. DOI: [10.1051/0004-6361/200911967](https://doi.org/10.1051/0004-6361/200911967).
- [Pap72] A.C. Pappas et al. “Gross properties of delayed neutron emission and β -strength functions”. In: *Nucl. Phys.* 188.1 (1972), pp. 48–64. DOI: [https://doi.org/10.1016/0375-9474\(72\)90179-0](https://doi.org/10.1016/0375-9474(72)90179-0).
- [Pfe02] B. Pfeiffer et al. “Status of delayed-neutron precursor data: half-lives and neutron emission probabilities”. In: *Prog. Nucl. Energy* 41 (2002), p. 39.
- [Pho17] Vi Ho Phong. *LuckyDoll*. July 2017. URL: <https://github.com/vihophong/LuckyDoll>.
- [Qui12] M. Quinn et al. “ β decay of nuclei around ^{90}Se : Search for signatures of a $N = 56$ subshell closure relevant to the r process”. In: *Phys. Rev. C* 85 (3 Mar. 2012), p. 035807. DOI: [10.1103/PhysRevC.85.035807](https://doi.org/10.1103/PhysRevC.85.035807).

- [Rau00] T. Rauscher et al. “Astrophysical Reaction Rates From Statistical Model Calculations”. In: *At. Data Nucl. Data Tables* 75.1 (2000), pp. 1–351. DOI: <https://doi.org/10.1006/adnd.2000.0834>.
- [REACLIB] *REACLIB web page*. URL: <https://reaclib.jinaweb.org/library.php?action=viewsnapshots> (visited on 2019).
- [Rob39a] R. B. Roberts et al. “Further Observations on the Splitting of Uranium and Thorium”. In: *Phys. Rev.* 55 (5 Mar. 1939), pp. 510–511. DOI: [10.1103/PhysRev.55.510.2](https://doi.org/10.1103/PhysRev.55.510.2).
- [Rob39b] R. B. Roberts et al. “The Delayed Neutron Emission which Accompanies Fission of Uranium and Thorium”. In: *Phys. Rev.* 55 (7 Apr. 1939), pp. 664–664. DOI: [10.1103/PhysRev.55.664](https://doi.org/10.1103/PhysRev.55.664).
- [Roe14] I. U. Roederer et al. “New detections of arsenic, selenium, and other heavy elements in two metal poor stars”. In: *ApJ* 791.1 (July 2014), p. 32. DOI: [10.1088/0004-637x/791/1/32](https://doi.org/10.1088/0004-637x/791/1/32).
- [Rud76] G. Rudstam et al. “Delayed-neutron activities produced in fission: Mass range 79–98”. In: *Phys. Rev. C* 13 (1 Jan. 1976), pp. 321–330. DOI: [10.1103/PhysRevC.13.321](https://doi.org/10.1103/PhysRevC.13.321).
- [Rud93] G. Rudstam et al. “Delayed-Neutron Branching Ratios of Precursors in the Fission Product Region”. In: *Atomic Data and Nuclear Data Tables* 53.1 (1993), pp. 1–22. DOI: <https://doi.org/10.1006/adnd.1993.1001>.
- [San08] P. Santi et al. “Reevaluation of Prompt Neutron Emission Multiplicity Distributions for Spontaneous Fission”. In: *Nucl. Sci. Eng.* 160.2 (2008), pp. 190–199. DOI: [10.13182/NSE07-85](https://doi.org/10.13182/NSE07-85).
- [Sch17] BRIKEN experiment Schedule. June 2017. URL: <http://www.nishina.riken.go.jp/rarfmt/pc-17041803.html> (visited on 12/2019).
- [Shi19] M. Shibata et al. “Merger and Mass Ejection of Neutron Star Binaries”. In: *Annu. Rev. Nucl. Part. Sci.* 69.1 (2019), pp. 41–64. DOI: [10.1146/annurev-nucl-101918-023625](https://doi.org/10.1146/annurev-nucl-101918-023625).
- [Sin95] Balraj Singh. “Nuclear Data Sheets Update for A = 76”. In: *Nuclear Data Sheets* 74.1 (1995), pp. 63–164. DOI: <https://doi.org/10.1006/ndsh.1995.1005>.
- [Skr74] K. Skrable et al. “A general equation for the kinetics of linear first order phenomena and suggested applications”. In: *Health Physics* 27(1) (1974), pp. 155–157.
- [Sne08] C. Sneden et al. “Neutron-Capture Elements in the Early Galaxy”. In: *Annu. Rev. Astron. Astrophys.* 46.1 (2008), pp. 241–288. DOI: [10.1146/annurev.astro.46.060407.145207](https://doi.org/10.1146/annurev.astro.46.060407.145207).

Bibliography

- [SYS] *Struck Innovative Systeme*. URL: <https://www.struck.de/index.html> (visited on 12/2019).
- [Tac90] T. Tachibana et al. “Improvement of the Gross Theory of Beta Decay. II: One-Particle Strength Function”. In: *Prog. Theor. Phys.* 84.4 (Oct. 1990), pp. 641–657. DOI: 10.1143/ptp/84.4.641.
- [Tak73] K. Takahashi et al. “Beta-decay half-lives calculated on the gross theory”. In: *At. Data Nucl. Data Tables* 12.1 (1973), pp. 101–142. DOI: [https://doi.org/10.1016/0092-640X\(73\)90015-6](https://doi.org/10.1016/0092-640X(73)90015-6).
- [Tan11] O. Tange. “GNU Parallel - The Command-Line Power Tool”. In: *The USENIX Magazine* 36.1 (Feb. 2011), pp. 42–47. DOI: <http://dx.doi.org/10.5281/zenodo.16303>.
- [Tar08] O.B. Tarasov et al. “LISE++: Radioactive beam production with in-flight separators”. In: *Nuclear Instruments and Methods in Physics Research Section B: Beam Interactions with Materials and Atoms* 266.19 (2008), pp. 4657–4664. DOI: <https://doi.org/10.1016/j.nimb.2008.05.110>.
- [Tar17] A. Tarifeño-Saldivia et al. “Conceptual design of a hybrid neutron gamma detector for study of β -delayed neutrons at the RIB facility of RIKEN”. In: *Journal of Instrumentation* 12.4 (Apr. 2017), P04006. DOI: 10.1088/1748-0221/12/04/p04006.
- [Tes14] D. Testov. *Effect of shell closure $N = 50$ and $N = 82$ on the structure of very neutron-rich nuclei produced at ALTO. Measurements of neutron emission probabilities and half lives of nuclei at astrophysical r-process path*. PhD thesis. NNT: 2014PA112012. Université Paris Sud, Paris, France., 2014.
- [TFA474] ORTEC, *Timing Filter Amplifier 474*. URL: <https://www.ortec-online.com/products/electronics/amplifiers/474> (visited on 12/2019).
- [Thi11] F.-K. Thielemann et al. “What are the astrophysical sites for the r-process and the production of heavy elements?” In: *Prog. Part. Nucl. Phys.* 66.2 (2011), pp. 346–353. DOI: <https://doi.org/10.1016/j.ppnp.2011.01.032>.
- [Tol19] A. Tolosa-Delgado et al. “Commissioning of the BRIKEN detector for the measurement of very exotic beta-delayed neutron emitters”. In: *Nucl. Instrum. Methods Phys. Res. A* 925 (2019), pp. 133–147. DOI: <https://doi.org/10.1016/j.nima.2019.02.004>.
- [Van05] J. Van Roosbroeck et al. “Evolution of the nuclear structure approaching ^{78}Ni : β decay of $^{74-78}\text{Cu}$ ”. In: *Phys. Rev. C* 71 (5 May 2005), p. 054307. DOI: 10.1103/PhysRevC.71.054307.

- [Ver17] D. Verney et al. “Pygmy Gamow-Teller resonance in the $N = 50$ region: New evidence from staggering of β -delayed neutron-emission probabilities”. In: *Phys. Rev. C* 95 (5 May 2017), p. 054320. DOI: 10.1103/PhysRevC.95.054320.
- [Vre05] D. Vretenar et al. “Relativistic Hartree–Bogoliubov theory: static and dynamic aspects of exotic nuclear structure”. In: *Physics Reports* 409.3 (2005), pp. 101–259. DOI: <https://doi.org/10.1016/j.physrep.2004.10.001>.
- [Wat19] Darach Watson et al. “Identification of strontium in the merger of two neutron stars”. In: *Nature* 574.7779 (2019), pp. 497–500. DOI: 10.1038/s41586-019-1676-3.
- [WC17] *Nuclear Wallet Cards*. 2017.
- [Win09] J. A. Winger et al. “Large β -Delayed Neutron Emission Probabilities in the ^{78}Ni Region”. In: *Phys. Rev. Lett.* 102 (14 Apr. 2009), p. 142502. DOI: 10.1103/PhysRevLett.102.142502.
- [Win10] J. A. Winger et al. “New subshell closure at $N = 58$ emerging in neutron-rich nuclei beyond ^{78}Ni ”. In: *Phys. Rev. C* 81 (4 Apr. 2010), p. 044303. DOI: 10.1103/PhysRevC.81.044303.
- [Win12] C. Winteler et al. “Magnetorotationally driven supernovae as the origin of early galaxy r-process elements?” In: *ApJ* 750.1 (Apr. 2012), p. L22. DOI: 10.1088/2041-8205/750/1/122.
- [Win13] C. Winteler. “Light element production in the big bang and the synthesis of heavy elements in 3D MHD jets from core-collapse supernovae”. PhD thesis. Nov. 2013.
- [Win90] J. A. Winger et al. “Structure of ^{76}Zn from ^{76}Cu decay and systematics of neutron-rich Zn nuclei”. In: *Phys. Rev. C* 42 (3 Sept. 1990), pp. 954–960. DOI: 10.1103/PhysRevC.42.954.
- [Xu14a] Z. Xu. “Beta-decay spectroscopy on neutron-rich nuclei in a range of $Z = 26 - 32$ ”. PhD thesis. Univ. of Tokyo, 2014.
- [Xu14b] Z. Y. Xu et al. “ β -Decay Half-Lives of $^{76,77}\text{Co}$, $^{79,80}\text{Ni}$, and ^{81}Cu : Experimental Indication of a Doubly Magic ^{78}Ni ”. In: *Phys. Rev. Lett.* 113 (3 July 2014), p. 032505. DOI: 10.1103/PhysRevLett.113.032505.
- [Zhi13] Q. Zhi et al. “Shell-model half-lives including first-forbidden contributions for r -process waiting-point nuclei”. In: *Phys. Rev. C* 87 (2 Feb. 2013), p. 025803. DOI: 10.1103/PhysRevC.87.025803.